Volume 6 Issue 2 (2020) · ISSN 2424-7723

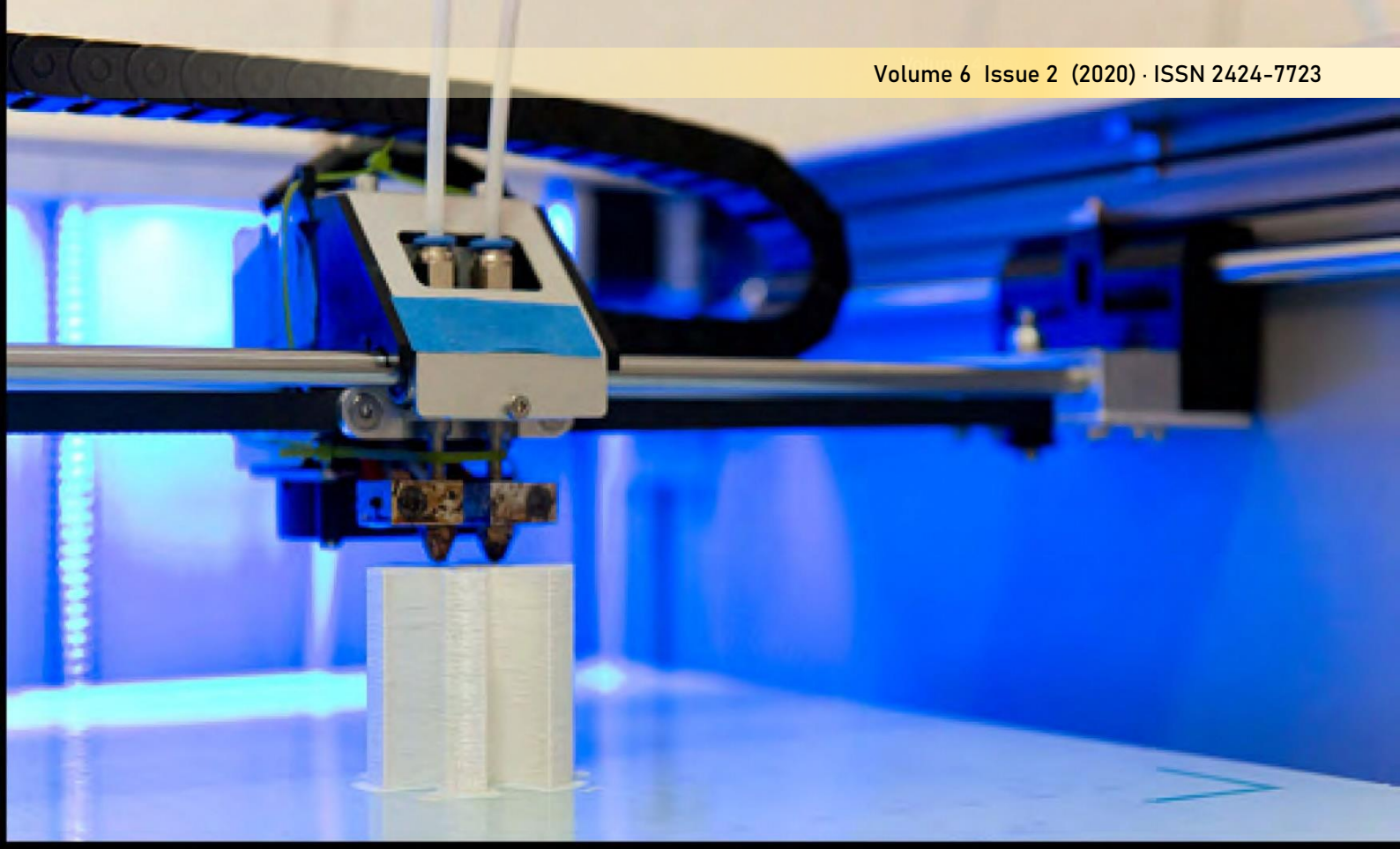

INTERNATIONAL JOURNAL OF BIOPRINTING

WHIOCE PUBLISHING PTE. LTD.
PROVIDING
FIRST-CLASS SCIENTIFIC INFORMATION
FOR TOP SCHOLARS

Volume 6 Issue 2• 2020
ISSN 2424-7723 (print) ISSN 2424-8002 (online)

INTERNATIONAL JOURNAL OF BIOPRINTING

Editor-in-Chief

Chee Kai Chua

Singapore University of Technology and Design, Singapore

WHIOCE PUBLISHING PTE. LTD.

Volume 6 | Issue 2 | 2020 | Page 1 – 124 |

International Journal of Bioprinting

https://ijb.whioce.com/index.php/int-j-bioprinting

CONTENTS

REVIEW ARTICLE

Electrically Conducting Hydrogels for Health care: Concept, Fabrication Methods, and Applications

Shweta Agarwala

Department of Engineering, Aarhus University, Aarhus, Denmark

Abstract: Electrically conducting hydrogels are gaining increasing attention due to their potential application in smart patches, biosensors, functional tissue engineering scaffolds, wound management, and implants. The current review focuses on these novel materials, their synthesis routes, and their composites. Special attention is paid to fabrication routes to produce functional composites with organic and inorganic components. The design of conductive hydrogels leads to inheritance of the advantages of each component and offers new features from the synergistic effects between the components, thus opening new application areas. The review also discusses the emerging role of 3D printing as an advanced approach toward new design, functionality, and material combination possibilities. The issue of lack of the spatial control with current techniques is highlighted, and possible new routes to solve it are discussed. The review will provide readers with knowledge tool to select appropriate methodology for designing desired hydrogel material composites.

Keywords: Conducting hydrogel, hydrogel composite, 3D printing, tissue engineering

***Corresponding Author:** Shweta Agarwala, Department of Engineering, Aarhus University, Aarhus, Denmark; Email: shweta@eng.au.dk

Received: March 20, 2020; ***Accepted:*** April 19, 2020, ***Published Online:*** April 30, 2020

Citation: Agarwala, 2020. Electrically Conducting Hydrogels for Health care: Concept, Fabrication Methods, and Applications, *Int J Bioprint*, 6(2):273. DOI: 10.18063/ijb.v6i2.273

1 Introduction

Biological functions are complex and replicating them requires understanding and transforming variety signals such as biochemical, electrical, and mechanical. A large number of materials have been developed as bioactive scaffolds to transmit such signals. Hydrogels have been at the forefront of the material development especially for tissue engineering. They possess ideal characteristics of extra-cellular matrix (ECM), cell support, biocompatibility, and Young's modulus close to human tissue[1,2]. Hydrogels have spatially cross-linked chain network composed of natural and/or synthetic hydrophilic polymer chains that can absorb a large amount of water while maintaining 3D structure, which makes them highly compatible for biomedical applications[2].

Human body is a resident for electrical energy. Many research work has been focusing on understanding the effect of electrical signal on cells[3]. It is predicted that electrical stimulation can impact cells adhesion, differentiation, and growth, but the underlying phenomenon is not well understood. Recent developments in bioelectronics, bioionics, and neural interfaces have placed demands for electrically conducting scaffolds[4,5]. Although hydrogels have found niche application in tissue engineering, they are inherently insulating by nature. Recent research has shown that hydrogels not only possess necessary characteristics to support biological species but can also interface with electrical circuitry if modified[4,5]. Hence, research on conducting hydrogels have gained widespread interest for applications such as health recording electrodes,

stimulating electrodes, biosensors, biomedical patches, implantable devices, and electronic skin (**Figure 1**).

This review is dedicated to conducting hydrogels and their fabrication methods. The paper delves on modification aspects of hydrogels, to make them conducting through addition of metal nanoparticles, carbon-based materials, and conducting polymers. The conducting material may be physically or chemically attached to the hydrogel matrix. The electrical conductivity is influenced by the sizes of the nanoparticles, the presence of water bound by hydrogels, and the presence of any additional components that may affect the conductivity. Although copolymerization and mixing of materials are the standard approach to synthesize the conducting hydrogels, additive manufacturing has proven time-effective and added customization to the characteristics. The review will focus on discussing the work carried out on 3D printing of conducting hydrogels. The in-depth discussion of various 3D printing techniques and equipment is beyond the scope of this review. The review will highlight key research findings to generate electrically active, mechanical stiff, and multi-functional hydrogels.

2 Material Innovation

This section will discuss material synthesis for electrically conducting hydrogels. Most hydrogels

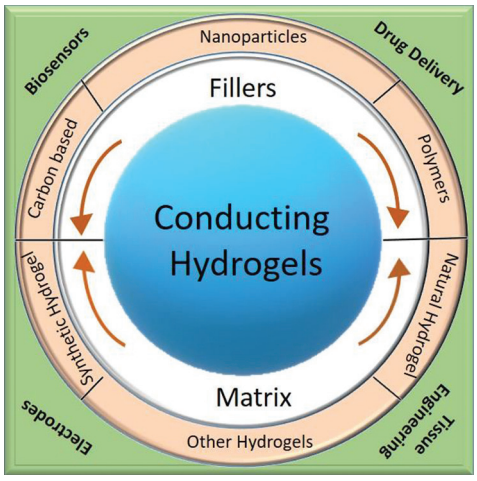

Figure 1. Schematic illustration of conducting hydrogels, their components and applications.

are inherently insulating, and additives enhance their electrical behavior. The conductivity of most of the hydrogels is at or below tens $mS.cm^{-1}$. It is to be noted that most of the time the conductivity reported in the literature refers to the ionic conductivity of the electrolyte that swells them. The contribution from additives materials to overall conductivity in such cases is small. However, recent research efforts in this direction have shown promise in inducing electrical conductivity from the additive materials. Table 1 summarizes the achieved electrical conductivities in various hydrogels.

2.1 Conducting hydrogels with metal nanoparticles

Metal nanoparticles are well known to possess good electrical conductivity and are also easier to process. This makes them an obvious choice

Table 1. Summary of the material composites and their electrical conductivities achieved to make conducting hydrogels.

Hydrogel	Additive	Conductivity ($mS.cm^{-1}$)	Reference
PANI	Cellulose	70	39
	MWCNT	1540	27
	Graphene	182	31
PPy	PEG	4.3	43
	PAA	5	47
	Cellulose	7.8	40
	CuPcTs	780	49
	rGO	480	32
PEDOT	PAA	1.2	48
	PAAM	2.6	46
	PEG	16.9	37
	PU	120	38
PAA	Silver	572	13
	Gum	33.5	88
	Graphene	10^{-3}	28
PAAM	Graphene	0.2	27
Chitosan	Graphene	1	26
PNIPAM	GO	285×10^{4}	25
	CNT	0.7	25
Collagen	CNT	10^{-7}	20
PEDOT:PSS	CNT	10^{5}	24
Gelatin methacrylate	CNT	10^{2}	21
PTAA	MAAG	0.1	36

for reinforcement material in hydrogel matrix. The final composite is synergistic, unique and has desired properties that are not found in individual components. The final properties depend on the type of nanoparticles incorporated, which in turn determines the proposed application. Silver (Ag) and gold (Au) are the most commonly used conducting materials for hydrogels. Silver has an added antimicrobial property and for this reason, it is blended with hydrogels to make functional coatings[6]. A study done by Endo *et al*. revealed the relationship between silver ion concentration and swelling rate of hydrogel[7]. A higher concentration of silver ions results in better conductivity, but reduced the swelling ratio and vice versa. So far, silver nanoparticles have been added to many hydrogels, namely polyacrylamide (PAAM), polyacrylic acid (PAA), *N*-isopropylacrylamide (NIPAAm), methyl methacrylate, and polyvinyl alcohol (PVA)[8-12]. Silver nanoparticles added to PAA through *in situ* reduction and polymerization showed swelling dependent electrical conductivity, which could be varied from 13.6 to 572 $mS.cm^{-1}$[13]. The use of gold for making conducting hydrogel remains limited due to its high cost. Gold nanoparticles were utilized to make conducting poly(3,4-ethylenedioxythiophene)/ poly(acrylic acid) (PEDOT/PAA) hydrogel, which exhibited excellent catalytical activity for p-nitophenol[14]. It has been proven that by varying gold concentrations, it is possible to change the properties of the final composite. There are sporadic reports on employing metal nanoparticles for making conducting hydrogels. Platinum (Pt) nanoparticles have also been deployed in polyaniline (PANI) hydrogel to make heterostructures for a glucose sensor[15]. The porous structure of hydrogels favors trapping the nanoparticles and immobilizing enzymes for glucose sensing. In one of the early reports, Fuhrer *et al.* incorporated magnetic cobalt nanoparticles to hydrogel backbone[16]. The cobalt nanoparticles were encapsulated in stable carbon shells, which were covalently modified to have vinyl-termination groups. Copolymerization of carbon coated cobalt and 2-hydroxyethyl methacrylate was carried out to form a magnetically active hydrogel. Crosslinking cobalt nanomagnets into the hydrogel provided a safe way to reduce magnetic particle migration or loss. Iron oxide magnetic nanoparticles have been added in a hydrogel to provide remedy for methylene blue contaminated water[17].

Apart from 3D nanoparticles, 1D (one-dimensional) nanostructures have been used to enhance the electrical conductivity of hydrogels. This is motivated by the fact that 1D nanostructures have better electrical transport[18]. Stretchability is an additional property that can be achieved in the final hydrogel composite through 1D nanostructures, as they act as electrical connectors during bending, stretching, or flexing of the material[19]. A recent report by Lim *et al.* confirmed the theory where silver nanowires were chosen as fillers for alginate hydrogel[20]. A wearable antenna patch was fabricated using the silver nanowire alginate composite with excellent conductivity, tough structural integrity, and stretchability. The fabrication procedure did not involve formation of covalent bonds by polymerization, thus making it compatible to incorporate different inorganic and metallic nanomaterials.

2.2 Conducting hydrogels with carbon material

Carbon based materials such as carbon nanotubes (CNT), carbon black (CB), and graphene have played an important role in wide range of research fields due to their electrical, thermal, and mechanical properties. Their enhanced electrical properties are highly attractive, and this shows their potential to be used as reinforcement and additive material for composites. Hence, metal nanoparticles are being replaced by carbon-based materials such as carbon nanotubes, graphene, and carbon black to add more functionalities, especially because they have shown higher compatibility for biological species compared to metal counterparts. Better response to biological species comes from the fact that carbon-based materials can be trapped in synthetic and natural hydrogels. This immobilization leads to better biocompatibility. An early attempt was made by Cho *et al.* to encapsulate CNTs into collagen to electrically stimulate PC12 cells[21]. A loading of <1% CNTs

in collagen led to enhanced conductivity and flexibility. It is argued that adding CNTs in collagen has many advantages compared to pure CNT or only collagen scaffolds. First, CNTs enhances the structural integrity of the fabricated scaffold. Second, such composites reduce the mismatch between Young's modulus of human tissues and rigid electrodes. Third, collagen matrix is effective in confining CNTs and thus reducing harmful effect due to migration. Khademhosseini's research group developed conducting cardiac patches by mixing CNT in gelatin methacrylate (GelMA) hydrogel[22]. The composite material not only had excellent mechanical integrity but also showed advanced electrophysiological functions. In a similar work, to construct heart patches, Pok *et al*. added CNTs to chitosan[23]. The resulting scaffold supported cardiomyocyte functionalization and speeded up conduction velocity to achieve beating heart functionality of a rat. CNTs have been added repeatedly to various hydrogels such as chitosan, poly(3,4-ethylenedioxythiophene) doped with poly(4-styrenesulfonate) (PEDOT:PSS), and poly (N-Isopropylacrylamide) (PNIPAM) for electrocatalysis, battery electrode, and fuel cell[24-26]. A different morphology of core-shell of hydrogel composite was synthesized using PANI and CNT[27].

CNTs were replaced with graphene in chitosan for tissue engineering application. It showed similar swelling mechanism and yielded higher mechanical strength of the final composite material[28]. Biological scaffold made of graphene oxide and PAAM composite hydrogel displayed muscle such as stiffness apart (Young's modulus of approximately 50 kPa) from conductivity[29]. Enhanced proliferation and myogenic differentiation were observed in the scaffold. Graphene oxide shows good suspension in water but aggregates in acidic medium. In a modified approach, Alam *et al.* tailored the oxidation degree of graphene sheets by controlling the sonication time and acid concentration[30]. Graphene/polyacrylic acid hydrogel was formed using *in situ* polymerization process, where graphene sheets are mixed with acrylic acid in the presence of a cross-linker and an initiator. The synthesized composite demonstrated high mechanical performance with low percolation threshold of electrical conductivity at 0.4% with added feature of pH sensitivity[30]. Graphene was also added to PANI and PPy[31,32]. Most of the other work on graphene-based hydrogels was targeted toward electro-chemical and electrical applications[33,34].

2.3 Conducting hydrogels with polymers

Concerns on biocompatibility of metal nanoparticles and carbon-based materials have led to increased interest in replacing them with polymeric materials. Polymeric materials are used in various forms namely particles, core-shells, micelles, and dendrimers[35-38]. There are two common routes through which polymers are added into the hydrogels, (i) electro- or chemical polymerization of conducting monomer in prefabricated hydrogel and (ii) mixing the precursor monomer followed by polymerization. The main idea is to entrap the conducting polymer chains in the hydrogel matrix. Polyaniline (PANI) and cellulose composite hydrogel exhibited a continuous and linear crawling motion under a low applied electric field, apart from high compressive strength[39]. Cellulose was also mixed with polypyrrole (PPy) in an ionic liquid, giving rise to high electrical conductivity of 7.83×10^{-3} $S.cm^{-1}$[40]. Gilmore *et al.* demonstrated the fabrication of hybrid composite composed of PPy and PAAM. PPy was directly electropolymerized on the hydrogel[41]. The work has since led to plethora of polymer-hydrogel combinations for various applications. Most common tissue engineering application is for cardiac tissues. Poly(triaryl amine) (PTAA) was homogeneously combined with methacrylate hydrogel achieving conductivity similar to myocardial tissues[42]. High-quality conductive composite hydrogels composed of single-walled carbon nanotubes (SWNTs), polypyrrole (PPy) and poly(ethylene glycol) diacrylate (PEGDA) hydrogel were successfully fabricated through interfacial polymerization (IP)[43]. PEDOT:PSS is a high conductivity polymer and heavily used in organic electronic applications. PEDOT:PSS was mixed with polyethylene glycol (PEG) to make

electrically conductive scaffold for muscle and nerve tissues[44]. Sasaki *et al.* reported the fabrication of the hydrogel-based devices with high electrically conductivity using a combination of chemical polymerization and electropolymerization of PEDOT and polyurethane (PU)[45]. Mechanically strong conducting hydrogels composed of PAAM and PEDOT-PSS was synthesized through the construction of a special double-network (sDN) structure[46]. PAA has been polymerized with both PPy and PEDOT resulting in pH responsive and gel with high mechanical strength, respectively[47,48]. Experimenting with a different class of materials, copper phthalocyanine-3,4′,4″,4‴-tetrasulfonic acid tetrasodium salt (CuPcTs) was added to PPy through a supramolecular self-assembly approach[49]. The steric and electrostatic interactions between CuPcTs and PPy favored the self-assembly of PPy chains, which promotes the 1D growth of PPy and resulted in the formation of interconnected nanofibers.

3 Methods of Fabrication

3.1 Traditional approaches

Several approaches have been taken to synthesize conducting hydrogels depending on the nature of the additive and hydrogel matrix. The most common method for aqueous compatible conducting materials is to simply mix with the hydrogel components aided by ultrasonic energy or heating. However, there are five other main approaches that have been identified in the literature to synthesize conducting hydrogel composites with uniform distribution, as shown in **Figure 2.** These includes hydrogel monomers with cross-linkers and nanoparticles gelated together[50]; physically embedding nanoparticles into hydrogel matrix after gelation[51]; reactive nanoparticle formation aided by the hydrogel network where nanoparticle precursors are loaded in the gel[52]; cross-linking using nanoparticles to form hydrogels[53]; and hydrogel formation using nanoparticles, polymers, and other molecules[54].

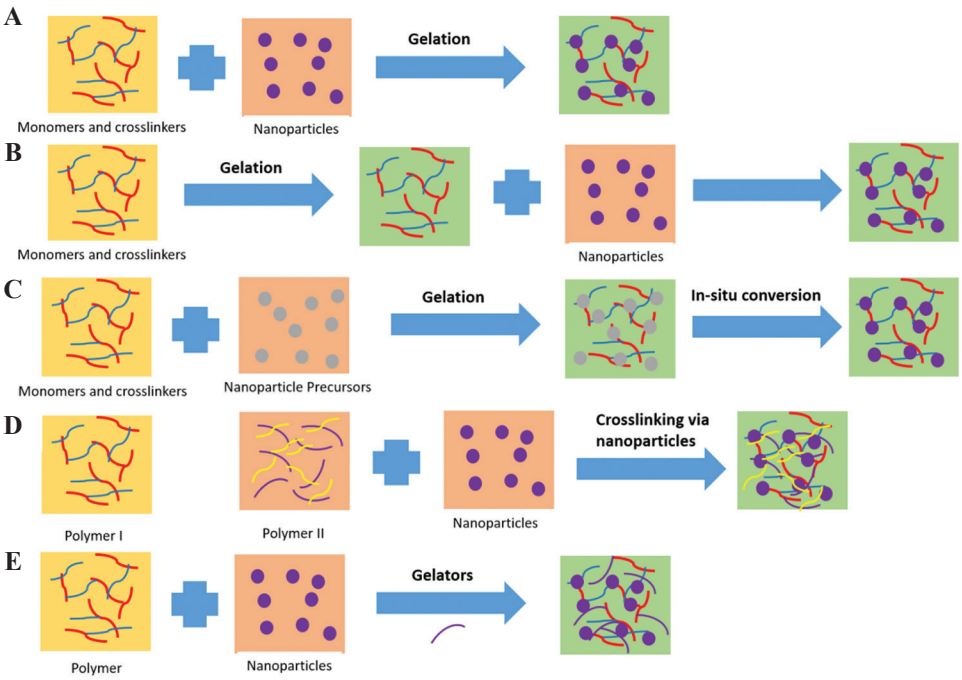

Figure 2. Schematic diagram depicting various approaches to synthesize conducting hydrogel: (A) hydrogel monomers with cross-linkers and nanoparticles gelated together; (B) physically embedding nanoparticles into hydrogel matrix after gelation; (C) reactive nanoparticle formation aided by the hydrogel network where nanoparticle precursors are loaded in the gel; (D) cross-linking using nanoparticles to form hydrogel; and (E) hydrogel formation using nanoparticles, polymers, and other molecules.

Gold nanoparticles were added into the solution of monomer of *N*-isopropylacrylamide/acrylamide (NIPAAm/AAm) followed by addition of the gelation initiator ammonium persulfate (APS) and accelerator tetramethylethylenediamine (TMEDA) by Sershen *et al.* to form gold-hydrogel composite[51]. Gold nanoparticles tend to agglomerate under electric field and hence cannot be electropolymerized. To this end, gold nanoparticles were incorporated in PAAM hydrogel after the gel has been formed. The hydrogel was formed through a "breathing in" process which consists of (i) collapsing the gel by placing it in acetone and causing the water to be expelled; and (ii) placing the dehydrated gel in aqueous solution of gold nanoparticles. This step caused the hydrogel to swell up again, termed as breathing in; and (iii) washing the hydrogel with water to remove any weakly surface-adsorbed nanoparticles. The above steps were repeated many times to obtain the desired nanoparticle density in the final hydrogel composite. There are many reports available, which involve loading the nanoparticle precursors into the hydrogel matrix rather than adding the preformed nanoparticles. Although Langer's group initiated the work in this direction[52], Saravanan *et al.* improved the methodology to form silver laden NIPAAm hydrogel[55]. The group carried out free-radical cross-linking polymerization of acrylamide monomer in an aqueous medium containing silver ions. Different reducing agent for nanoparticle ions and precursors has been reported. The benefit of this method is the formation of hydrogels with enhanced mechanical strength. In an alternate approach, the surface of nanoparticles was functionalized by adding cross-linking groups to bind with the hydrogel. Zhang *et al.* extensively studied several combination of semiconductor nanoparticle-hydrogel composites through self-initiated polymerization under light irradiation[56]. Silicon nanoparticles were added to a hydrogel framework by *in situ* polymerization to synthesize a well-connected 3D structure.

Fabricating electrically conducting hydrogels mostly employs traditional approaches. They may be well-established, but there are some limitations. One of the most common issues encountered is agglomeration and poor dispersion of the additives in the hydrogel matrix. As discussed above, this issue can be overcome to some extent by selecting suitable solvents for dispersion. Due to the use of metal nanoparticles, namely, silver and gold, the overall cost of the final material may be high. This prevents their use in commercial application. There are also some reports wherein the response time of devices fabricated using conducting hydrogels is slower. Much work needs to be done to improve the overall device performance in conducting hydrogels.

3.2 3D printing

Additive manufacturing, also called 3D printing, is defined as "process of joining materials to make parts from 3D model data, usually layer on layer, as opposed to subtractive manufacturing and formative manufacturing methodologies" according to the International Organization for Standardization (ISO)/American Society for Testing and Materials (ASTM) 52900:2015 standard. It has been a disruptive technology for fabricating complex shapes in various materials, thus overcoming the limitations of traditional manufacturing techniques[57,58]. 3D printing of metals is a mature technology and polymer printing is making its way to industries. This technology has forayed into electronic and biomaterials and opened doors for design and device innovation[59-61]. Conducting hydrogels have seen a surge in being processed using 3D printing technique due to ease of constructing complex shapes, customized constructs, and time efficient processing[61-64]. 3D printing is an umbrella term and mostly three different techniques have been applied to print conducting hydrogels namely 3D bioplotting, inkjet, and light-based technique[65-67]. In 3D bioplotting, the conducting hydrogel material is extruded from an orifice on to a substrate of choice (**Figure 3A**). The technique generally relies on the shear thinning behavior of the hydrogels, thus making them flow on applying pressure and allowing their deposition[65,68]. Inkjet technique uses a piezoelectric head for the orifice.

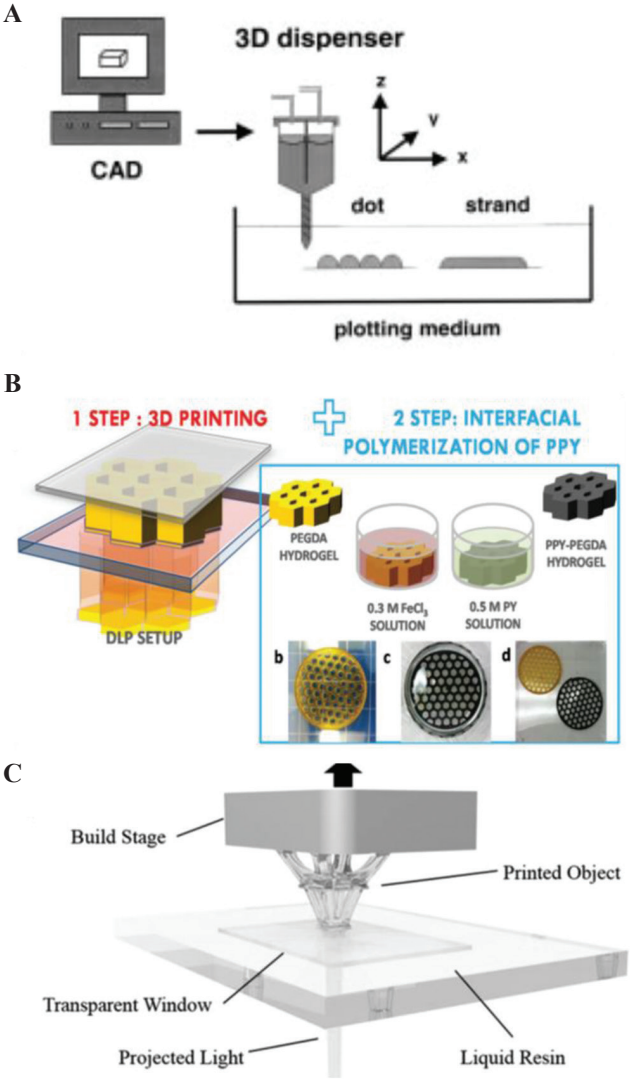

Figure 3. Sketch of (A) 3D bioplotting system (Reproduced with permission[65]) (B) digital light projector (DLP) 3D printing system to 3D print conducting hydrogel scaffolds (Reproduced with permission[74]), and (C) stereolithography process (Reproduced with permission[75]).

A piezoelectric material deforms on applying voltage or current. Thus, the orifice opening can be controlled by varying the voltage applied to the printer head. Inkjet printing creates small droplets (sub-micron volume), which are deposited on the surface. Small volume of material deposition, as against large material ejection through extrusion, helps to print high-resolution constructs and scaffolds[66]. Stereolithography (SLA) and direct-laser writing (DLW) are light-based techniques, wherein either a material precursor is illuminated by light or a pattern is projected[67,69]. Curing of the material takes places in selected regions where the light hits it. In most printers, the printhead and platform move in *X*-*Y* directions relative to each other. However, here a *Z*-displacement of the precursor reservoir is performed to fabricate a 3D shape. Detailed discussion on operation and methodology of these techniques is beyond the scope of this review. Hydrogel to be processed through the printer needs to be converted into an ink format. Ink development is considered one of the most important aspects of 3D printing. Hydrogel inks need to have the right rheological properties to fulfill the physical and mechanical needs of the orienting process. Ink formulation, properties, and optimization are a widely researched[70-72] area and will not be discussed in this paper.

Sayyar *et al*. used extrusion based bioplotting system to print graphene-chitosan composite biocompatible scaffolds. Addition of 3% of graphene in the composite resulted in 200% enhancement of mechanical strength[28]. They further developed a new UV-crosslinkable conducting hydrogel based on the same materials[73]. Functionalized chitosan served as the host polymer and chemically converted graphene as the filler. The incorporation of graphene into chitosan resulted in cytocompatible matrix with enhanced mechanical, cell adhesion, and electrical properties. In creating a composite of two polymers, namely, poly(ethylene glycol)diacrylate and polypyrrole digital light processing 3D printing technique was combined with interfacial polymerization[74] (**Figure 3B**). The achieved composite material was electroactive and could be drawn into complex geometry. Silica nanoparticle has been used as additives for many hydrogels to impart novel functionalities. Odent *et al.* added silica nanoparticles to ammonium containing PAAM and processed through SLA machine[75] (**Figure 3C**). The resulting composite hydrogel was stretchable, mechanically tough and ionically conducting, and the enhanced properties were due to addition of anion charged sulfonated silica nanoparticles. It was found that the stiffness of the composite hydrogel increased with increasing

amount of silica nanoparticles. In another report, a hybrid hydrogel of silica/alumina was modified by adding poly(N-isopropylacrylamide) (PNIPAm) microparticles, resulting in a printable material that responded to both heat and electrical stimuli[76]. The water molecules trapped in PNIPAm are released to the silica/alumina matrix on heating. PNIPm particles are dehydrated and act as light scattering centers leading to an optical change from opaque to transparent. The response of the material to electrical stimulation was exploited for fabricating an optical switch. Resin based SLA was also used to print all polymer-based composite based on the polyethylene glycol diacrylate (PEGDA). Poly(3,4-ethylenedioxythiophene) (PEDOT):polystyrene sulfonate (PSS) aqueous solution was freeze-dried and mixed with PEGDA to make it conducting[77]. Increasing the PEDOT:PSS concentration, enhanced the electrochemical characteristics of the printed platform, which was used to electrically stimulate cells for neuronal differentiation. 3D printing enables fabricating complex construct shapes with customization as anatomy of humans are very different from each-other.

Commercialization of 3D printing whether for conducting hydrogels or other biomaterials is still far away. This is due to many issues that need to be resolved before industries can take it up for mass-production. Hydrogels are considered soft materials and their lack of mechanical strength poses limitation in printing sturdy 3D constructs and shapes. These materials are unable to follow the original design models, as the printed construct does not retain the original shape. Achieving functional gradients and hierarchical properties have also been challenging and new design approaches are being developed to tackle them. 3D printing is heralded as a unique solution to print human organs off-the-shelf to counter their storage. However, precision printing in layer-by-layer fashion mimicking human tissues is a mammoth task. A prominent weakness is the lack of precise control on the cellular microenvironment, which governs cell attachment and proliferation. Various professional and off-the-shelve hobbyist 3D printers are available, but few are open-source which allows users to define desired toolpaths. Lack of such a capability does not allow the users to write customized codes or load their model files.

3.3 Fabrication enabling spatial distribution

Conducting hydrogels can now be processed into complex shapes and structures with the help of 3D printing. However, one critical challenge still plagues them. When conducting material is added to the hydrogel, they may be distributed homogeneously but they cannot be confined spatially in desired spots. There has been growing needs to confine conducting material in space within hydrogels and not distribute evenly. This can lead to building electrical circuits encompassed within hydrogels. Some emerging applications may require the conducting material not distributed in the entire hydrogel matrix but be restricted in specific spots to enable electrical stimulation. This section of the paper deals with latest research efforts directed to print soft electrical circuits on hydrogels. With the assistance of transfer techniques and 3D printing, it is now possible to lay circuits on hydrogel surfaces. Such platforms find application in wound management, drug delivery, on-skin patches, implantable, and bioelectronic devices. In one of the early reports, Sekine *et al.* used micropatterning to lay down PEDOT on agarose hydrogel in a predefined fashion[78]. The fabricated platform was organic, moist and served as flexible electrode to cultivate contractile myotubes. A similar peel and transfer process were applied to fabricate silver nanowire (AgNW)-based microelectrode on polydimethylsiloxane (PDMS) substrate[79] (**Figure 4A**). The desired microelectrode pattern was first fabricated on glass substrate using photolithography and later directly transferred to PDMS based hydrogel. Electrical conductivity could be control by varying the density of silver nanowires. Peel and transfer methods are neither reproducible nor up-scalable for commercial use. Shay *et al.* and their group created microfluidic channels through soft lithography in PDMS[80]. Combination of acrylamide (AAm) and acrylic acid (AA) was used as the hydrogel material to fill the

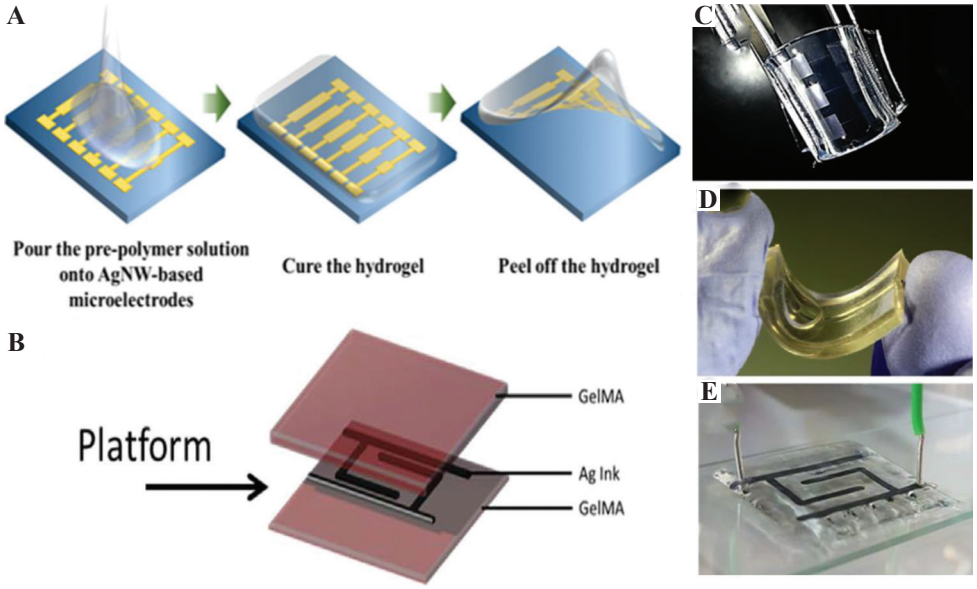

Figure 4. Schematic representation of (A) peel and transfer process (Reproduced with permission[79]), and (B) 3D printing microvalve process for spatially resolved microelectrode circuits on hydrogel substrates (Reproduced with permission[81]). Photograph of (C) bended AgNW-based microelectrodes on hydrogel (Reproduced with permission[79]), (D) liquid metal injected PDMS layers for ECG electrode (Reproduced with permission[80]), and (E) interdigitated electrode sandwiched between two hydrogel layers (Reproduced with permission[81]).

holes, while liquid metal eutectic gallium indium (EGaIn) was injected into the channels to form flexible electrodes. Agarwala *et al.* demonstrated the usability of 3D printing by printing silver nanoparticle ink over gelatin methacryloyl (GelMA) hydrogel[81]. They printed interdigitated electrode and micro-heater design with the silver nanoparticle ink sandwiched between printed layers of hydrogel loaded with cells (C2C12 mouse cells and human fibroblast cells) (**Figure 4B**). Authors studied cell proliferation under electrical stimulation.

4 Biomedical Applications for Conducting Hydrogels

4.1 Biosensors

Biosensors have been at the forefront of the biomedical research in helping to collect clinically relevant data for medicinal activity, surgery, and intensive care[82]. Electrodes used for sensing biological functions or stimulating tissues usually require non-fouling surface, which are resistant to protein adsorption. Fouling can significantly reduce the performance of the electrodes by adsorption of biological materials such as proteins, cells, and oligonucleotides[83]. Implantable devices and electrodes have been found to give rise to inflammatory response due to exposure to body fluids. This leads to tissue damage and can be tackled through material – tissue interactions that include the electro-stimulated release of bioactive agents at the site of implantation. Non-conducting hydrogel coatings have shown high interfacial impedance and thus, conducting hydrogels are finding much use in such scenarios. Composites of poly(HEMA-co-PEGMA) and a cross-linker, tetraethylene glycol diacrylate (TEGDA), have been formulated for biosensing applications[84].

4.2 Drug delivery vehicles

Drug delivery vehicles are scaffolds and platforms that allow a pharmaceutical compound to be released on or within human body for therapeutic effects. Hydrogels are natural candidate for such application due to their porous network, which can be controlled by managing the density of cross-linkers. Electroactive hydrogels are the

new generation of smart materials that allow the direct delivery of electrical signals to control the delivery of the drug. PAAM and PPy were used to make a cylindrical drug delivery device[85]. Controlled release of compounds was demonstrated for the treatment of schizophrenia and bipolar disorder. Some treatments may require delayed release of the medicinal compounds. To this end, poly(p-phenylenevinylene) (PPV) was used to create a hydrogel with PAAM, where the release profile was optimized using cathodic potential[86]. The release of salicylic acid was delayed from 3 h to 15 h after application of appropriate potential. Some other conducting hydrogels investigated for drug delivery are based on gum ghatti, vinyl monomers, and aniline[87-89]. The electro-stimulated devices made from these materials benefit from high loading capacity and low voltage actuation. There are, however, many limitations to the current system of drug delivery using conducting hydrogels. First, there are active and passive losses of the loaded drug through exchange with the environment and by diffusion, respectively. Second, many of these materials suffer from low diffusion coefficients of the drug resulting in poor release kinetics. Finally, many of these materials are affected from low drug loading capacity. Incorporating nanoparticles is not just impart electrical conductivity but also improves drug loading capacity through increase in surface area[90]. Graphene oxide (GO) has been widely researched to make conducting hydrogels, where the resulting material has shown no passive drug diffusion[91,92]. GO was combined with PPy and PEDOT to generate electrically active composite.

4.3 Tissue engineering

Hydrogels have been a success in tissue engineering and tissue regeneration for various human organs. Conducting hydrogels have been attractive for cell growth, adhesion, and proliferation of muscles, cardiovascular nerves, and bone tissue cells[78,93-95]. PTAA and methacrylate aminated gelatin were used in cardiac tissue engineering demonstrating a conductivity up to 10^{-1} m.S.cm^{-1}, which is similar to the conductivity of myocardial tissue. This study demonstrated positive effects on cardiac differentiation efficiency[42]. A conducting hydrogel composed of PPy/graphene/chitosan composite good adhesion, proliferation, and viability toward fibroblast cells[28]. A conducting tissue engineering scaffold for muscle and nerve tissues was fabricated using PEDOT:PSS and PEG hydrogel mix[44]. In another variation, PEDOT and PU were mixed to fabricate a hydrogel-based device. The PEDOT/PU hydrogel exhibited high electrical conductivity of up to 120 S. cm^{-1} at 100% elongation[45].

5 Conclusion and Outlook

We have reviewed conducting hydrogel composites as the state-of-the-art and versatile class of materials that are gaining attention due to their suitability for various applications. The review summarizes synthesis methods and strategies to achieve electrical conduction in otherwise insulating hydrogels. Incorporation of nanoparticles, carbon-based materials, and polymers has been discussed, and this provides better understanding to the readers to design novel combination of materials for desired applications. Working with conducting hydrogels has its own limitations, especially at the hydrogel device interface. Adhesion of hydrogels layers and their dehydration over longer time span pose stability issues. In many reports, the biocompatibility tests are limited to *in vitro* screening, and further animal studies may be required. Conducting scaffolds can provide ideal platform for regenerative tissue engineering. However, role of electrical stimulation for cell growth is poorly understood. We have also delved into the area of 3D printing for conducting hydrogels. Much work is needed to determine most promising printing technique and functionalization approaches for 3D printed conducting hydrogels. We have also discussed on how 3D printing can lay down materials in desired locations within a hydrogel, thus creating flexible circuits instead of homogeneous conducting material. The area of conducting hydrogels is still full of unresolved technological challenges, and thus provides researchers with opportunity for

development, as this field is growing fast beyond its early stage. Improvement in the conductivity of the hydrogels may be one research direction, while incorporating new functionalities such as biodegradability and mechanical strength can open new avenues for applications. Innovation is also required in fabrication methods to allow varied composition of hydrogels to be laid down in desired fashion.

Acknowledgments

The work was supported by the Department of Engineering, Aarhus University, Denmark.

References

1. Miyata T, Uragami T, Nakamae K, 2002, Biomolecule-sensitive Hydrogels. *Adv Drug Deliv Rev*, 54:79–98. DOI: 10.1016/s0169-409x(01)00241-1.
2. Hoffman AS, 2012, Hydrogels for Biomedical Applications. *Adv Drug Deliv Rev*, 64:18–23.
3. Hardy JG, Villancio-Wolter MK, Sukhavasi RC, 2015, Electrical Stimulation of Human Mesenchymal Stem Cells on Conductive Nanofibers Enhances their Differentiation Toward Osteogenic Outcomes. *Macromol Rapid Commun*, 36:1884–90. DOI: 10.1002/marc.201500233.
4. Guiseppi-Elie A, 2010, Electroconductive Hydrogels: Synthesis, Characterization and Biomedical Applications. *Biomaterials*, 31:2701–16. DOI: 10.1016/j.biomaterials.2009.12.052.
5. Distler T, Boccaccini AR, 2019, 3D Printing of Electrically Conductive Hydrogels for Tissue Engineering and Biosensors-a Review. *Acta Biomater*, 101:1–13. DOI: 10.1016/j.actbio.2019.08.044.
6. Nair LS, Laurencin CT, 2007, Silver Nanoparticles: Synthesis and Therapeutic Applications. *J Biomed Nanotechnol*, 3:301–16.
7. Endo T, Ikeda R, Yanagida Y, *et al*., 2008, Stimuli-responsive Hydrogel-silver Nanoparticles Composite for Development of Localized Surface Plasmon Resonance-based Optical Biosensor. *Anal Chim Acta*, 611:205–11. DOI: 10.1016/j.aca.2008.01.078.
8. Vimala K, Sivudu KS, Mohan YM, *et al*., 2009, Controlled Silver Nanoparticles Synthesis in Semi-hydrogel Networks of Poly (Acrylamide) and Carbohydrates: A Rational Methodology for Antibacterial Application. *Carbohydr Polym*, 75:463–71. DOI: 10.1016/j.carbpol.2008.08.009.
9. Bardajee GR, Hooshyar Z, Rezanezhad H, 2012, A Novel and Green Biomaterial Based Silver Nanocomposite Hydrogel: Synthesis, Characterization and Antibacterial Effect. *J Inorg Biochem*, 117:367–73. DOI: 10.1016/j.jinorgbio.2012.06.012.
10. Mohan YM, Lee K, Premkumar T, *et al*., 2007, Hydrogel Networks as Nanoreactors: A Novel Approach to Silver Nanoparticles for Antibacterial Applications. *Polymer*, 48:158–64. DOI: 10.1016/j.polymer.2006.10.045.
11. Wei QB, Fu F, Zhang YQ, *et al*., 2014, Preparation, Characterization, And Antibacterial Properties Of Ph-Responsive P(MMA-Co-MAA)/Silver Nanocomposite Hydrogels. *J Polym Res*, 21:349. DOI: 10.1007/s10965-013-0349-4.
12. Juby KA, Dwivedi C, Kumar M, *et al*., 2012, Silver Nanoparticle-loaded PVA/gum Acacia Hydrogel: Synthesis, Characterization and Antibacterial Study. *Carbohydr Polym*, 89:906–13. DOI: 10.1016/j.carbpol.2012.04.033.
13. Devaki SJ, Narayanan RK, Sarojam S, 2014, Electrically Conducting Silver Nanoparticle-polyacrylic Acid Hydrogel by *In situ* Reduction and Polymerization Approach. *Mater Lett*, 116:135–8. DOI: 10.1016/j.matlet.2013.10.110.
14. Xiao H, Xia Y, Cai C, 2013, Conducting Polymer Hydrogel Reactor for Synthesizing Au Nanoparticles and Its Use in the Reduction of P-nitrophenol. *J Nanopart Res*, 15:1521. DOI: 10.1007/s11051-013-1521-9.
15. Zhai D, Liu B, Shi Y, 2013, Highly Sensitive Glucose Sensor Based on Pt Nanoparticle/Polyaniline Hydrogel Heterostructures. *ACS Nano*, 7:3540–6. DOI: 10.1021/nn400482d.
16. Fuhrer R, Athanassiou EK, Luechinger NA, *et al*., 2009, Crosslinking Metal Nanoparticles into the Polymer Backbone of Hydrogels Enables Preparation of Soft, Magnetic Field-driven Actuators with Muscle-like Flexibility. *Small*, 5(3):383–8. DOI: 10.1002/smll.200801091.
17. Mittal H, Ballav N, Mishra SB, 2014, Gum Ghatti and Fe_3O_4 Magnetic Nanoparticles Based Nanocomposites for the Effective Adsorption of Methylene Blue from Aqueous Solution. *J Ind Eng Chem*, 20:2184–92. DOI: 10.1016/j.jiec.2013.09.049.
18. Yuan B, Cademartiri L, 2015, Flexible One-dimensional Nanostructures: A Review. *J Mater Sci Technol*, 31: 607–15.
19. Gong S, Cheng W, 2017, One-dimensional Nanomaterials for Soft Electronics. *Adv Electron Mater*, 3:1600314. DOI: 10.1002/aelm.201600314.
20. Lim C, Shin Y, Jung J, 2019, Stretchable Conductive Nanocomposite Based on Alginate Hydrogel and Silver Nanowires for Wearable Electronics. *APL Mater*, 7:031502.

DOI: 10.1063/1.5063657.

21. Cho Y, Borgens RB, 2010, The Effect of An Electrically Conductive Carbon Nanotube/Collagen Composite on Neurite Outgrowth of PC12 Cells. *J Biomed Mater Res A*, 95:510–7. DOI: 10.1002/jbm.a.32841.
22. Shin SR, Jung SM, Zalabany M, *et al*., 2013, Carbon-nanotube-embedded Hydrogel Sheets for Engineering Cardiac Constructs and Bioactuators. *ACS Nano*, 7:2369–80. DOI: 10.1021/nn305559j.
23. Pok S, Vitale F, Eichmann SL, *et al*., 2014, Biocompatible Carbon Nanotube Chitosan Scaffold Matching the Electrical Conductivity of the Heart. *ACS Nano*, 8:9822–32. DOI: 10.1021/nn503693h.
24. Liu XW, Huang YX, Sun XF, *et al*., 2014, Conductive Carbon Nanotube Hydrogel as a Bioanode for Enhanced Microbial Electrocatalysis. *ACS Appl Mater Interfaces*, 6:8158−64. DOI: 10.1021/am500624k.
25. Chen Z, To JW, Wang C, *et al*., 2014, A Three-dimensionally Interconnected Carbon Nanotube-conducting Polymer Hydrogel Network for High-performance Flexible Battery Electrodes. *Adv Energy Mater*, 4:1400207. DOI: 10.1002/aenm.201400207.
26. Kumar GG, Hashmi S, Karthikeyan C, *et al*., 2014, Graphene Oxide/Carbon Nanotube Composite Hydrogels-Versatile Materials for Microbial Fuel Cell Applications. *Macromol Rapid Commun*, 35:1861–5. DOI: 10.1002/marc.201400332.
27. Chen PY, Courchesne NM, Hyder MN, *et al*., 2015, Carbon Nanotube-polyaniline Core-shell Nanostructured Hydrogel for Electrochemical Energy Storage. *RSC Adv*, 5:37970–9977. DOI: 10.1039/c5ra02944a.
28. Sayyar S, Murray E, Thompson BC, *et al*., 2015, Processable Conducting Graphene/Chitosan Hydrogels for Tissue Engineering. *J Mater Chem B*, 3:481-90.
29. Jo H, Sim M, Kim S, *et al*., 2017, Electrically Conductive Graphene/Polyacrylamide Hydrogels Produced by Mild Chemical Reduction for Enhanced Myoblast Growth and Differentiation. *Acta Biomater*, 48:100–9. DOI: 10.1016/j.actbio.2016.10.035.
30. Alam A, Meng Q, Shi G, *et al*., 2016, Electrically Conductive, Mechanically Robust, pH-sensitive Graphene/Polymer Composite Hydrogels. *Compos Sci Technol*, 127:119–26. DOI: 10.1016/j.compscitech.2016.02.024.
31. Baniasadi H, Ramazani AS, Mashayekhan S, 2015, Fabrication and Characterization of Conductive Chitosan/Gelatin-Based Scaffolds for Nerve Tissue Engineering. *Int J Biol Macromol*, 74:360–6. DOI: 10.1016/j.ijbiomac.2014.12.014.
32. Wang J, Li BY, Ni T, *et al*., 2015c, One-step Synthesis of Iodine Doped Polyaniline-Reduced Graphene Oxide Composite Hydrogel with High Capacitative Properties. *Compos Sci Technol*, 109:12–7.
33. Zhang L, Shi G, 2011, Preparation of Highly Conductive Graphene Hydrogels for Fabricating Supercapacitors with High Rate Capability. *J Phys Chem C*, 115:17206–12. DOI: 10.1021/jp204036a.
34. Xu Y, Lin Z, Huang X, *et al*., 2013, Flexible Solid-state Supercapacitors Based on Three-dimensional Graphene Hydrogel Films. *ACS Nano*, 7:4042–9. DOI: 10.1021/nn4000836.
35. Moughton AO, Hillmyer MA, Lodge TP, 2012, Multicompartment Block Polymer Micelles. *Macromolecules*, 45:2-19. DOI: 10.1021/ma201865s.
36. Li GL, Mohwald H, Shchukin DG, 2013, Precipitation Polymerization for Fabrication of Complex Core-shell Hybrid Particles and Hollow Structures. *Chem Soc Rev*, 42:3628–46. DOI: 10.1039/c3cs35517a.
37. Schlüter AD, Halperin A, Kröger M, *et al*., 2014, Dendronized Polymers: Molecular Objects Between Conventional Linear Polymers and Colloidal Particles. *ACS Macro Lett*, 3:991–8. DOI: 10.1021/mz500376e.
38. McLeish TC, 2007, Macromolecular Engineering: Precise Synthesis, Materials Properties, Applications. Weinheim, Germany: Wiley-VCH. p1605.
39. Shi XW, Hu YL, Tu K, *et al*., 2013, Electromechanical Polyaniline-cellulose Hydrogels with High Compressive Strength. *Soft Matter*, 9:10129–34. DOI: 10.1039/c3sm51490k.
40. Liang XT, Qu B, Li JR, *et al*., 2015, Preparation of Cellulose-based Conductive Hydrogels with Ionic Liquid. *React Funct Polym*, 86:1–6.
41. Gilmore K, Hodgson AJ, Luan B, *et al*., 1994, Preparation of Hydrogel/conducting Polymer Composites. *Polym Gels Netw*, 2:135–43. DOI: 10.1016/0966-7822(94)90032-9.
42. Yang B, Yao F, Hao T, *et al*., 2016, Development of Electrically Conductive Double-Network Hydrogels via One-Step Facile Strategy for Cardiac Tissue Engineering. *Adv Healthc Mater*, 5:474–88. DOI: 10.1002/adhm.201500520.
43. Xiao YH, He L, Che JF, 2012, An Effective Approach for the Fabrication of Reinforced Composite Hydrogel Engineered with SWNTs, Polypyrrole and PEGDA Hydrogel. *J Mater Chem*, 22:8076–82. DOI: 10.1039/c2jm30601h.
44. Kim YS, Cho K, Lee HJ, *et al*., 2016, Highly Conductive and Hydrated PEG-Based Hydrogels for the Potential Application of a Tissue Engineering Scaffold. *React Funct Polym*, 109:15–22. DOI: 10.1016/j.reactfunctpolym.2016.09.003.

45. Sasaki M, Karikkineth BC, Nagamine K, *et al*., 2014, Highly Conductive Stretchable and Biocompatible Electrode-Hydrogel Hybrids for Advanced Tissue Engineering. *Adv Healthc Mater*, 3:1919–27. DOI: 10.1002/adhm.201400209.
46. Dai TY, Qing XT, Zhou H, *et al*., 2010, Mechanically Strong Conducting Hydrogels with Special Double-network Structure. *Synth Met*, 160:791–6. DOI: 10.1016/j.synthmet.2010.01.024.
47. Elyashevich GK, Smirnov MA, 2012, New pH-responsive and Electroactive Composite Systems Containing Hydrogels and Conductive Polymers on a Porous Matrix. *Polym Sci A*, 54:900–8. DOI: 10.1134/s0965545x12110028.
48. Dai TY, Qing XT, Xia YY, 2009, Conducting Hydrogels with Enhanced Mechanical Strength. *Polymer*, 50:5236–41. DOI: 10.1016/j.polymer.2009.09.025.
49. Wang YQ, Shi Y, Pan LJ, *et al*., 2015, Dopant-enabled Supramolecular Approach for Controlled Synthesis of Nanostructured Conductive Polymer Hydrogels. *Nano Lett*, 15:7736–41. DOI: 10.1021/acs.nanolett.5b03891.
50. Sershen SR, Westcott SL, Halas NH, *et al*., 2002, Independent Optically Addressable Nanoparticle-polymer Optomechanical Composites. *Appl Phys Lett*, 80:4609. DOI: 10.1063/1.1481536.
51. Pardo-Yissar V, Gabai R, Shipway AN, *et al*., 2001, Gold Nanoparticle/Hydrogel Composites with Solvent-Switchable Electronic Properties. *Adv Mater*, 13:1320–3. DOI: 10.1002/1521-4095(200109)13:17<1320::aid-adma1320>3.0.co;2-8.
52. Wang C, Flynn NT, Langer R, 2004, Controlled Structure and Properties of Thermoresponsive Nanoparticle-hydrogel Composites. *Adv Mater*, 16:1074–9. DOI: 10.1002/adma.200306516.
53. Souza GR, Christianson DR, Staquicini FI, *et al*., 2006, Networks of Gold Nanoparticles and Bacteriophage as Biological Sensors and Cell-targeting Agents. *Proc Natl Acad Sci USA*, 103:1215–20. DOI: 10.1073/pnas.0509739103.
54. Wu H, Yu G, Pan L, *et al*., 2013, Stable Li-ion Battery Anodes by *In situ* Polymerization of Conducting Hydrogel to Conformally Coat Silicon Nanoparticles. *Nat Commun*, 4:1943. DOI: 10.1038/ncomms2941.
55. Saravanan P, Raju MP, Alam S, 2007, A Study on Synthesis and Properties of Ag Nanoparticles Immobilized Polyacrylamide Hydrogel Composites. *Mater Chem Phys*, 103:278–82. DOI: 10.1016/j.matchemphys.2007.02.025.
56. Zhang D, Yang J, Bao S, *et al*., 2013, Semiconductor Nanoparticle-based Hydrogels Prepared Via Self-initiated Polymerization Under Sunlight, Even Visible Light. *Sci Rep*, 3:1399. DOI: 10.1038/srep01399.
57. Vaezi M, Chianrabutra S, Mellor B, *et al*., 2013. Multiple Material Additive Manufacturing-Part 1: A Review. *Virtual Phys Prototyp*, 8:19–50. DOI: 10.1080/17452759.2013.778175.
58. Cheng K, Mukherjee P, Curthoys I, 2017, Development and Use of Augmented Reality and 3D Printing in Consulting Patient with Complex Skull Base Cholesteatoma. *Virtual Phys Prototyp*, 12:241–8. DOI: 10.1080/17452759.2017.1310050.
59. Espalin D, Muse DW, MacDonald E, *et al*., 2014, 3D Printing Multifunctionality: Structures with Electronics. *Int J Adv Manuf Technol*, 72:963–78. DOI: 10.1007/s00170-014-5717-7.
60. Zhao D, Liu T, Park JG, 2012, Conductivity Enhancement of Aerosol-jet Printed Electronics by Using Silver Nanoparticles Ink with Carbon Nanotubes. *Microelectron Eng*, 96:71–5. DOI: 10.1016/j.mee.2012.03.004.
61. Wang S, Lee JM, Yeong WY, 2015, Smart Hydrogels for 3D Bioprinting. *Int J Bioprint*, 1:3–14.
62. Murphy SV, Atala A, 2014, 3D Bioprinting of Tissues and Organs. *Nat Biotechnol*, 32:773–85. DOI: 10.1038/nbt.2958.
63. Cui H, Nowicki M, Fisher JP, *et al*., 2017, 3D Bioprinting for Organ Regeneration. *Adv Healthc Mater*, 6: 1601118. DOI: 10.1002/adhm.201601118.
64. Lee JM, Ng WL, Yeong WY, 2019, Resolution and Shape in Bioprinting: Strategizing Towards Complex Tissue and Organ Printing. *Appl Phys Rev*, 6(1):011307. DOI: 10.1063/1.5053909.
65. Landers R, Mülhaupt R, 2000, Desktop Manufacturing of Complex Objects, Prototypes and Biomedical Scaffolds by Means of Computer-assisted Design Combined with Computer-guided 3D Plotting of Polymers and Reactive Oligomers. *Macromol Mater Eng*, 282:17–21. DOI: 10.1002/1439-2054(20001001)282:1<17::aid-mame17>3.0.co;2-8.
66. Sun J, Ng JH, Fuh YH, *et al*., 2009, Comparison of Micro-dispensing Performance Between Micro-valve and Piezoelectric Printhead. *Microsyst Technol*, 15:1437–48. DOI: 10.1007/s00542-009-0905-3.
67. Chua CK, Leong KF, 2015, 3D Printing and Additive Manufacturing: Principles and Applications. 4th ed. Singapore: World Scientific Publishing.
68. Luo Y, Lode A, Akkineni AR, *et al*., 2015, Concentrated Gelatin/alginate Composites for Fabrication of Predesigned Scaffolds with a Favorable Cell Response by 3D Plotting.

RSC Adv, 5:43480–8. DOI: 10.1039/c5ra04308e.

69. Sun C, Fang N, Wu DM, *et al*., 2005, Projection Microstereolithography Using Digital Micro-mirror Dynamic Mask. *Sens Actuators A Phys*, 121:113–20. DOI: 10.1016/j.sna.2004.12.011.
70. Hölzl K, Lin S, Tytgat L, *et al*., 2016, Bioink Properties Before, During and after 3D Bioprinting. *Biofabrication*, 8:032002. DOI: 10.1088/1758-5090/8/3/032002.
71. Jang TS, Jung HD, Pan HM, *et al*., 2017, 3D Printing of Hydrogel Composite Systems: Recent Advances in Technology for Tissue Engineering. *Int J Bioprint*, 4:1–28.
72. Donderwinkel I, van Hest JC, Cameron NR, 2017, Bio-inks for 3D Bioprinting: Recent Advances and Future Prospects. *Polym Chem*, 8:4451–71. DOI: 10.1039/c7py00826k.
73. Sayyar S, Gambhir S, Chung J, *et al*., 2017, 3D Printable Conducting Hydrogels Containing Chemically Converted Graphene. *Nanoscale*, 9:2038–50. DOI: 10.1039/c6nr07516a.
74. Fantino E, Roppolo I, Zhang D, *et al*., 2018, 3D Printing/Interfacial Polymerization Coupling for the Fabrication of Conductive Hydrogel. *Macromol Mater Eng*, 303:1700356. DOI: 10.1002/mame.201700356.
75. Odent J, Wallin TJ, Pan W, *et al*., 2017, Highly Elastic, Transparent, and Conductive 3D-Printed Ionic Composite Hydrogels. *Adv Funct Mater*, 27:1701807. DOI: 10.1002/adfm.201701807.
76. Zhou Y, Layani M, Wang S, *et al*., 2018, Fully Printed Flexible Smart Hybrid Hydrogels. *Adv Funct Mater*, 28:1705365. DOI: 10.1002/adfm.201705365.
77. Heo DN, Lee SJ, Timsina R, *et al*., 2019, Development of 3D Printable Conductive Hydrogel with Crystallized PEDOT:PSS for Neural Tissue Engineering. *Mater Sci Eng C Mater Biol Appl*, 99:582–90. DOI: 10.1016/j.msec.2019.02.008.
78. Sekine S, Ido Y, Miyake T, *et al*., 2010, Conducting Polymer Electrodes Printed on Hydrogel. *J Am Chem Soc*, 132:13174–5. DOI: 10.1021/ja1062357.
79. Ahn Y, Lee H, Lee D, *et al*., 2014, Highly Conductive and Flexible Silver Nanowire-Based Microelectrodes on Biocompatible Hydrogel. *ACS Appl Mater Interfaces*, 6:18401–7. DOI: 10.1021/am504462f.
80. Shay T, Velev OD, Dickey MD, 2018, Soft Electrodes Combining Hydrogel and Liquid Metal. *Soft Matter*, 14:3296–303. DOI: 10.1039/c8sm00337h.
81. Agarwala S, Lee JM, Ng WL, *et al*., 2018, A Novel 3D Bioprinted Flexible and Biocompatible Hydrogel Bioelectronic Platform. *Biosens Bioelectron*, 102:365–71. DOI: 10.1016/j.bios.2017.11.039.
82. Jaffari SA, Turner AP, 1995, Recent Advances in Amperometric Glucose Biosensors for *In vivo* Monitoring. *Physiol Meas*, 16:1–15. DOI: 10.1088/0967-3334/16/1/001.
83. Wisniewski N, Moussy F, Reichert WM, 2000, Characterization of Implantable Biosensor Membrane Biofouling. *Fresenius J Anal Chem*, 366:611–21. DOI: 10.1007/s002160051556.
84. Abraham S, Brahim S, Ishihara K, *et al*., 2005, Molecularly Engineered p(HEMA)-Based Hydrogels for Implant Biochip Biocompatibility. *Biomaterials*, 26:4767–78. DOI: 10.1016/j.biomaterials.2005.01.031.
85. Saha S, Sarkar P, Sarkar M, *et al*., 2015, Electroconductive Smart Polyacrylamide-polypyrrole (PAC-PPY) Hydrogel: A Device for Controlled Release of Risperidone. *RSC Adv*, 5, 27665–73. DOI: 10.1039/c5ra03535j.
86. Tao Y, Cheng G, Zhang M, *et al*., 2015, A General Route to 2D Nanoleaves and Nanoplates of Polyaniline. *Russ J Phys Chem A*, 89:2267–70.
87. Sharma K, Kaith BS, Kumar V, *et al*., 2014, Gum Ghatti Based Novel Electrically Conductive Biomaterials: A Study of Conductivity and Surface Morphology. *Express Polym Lett*, 8:267–81. DOI: 10.3144/expresspolymlett.2014.30.
88. Sharma K, Kumar V, Kaith BS, *et al*., 2015, Evaluation Of Conducting Interpenetrating Network Based On Gum Ghatti-G-Poly (Acrylic Acid-Aniline) As Colon-Specific Delivery For Amoxicillin Trihydrate And Paracetamol. *New J Chem*, 39:3021–34. DOI: 10.1039/c4nj01982b.
89. Sharma K, Kumar V, Chaudhary B, *et al*., 2016, Application of Biodegradable Superabsorbent Hydrogel Composite Based on Gum Ghatti-co-poly (Acrylic Acid-aniline) for Controlled Drug Delivery. *Polym Degrad Stab*, 124:101–11. DOI: 10.1016/j.polymdegradstab.2015.12.021.
90. Tandon B, Magaz A, Balint R, *et al*., 2018, Electroactive Biomaterials: Vehicles for Controlled Delivery of Therapeutic Agents for Drug Delivery and Tissue Regeneration. *Adv Drug Deliv Rev*, 129:148–68. DOI: 10.1016/j.addr.2017.12.012.
91. Weaver CL, LaRosa JM, Luo X, *et al*., 2014, Electrically Controlled Drug Delivery from Graphene Oxide Nanocomposite Films. *ACS Nano*, 8:1834–43. DOI: 10.1021/nn406223e.
92. Catt K, Li H, Hoang V, *et al*., 2018, Self-powered Therapeutic Release from Conducting Polymer/graphene Oxide Films on Magnesium. *Nanomed Nanotechnol Biol Med*, 14:2495–503. DOI: 10.1016/j.nano.2017.02.021.
93. Balint R, Cassidy NJ, Cartmell SH, 2014, Conductive Polymers: Towards a Smart Biomaterial for Tissue Engineering. *Acta Biomater*, 10:2341–53. DOI: 10.1016/j.actbio.2014.02.015.

94. Kawahara Y, Yamaoka K, Iwata M, *et al*., 2006, Novel Electrical Stimulation Sets the Cultured Myoblast Contractile Function to On. *Pathobiology*, 73:288–94. DOI: 10.1159/000099123.

95. Pedrotty DM, Koh J, Davis BH, *et al*., 2005, Engineering Skeletal Myoblasts: Roles of Three-dimensional Culture and Electrical Stimulation. *Am J Physiol Heart Circ Physiol*, 288:H1620–6. DOI: 10.1152/ajpheart.00610.2003.

ORIGINAL ARTICLE

Patient-specific 3D-printed Splint for Mallet Finger Injury

Ali Zolfagharian[1]*, Timothy M. Gregory[1], Mahdi Bodaghi[2], Saleh Gharaie[1], Pearse Fay[3]

[1]School of Engineering, Deakin University, Geelong 3216, Australia

[2]Department of Engineering, School of Science and Technology, Nottingham Trent University, Nottingham NG11 8NS, UK

[3]School of Health and Social Development, Deakin University, Geelong 3220, Australia

Abstract: Despite the frequency of mallet finger injuries, treatment options can often be costly, time-consuming, and ill-fitted. Three-dimensional (3D) printing allows for the production of highly customized and inexpensive splints, which suggests potential efficacy in the prescription of casts for musculoskeletal injuries. This study explores how the use of engineering concepts such as 3D printing and topology optimization (TO) can improve outcomes for patients. 3D printing enables the direct fabrication of the patient-specific complex shapes while utilizing finite element analysis and TO in the design of the splint allowed for the most efficient distribution of material to achieve mechanical requirements while reducing the amount of material used. The reduction in used material leads to significant improvements in weight reduction and heat dissipation, which would improve breathability and less sweating for the patient, greatly increasing comfort for the duration of their recovery.

Keywords: Patient-specific, Three-dimensional printing, Splint, Topology optimization

***Corresponding Author:** Ali Zolfagharian, School of Engineering, Deakin University, Geelong 3216, Australia; a.zolfagharian@deakin.edu.au

Received: January 28, 2020; ***Accepted:*** February 28, 2020; ***Published Online:*** March 27, 2020

Citation: Zolfagharian A, Gregory TM, Bodaghi M, *et al*., 2020, Patient-specific 3D-printed Splint for Mallet Finger Injury. *Int J Bioprint*, 6(2):259. DOI: 10.18063/ijb.v6i2.259

1 Introduction

Mallet finger is one the most common upper limb athletic injury that may occur due to bony avulsion or tendentious lesion[1]. This injury could significantly affect individuals overall function, impairing their work-related skills and social capability to perform daily living activities[2]. The current treatment involves immobilizing the affected joint using a splint made of thermoplastic or plaster in a neutral position. The splint could be prefabricated; however, in most cases, a trained health professional cast a splint for the patient. Intrinsically, the outcome will be highly dependent on the skills and knowledge of the medical practitioner. Even with highly trained health professionals completing this, there are many factors that impact on the wearing of splints resulting in non-adherence and decreased outcomes[3]. In addition, it is a lengthy and labor-intensive process requiring the fabrication of multiple casts leading to excessive use of materials and efforts. Yet, additive manufacturing (AM) technology recently allows for the fabrication of individualized prosthetics based on patient anthropometrics[4].

Additively manufactured orthosis orthopedics for injuries treatments or rehabilitation are not currently in widespread use, though, it could potentially offer a way to reduce the cost of production and enable easy customization to an individual in biomedical treatments that addresses many of the current barrier to adherence[5,6].

Effective use of AM may lead to a reduction in size and weight of the splint making it more comfortable for the user. This paper presents an investigation into the use of a fused deposition modeling (FDM) printer to trial printing methods to produce a person and injury-specific mallet finger splint at a low-cost and optimized weight and comfortability.

1.1 Mallet finger injury

Mallet finger is the extremely common finger injury where the fingers extensor ability is disrupted at its terminal portion, causing an inability to extend at the distal interphalangeal joint[7]. This disruption is either due to rupture of the fingers extensor tendon or an avulsion fracture (fracture to the bone in a location where a tendon or ligament attaches)[8] of the distal phalange. Swelling and tenderness can occur together with reduced ability to extend the distal phalanx, resulting in extension lag of anywhere from a couple of degrees up to several dozen. The cause can be either direct blow to the distal phalanx, sharp, or blunt injury to the distal interphalangeal joint[9]. This injury is commonly seen in ball sports such as Basketball, Volleyball, and Cricket. Injuries to the lower arm, including hand and wrist, are extremely common, accounting for 20% of all emergency presentations[10].

The economic burden for these injuries is extensive with the direct, indirect, and intangible costs associated and increases with the severity or complexity of the injury[10]. Although, in most cases, the patient will make a full recovery, often, a long period of recovery is required, and some will not recover full function and may potentially have a lasting disability (**Figure 1**). Mallet finger is often left untreated by patients unless severe restriction in extensor ability is present, or there is lingering pain[11]. This injury, in the case, that there are functional shortfalls, can impede the whole hand in everyday fine motor skill tasks. Furthermore, this deformity can develop additional medical conditions in the finger and hand as overcompensation can create hyperextension of proximal interphalangeal joint, a swan neck deformity[7].

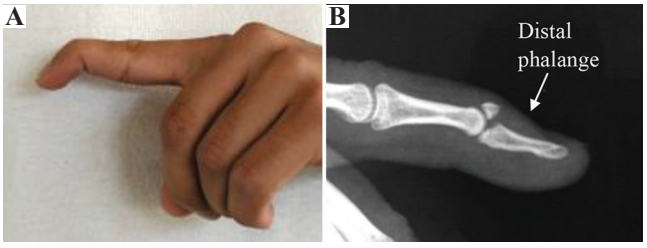

Figure 1. (A) Mallet finger fracture (Image courtesy from Sachin J Shah, MD, online), (B) anatomy of finger[12].

The use of a movement restriction device called a splint is the common form of treatment for this injury. The splint is designed to hold the affected area of the finger in neutral or a small degree of hyperextension while the tendon or avulsion fracture can heal.

1.2 Current mallet finger treatments

The conservative and post-surgical management of mallet finger injuries require the use of splints to aid in recovery. Preventing any movement in the distal interphalangeal joint is crucial as flexion of the joint will separate the torn ends of the tendon or avulsion fracture, halting the recovery process. In this case, the finger would need to be returned to full extension, and the healing process would start again from the beginning. There are several types of splints that can be used for this condition; the three commonly used splints are the stack (prefabricated), dorsal aluminum, and personalized thermoplastic splints (**Figure 2**).

Beyond the use of the dorsal aluminum splint, there are specifically designed mallet finger splints

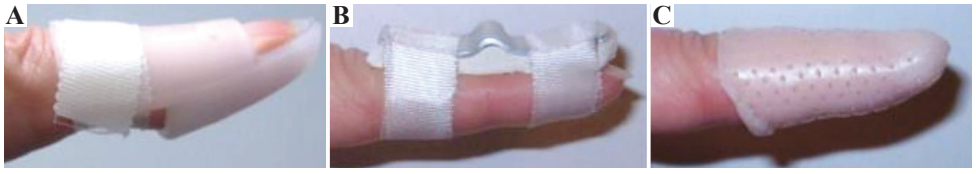

Figure 2. (A) Stack, (B) dorsal aluminum, and (C) personalized thermoplastic splints[13].

used in the treatment of this condition. Either cast molded products known as "off the shelf," which are manufactured in three ready-made sizes or personalized molded thermoplastic products that a health professional makes for the patient at the clinic. The stack splint is generally made from polypropylene and is largely enclosed with limited holes in the top section for airflow. The stack splint is applied to the patient's finger and then attached to the skin on the proximal phalange with skin tape or strapping tape to help prevent movement. However, the "off the shelf" splints embody a one size fits all approach which cannot accommodate all patients.

The dorsal aluminum splint is a commonly prescribed method for treating mallet finger. This method utilizes a splint on the dorsal section of the finger and then taped onto the finger at the distal phalange and the intermediate phalange. This method provides greater airflow than the stack splint as the ventral section of the finger and the fingertip is left open to the air. This theoretically provides an advantage over stack splint in that decreased pressure is exerted to the distal interphalangeal joint, allowing better blood supply[7].

Personalized thermoplastic splints are applied by trained health professionals, which involves taking the measurements of a patient's finger and then cutting a piece of thermoplastic to a specific splint design. The thermoplastic is heated, and the finger is wrapped in the thermoplastic with the tabs joining the piece over the top of the finger. Using scissors, a health professional can trim the ends further to better fit the patient. The thermoplastic conforms to the skin and sets when it cools, maintaining the finger in the position that it has been molded to. There are several complexities with this manufacturing process, including that the manufacturing process is manual and highly skill dependent. The splint received from a graduate health professional may be completely different in quality to the veteran therapist who has been creating these splints by hand for years. The splint, if poorly fitted, can result in shear stress, directional misalignment, and pressure over bony prominences[9]. A comparison study of these three splints in the treatment of mallet finger has been reported by O'Brien[13]. All three types of splints are required to be worn for 6 – 8 weeks. Treatment failure or complications include skin irritation, poor splint fit, splint breakage, pain, or discomfort wearing the splint or patient dissatisfaction with splint appearance or cumbersome nature. When worn for the entirety of this period, there was no extensor lag difference found between the three splint types, but custom-made thermoplastic splints were significantly less likely to result in treatment failure[13].

This suggests that customized splints, fitted to the exact dimensions of a patient's finger, have the ability to provide successful treatment in more cases than the other two splint types. This finding propelled the current study to use AM technology to rapidly produce the personalized fitted shape splint customized to the patient. This technology could provide a standardized and efficient approach to manufacturing mallet splints that may reduce cost, improve adherence, and have less impact on patient's hand function while wearing the splint.

1.3 AM

AM is a promising and developing manufacturing method. Historically, AM technology was utilized for prototype creation; increasingly, however, it is being seen and has become a production technique in its own right[14,15]. The AM groups a large number of technologies and techniques that can utilize different materials with vastly differing properties to create parts for a range of applications[16].

The three-dimensional (3D) printing has become a large part of the new frontier of medical technology and treatment. Medical treatments that use 3D printing techniques include: Facial reconstruction, orthodontics, exoskeletons, prosthesis, tumor detection, chirurgical optimization and biocompatible organ, and tissue printing[17,18]. In the medical field, using traditional manufacturing methods take a lot of production time and are not easily customizable to patients; hence, its use is becoming more limited. FDM, also known as fused filament fabrication, is one of the most common AM technologies using numerous varieties of thermoplastic materials[19,20].

During the early years of the introduction of the FDM technique, it was used to print prototypes, souvenirs, and other useful domestic appliances[21,22]. However, FDM technology is rapidly maturing and is reportedly showing unlimited potential in various applications, including in the medical, automotive, and aeronautical fields[23-25]. FDM can benefit the mallet finger treatment through making complex shapes that could not be made by traditional manufacturing methods as well as its ability to utilize alternative materials with improved performance characteristics[7,26].

The first step of FDM printing is to develop a computer-aided drawing (CAD) of the component. That CAD file is then exported as a stereolithography (STL) file. This STL file is then "sliced" by the 3D printer's software and read by the printer to print the component in a series of layers[27]. FDM prints thin layers of plastic layer by layer to create the part. Plastic is fed into the extrusion head and then heated so that it enters a semi-liquid state; the plastic is then pushed out of a small nozzle to produce a fine thread of plastic that it layers onto the previous layer or onto the base support piece. Because of this layer on the layer structure of the material, the mechanical properties and surface finish of an FDM printed part are dependent on the orientation of which it is printed. This means even the same part can have different mechanical properties if printed in different orientations[28].

Despite previous studies into AM for use in lower limb prosthetics and orthotics, the use of 3D printing technologies for the use on the upper extremities of the arm, including wrist, hand, and fingers, has yet to be investigated broadly[11]. Up to the present time, there has been limited research in the area of upper extremity splinting with engineering design and analysis motivation[5,29].

The interest in 3D printing in this area is due to multiple reasons. One is the scalability with respect to the range of sizes. It is completely customizable to the patient's injury. In addition, multiple splints can be printed for the patient over the course of their recovery as swelling reduces to ensure the splint is optimally fitted at all times throughout their recovery[30]. This practice potentially provides the best outcome for the patient. Further, 3D printed splints can also be made to accommodate extremes of size or deformities that off the shelf splints cannot. Utilizing this technology means that a patient can receive the same quality of care regardless of the health professionals level of skill and experience in splint manufacturing immediately after an injury the patient gets their finger scanned and a medical professional selects the template for their finger injury that is then automatically updated with the exact dimensions of their finger. A personalized finger splint is then printed off, tailored to them exactly, to allow for the chance at the most optimal recovery followed by ongoing rehabilitation with a health professional.

The personalized FDM 3D-printed thermoplastic finger splint in this study could potentially address all those common causes of treatment failure, such as skin irritation, poor splint fit and discomfort wearing the splint, which would lead to less treatment failure and therefore more successful recovery cases.

2 Methodology

The goal of this study is to utilize the FDM method to develop a patient-specific 3D-printed finger splint that could potentially have the properties required to match and exceed those of the current hand-molded thermoplastic splints. The original splint will be compared with the topology-optimized splints in terms of structural and thermal performance. With these processes, splints can be produced with much better mechanical properties requiring less material for more breathability and comfort while having the same strength. The detailed steps of achieving this aim are outlined in the following.

2.1 Measurements of finger and personalized CAD splint

The patient-specific splint was designed by measuring seven parameters of a patient's index finger, as shown in **Figure 3**. To measure the maximum force that could be applied by the index finger, the intermediate and proximal joints of the finger were locked in position using medical tape to the bottom of the finger. This left the distal interphalangeal joint of the finger, the joint

affected by mallet finger, the only joint with a degree of freedom.

Using Autodesk Inventor Software and the measurements, the patient-specific splint is designed. As shown in **Figure 4**, a constraint was designed at the rear of the splint to prevent leeway in the splint when being worn. When the user clenches their fist, without this material removed, the skin of their middle phalanx finger can push into the back of the splint dislodging its correct position. The stack splint is designed with an open ventilation section above the fingernail to allow some airflow to reduce sweat when being worn and to allow limited access for washing. The top section of the splint extends to the proximal interphalangeal joint. This allows the user some flexion of the finger without hindering recovery. A benefit of using topology optimization (TO) is that areas of the finger and finger pad remain exposed, so a person can still feel and get sensation through the finger when performing everyday tasks such as writing with a pen or using their toothbrush. This is opposed to a molded splint that is fully enclosed, which makes the finger become less functional for the recovery period. The maximum pressure load calculated from the distal interphalangeal joint, simulating the maximum force a person could generate in their index finger solely from the flexion of the distal interphalangeal joint, was applied to the rim of the finger splint. This was chosen because the finger "pad" section of the splint is a large space that will be optimized in all topology-optimized splints. Because of this, the area and geometry in that section changed for each splint. By applying the pressure load to the rim of the splint, it was a consistent way to compare all splints.

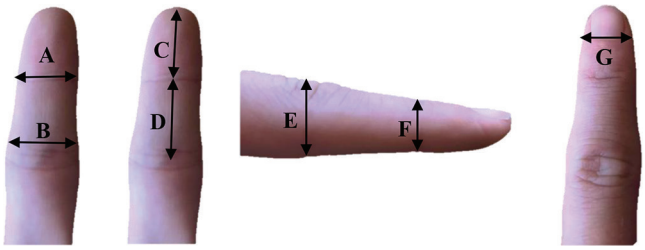

Figure 3. The seven measurements required to create a personalized finger splint computer-aided drawing model.

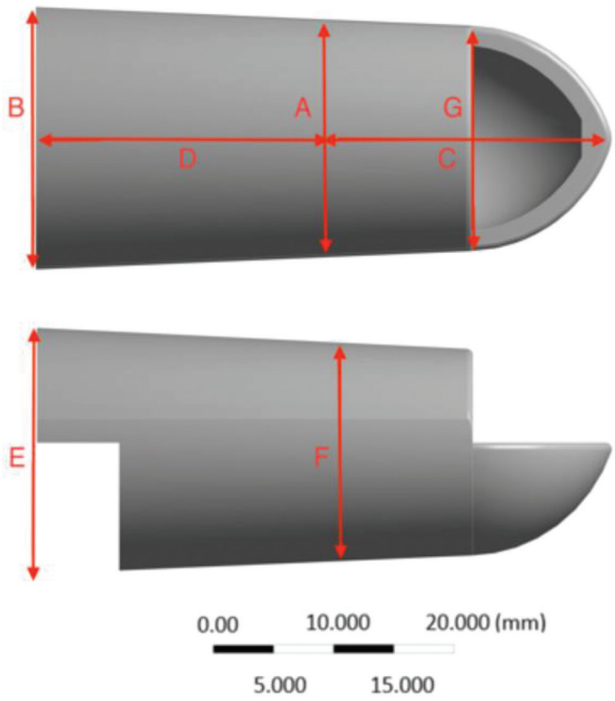

Figure 4. Geometry of a sample 100% mass design according to a patient's finger.

2.2 3D Printing patient-specific finger splint

A number of materials could potentially be used in FDM having the properties required to match and exceed those of the current hand-molded thermoplastic splints. These materials include poly-lactic-acid (PLA), acrylonitrile-butadiene-styrene, polyamide, thermoplastic polyurethane, polycarbonates, polystyrene, and poly-ether-ether-ketone. Environmental considerations were considered as the use of this product is highly personal; it cannot be passed onto the next patient, so it must be disposed of after treatment. The non-recyclability of casts and splints causes large amounts of waste. In fact, in the US, according to the National Ambulatory Medical Care Survey and American Academy of Orthopaedics, 2.4% of the population experiences some fracture[31], producing an average of 670,000 kg of waste per year[17,32]. However, PLA being derived from natural sources, corn, beet, and cassava among others, is biodegradable. Because of this, PLA splints can be composted after their 6 – 8 weeks use, rather than

contribute to landfills. The PLA is used in this study as it has been found to be feasible for the production of scaffolds with different architectures and controlled porosities which are tailored for use as temporary fixtures in biomedical applications[33,34]. In addition, polyvinyl alcohol used as support materials, which is a water-soluble, biodegradable polymer under both aerobic and anaerobic conditions[35].

2.3 TO

TO is utilized here to create a series of splints optimized for the loading conditions. The original splint will be compared with the topology-optimized splints in mechanical performance and in thermal qualities that will affect the users' comfort experience. With these processes, splints can be produced with much better mechanical properties requiring less material, for more breathability and comfort, while having equal strength. In this study, a splint is developed based on TO in which the algorithm starts from a solid model of the material. Distributed loading and boundary conditions are defined based on the specifications of the splint finger, as shown in **Figure 5**. The main objective here is to remove the maximum material while preserving the volume fraction and maximum stiffness of the 3D-printed splint[36,37].

The theory of the optimality criteria (OC) is used in ANSYS Workbench. The OC method uses an estimation of the optimality conditions to update the design variables of each point[38]. The designs are updated independently using this method, the material is added in the areas in which the estimation of the strain energy is too high[39].

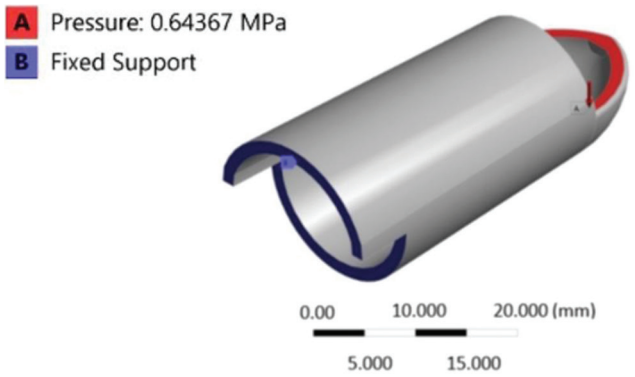

Figure 5. Schematic view of boundary conditions on a sample splint design.

2.4 Finite element analysis (FEA) and mesh convergence

TO with the minimum compliance criteria was coupled with a structural analysis module in ANSYS 2019 R2 to evaluate varying splint designs. Since, the mechanical properties of the 3D printed parts are affected by the 3D printing parameters, for example, layer thickness and raster width, Young's modulus and Poisson's ratio of PLA were obtained according to Type I ASTM D638 test standard. PLA with a density of m^3, Young's modulus of 2850 MPa, and Poisson's ratio of 0.25 were defined for the material properties of the splint. The maximum pressure exerted was estimated to be 64×10^4 Pa applied at the rim of the splint, and the base was assumed to fix (**Figure 5**).

The domains of 100%, 79.49%, 71.13%, and 62.51% mass were discretized by unistructural tetrahedral elements with 394,439, 140,904, 104,634, and 104,026 elements, respectively, as shown in **Figure 6**, where higher mesh density was selected for the region of interest and local mesh refinement was conducted to achieve high mesh quality. Note that mesh independence studies were

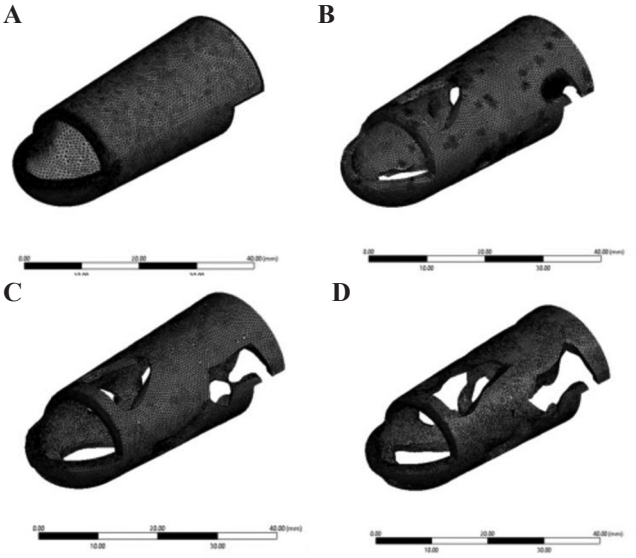

Figure 6. Domains discretization with tetrahedral elements for (A) 100%, (B) 79.49%, (C) 71.13%, and (D) 62.51% mass.

conducted with varying element sizes and model that had <5% variation in maximum stress was selected.

2.5 Thermal heat analysis

Using the four splints created, thermal analysis of the prototypes was undertaken. The Static Structural module in ANSYS used to test for deflection and stress values were linked with steady-state thermal module to link the data. The internal face of each of the splints was selected and set at 31.7°C, the temperature of the skin at room temperature[40]. The convection coefficient of air at 22°C in free convection was selected as 10 W/(m^2.K). The total heat generation of the human body for this project is selected 110 W[41]. A heat flux was also created for the internal face assuming that the average body surface area of human adult is 2 m^2. **Table 1** details the properties calculated above.

To clarify, for the topology-optimized splints, meshing was done for TO using a low element number, default mesh. Once the topology-optimized shape was obtained, it was then inserted into back into static structural, and a new refined mesh with a high number of elements was used to ensure that data values obtained regarding deflection, stress, and heat are as accurate as possible.

3 Results and discussion

The low-cost 3D printer used in this study was the Ultimaker2 Extended+ (Ultimaker B.V., Geldermalsen, The Netherlands). The splints were printed at 100% infill, nozzle speed of 20mm/s, heat bed of 50°C, and layer thickness of 0.2 mm. The dog-bone type PLA samples were 3D-printed according to Type I ASTM D638 with a width of 13 mm, the thickness of 5 mm, and a gauge length of 50 mm. To determine basic mechanical properties, tensile tests, as shown in **Figure 7**, were conducted on 3D-printed dog-bone specimens. The tests were performed in an Instron 300LX (Instron, High Wycombe, UK) with a crosshead speed of 5 mm/min. Tensile

Table 1. Heat simulation analysis settings

Internal splint surface temperature (°C)	31.7
Convection coefficient of air $\left(\frac{W}{m^2 \cdot K}\right)$	10
Total heat generation of human body (W)	110
Average body surface area of human adult (m^2)	2

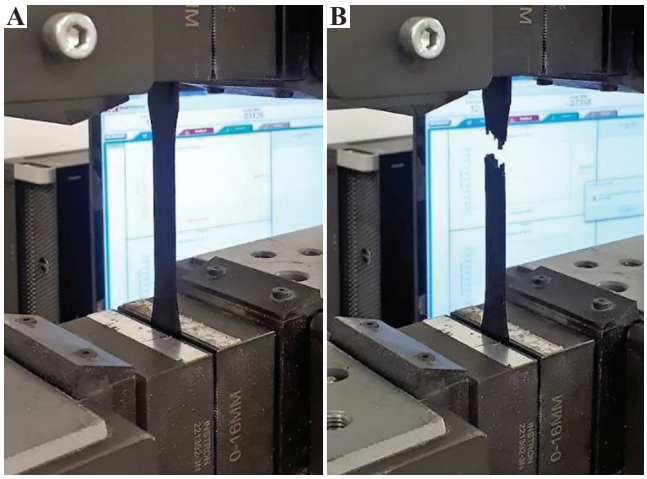

Figure 7. A three-dimensional-printed dog-bone poly-lactic-acid sample (A) before, and (B) after tensile test.

strength and modulus of the 3D-printed samples were determined 52.2 MPa and 2.86 GPa, respectively. In FDM topology optimized and original design, finger splints were fabricated, original (100% mass), 62.51% mass, 71.13% mass, and 79.49% mass, by the same 3D printer and processing parameters used for the dog-bone specimens (**Figure 8**).

To test the maximum deflection of the splints under realistic conditions, the rear of the splint was the fixed end with the load to be applied at the front of the splint near the tip of the finger. This was used to simulate how the splint would deform under the force applied solely by the final joint of the finger (distal interphalangeal joint). As the splint does not extend onto the second joint of the finger, only the force that could be produced by the final joint was considered. In FEA, the fixed support geometry was consistent across all simulations and excluded from TO. To complete the mesh convergence study, the measured force value was applied to the rim of the finger pad area.

Figure 8. From left to right 62.51%, 71.13%, 79.49%, and 100% mass splints.

The maximum deflection and maximum stress values were recorded for each mesh. Then, the mesh was refined, increasing the number of cells, and then the maximum deflection and maximum stress values were recorded again. Once both the deflection and maximum stress values were within 2% of previous deflection and stress values from the previous mesh, the mesh was called converged. This means the results obtained from any simulation can be assumed accurate enough that they are no longer significantly impacted by the mesh once mesh convergence was achieved off the original splint. Deflection and stress values were calculated through ANSYS simulation to establish the printable material with the best mechanical properties.

The stress and deflection simulation results of the splints are obtained and shown in **Figures 9 and 10**. All splints had stress concentrations at the corner between the finger pad rim and the rim of the enclosed top section. This was the location of the highest stress values for each splint. The highest values of deflection were obtained at the tip of the finger pad rim section. As would be expected when removing material from a loaded structure, its deflection increases as more material is removed. What is noteworthy though, according to **Figure 11A and 11B**, the 79.49% splint had a reduced mass of 20.51% but only deflected 0.24 mm, which was only 24% more than the original, 100% mass, splint. However, there appears to be an optimum percentage of mass reduction as the 71.13% splint deflected 0.31 mm, which is almost 50% more than the 100% mass splint. This result shows that there is appoint of diminishing returns in removing material from the structure. This indicates the effectiveness of the TO in splint finger design.

In line with the increase in deflection as the splints had a reduction in material, the maximum stress values decreased. There was however an outlier in the 71.13% splint, which recorded 31.16 MPa that experienced the least stress among all. This result would appear as the objective of the TO in this study was set for the least deflection only.

The heat distribution results of the splints are also simulated and shown in **Figures 11C and 12**. With each iteration of the topology-optimized finger splint with less material, the average heat dissipation in the splint increased slightly as expected. The heat flux upturn in between splints was roughly proportional to the decrease in percentage mass to the previous splint, with one exception. The splint with 71.13% mass performed the best in heat dissipation.

In general, it was observed that the deflection results had not a perfect correlation with the heat dissipation of the splints. At one end, the original splint with 100% mass, performed best mechanically, while the 71.13% mass splint performed best in heat dissipation. Therefore, a trade-off analysis is required to opt for the most appropriate splint.

The trade-off results are shown in **Figure 13** that the topology-optimized splint with 71.13% mass-produced reasonable mechanical properties

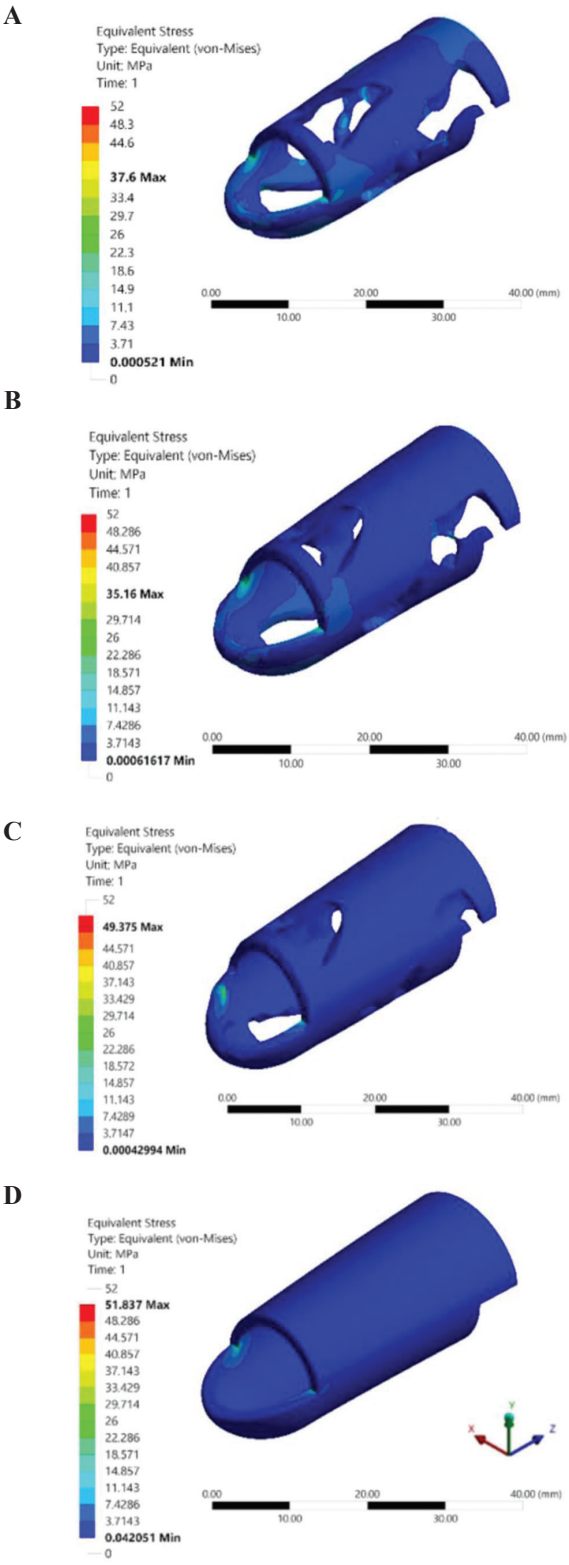

Figure 9. Stress simulation results of topology-optimized (A) 62.51% mass, (B) 71.13% mass, (C) 79.49% mass, and (D) original three-dimensional-printed 100% mass, splints.

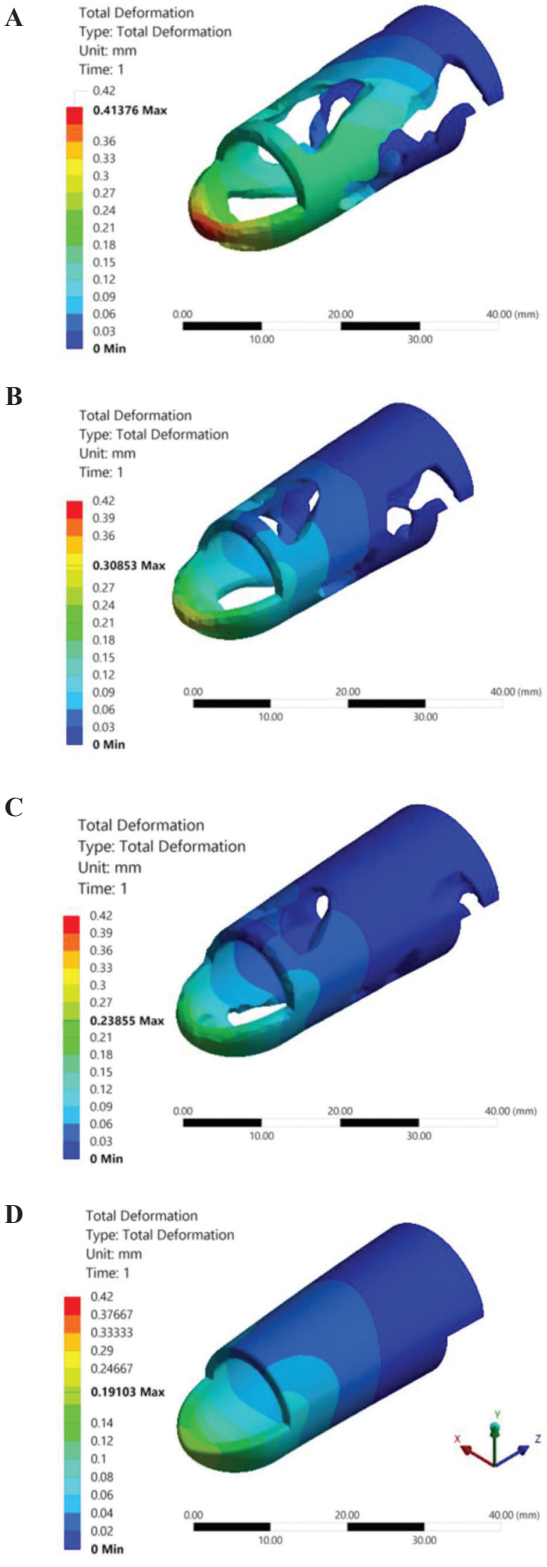

Figure 10. Deflection simulation results of topology-optimized (A) 62.51% mass, (B) 71.13% mass, (C) 79.49% mass, and (D) original three-dimensional-printed 100% mass, splints.

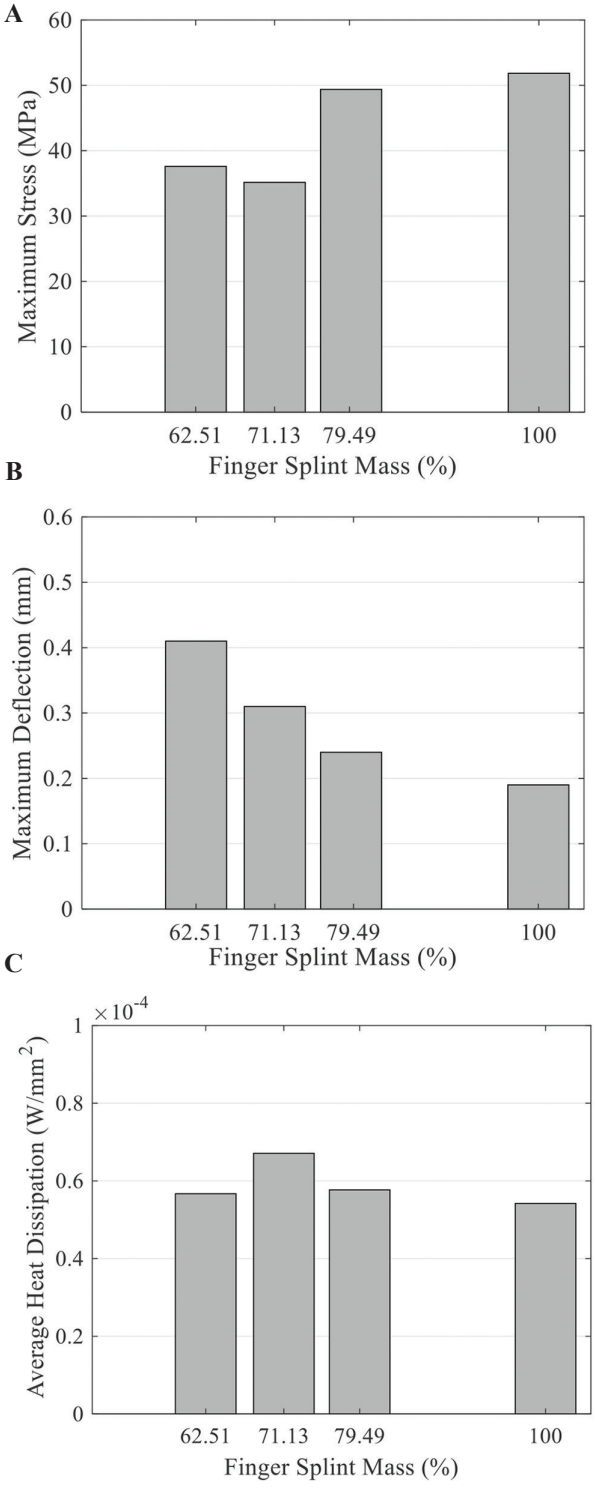

Figure 11. Comparison of the three-dimensional-printed splints simulation results (A) Maximum Equivalent (von-Mises) stress; (B)maximumdeflection;(C)averageheatdissipation.

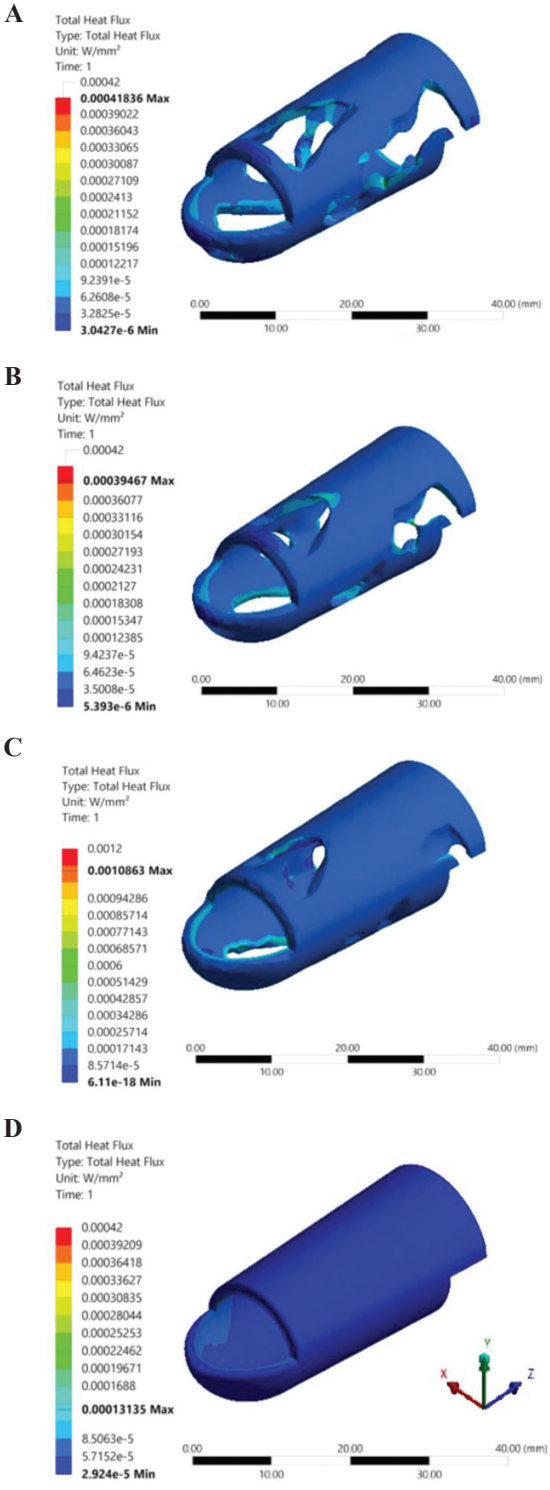

Figure 12. Heat distribution simulation results of topology-optimized (A) 62.50% mass, (B) 71.13% mass, (C) 79.49% mass, and (D) original three-dimensional-printed 100% mass, splints.

considering both maximum stress and deflection values while reducing the heat trapped around the finger by a significant amount. This splint is simpler to print than lower percentage mass splints that can require more printing support structures. It was found that inevitably reducing the amount of material in a load-bearing finger splint would increase the deflection of it. However, when the distribution of that material is chosen to optimize the stiffness in that situation, the deflection value was low enough to justify its use.

For verifying the simulation results, some experiments were carried out to find the maximum deflection that occurred at the tip of the 3D-printed splints. A set up, as shown in **Figure 14A**, was used in an Instron 300LX (Instron, High Wycombe, UK) to measure the average maximum deflection of the three splints from each design. The comparison results, shown in **Figure 14B**, imply good agreement of the experimental findings with the simulations.

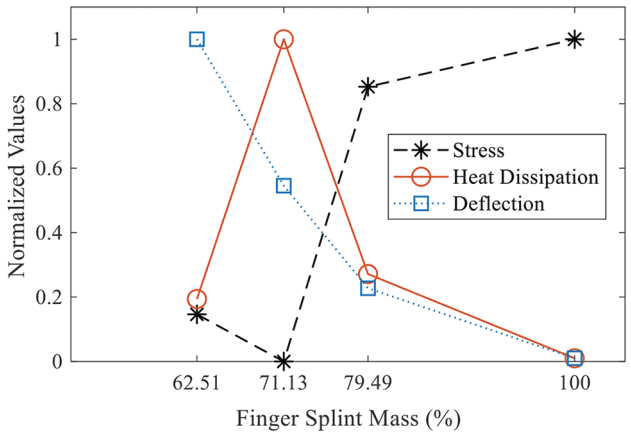

Figure 13. A trade-off among deflection, stress, and heat dissipation of three-dimensional-printed splints.

Surface finish and appearance are important considerations in comfort and appeal to the user. The parameters that optimize the quality of 3D printing need to be explored in this area to compete with the thermoplastic hand molded thermoplastic splints. There are some complications on achieving more strength of splints through print orientations on the expense of losing the surface finish quality, which could be the subject for future work.

Investigation in the future needs to be undertaken into the duration of time before PLA splints begin to experience mechanical property decline. It should be investigated at what point in the lead up to hydrolysis does mechanical performance decline. Fatigue testing should be investigated in the future. Cyclic loading of a finger splint with sub-maximal loads may place a more realistic loading pattern on the splint than one large one off-load. In the day-to-day wearing of a finger splint, the user would apply small repeat loads into the splint. This over the course of the 6 – 8-week recovery period may cause degradation or decline in mechanical properties of the splint.

Measurements of the finger were taken with calipers. Taking seven dimensions of the

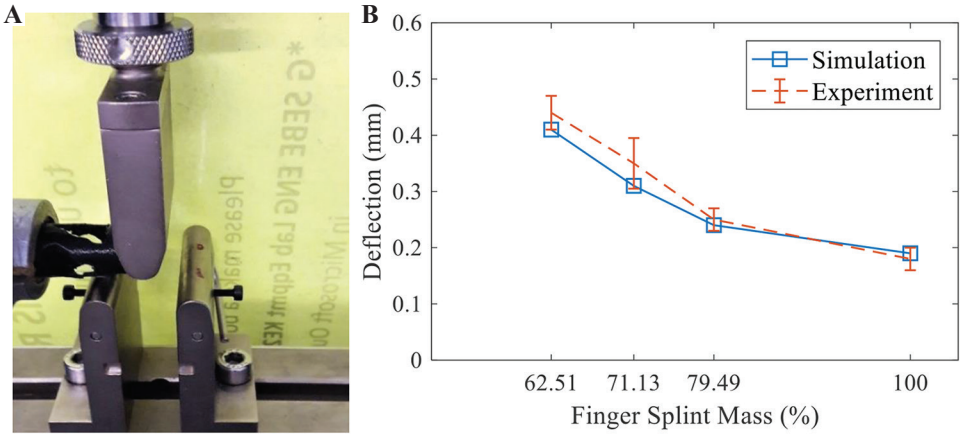

Figure 14. (A) A topology optimized three-dimensional-printed splint under deflection test; (B) comparison of experiments versus simulations of splints deflection.

finger to provide enough detail to get a highly specific customized splint to the user's finger. A progression for this project will be to use a 3D scanner to obtain the dimensions of the user's finger. This will provide an even higher level of accuracy and specificity to the patient.

4 Conclusion

In this work, a novel design of a patient-specific finger splint for a mallet finger treatment was proposed. The structure of the splint was fabricated in a size of a custom injured finger using AM. Utilizing FDM 3D printing provides a customizable fit specific to the patient. The FEA and TO were employed to create a splint with less material to reduce heat while conserving its satisfactory mechanical properties. This allows for much better breathability and less sweating for the patient, possibly lead to increase comfort for the duration of their recovery. Less material in the splint reduces the heat generated in the splint when in use, improving the comfort of the patient. Combining these two techniques optimizes mechanical properties and user comfort for the best chance of an optimal outcome for patients. This paper demonstrated how the use of engineering concepts and developing technologies could improve outcomes for patients in the treatment of mallet finger injury. The results of this project would pave the way for the medical industry to utilize superior advanced manufacturing and minimum materials that have been shape optimized to better serve their purpose while improving patient comfort.

References

1. Pegoli L, Pivato G, 2019, Mallet finger injuries. In: Sports Injuries of the Hand and Wrist. Springer, Berlin. pp. 1–13. DOI: 10.1007/978-3-030-02134-4_1.
2. Engdahl SM, Christie BP, Kelly B, *et al*., 2015, Surveying the Interest of Individuals with Upper Limb Loss in Novel Prosthetic Control Techniques. *J Neuroeng Rehabil*, 12:53. DOI: 10.1186/s12984-015-0044-2.
3. O'Brien L, 2010, Adherence to Therapeutic Splint Wear in Adults with Acute Upper Limb Injuries: A Systematic Review. *Hand Ther*, 15:3–12. DOI: 10.1258/ht.2009.009025.
4. Young KJ, Pierce JE, Zuniga JM, Assessment of Body-powered 3D Printed Partial Finger Prostheses: A Case Study. *3D Print Med*, 5:7. DOI: 10.1186/s41205-019-0044-0.
5. Choi H, Seo A, Lee J, 2019, Mallet Finger Lattice Casts Using 3D Printing. *J Healthc Eng*, 2019:4765043.
6. Koo DS, Lee JR, 2017, The Development of a Wrist Brace using 3D Scanner and 3D Printer. *Fashion Text Res J*, 19:312–9. DOI: 10.5805/sfti.2017.19.3.312.
7. Żyluk A, Piotuch B, 2010, Treatment of Mallet Finger a Review. *Pol J Surg*, 82:243–50.
8. Bazavar M, Rouhani A, Tabrizi A, 2014, Simultaneous Dorsal Base Fracture and FDP Avulsion of Distal Phalanx of the Little Finger. *Arch Bone Joint Surg*, 2:63.
9. Tuttle HG, Olvey SP, Stern PJ, 2006, Tendon Avulsion Injuries of the Distal Phalanx. *Clin Orthop Relat Res*, 445:157–68.
10. Robinson LS, Sarkies M, Brown T, *et al.*, 2016, Direct, Indirect and Intangible Costs of Acute Hand and Wrist Injuries: A Systematic Review. *Injury*, 47:2614–26. DOI: 10.1016/j.injury.2016.09.041.
11. Brunet M, Haddad RJ, Sanchez J, *et al*., 1984, How i Manage Sprained Finger in Athletes. *Phys Sportsmed*, 12:99–108. DOI: 10.1080/00913847.1984.11701926.
12. Imoto FS, Leão TA, Imoto RS, *et al*., 2016, Osteosynthesis of Mallet Finger Using Plate and Screws: Evaluation of 25 Patients. *Rev Bras Ortop*, 51:268–73. DOI: 10.1016/j.rboe.2015.09.013.
13. O'Brien LJ, Bailey MJ, 2011, Single Blind, Prospective, Randomized Controlled Trial Comparing Dorsal Aluminum and Custom Thermoplastic Splints To Stack Splint For Acute Mallet Finger. *Arch Phys Med Rehabil*, 92:191–8. DOI: 10.1016/j.apmr.2010.10.035.
14. Berman B, 2013, 3D Printing: The New Industrial Revolution. *IEEE Eng Manag Rev*, 41:72–80. DOI: 10.1109/emr.2013.6693869.
15. Goh G, Yap YL, Tan HK, et al., 2019, Process-structure-properties in Polymer Additive Manufacturing Via Material Extrusion: A Review. *Crit Rev Solid State Mater Sci*, 45:1–21. DOI: 10.1080/10408436.2018.1549977.
16. Brenken B, Barocio E, Favaloro A, *et al*., 2018, Fused Filament Fabrication of Fiber-reinforced Polymers: A Review. *Addit Manuf*, 21:1–16. DOI: 10.1016/j.addma.2018.01.002.
17. Blaya F, Pedro PS, Silva JL, *et al*., 2018, Design of an Orthopedic Product by Using Additive Manufacturing Technology: The Arm Splint. *J Med Syst*, 42:54.
18. Yu C, Jiang J, 2020, A Perspective on Using Machine Learning in 3D Bioprinting. *Int J Bioprinting*, 6:95. DOI: 10.18063/ijb.v6i1.253.
19. Durgun I, Ertan R, 2014, Experimental Investigation of

FDM Process for Improvement of Mechanical Properties and Production Cost. *Rapid Prototyp J*, 20:228–35. DOI: 10.1108/rpj-10-2012-0091.

20. Bodaghi M, Noroozi R, Zolfagharian A, *et al*., 2019, 4D Printing Self-morphing Structures. *Materials*, 12:1353. DOI: 10.3390/ma12081353.
21. Rahim TN, Abdullah AM, Akil HM, 2019, Recent Developments in Fused Deposition Modeling-based 3D Printing of Polymers and their Composites. *Polym Rev*, 59(4):589-624. DOI: 10.1080/15583724.2019.1597883.
22. Jiang J, Xu X, Stringer J, 2019, Optimisation of Multi-part Production in Additive Manufacturing for Reducing Support Waste. *Virtual Phys Prototyp*, 14:219–28. DOI: 10.1080/17452759.2019.1585555.
23. Bodaghi M, Serjouei A, Zolfagharian A, *et al*., 2020, Reversible Energy Absorbing Meta-Sandwiches by 4D FDM Printing. *Int J Mech Sci*, 173:105451. DOI: 10.1016/j.ijmecsci.2020.105451.
24. Zolfagharian A, Kouzani A, Khoo SY, *et al*., 2018, 3D Printed Soft Parallel Actuator. *Smart Mater Struct*, 27:45019. DOI: 10.1088/1361-665x/aaab29.
25. Zolfagharian A, Kaynak A, Kouzani A, 2019, Closed-loop 4D-printed Soft Robots. *Mater Des*, 188:108411. DOI: 10.1016/j.matdes.2019.108411.
26. Jiang J, Xu X, Stringer J, 2018, Support Structures for Additive Manufacturing: A Review. *J Manuf Mater Process*, 2:64.
27. Gordelier TJ, Thies PR, Turner L, *et al*., 2019, Optimising the FDM Additive Manufacturing Process to Achieve Maximum Tensile Strength: A State-of-the-art Review. *Rapid Prototyp J*, 25:953-971. DOI: 10.1108/rpj-07-2018-0183.
28. Mohamed OA, Masood SH, Bhowmik JL, 2015, Optimization of Fused Deposition Modeling Process Parameters: A Review of Current Research and Future Prospects. *Adv Manuf*, 3:42–53. DOI: 10.1007/s40436-014-0097-7.
29. Wong JY, 2015, On-site 3D Printing of Functional Custom Mallet Splints for Mars Analogue Crewmembers. *Aerosp Med Hum Perform*, 86:911–4. DOI: 10.3357/amhp.4259.2015.
30. Cazon A, Kelly S, Paterson AM, *et al*., 2017, Analysis and Comparison of Wrist Splint Designs Using the Finite Element Method: Multi-material Three-dimensional Printing Compared to Typical Existing Practice with Thermoplastics. *Proc Inst Mech Eng H*, 231:881–97. DOI: 10.1177/0954411917718221.
31. Dhanwal DK, Dennison EM, Harvey NC, *et al*., 2011, Epidemiology of Hip Fracture: Worldwide Geographic Variation. *Indian J Orthop*, 45:15–22. DOI: 10.4103/0019-5413.73656.
32. Lee RJ, Mears SC, 2012, Greening of Orthopedic Surgery. *Orthopedics*, 35:e940–4. DOI: 10.3928/01477447-20120525-39.
33. Teo AJ, Mishra A, Park I, *et al*., 2016, Polymeric Biomaterials for Medical Implants and Devices. *ACS Biomater Sci Eng*, 2:454–72.
34. Jiang J, Xu X, Stringer J, 2019, Optimization of Process Planning for Reducing Material Waste in Extrusion Based Additive Manufacturing. *Robot Comput Integr Manuf*, 59:317–25. DOI: 10.1016/j.rcim.2019.05.007.
35. Liu X, Song R, Zhang W, *et al*., 2017, Development of Eco-friendly Soy Protein Isolate Films with High Mechanical Properties Through HNTs, PVA, and PTGE Synergism Effect. *Sci Rep*, 7:1–9. DOI: 10.1038/srep44289.
36. Yang R, Chen C, 1996, Stress-based Topology Optimization. *Struct Optim*, 12:98–105.
37. Zolfagharian, A., Denk, M., Bodaghi, M, *et al*., 2019, Topology-optimized 4D Printing of a Soft Actuator. *Acta Mech Solid Sin*, 1:1-13. DOI:10.1007/s10338-019-00137-z.
38. Labanda, S.R, 2015, Mathematical Programming Methods for Large-scale Topology Optimization Problems. PhD Thesis, DTU.
39. Bendsøe MP, 2009, Topology Optimization. Springer, Berlin.
40. Price MJ, Trbovich M, 2018, Thermoregulation following spinal cord injury. In: Handbook of Clinical Neurology. Elsevier, Amsterdam. pp. 799–820. DOI: 10.1016/b978-0-444-64074-1.00050-1.
41. Stevens M, 2016, Human Body Heat as a Source for Thermoelectric Energy Generation, Submitted as Coursework for PH240. Stanford University, United States.

ORIGINAL ARTICLE

3D Freeform Printing of Nanocomposite Hydrogels through *in situ* Precipitation in Reactive Viscous Fluid

Shengyang Chen[1], Tae-Sik Jang[2], Houwen Matthew Pan[1], Hyun-Do Jung[2], Ming Wei Sia[1], Shuying Xie[1], Yao Hang[3], Seow Khoon Mark Chong[1], Dongan Wang[4], Juha Song[1]*

[1]School of Chemical and Biomedical Engineering, Nanyang Technological University, 70 Nanyang Drive, 637457, Singapore

[2]Liquid Processing and Casting Technology R&D Group, Korea Institute of Industrial Technology, Incheon 406-840, Republic of Korea

[3]School of Chemistry and Chemical Engineering, Yangzhou University, Yangzhou 225009, Jiangsu, P. R. China

[4]Department of Biomedical Engineering, City University of Hong Kong,83 Tat Chee Avenue, Kowloon Tong, Hong Kong

Abstract: Composite hydrogels have gained great attention as three-dimensional (3D) printing biomaterials because of their enhanced intrinsic mechanical strength and bioactivity compared to pure hydrogels. In most conventional printing methods for composite hydrogels, particles are preloaded in ink before printing, which often reduces the printability of composite ink with little mechanical improvement due to poor particle-hydrogel interaction of physical mixing. In contrast, the *in situ* incorporation of nanoparticles into a hydrogel during 3D printing achieves uniform distribution of particles with remarkable mechanical reinforcement, while precursors dissolved in inks do not influence the printing process. Herein, we introduced a "printing in liquid" technique coupled with a hybridization process, which allows 3D freeform printing of nanoparticle-reinforced composite hydrogels. A viscoplastic matrix for this printing system provides not only support for printed hydrogel filaments but also chemical reactants to induce various reactions in printed objects for *in situ* modification. Nanocomposite hydrogel scaffolds were successfully fabricated through this 3D freeform printing of hyaluronic acid (HAc)-alginate (Alg) hydrogel inks through a two-step crosslinking strategy. The first ionic crosslinking of Alg provided structural stability during printing, while the secondary crosslinking of photo-curable HAc improved the mechanical and physiological stability of the nanocomposite hydrogels. For *in situ* precipitation during 3D printing, phosphate ions were dissolved in the hydrogel ink and calcium ions were added to the viscoplastic matrix. The composite hydrogels demonstrated a significant improvement in mechanical strength, biostability, as well as biological performance compared to pure HAc. Moreover, the multi-material printing of composites with different calcium phosphate contents was achieved by adjusting the ionic concentration of inks. Our method greatly accelerates the 3D printing of various functional or hybridized materials with complex geometries through the design and modification of printing materials coupled with *in situ* post-printing functionalization and hybridization in reactive viscoplastic matrices.

Keywords: Three-dimensional freeform printing, *in situ* precipitation, Hydrogels, Nanocomposites, Viscous fluid matrix, Multi-materials

***Corresponding Author:** Juha Song, School of Chemical and Biomedical Engineering, Nanyang Technological University, 70 Nanyang Drive, 637457, Singapore; songjuha@ntu.edu.sg

Received: January 28, 2020**;** ***Accepted:*** March 03, 2020**;** ***Published Online:*** April 02, 2020

Citation: Chen S, Jang TS, Pan HM, *et al*., 2020, 3D Freeform Printing of Nanocomposite Hydrogels through *in situ* Precipitation in Reactive Viscous Fluid., *Int J Bioprint*, 6(2):258. DOI: 10.18063/ijb.v6i2.258.

1 Introduction

Recent advances in three dimensional (3D) printing technologies have facilitated the development of composite biomaterials through the ability to fabricate structurally, functionally, and compositionally intricate constructs[1-4]. Particularly, composite hydrogels have gained a great attention as 3D printing biomaterials

because of their materiality, micro- and macro-structures and functions are comparable to those of biological tissues, with their enhanced intrinsic mechanical strength and bioactivity compared to pure hydrogel systems[5-8] Among various hydrogel systems, hyaluronic acid (HAc)-based composite hydrogels have been applied for tissue scaffolds due to non-immunogenic, biocompatible, and enzymatically biodegradable natures of HAc[9-11]. By incorporating calcium phosphate (CaP), HAc composites exhibited significantly improved mechanical, biochemical, and biological properties, which could be used for dermal fillers or spacers[6,12,13]. Most inorganic-hydrogel composites are printed using composite inks consisting of inorganic particles dispersed in a hydrogel-forming ink before 3D printing[6,7]. This simple mixing approach to prepare composites not only allows easy control over the loading of inorganic particles but is also cell-friendly to enable bioprinting with cells. However, optimizing the printability of the composite inks and print quality often becomes more challenging with increased particle loading. The previous studies have demonstrated that composite inks with only up to 10% nanoparticle loading show suitable printability and structural accuracy. Moreover, the mechanical properties of composite hydrogels depend on the particle-hydrogel interactions and often require an additional modification of either the particles or hydrogels for enhancement of mechanical properties[6].

To overcome these limitations, *in situ* incorporation of nanoparticles has been proposed, whereby permeated ions within the hydrogel structures are reacted by drastically increasing the pH, and nanocrystals are nucleated on the functional groups of the polymer chains within the hydrogels. This *in situ* precipitation method achieves uniform distribution of the nanoparticles, strong particle–polymer bonding, and remarkable mechanical reinforcement in the hydrogel[5,13,14]. One of the possible printing methods to enable *in situ* precipitation-coupled 3D printing is freeform printing in viscous fluid matrices. Freeform 3D printing allows an omnidirectional printing path using mechanically unstable hydrogels with a relatively slow solidification rate[15-19]. Compared with conventional 3D printing in air, embedded freeform 3D printing requires the two shear thinning materials to have matching properties, particularly their shear moduli and shear thinning yield stresses[19,20]. How material parameters influence printability and print quality has been extensively studied[15,20]. Shear thinning of viscous matrices has been achieved by fabricating polymer–nanoparticle composites or dispersing the hydrogel particles in water[15,17,19,20]. Moreover, in addition to the mechanical support provided by the printed soft filaments, a crosslinking agent that induces the solidification of the printed material is often included in the matrix. Alginate (Alg) or silk fibroin-based inks have been successfully printed and crosslinked within hydrogel-based beds for biomedical applications[17,19]. One of the greatest advantages of printing in the liquid is the unique flexibility of the chemical environment. However, despite the revolutionary achievements in freeform printing, viscous fluid matrices have not been used for the functionalization or hybridization of printed materials.

Here, we present a hybridization process for a 3D freeform printing system to fabricate composite hydrogel scaffolds in conjunction with *in situ* precipitation of a mineral phase. By varying the concentration of CaP in a HAc-Alg hydrogel, we developed HAc-Alg/CaP nanocomposite scaffolds with a two-step crosslinking strategy, including physical crosslinking of Alg and photo-crosslinking of glycidyl methacrylate HAc (GM-HAc). To review the effectiveness of our method, we compared the structural compositions, mechanical, physiological, and biological properties between our printed HAc-CaP nanocomposite scaffolds and pure hydrogels or composite hydrogels generated through *ex situ* CaP incorporation. Furthermore, by varying the concentrations of calcium or phosphate ions, multi-material printing of HAc-Alg/CaP with the differing extent of mineralization was achieved with high precision. Taken together, we envisage that our method can accelerate 3D printing using various functional or hybridized materials with complex geometries through the design

and modification of printing materials coupled with *in situ* post-printing functionalization and hybridization in reactive viscoplastic matrices.

2 Materials and methods

2.1 Materials

HAc sodium salt from *Streptococcus equi* (molecular weight ≈ 1.5~1.8 MDa), phosphate-buffered saline (PBS), dimethylformamide (DMF), GM, tetrabutylammonium bromide, triethylamine, acetone, alginic acid sodium salt from brown algae, N-vinylpyrrolidinone (NVP), Irgacure 2959 (2-Hydroxy-4′-(2-hydroxyethoxy) -2-methylpropiophenone), calcium chloride ($CaCl_2$), ammonium phosphate dibasic ($(NH_4)_2HPO_4$), and gelatin from bovine skin (Type B) was purchased from Sigma-Aldrich and used without further purification.

2.2 Preparation of GM-HAc

GM-HAc was synthesized using a previously developed protocol[9]. HAc (1% wt/v) was dissolved in a mixture of PBS and DMF at the volume ratio of 1:1. Then, triethylamine (4.4% v/v), GM (4.4% v/v), and tetrabutylammonium bromide (4.4% wt/v) were added in sequence. After stirring overnight at room temperature, GM-HAc was precipitated with acetone and dissolved in distilled water to remove excess reactants. The solution was dialyzed in distilled water for 2 days, lyophilized, and stored at 4°C. Through the characterization of GM-HAc using nuclear magnetic resonance (Bruker Avance II 300 MHz, Bruker, Germany), the degree of methacrylation was found to be ~15% (**Supplementary Figure 12**).

2.3 Preparation of bulk hydrogel specimens through molding

For the fabrication of HAc-Alg and HAc-Alg/CaP bulk specimens, GM-HAc (1% wt/v) was mixed with Alg (0.125% wt/v), NVP (NVP; 5% v/v), and Irgacure 2959 (1% wt/v) with or without $(NH_4)_2HPO_4$, varying the amount of $(NH_4)_2HPO_4$ from 0.046 M up to 0.092 M, to yield CaP content ranging from 15 to 30 wt%. Then, 1 mL of the resulting solution was transferred to a plastic mold and exposed to ultraviolet (UV) light for 5 min. The gel piece was subsequently physically crosslinked in a 0.153 M $CaCl_2$ solution for 3 h and dialyzed in distilled water for 24 h. To compare composite hydrogels through *in situ* precipitation with those through physically mixing with CaP nanoparticles, CaP nanoparticles were prepared by mixing $CaCl_2$ solution (0.153 M) and $(NH_4)_2HPO_4$ (0.092 M). The CaP precipitate was then centrifuged and lyophilized. GM-HAc (1% wt/v) was mixed with Alg (0.125% wt/v), CaP (0.34% wt/v), NVP (5% v/v), and Irgacure 2959 (1% wt/v). Then, 1 mL of the resulting solution was transferred to a plastic mold and exposed to UV light for 5 min. The gel piece was subsequently physically crosslinked in a 0.153 M $CaCl_2$ solution for 3 h and dialyzed in distilled water for 24 h.

2.4 Preparation of 3D printed hydrogel scaffolds

The gelatin bath was prepared using a previously developed protocol[17]. In brief, gelatin (5% wt/v) was dissolved in a 0.153 M $CaCl_2$ solution at 40°C. The solution was then gelled at 4°C. Subsequently, 5 mL of the gelatin gel and 15 mL of the 0.153 M $CaCl_2$ solution was homogenized at 10,000 rpm for 1 min. The mixture was centrifuged at 4000 rpm for 2 min, and the supernatant was removed to obtain a gelatin slurry support bath.

For 3D printing of HAc-Alg scaffolds, GM-HAc (4% wt/v) was mixed with Alg (0.5% wt/v), NVP (10% v/v), and Irgacure 2959 (2% wt/v) to prepare the ink for 3D printing. The HAc-Alg pure hydrogel scaffold was then printed in the gelatin slurry support bath at a feed rate of 5 mm/s and air pressure of 2.5 bar using a regenHU 3D discovery printer. The scaffold was then exposed to UV light for 5 min and incubated at 37°C to melt and remove the support bath.

For HAc-Alg/CaP composite hydrogel scaffolds, the hydrogel inks were prepared by mixing GM-HAc (4% wt/v) with Alg (0.5% wt/v), NVP (10% v/v), and Irgacure 2959 (2% wt/v) with $(NH_4)_2HPO_4$ (0.092 M) and then printed in the gelatin slurry support bath at a feed rate of 5 mm/s and air pressure of 2.5 bar using the regenHU 3D discovery printer. The scaffold was then exposed

to UV light for 5 min and incubated at 37°C to melt and remove the support bath.

2.5 Characterization of the HAc-Alg and HAc-Alg/CaP hydrogels

HAc-Alg and HAc-Alg/CaP hydrogels were observed using a field emission scanning electron microscope (FE-SEM; Quanta 200F, FEI Company, USA) equipped with energy-dispersive X-ray spectroscopy (EDS). All hydrogel specimens were carefully dried in a three-step process. First, the hydrogels were immersed in a 2.5% glutaraldehyde solution overnight. Subsequently, they were dehydrated using a series of ethanol solutions with the following concentrations: 30%, 50%, 70%, 80%, 90%, 95%, and 100%. Finally, the samples were dried using a critical point dryer (K850, Quorum Technologies, UK). The morphology and chemical composition of precipitated CaP were examined using a transmission electron microscope (TEM; TECHNI G2 ST-F20, FEI, USA) operated at 200 kV acceleration voltage, equipped with EDS. For this analysis, the nanocomposite hydrogels were loaded onto mesh copper grids during the fabrication process and dried in air for 12 h.

The mineral phases of the fabricated hydrogels were analyzed using an X-ray diffractometer (XRD; D/MAX-2500/PC, Rigaku Co., Japan). Three types of the specimen (HAc-Alg and two HAc-Alg/CaP composite hydrogels prepared by physical mixing and *in situ* precipitation) were scanned over a 2θ range of 10 – 70° with a scanning rate of 0.1°/min. The chemical structures of the HAc-Alg and HAc-Alg/CaP scaffolds after degradation were characterized by Fourier-transform infrared (FTIR) spectroscopy (FT-IR; Spectrum One FTIR, PerkinElmer, USA). The amount of CaP incorporated into the nanocomposite hydrogels was measured by thermogravimetric analysis (TGA; STA 409 PC, NETZESCH, Germany). HAc-Alg and HAc-Alg/CaP hydrogels (*in situ* precipitation) were lyophilized and heated at 1000°C at a rate of 5 K/min in nitrogen (N_2) flow.

2.6 Mechanical properties of the HAc-Alg and HAc-Alg/CaP scaffolds

Pieces of HAc-Alg and HAc-Alg/CaP hydrogel fabricated both by mixing and *in situ* precipitation were subjected to rheological tests. All the gel pieces were prepared with a diameter of 25 mm and a thickness of 2 mm. Frequency sweeps were carried out in the angular frequency range of 0.1 – 100 rad/s at 1% strain. Compressive tests of the 3D-printed HAc-Alg and HAc-Alg/CaP porous scaffolds were performed at a strain rate of 10 μm/s up to a predefined strain of 80% using a MicroTester (MTS C42, USA). All of the scaffolds were prepared on a 10 mm × 10 mm × 5 mm scale by 3D printing with or without *in situ* precipitation. The slope of the linear fit for 20 – 30% strain of the stress-strain plot was used as a measurement of the compressive modulus.

2.7 Physiological tests of the HAc-Alg and HAc-Alg/CaP hydrogels

The swelling ratios of HAc-Alg and HAc-Alg/CaP composite hydrogel pieces fabricated with both mixing and mineralization were determined. All of the gel pieces were prepared with a diameter of 25 mm and a thickness of 2 mm. The swelling ratio was evaluated in a PBS solution at 37°C. The gel pieces were lyophilized and weighed to record the initial weight of the dry gel (W_i). They were then immersed in PBS for 24 h and reweighed to record the weight of hydrated gel (W_h). The swelling ratio was calculated according to the equation,

$$\text{Swelling ratio (g/g)} = (W_h - W_i)/W_i \quad (1)$$

HAc-Alg and HAc-Alg/CaP hydrogel scaffolds were prepared by 3D printing and used for degradation tests. All of the scaffolds were prepared with dimensions of 10 mm × 10 mm × 5 mm. The scaffolds were immersed in a PBS solution at 37°C with hyaluronidase at a concentration of 100 – 250 UI/ml. The degradation rates were investigated by measuring the weight changes as follows:

$$\text{Remaining weight (\%)} = (W_r/W_i) \times 100 \quad (2)$$

where W_r is the remaining weight and W_i is the initial weight.

2.8 *In vitro* cytotoxicity test

HAc-Alg and HAc-Alg/CaP hydrogel pieces cast in plastic molds were used for the cell viability tests. All of the gel pieces were prepared in 12-well plates. The fibroblast cell line L929 (a derivative of *Mus musculus* strain L) was used to assess the cellular responses to the hydrogels. Before seeding, the samples were washed with Dulbecco's PBS and then sterilized under UV irradiation for 1 h. The cells were seeded at a density of 5×10^4 cells/mL. They were cultured in minimum essential medium (MEM)-alpha medium with 10% fetal bovine serum (FBS) and 1% penicillin-streptomycin in an incubator with 5% CO_2 at 37°C. Cell viability was tested via the AlamarBlue assay after 3 and 5 days of culturing. Cellular morphology on the surfaces of both hydrogel specimens was observed using FE-SEM (FE-SEM; Quanta 200F, FEI Company, USA) after 5 days of culturing. All of the samples were washed 3 times using PBS. They were then fixed in 2.5% glutaraldehyde solution and were gradually dehydrated with a series of ethanol solutions with the following concentrations: 30%, 50%, 70%, 80%, 90%, 95%, and 100%.

For cell attachment tests of 3D-printed composite hydrogels, fluorescence microparticles (FluoSpheres carboxylate-modified microspheres, 1.0 μm, blue fluorescent [350/440], Invitrogen, Thermo Fisher Scientific, USA) were incorporated into the inks to stain the printed scaffolds for imaging. The cells were seeded at a density of 5×10^5 cells/ml and cultured for 7 days. The cells were stained with nucleic acid stain (Hoechst 33342, trihydrochloride, trihydrate, Invitrogen, Thermo Fisher Scientific, USA) and plasma membrane stain (CellMask, deep red plasma membrane stain, Invitrogen, Thermo Fisher Scientific, USA). Cell adhesion was observed using a confocal laser scanning microscope (CLSM, LSM 800, ZEISS, Germany).

For the cell viability test of cell-laden HA-Alg porous scaffolds, pure hydrogel inks consisting of 4% w/v GMHA, 0.5% w/v Alg, 0.5% v/v NVP, 0.9% w/v NaCl, and 0.5% w/v Irgacure 2959 were prepared for 3D printing. Cell-laden Alg microparticles with a cell density of 6×10^6 cells/ml were prepared as previously described Pan *et al*.[21] The cell-laden microparticles were mixed with the HA-Alg ink at a mass ratio of 1:3. The cell-laden inks were printed in the gelatin slurry support bath at a feed rate of 5 mm/s and air pressure of 0.5 bar using the 3D printer with a 0.51 mm nozzle. The printed scaffolds were then exposed to UV light for 2.5 min and incubated at 37°C to melt and remove the support bath. All of the cell-laden scaffolds were the washed 3 times with PBS to remove any remaining gelatin and were then incubated with live/dead staining solution containing 2 μM calcein-AM and 4 μM ethidium homodimer-I stains for 30 min at 37 °C. The stained cells were observed using CLSM (LSM 800, ZEISS, Germany).

2.9 *In vitro* differentiation test

Osteogenic differentiation was evaluated using MC3T3-E1 pre-osteoblast cells cultured in MEM-alpha medium (no ascorbic acid, Gibco, Thermo Fisher Scientific, USA) with 10% FBS and 1% penicillin and streptomycin in an incubator with 5% CO_2 at 37°C. The cells were seeded at a density of 2×10^5 cells/well on a 12-well plate for the control and 1×10^6 cells/scaffold for the HAc-Alg/CaP composite hydrogel scaffolds. They were cultured in either cell maintenance medium or osteogenic medium (cell maintenance medium supplemented with 0.05 mg/mL ascorbic acid and 10 mM β-glycerophosphate) for 2 weeks. Gene expression was evaluated by quantitative real-time polymerase chain reaction (qPCR) after 14 days of culturing. RNA was extracted from the cells by TRIzol (Invitrogen, Thermo Fisher Scientific, USA) and then converted to cDNA through reverse transcription by Moloney Murine Leukemia Virus reverse transcriptase (Promega, USA). To test *in vitro* cell differentiation, the following four markers, Runx2, Collagen type 1 (COL1), osteopontin (OPN), and osteocalcin (OCN), were chosen, while actin was used as a reference gene [ref]. The sequences of each gene are shown in **Table 1**. The qPCR was conducted using a CFX Connect real-time system (Bio-Rad, USA) with SsoAdvanced Universal SYBR Green

Table 1. Sequence of primers for the RT-qPCR.

Gene	Forward primer sequence	Reverse primer sequence
Actin	5'-GTGCTATGTTGCCCTAGACTTCG-3'	5'-GATGCCACAGGATTCCATACCC-3'
Col 1	5'-CAAGATGTGCCACTCTGACT-3'	5'-TCTGACCTGTCTCCATGTTG-3'
RunX2	5'-GCATGGCCAAGAAGACATCC-3'	5'-CCTCGGGTTTCCACGTCTC-3'
OCN	5'-CTTTCTGCTCACTCTGCTG-3'	5'-TATTGCCCTCCTGCTTGG-3'
OPN	5'-CACTTTCACTCCAATCGTCCCTAC-3'	5'-ACTCCTTAGACTCACCGCTCTTC-3'

RT-qPCR: Quantitative real-time polymerase chain reaction, OCN: Osteocalcin, OPN: Osteopontin

Supermix (Bio-Rad, USA). For analysis, the gene expression values were first normalized to the reference gene (Actin) and then normalized to the control group in cell maintenance medium.

2.10 3D printing of multiphase HAc-CaP scaffolds

HAc-Alg/10wt% CaP and HAc-Alg/30 wt% CaP composite hydrogel inks were prepared, as described in the previous section. Both hydrogel inks were preloaded into the cartridge before 3D printing. For the vertical stacking scaffold, six layers of HAc-Alg/30 wt% CaP ink were first extruded into the gelatin bath. Then, the cartridge was changed and six layers of HAc-Alg/10 wt% CaP ink were printed on top of the printed structure. For horizontal stacking, six layers of HAc-Alg/10 wt% CaP were first printed to form an inner core structure. Subsequently, the HAc-Alg/30 wt% CaP ink was extruded, surrounding the inner structure to create the outer shell part. Subsequently, post-curing with UV irradiation was performed to stabilize the multi-material scaffolds.

2.11 Statistical analysis

All experimental results were presented as mean ± standard deviation (SD) for $n \geq 3$. One-way analysis of variance was used to determine the difference between groups, and $P < 0.05$ was considered statistically significant.

3 Results and discussion

3.1 3D freeform printing of composite hydrogels

To enable *in situ* precipitation of CaP during 3D printing of HAc filaments, we considered two key issues. First, for *in situ* precipitation, it is necessary to incorporate calcium and phosphate ions into the hydrogel ink and the supportive viscous fluid matrix, respectively. Second, *in situ* precipitation should not inhibit either the crosslinking of the printed hydrogel filaments or interlayer bonding between the printed layers. To resolve these two issues, HAc-Alg hydrogels were used for dual crosslinking in conjunction with *in situ* CaP precipitation (**Figure 1**). The first physical crosslinking of Alg was induced within a gelatin-based viscoplastic matrix containing excess calcium ions, while the *in situ* precipitation occurred throughout the printed filaments. The crosslinked Alg maintained the structural integrity of the printed filaments within the fluid during the reaction. Pure HAc hydrogels were also printed to compare with HAc-Alg hydrogels. The printed structure of HAc hydrogels could not be well-maintained inside the gelatin slurry since the inks remained unsolidified. As a result, the printing quality of pure HAc scaffolds is significantly lower than that of HAc-Alg. Moreover, the printed HAc scaffolds were mechanically weak. The storage modulus of HAc hydrogels was one order of magnitude smaller than that of HAc-Alg hydrogels (**Supplementary Figure 7-A**). Thus, we clearly confirmed that the physical crosslinking process with Alg significantly improves the mechanical stability of printed HAc hydrogels during printing and even after UV crosslinking.

After the completion of 3D printing, the mineralized scaffold was irradiated with UV for 10 min. The photocrosslinking of GM-HAc caused complete solidification of the entire scaffold, which increased the mechanical and chemical stability of the hydrogel. The Alg/HAc ratio was optimized to moderate the onset of the sol-gel transition of HAc-Alg after the physical crosslinking of the Alg. The printability of hydrogel-forming inks and the

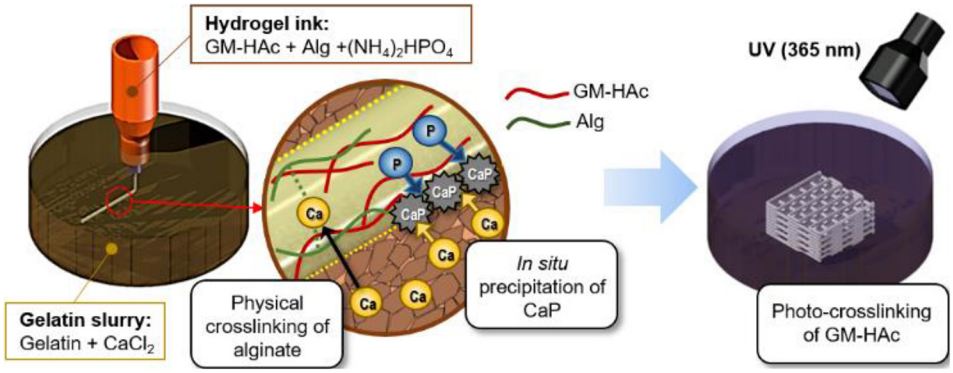

Figure 1. Schematic of three-dimensional freeform printing system of nanocomposite hydrogels through a two-step crosslinking process coupled with *in situ* precipitation.

interlayer bonding of mineralized filaments were markedly influenced by the amount of crosslinked Alg within the HAc-Alg during 3D printing. The optimal Alg/HAc ratio was found to be 1:8.

The ink composed of GM-HAc and Alg with $(NH_4)_2HPO_4$ is extruded into a gelatin supporting bath with $CaCl_2$. Physical crosslinking of Alg and *in situ* precipitation of CaP take place simultaneously during the 3D printing process. The printed construct is post-treated with photocrosslinking by UV irradiation. The amount of precipitated CaP is controlled by varying the concentration of $(NH_4)_2HPO_4$ in ink.

The 3D hydrogel structures were fabricated within a supportive viscous fluid matrix composed of gelatin microparticles and calcium chloride[17]. As the rheological behavior of gelatin is affected by pH, HAc-Alg solutions with phosphate (PO_4^{3-}) ions are required to be at pH 7 – 8 to achieve good print quality. We used diammonium hydrogen phosphate (diammonium phosphate [DAP]) instead of phosphoric acid to facilitate the reaction described by Eq. (3), aiming to obtain dicalcium phosphate dehydrate ($CaHPO_4{\cdot}2H_2O$, dicyclopentadiene [DCPD]), which is known to be a common precursor of hydroxyapatite[13,22].

$$(NH_4)_2HPO_4 + CaCl_2 \rightarrow CaHPO_4{\cdot}2H_2O + 2NH_4 + 2Cl^- \quad \text{at pH 8, 25°C} \qquad (3)$$

It is noteworthy that the rheological properties of inks for both HAc-Alg and HAc-Alg/CaP hydrogels are almost identical regardless of the existence of phosphate ions. Thus, the printing parameters for both inks were exactly the same, without additional optimization depending on mineral contents of inks since the particles post-loaded into the hydrogel should not hinder the printing process.

Figure 2 shows both pure and composite hydrogels printed with ten layers. The transparency of the printed scaffolds was used as an indicator of mineral incorporation (**Supplementary Videos 1 and 2**). The lateral view optical images of the printed porous scaffolds exhibited an almost circular cross-sectional area regardless of the material composition. During the UV treatment, gelatin microgels became fully fluidized due to the heat generated from the crosslinking reactions, thereby releasing the solidified printed objects (**Supplementary Videos 3 and 4**). Moreover, we printed composite hydrogels on a glass slide without any supporting matrix (**Supplementary Figure 1**). The printed structure of the hydrogels was almost collapsed due to lack of self-supportability. Therefore, printing in liquid clearly improved printability of soft materials with good printing quality in addition to functionalization of printed materials.

3.2 Structural characterization of the printed scaffolds

After critical point drying, the surface and cross-sectional morphologies of the printed scaffolds were observed using SEM (**Figure 3**). While pure hydrogel scaffolds exhibited macroscopically rough and porous surfaces, mineralized composite

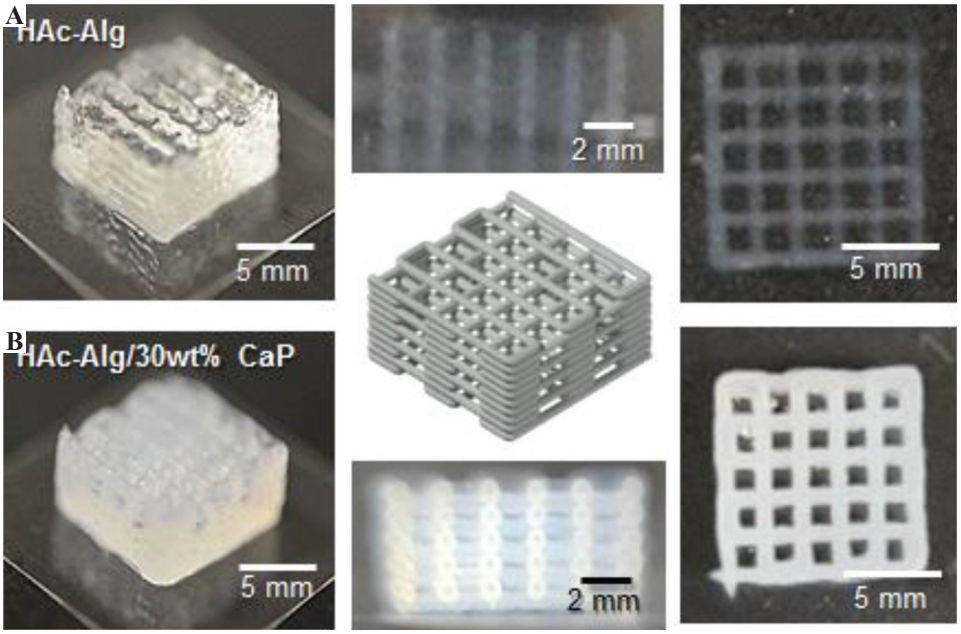

Figure 2. Schematics and optical images of three-dimensional-printed scaffolds. (A) Hyaluronic acid-alginate (HAc-Alg) hydrogel scaffolds (perspective view, top view, and side view). (B) HAc-Alg/30 wt% calcium phosphate composite hydrogel scaffolds (perspective view, top view, and side view).

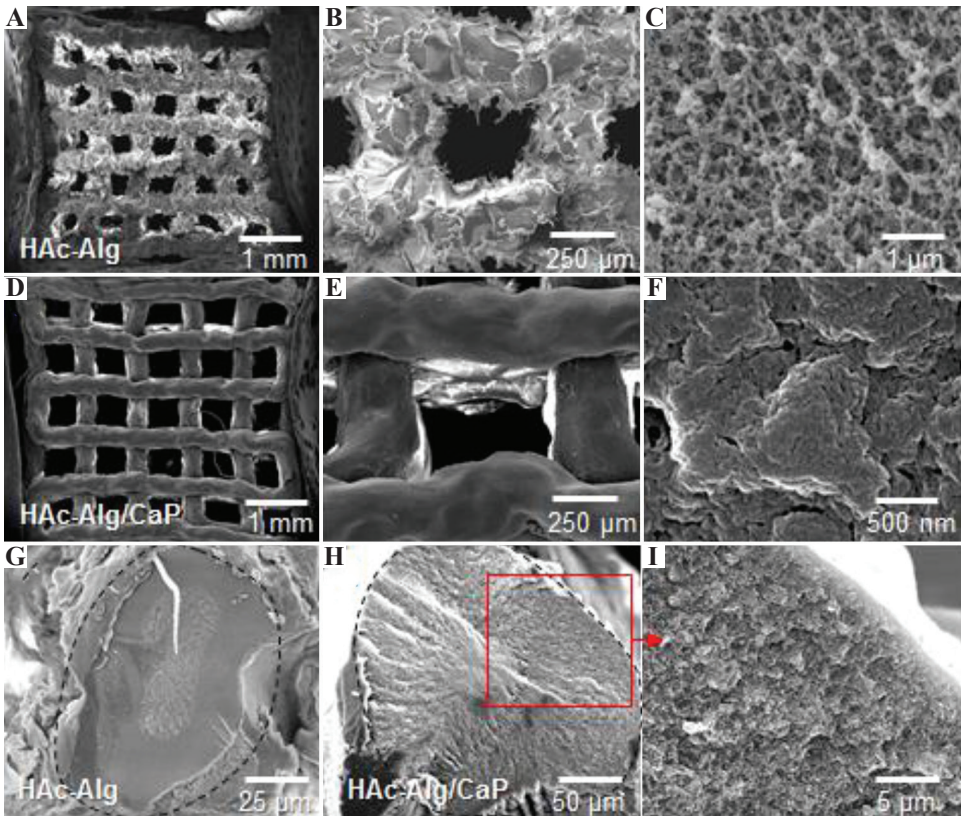

Figure 3. Surface and cross-sectional morphologies of dehydrated 3D-printed scaffolds. (A-C) Surface morphology of hyaluronic acid-alginate (HAc-Alg) hydrogel scaffolds. (D-F) Surface morphology of HAc-Alg/30 wt% calcium phosphate (CaP) composite hydrogel scaffolds. (G) Cross-sectional morphology of a printed HAc-Alg filament. (H and I) Cross-sectional morphology of a printed HAc-Alg/30 wt% CaP filament.

scaffolds exhibited smooth and dense surfaces (**Figure 3A-F**). The high-resolution SEM image of HAc-Alg indicated the presence of spherical nanoparticles with sizes ranging from five to a few tens of nanometers on the nanoporous polymeric network (**Figure 3C**). In contrast, the HAc-Alg/CaP hydrogel exhibited densely packed nanoparticles that formed a continuous mineral network throughout the printed scaffold (**Figure 3D**).

The increased CaP content (from 10 wt% to 30 wt%) was caused by the increased number of CaP particles and not the crystal growth of nanoparticles (**Supplementary Figure 2 and Supplementary Table 1**). The nucleation rate of nanoparticle formation is often experimentally described in terms of supersaturation of the solution (S), free surface energy (γ) of particles and temperature (T) as follows, where A and C are constants[23]:

$$\frac{dN}{dt} = Aexp(C \bullet \frac{\gamma^3}{T^3 (lnS)^2}) \quad (4)$$

According to Eq. (4), the total number of CaP nuclei should be significantly larger for 30 wt% CaP compared with 10 wt% CaP at room temperature, due to the higher level of supersaturation induced by increased phosphate ions in the presence of excess calcium ions (assuming that the CaP of both systems has the same free surface energy)[23]. Meanwhile, the total reaction time was limited to 20 min, which constrained the growth of nanoparticles. As a result, CaP nanoparticles for HAc-Alg/30 wt% CaP formed the continuous inorganic phase through the aggregation of densely packed nano-precipitates, which uniformly coated the surface of the polymer matrix, reducing the surface roughness (**Figure 3E and F**).

We presumed that the obtained mineral phase was mainly DCPD based on the chemical reaction, as shown in Eq. (3). To analyze the mineral phase of the composite hydrogels, the nanocrystals were characterized using TEM, X-ray diffraction, and EDS. The XRD pattern of HAc-Alg revealed the existence of calcium carbonate nanocrystals (**Figure 4A**). These nanoparticles were either vaterite or calcite. In a Ca^{2+}-gelatin bath, HAc-Alg undergoes ionic crosslinking, whereby calcium carbonate is formed through the reaction between calcium and carbonate ions. Carbonate ions are known to exist in aqueous solution due to the dissolved carbon dioxide[24]. Hosoda and Kato previously demonstrated the formation of a thin calcium carbonate crystalline layer in a reactive Ca^{2+}-containing solution in the presence of insoluble and soluble acidic polymers with carboxyl groups[25]. The HAc-Alg units inside the gelatin bath should act as insoluble acidic polymers and soluble acidic biomacromolecules, allowing calcium carbonate crystals to grow on the polymer matrix. Due to the interactions between the calcium ions and carboxyl groups, the localized calcium concentration around the HAc-Alg matrix is likely to induce crystal growth.

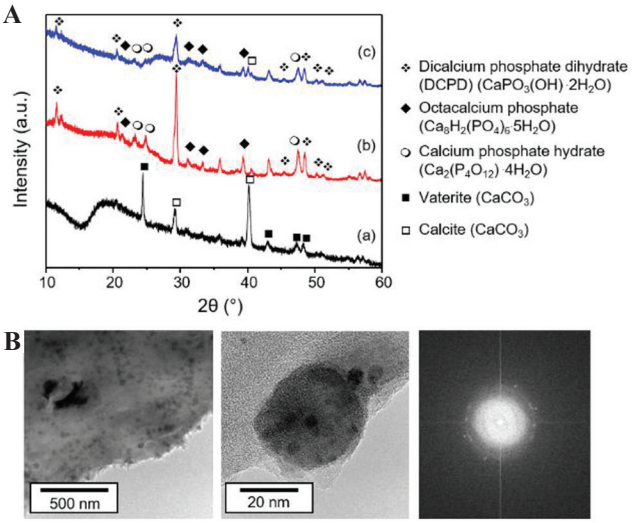

Figure 4. Mineral phases of hyaluronic acid-alginate (HAc-Alg)/calcium phosphate (CaP) hydrogels. (A) X-ray diffractometer patterns of (a) HAc-Alg hydrogels, (b) HAc-Alg/30 wt% CaP composite hydrogels prepared by mixing, and (c) HAc-Alg/30 wt% CaP composite hydrogels prepared by *in situ* precipitation. (B) Transmission electron microscope images of CaP nanoparticles in HAc-Alg/CaP composite hydrogels (prepared by *in situ* precipitation) and corresponding selected-area electron diffraction patterns of CaP nanoparticles.

The XRD patterns of two HAc-Alg/CaP composite specimens prepared by *ex situ* incorporation and *in situ* precipitation were almost identical, implying that the existence of the polymer template did not alter the CaP phases. The dominant CaP nano-precipitates were DCPD crystals. We also identified other CaP precipitates such as octacalcium phosphate (OCP) and CaP hydrate with a small amount of calcite. For a clearer observation of the CaP nanoparticles formed on HAc-Alg, a ten-fold diluted HAc-Alg ink with DAP solution (to maintain the ionic concentrations) was used. The increased pore size due to the lower polymer concentration prevented cohesive agglomeration of the CaP precipitates. The TEM revealed uniform spherical nanoparticles of ~60 nm, which was consistent with the morphology of CaP on HAc-Alg obtained using SEM. The selected area electron diffraction (SAED) pattern of the CaP nanoparticles indicated a characteristic polycrystalline ring, which correlated with the multiple characteristic peaks in the XRD pattern. EDS mapping of the composite hydrogels confirmed that these nanoparticles were composed of calcium, phosphorus, and oxygen (**Supplementary Figures 3-5**). As expected, the quantitative EDS analyses indicated that the nanocrystals contained 10 at.% Ca, 17 at.% P, and 73 at.% O (a Ca/P ratio of ~0.6). As the Ca/P ratios of OCP, DCPD, and CaP hydrate were 1.33, 1, and 0.5, respectively, the quantified Ca/P ratio indicated that the CaP nanocrystals were a mixture of OCP, DCPD, and CaP hydrate.

The weight fraction of inorganic nanoparticles in the printed hydrogels was determined using TGA (**Supplementary Figure 6**). The TGA result for the HAc-Alg scaffold indicated that the weight fraction of calcium carbonate was ~5 wt% before the decomposition of calcium carbonate to calcium oxide above 600°C[26]. In contrast, the weight fractions of calcium carbonate and CaP for HAc-Alg/CaP scaffolds were estimated to be ~4 and ~32 wt%, respectively. The desired mineral content could be achieved solely through *in situ* precipitation during 3D printing. The size of the mineral particles observed in this study (~60 nm) was much smaller than that observed in our previous study (200~350 nm), where the CaP content of the HAc-CaP bulk hydrogels fabricated by *in situ* precipitation was influenced by the size of the CaP nanoparticles[5]. Instead, the increased phosphate concentration in the presence of excess calcium ions is likely to have accelerated the nucleation rate of CaP nanoparticles (**Supplementary Table 2**)[23]. As the total precipitation time of our system was limited to 20 min, the average sizes of nanoparticles were almost identical regardless of the mineral contents in the HAc-Alg/CaP hydrogels **(Supplementary Figure 2 and Supplementary Table 2**). Taken together, our results indicate that the mineral content of HAc-Alg/CaP hydrogels can be effectively modulated by varying the phosphate concentration in the inks.

3.3 Mechanical behavior of the composite gels and scaffolds

Hydrogels are often regarded as soft materials that are not suitable for various load-bearing conditions. Thus, nanocomposite biomaterials are more suitable to be used as various tissue scaffolds or fillers that require structural integrity and mechanical stability during cell proliferation and differentiation[5,7,14,27]. To compare the mechanical properties of the different composite hydrogels and pure hydrogels, various mechanical tests were performed (**Table 2**). Rheological tests on bulk hydrogels revealed that the storage moduli of the HAc-Alg/CaP nanocomposite hydrogels were 4 times higher than those of the HAc-Alg hydrogels (**Supplementary Figure 7-B**). Furthermore, significant differences were found in all pair-wise comparisons conducted between the HAc-Alg/30 wt% CaP generated by *in-situ* precipitation and HAc-Alg/30 wt% CaP generated by *ex situ* incorporation, indicating that the HAc-Alg/30 wt% CaP generated by *in situ* precipitation exhibited a remarkable improvement in mechanical and swelling behaviors compared with the HAc-Alg/30 wt% CaP generated by *ex situ* incorporation. We also fabricated HAc-Alg and HAc-Alg/CaP scaffolds using a 3D printer and measured their local and global mechanical properties. In fact, the composite HAc-Alg/30

Table 2. Mechanical behavior of fully hydrated HAc-Alg hydrogels, and HAc-Alg/ 30wt% CaP composite hydrogels prepared by mixing and *in situ* precipitation (n>3).

Specimen	Swelling ratio (g/g)	Bulk gel[a]	3D printed porous scaffold	
		G' (Pa)[b]	E (kPa)	σ_c (kPa)[c]
HAc-Alg	31±2	298±58	3.3±0.6	18.9±2.1
HAc-Alg/30wt% CaP (mixing)[d]	28±1	502±62	N.A.	N.A.
HAc-Alg/30wt% CaP (*in situ precipitation*)	25±1	1397±194	6.4±1.2	35.9±2.9

[a]hydrogel specimens fabricated by direct casting using a cylindrical mold and assessed by a rheometer, [b]storage modulus at frequency of 1 Hz, [c]maximum stress at compressive strain, ε=0.8, [d]HAc-Alg/ 30wt% CaP ink prepared by mixing CaP with HAc-Alg has very low printability due to high viscosity and inconsistent extrusion behavior; thus, its 3D printed scaffolds could not be fabricated for mechanical tests. HAc-Alg: Hyaluronic acid-alginate, CaP: Calcium phosphate, 3D: Three-dimensional

wt% CaP inks prepared by *ex situ* incorporation could not be printed due to severe clogging issues associated with high viscosity and particle agglomeration. Thus, only HAc-Alg/CaP scaffolds prepared by *in situ* precipitation were used in our mechanical tests.

Next, we performed unconfined, uniaxial compression test to assess the mechanical characteristics of the printed scaffolds under significant deformation conditions using fully hydrated HAc-Alg and HAc-Alg/CaP scaffolds (**Table 2 and Supplementary Figure 7-C**). Under a predefined deformation (ε = 80%), the rods and struts of both HAc-Alg and HAc-Alg/CaP hydrogels were crushed, and the porous scaffolds subsequently densified. Both scaffolds did not collapse until the predefined deformation point (ε = 80%) with significant densification. All specimens maintained their structural integrity after unloading. The incorporation of 30 wt% CaP precipitates in the hydrogels resulted in a two-fold enhancement of the compressive modulus and strength (**Table 2**). The precipitated CaP minerals improve the chain stiffness of the polymer networks due to (i) the strong electrostatic interactions between the minerals and carboxyl groups of the polysaccharide chains and (ii) homogeneous distribution of the minerals as opposed to the case of simple mixing[5,28]. Notably, the enhancements of compressive stiffness and strength in composite hydrogel scaffolds were not as striking as the enhancements in storage moduli of bulk gels and local stiffness of individual struts in the scaffolds. We speculated that this was due to the high porosity and structural instability associated with irregular, inhomogeneous pore structures of porous scaffolds, which counteracted mechanical enhancement[29]. In this study, we clearly demonstrated that *in situ* precipitation of CaP better enhanced the mechanical properties of the hydrogel composites compared with using *ex situ* CaP incorporation.

One of the advantages of our approach is that the printed hydrogels were not deformed in water due to the pre-swelling condition associated with 3D freeform printing in an aqueous medium. The swelling ratios of the printed hydrogels were studied within 24 h of the printing and subsequent post-UV curing processes (**Table 2 and Supplementary Figure 7-D**). In all cases, the equilibrium swelling ratios were almost reached, indicating that the HAc-Alg/CaP nanocomposite hydrogels exhibited reduced swelling ratios due to the increased chain stiffness and crosslinking density of the mineralized hydrogels[5,30]. During the printing of multiphase hydrogel composites with gradient compositions, one of the key concerns is the mismatch of swelling ratios among various gradient hydrogel materials after printing, as this can lead to significant structural distortion and structural instability of the printed constructs. Printing in a water-based slurry system can minimize any such issues associated with the swelling behavior of multiphase hydrogel systems.

3.4 *In vitro* biostability of the composite scaffolds

Enzymatic degradation of HAc often results in low biostability of the HAc-based scaffolds and requires physical or chemical crosslinking of the functionalized HAc. The *in vitro* biostability of the 3D printed hydrogels was evaluated in the presence

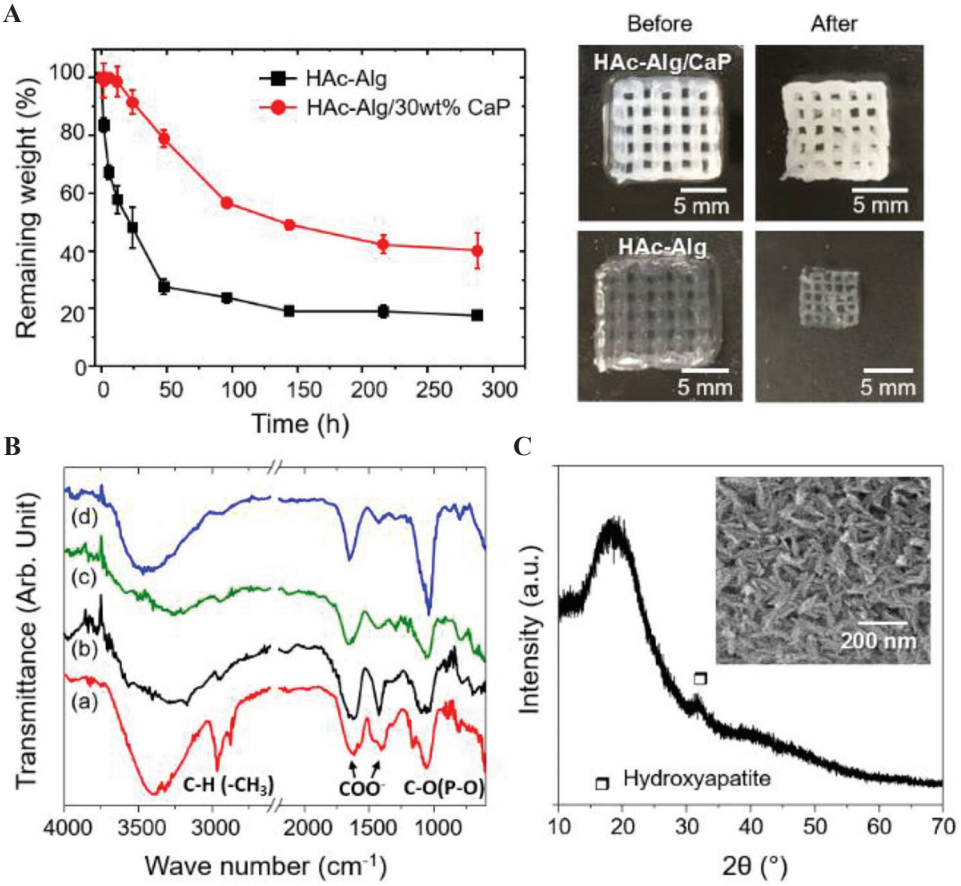

Figure 5. *In vitro* enzymatic degradation behavior of three-dimensional-printed scaffolds. (A) Remaining weight over incubation time after the hydrogel scaffolds were immersed in hyaluronidase solution, and optical images of the scaffolds before and after enzymatic degradation. (B) Fourier-transform infrared spectra of (a) glycidyl methacrylate-hyaluronic acid (HAc) hydrogel, (b) alginate hydrogel, (c) HAc-alginate (HAc-Alg) after degradation, and (d) HAc-Alg/30 wt% calcium phosphate (CaP) after degradation. (C) X-ray diffractometer pattern of HAc-Alg/30 wt% CaP scaffolds after degradation.

of hyaluronidase through a 7-day immersion study (**Figure 5A**). We found that approximately 85% of HAc in the HAc-Alg scaffolds was rapidly degraded after 2 days, whereas >50% of HAc remained in HAc-Alg/CaP, indicating that the nanocomposite hydrogels exhibited higher resistance against enzymatic degradation. The complete degradation of HAc in HAc-Alg and HAc-Alg/CaP took 6 and 12 days, respectively (**Supplementary Figure 8**). The optical images of the remnant hydrogels after degradation confirmed the outstanding biostability of the HAc-Alg/CaP hydrogels. The precipitation of nanocrystals on the HAc chains effectively blocked the access of enzyme molecules to HAc and enhanced its resistance to enzymatic degradation[5,31].

Our results indicate that Alg and minerals were the main components of the remaining scaffolds after hyaluronidase-mediated degradation, as confirmed by the FT-IR spectra (**Figure 5B**). The FT-IR spectra of GM–crosslinked HAc and Alg hydrogels had the following characteristic peaks: For GM–crosslinked HAc, amide N-H stretch from 3200 to 3600 cm^{-1}, C=O stretching and N–H bending in the 1595 – 1710 cm^{-1} range, C–H bending peak between 1350 and 1480 cm^{-1}, and C–O stretch of the proteoglycan sugar ring from 985 to 1140 cm^{-1}; and for Alg, stretching vibrations of the hydroxyl groups at 3430 cm^{-1} and stretching vibrations of the asymmetric and symmetric bands of carboxylate anions at 1619 and 1416 cm^{-1}, respectively[32,33]. The FT-IR

spectrum of degraded HAc-Alg was in line with that of Alg. In contrast, characteristic peaks of CaP were observed in addition to those of Alg for the HAc-Alg/CaP hydrogels: The FT-IR spectrum exhibited strong peaks at 1000 – 1100 cm^{-1} (ν3 bending) and 560 – 600 cm^{-1} (ν4 bending) for the PO_4^{3-} groups in addition to the bands of adsorbed water from 3600 to 2600 cm^{-1}[34]. We also observed significant discrepancies between the remaining weight obtained from the TGA analysis and enzymatic degradation tests. While the remaining weight of TGA analysis accounted for residual organic ashes and inorganic components, the remaining weight after enzymatic degradation was mainly due to swollen Alg (Alg + water) and inorganic components such as calcium carbonate and CaP. Moreover, the swelling behavior of the remaining Alg hydrogels varied depending on the mineral contents of the composite hydrogels (**Table 2**)[5]. The remaining weight difference between degraded HAc-Alg and HAc-Alg/CaP scaffolds was ~20 wt%, which was <30 wt% obtained from the TGA analysis.

HAc-Alg/CaP hydrogels after 2 weeks of immersed degradation were also analyzed using XRD and SEM to determine the mineral phases of CaP. A broad peak at 32−35° indicating apatite with low crystallinity was observed in the XRD pattern, while the characteristic peaks of DCPD or OCP crystallites had completely disappeared (**Figure 5C**). Furthermore, the morphology of the CaP precipitates changed from spherical to needle-like (**Supplementary Figure 9**). It is known that DCPD, one of the CaP crystalline phases found in HAc-Alg/CaP scaffolds, can be hydrolyzed in water or a buffer solution to form hydroxyapatite or anhydrous dicalcium phosphate[22].

$$5CaHPO_4 + H_2OHaH_5(PO_4)_3\,OH + 2H_3\,PO_4 \qquad (5)$$

In this hydrolytic reaction, the acidic by-product decreases the pH of the aqueous medium. We, therefore, used a PBS buffer solution in our degradation test to minimize the pH change of the system. The final pH of the enzymatic solution was around 7, which was slightly lower than the initial pH (pH 7.4). Through heat treatment, pure ceramic porous scaffolds could be obtained after the removal of the Alg remnants, with the crystallization of amorphous apatite phases.

In addition to confirming the improved biostability of HAc-Alg/CaP, two promising findings were discovered from our degradation tests. First, the precipitated minerals were well-connected with the polymer template and maintained their 3D structure after template removal. Thus, by developing an *in situ* precipitation method for nanoparticles, various minerals can be incorporated in the 3D printing process to obtain porous 3D foams of metals or ceramics. For example, gold nanoparticles can be nucleated and grown on a polymer matrix through the *in situ* reaction of its metal precursor (e.g., $HAuCl_4$) and a reducing agent (e.g., HCOONa)[35,36]. Second, by employing additional post-treatment processes, 3D printed materials can be further modified (e.g., by reduction of metal oxides)[37]. Importantly, this freeform 3D printing allows polymer templates to be chosen based on their functional roles instead of their 3D printability as the gelation of the polymer templates is carried out after 3D printing.

3.5 Biological performance of composite hydrogels

The biocompatibility and bioactivity of HAc-Alg/CaP were carefully evaluated and compared to that of HAc-Alg to confirm its potential as a biomaterial for various medical applications. The *in vitro* cellular responses of fibroblast cells on the bulk and 3D-printed hydrogels are shown in **Figure 6**. None of the hydrogels displayed any signs of cytotoxicity. The cells attached to the surface of HAc-Alg/CaP bulk hydrogels appeared stretched and flattened, similar to what is usually observed in two-dimensional cell cultures. In contrast, the cells attached to the surface of HAc-Alg hydrogels clustered to form spheroids (**Figure 6A**). The cell densities were remarkably higher on HAc-Alg/CaP surfaces than on HAc-Alg surfaces. After a 3-day culture, 80 – 90% of the HAc-Alg/CaP surface area was covered by the cells, whereas only ~20% of the HAc-Alg surface area was occupied by the cells (**Supplementary**

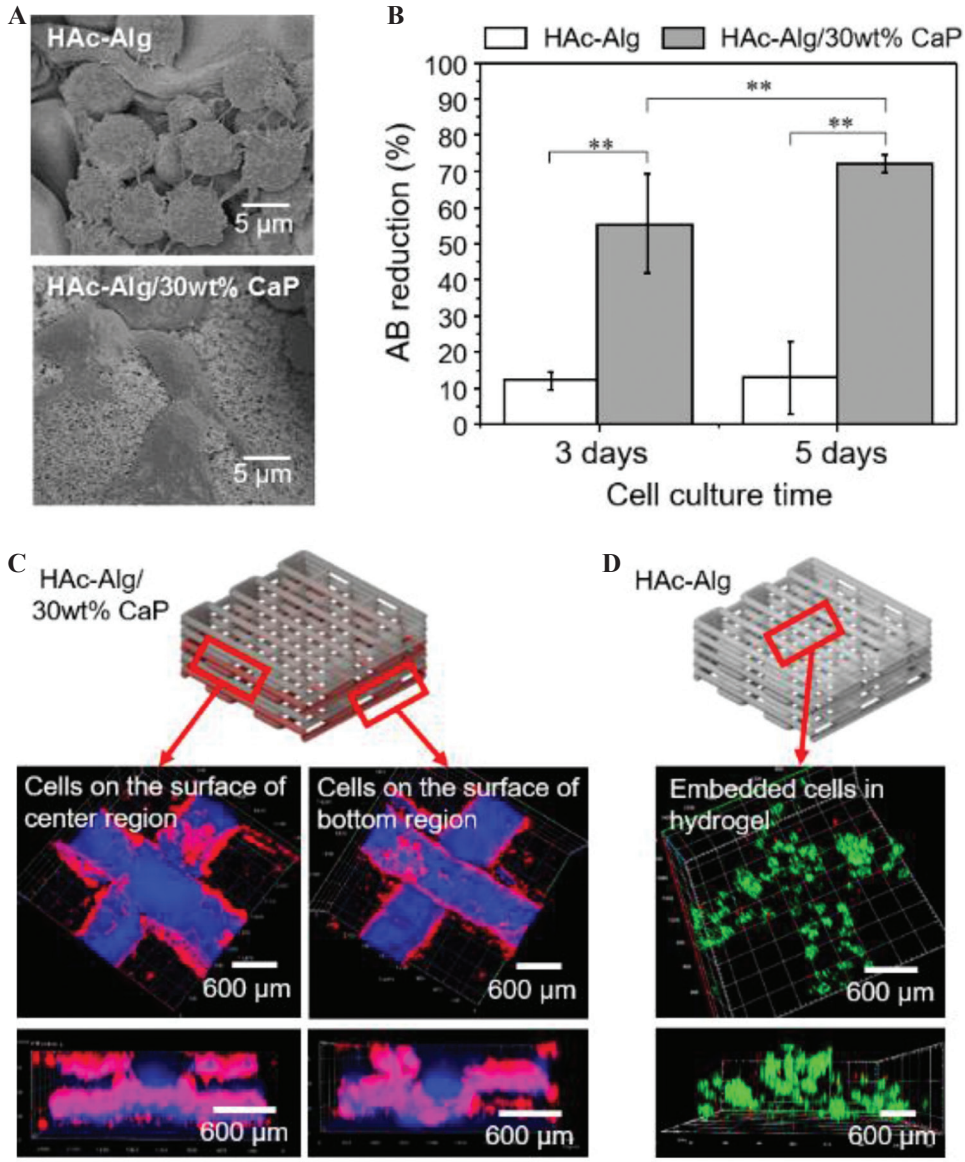

Figure 6. Cytocompatibility of hyaluronic acid-alginate (HAc-Alg) and HAc-Alg/30 wt% calcium phosphate (CaP) hydrogels using L929 fibroblasts. (A) Scanning electron microscope images of cells attached to the surfaces of HAc-Alg and HAc-Alg/30 wt% CaP hydrogels. (B) Cell viability of HAc-Alg and HAc-Alg/30 wt% CaP hydrogels measured by AlamarBlue assay after 3 and 5 days ($n > 3$, $^{**}P < 0.01$). (C) Confocal laser scanning microscope (CLSM) z-stack images of L929 fibroblasts adhered to HAc-Alg/30wt% CaP three-dimensional (3D) scaffolds after 7 days, indicating the selected parts for imaging. The two layers from the bottom and center regions were imaged to confirm the cell distribution throughout the scaffold. (D) CLSM z-stacked confocal images of L929 fibroblasts within the 3D printed scaffold after a 14-day incubation period.

Figure 10). This observation agreed well with the quantitative cell proliferation data obtained using the AlamarBlue assay (**Figure 6B**). The levels of fibroblast proliferation on the HAc-Alg/CaP hydrogels after 3 and 5 days of culture were, respectively, ~6 and 8 times higher than those on HAc-Alg. The relatively high SD in HAc-Alg on day 5 was due to the weak cell attachment on the hydrogel surface, whereas the higher SD for the HAc-Alg/CaP hydrogels was attributed to errors

in cell seeding. When the cell densities reached saturation on day 5 (almost covering the entire surface of the composite hydrogel), the errors were <5%. In most cases, CaP-containing biomaterial scaffolds promote cell growth[5,38,39]. DCPD-based brushite cements are non-inflammatory and biocompatible with both bone and soft tissues[40]. Moreover, the nanosized surface topography and improved matrix stiffness associated with the incorporated CaP precipitates may provide physical binding sites and stable mechanical support for the seeded cells[14,39].

Based on the observations of HAc-Alg and HAc-Alg/CaP bulk hydrogels, we found that different types of hydrogel scaffolds required different cell seeding strategies. In the case of 3D printed HAc-Alg/CaP scaffolds that exhibited excellent cell attachment performance, cells were directly seeded on the scaffolds after all of the processing steps were completed. The cell growth on 3D printed HAc-Alg/CaP was examined using CLSM. We found that cells migrated inside the pore channels of the hydrogel scaffold and almost fully covered the 3D surface (**Figure 6C**). As cells seeded on HAc-Alg attached and proliferated poorly, cell-laden HAc-Alg scaffolds were prepared and incubated for 14 days (**Figure 6D**). The encapsulated cells observed using CLSM were highly viable. For printing with cell-laden photocurable hydrogel inks, cell viability should be carefully considered due to UV irradiation during photo-crosslinking. Shorter UV irradiation often leads to reasonably high cell viability even though the mechanical stability of photocurable hydrogels is compromised[21,41]. Indeed, there is a significant trade-off between the mechanical performance and cell viability of cell-laden hydrogel scaffolds due to a cytotoxic crosslinking process. Thus, approaches for improving cell viability through a cell protection strategy through the incorporation of plant-derived polyphenols, such as pyrogallol (PG)[21] or improved crosslinking efficiency with dual-photoinitiators,[41] have been proposed. Particularly, using cell-encapsulated Alg microparticles with or without PG treatment, cell-laden hydrogel scaffolds were successfully prepared with minimal death of embedded cells during the whole biofabrication process regardless of UV irradiation time, in our previous study[21]. Thus, this two-step cell seeding approach can be used for gradient hydrogel systems to maximize cell viability during the long and complicated fabrication process.

As DCPD has been widely used for various biomedical applications, particularly in brushite bone cements composed of β-tricalcium phosphate and monocalcium phosphate monohydrate, we postulated that this material system could be utilized to augment bone tissues or soft/hard tissue interfaces in various forms[40]. We assessed the bioactivity of 3D printed HAc-Alg/CaP scaffolds by measuring the expression levels of four representative osteoblastic genes, Runx2, COL1, OPN, and OCN, using directly seeded MC3T3-E1 pre-osteoblasts[42]. As HAc-Alg did not exhibit good cell attachment performance, we were not able to obtain sufficient pre-osteoblasts for phenotypic assessments using the same setup. To overcome this, we set up a cell culture system as a negative control for this *in vitro* differentiation test using commercial cell culture plates. Two types of cell culture media were used in this assay: Cell maintenance medium (negative) and standard osteogenic medium (positive) containing ascorbic acid and Na-β-glycerophosphate (**Figure 7**). Pre-osteoblasts are known to express high levels of COL1 and RunX2 (key markers of early osteogenic differentiation)[42]. Our results indicated that the expression levels of COL1 and RunX2 remained almost the same regardless of the presence of osteogenic reagents or bioactive components such as CaP (**Figure 7A and B**). In contrast, osteogenic medium induced the upregulation of OPN and OCN expressions in pre-osteoblasts cultured in both HAc-Alg/CaP scaffolds and culture plates (**Figure 7C and D**). Although the pre-osteoblasts cultured in composite hydrogel scaffolds (in the presence of osteogenic reagents) exhibited significantly higher gene expression levels of RUX2 and OCN that those grown using culture plates, we could not conclude whether this composite hydrogel system was sufficiently osteoinductive. We have previously implemented HAc-30 wt% CaP hydrogels within subcutaneous

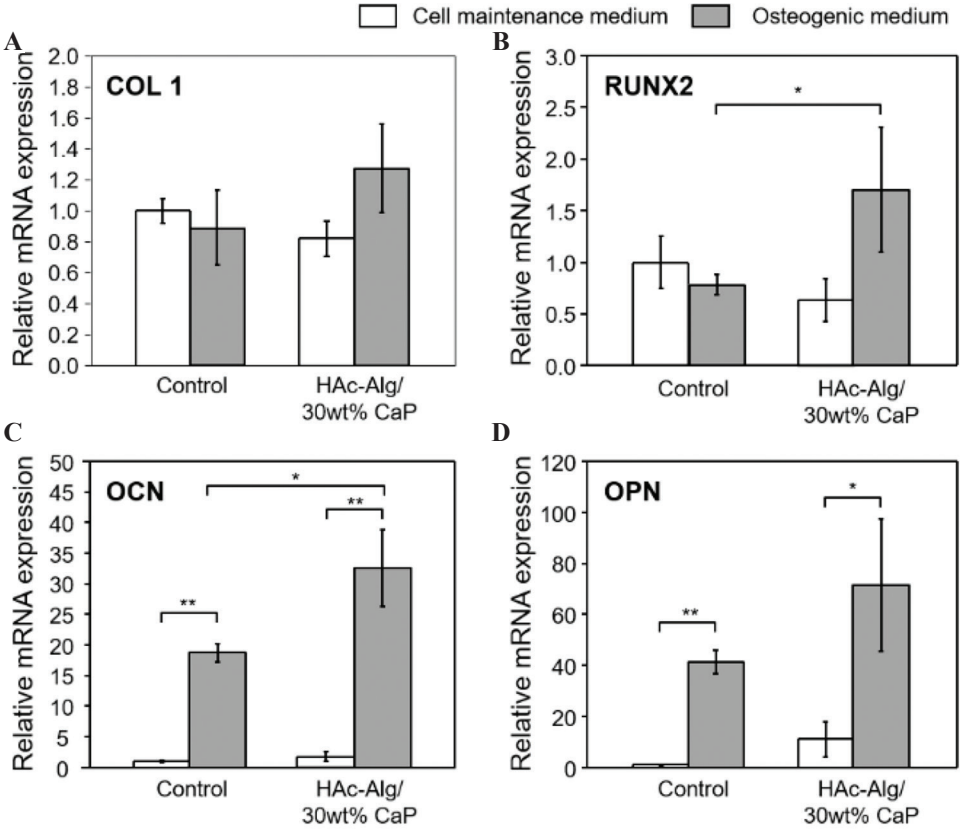

Figure 7. Quantitative gene expression of four markers for *in vitro* cell differentiation. (A) Collagen type 1, (B) RunX2, (C) osteocalcin, and (D) osteopontin of MC3T3-E1 cells after 14 days of culturing on well plate (Control) or three-dimensional printed hyaluronic acid-alginate/30 wt% calcium phosphate composite hydrogel scaffolds with cell maintenance medium or osteogenic medium ($n > 3$, $^{*}P < 0.05$ and $^{**}P < 0.01$).

sites in rats and found no significant mineralization or calcification (despite the strong promotion of soft-tissue regeneration)[5]. Moreover, the cell/matrix interaction is intricate, and numerous factors influence cell differentiation. For instance, the elastic modulus of hydrogels (11 – 30 kPa) was found to lead to osteogenic differentiation of primary human mesenchymal stem cells (hMSCs), whereas softer hydrogels with elastic modulus <5 kPa induce adipogenic lineage of hMSCs[43,44]. The elastic modulus of HAc-30 wt% CaP hydrogel scaffolds was ~ 6 kPa, thus might fail to induce osteogenic lineage of pre-osteoblasts due to insufficient matrix stiffness (**Table 2**). Thus, to enhance the osteoconductive and osteoinductive properties of HAc-Alg/CaP scaffolds, incorporation of additional bioactive additives (e.g., osteogenic reagents and bone growth factors) or mechanical reinforcement agents (e.g., increased mineral or Alg contents) to the hydrogel inks may be essential. In fact, DCPD/OCP has been reported to show lower bioactivity than DCPD with bioglass silica or magnesium[45]. Our follow-up research will expand the applicability of this system with extensive *in vitro* and *in vivo* assessments.

3.6 3D freeform printing for multiphase composite scaffolds

Multi-material 3D printing with nanocomposite hydrogels is challenging because the nanoparticle additives may change the rheological behavior of the composite hydrogel inks depending on the loading amount of the additives[6]. Furthermore, the uniform distribution of nanoparticles requires considerable care when the composite inks are prepared.

Finally, different swelling ratios of nanocomposite hydrogels containing various inorganic contents may lead to the deformation of the multi-material system in water[5]. To show that our method could overcome these problems, *in situ* precipitation of inorganic nanoparticles was carried out directly on

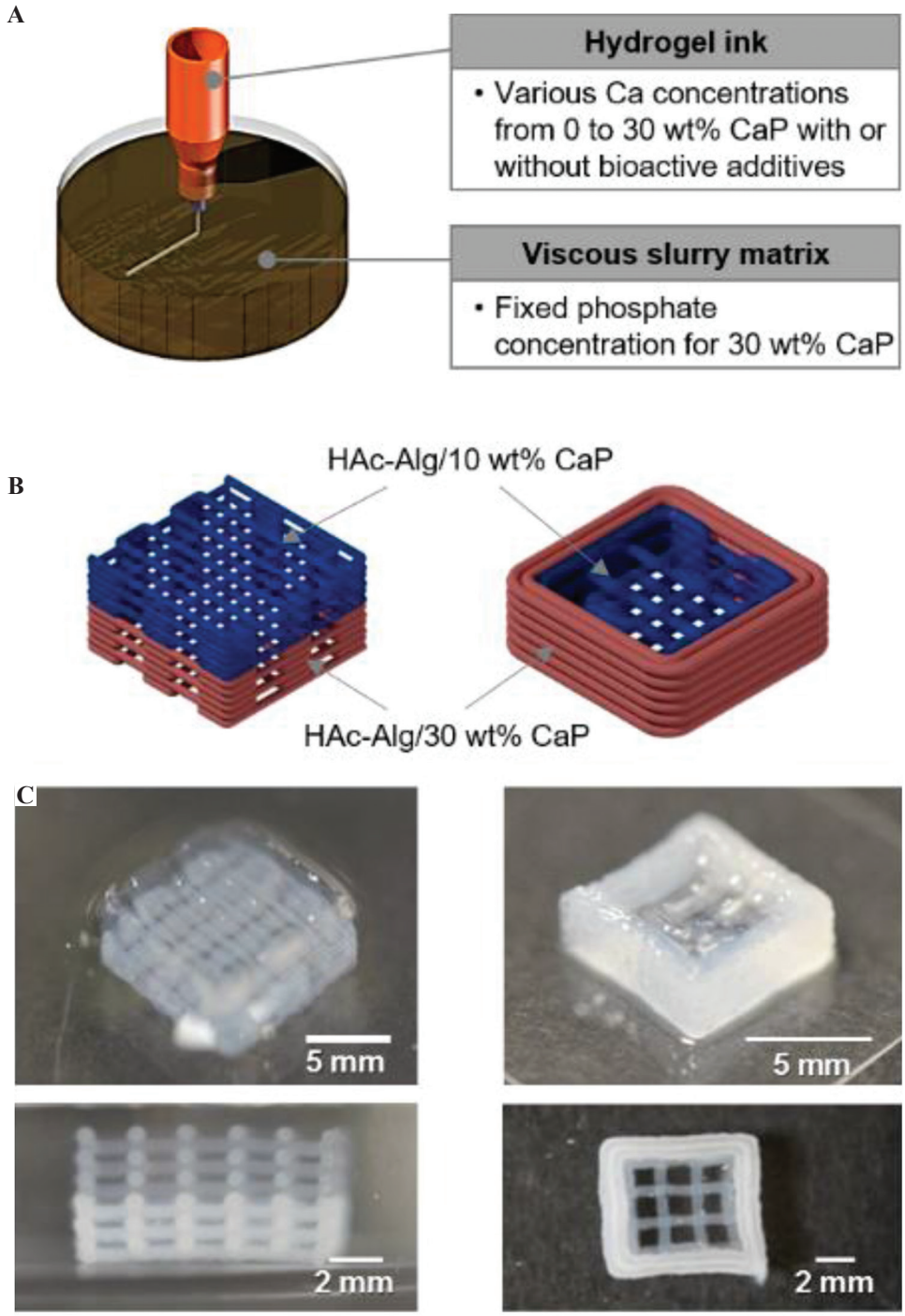

Figure 8. Multiphase material printing with composite hydrogel inks. (A) Three-dimensional (3D) printing strategy of multiphase materials for gradient biomaterials. (B) Schematics of proposed bi-material scaffolds varying mineral contents. (C) Optical images of 3D printed multiphase composite scaffolds composed of hyaluronic acid-alginate (HAc-Alg)/10 wt% calcium phosphate (CaP) and HAc-Alg/30wt% CaP.

a printed hydrogel using their precursors. As proof-of-concept, two multi-material structural designs were created and printed with two nanocomposite hydrogels, HAc-Alg/15 wt% CaP and HAc-Alg/30 wt% CaP (**Figure 8**).

The mineral contents of HAc-Alg/CaP were varied by altering the phosphate ion concentration in the HAc-Alg hydrogel inks, as illustrated in **Figure 8A**. As the precursors of CaP nanoparticles were ions, different concentrations of these precursors did not change the viscosity of the printing inks or gelatin-containing viscous medium. Two types of HAc-Alg inks with different phosphate ion concentrations were printed in a gelatin bath with excess $CaCl_2$ using the same printing parameters. We had already confirmed that the precipitated CaP nanocrystals distributed uniformly within the hydrogel matrix regardless of the precursor concentrations. During 3D printing, the printed inks contained the non-crosslinked GM-HAc liquid phase. Therefore, sequential 3D printing of two different hydrogel inks using only one printer head was feasible. This avoided any interfacial problem because the GM-HAc liquid diffused into the contact region around the joints of the printed filaments, which promoted joint fusion and improved bonding strength among the filaments of the adjacent layers. The two structural designs, vertical stacking and horizontal stacking of the two composite hydrogels resulted in different printing sequence and interfaces between the two materials with different mineral contents (**Figure 8B and C**). In the case of vertical stacking, the bottom layer of HAc-Alg/10 wt% CaP could be deposited on the top layer of HAc-Alg/30 wt% CaP, thus minimizing the time lapse between the printing of each material due to ink change. In contrast, horizontal stacking was achieved by printing the inner part with HAc-Alg/10 wt% CaP, followed by printing the external part of the structure with HAc-Alg/30 wt% CaP (**Supplementary Figure 11**). In this case, the time lapse between the first layers of the two materials was more than 5 min, which was equivalent to the summation of; printing time of the first material and ink change time. However, both printed structures exhibited good mechanical stability and no delamination at the interface of the two materials. More importantly, in the freeform printing of hydrogel inks in aqueous solutions, all of the printed gels were maintained in the swollen state and reacted *in situ* during printing. Thus, the introduction of different materials with various swelling behaviors did not induce any structural mismatch or distortion of the multi-material systems when the hydrogels were immersed in water.

The composite hydrogel systems can be applied for scaffolds of interface tissue engineering (ITE), which aims to regenerate the native enthesis or interface tissue between hard and soft tissues. Thus, ITE requires multiphase and gradient biomaterials to engineer both types of tissue[46-51]. As gradient biomaterials often mimic the complex structures and material properties of each soft and hard tissue, advanced micro- and nano-technologies such as microfluidics, electrospinning, and bioprinting have been introduced into the conventional fabrication process of biomaterials to capture these dimensions[47]. In particular, recent advances in 3D printing technologies have facilitated the development of composite biomaterials through the ability to fabricate structurally, functionally, and compositionally intricate constructs[1-4]. Thus, our approach for multiphase composite scaffolds can be applied for the fabrication of various functional or hybridized gradient biomaterials with complex geometries for ITE scaffolds.

4 Conclusion

In this study, by introducing an *in situ* inorganic nanoparticle precipitation process to a 3D freeform printing system with a two-step crosslinking strategy, we successfully fabricated HAc-Alg/CaP nanocomposite hydrogel scaffolds with various mineral contents and good structural integrity. The first ionic crosslinking of Alg provided structural stability during printing, while the secondary crosslinking of photo-curable GM-HAc improved the mechanical stability of the nanocomposite hydrogels by virtue of the superior bonding

strength of the adjacent layers with well-fused filament joints. The precipitated nanoparticles composed of DCPD and OCP, along with a small amount of calcium carbonate, were uniformly distributed throughout the entire printed hydrogel. The incorporated CaP nanocrystals significantly enhanced the mechanical, physiological, and biological characteristics of the pure hydrogel, suggesting its great potential as a biomaterial for various biomedical applications. In particular, the proposed printing approach allowed multi-phase gradient material printing with a single nozzle system, avoiding any issues caused by the introduction of materials with differences in printability and mechanical stability. Taken together, our results suggest that designing and modifying the printing materials coupled with *in situ* post-printing functionalization and hybridization in reactive viscoplastic matrices, our approach can accelerate the 3D printing of various functional or hybridized gradient biomaterials with complex geometries.

Conflicts of interest and funding

No conflicts of interest were reported by all authors. This research was supported by Nanyang Technological University Start up grant, and A*STAR Advanced Manufacturing and Engineering Individual Research Grants grant A1983c0031 from A*STAR.

Author contributions

Chen S. designed and performed the experiments, data analysis, and drafted the manuscript. Jang T.S. and Jung H.D. conducted SEM/TEM imaging, XRD and EDS analyses of hydrogel samples. Chen S., Pan, M, and Sia M.W performed cell tests. Chong M. and Wang D. designed and supervised the *in vitro* cell experiments. Song J designed the experiments and supervised the whole research. All authors have read the manuscript and given approval to the final version.

References

1. Liu W, Zhang YS, Heinrich MA, *et al*., 2017, Rapid Continuous Multimaterial Extrusion Bioprinting. *Adv Mater*, 29:1604630.
2. Kowsari K, Akbari S, Wang D, *et al*., 2018, High-efficiency High-resolution Multimaterial Fabrication for Digital Light Processing-based Three-dimensional Printing. *3D Print Addit Manuf*, 5:185–93. DOI: 10.1089/3dp.2018.0004.
3. Lopes LR, Silva AF, Carneiro OS, 2018, Multi-material 3D Printing: The Relevance of Materials Affinity on the Boundary Interface Performance. *Addit Manuf*, 23:45–52. DOI: 10.1016/j.addma.2018.06.027.
4. Jang TS, Jung HD, Pan HM, *et al*., 2018, 3D Printing of Hydrogel Composite Systems: Recent Advances in Technology for Tissue Engineering. *Int J Bioprinting*, 4:126.
5. Jeong SH, Koh YH, Kim SW, *et al*., 2016, Strong and Biostable Hyaluronic Acid-calcium Phosphate Nanocomposite Hydrogel via *In Situ* Precipitation Process. *Biomacromolecules*, 17:841–51. DOI: 10.1021/acs.biomac.5b01557.
6. Wust S, Godla ME, Muller R, *et al*., 2014, Tunable Hydrogel Composite with Two-step Processing in Combination with Innovative Hardware Upgrade for Cell-based Three-dimensional Bioprinting. *Acta Biomater*, 10:630–40. DOI: 10.1016/j.actbio.2013.10.016.
7. Thoniyot P, Tan MJ, Karim AA, *et al*., 2015, Nanoparticle-hydrogel Composites: Concept, Design, and Applications of These Promising, Multi-functional Materials. *Adv Sci* (*Weinh*), 2:1400010. DOI: 10.1002/advs.201400010.
8. Gaharwar AK, Schexnailder PJ, Dundigalla A, *et al*., 2011, Highly Extensible Bio-nanocomposite Fibers. *Macromol Rapid Commun*, 32:50–7. DOI: 10.1002/marc.201000556.
9. Leach JB, Bivens KA, Patrick CW, *et al*., 2003, Photocrosslinked Hyaluronic Acid Hydrogels: Natural, Biodegradable Tissue Engineering Scaffolds. *Biotechnol Bioeng*, 82:578–89. DOI: 10.1002/bit.10605.
10. Xu X, Jha AK, Harrington DA, *et al*., 2012, Hyaluronic Acid-based Hydrogels: From a Natural Polysaccharide to Complex Networks. *Soft Matter*, 8:3280–94. DOI: 10.1039/c2sm06463d.
11. Kisiel M, Martino MM, Ventura M, *et al*., 2013, Improving the Osteogenic Potential of BMP-2 with Hyaluronic Acid Hydrogel Modified with Integrin-specific Fibronectin Fragment. *Biomaterials*, 34:704–12. DOI: 10.1016/j.biomaterials.2012.10.015.
12. Li QH, Li M, Zhu PZ, *et al*., 2012, *In Vitro* Synthesis of Bioactive Hydroxyapatite Using Sodium Hyaluronate as a Template. *J Mater Chem*, 22:20257–65. DOI: 10.1039/c2jm33624c.
13. Egorov AA, Fedotov AY, Mironov AV, *et al*., 2016, 3D

Printing of Mineral-polymer Bone Substitutes Based on Sodium Alginate and Calcium Phosphate. *Beilstein J Nanotechnol*, 7:1794–9. DOI: 10.3762/bjnano.7.172.

14. Lee H, Kim Y, Kim S, *et al.*, 2014, Mineralized Biomimetic Collagen/Alginate/Silica Composite Scaffolds Fabricated by a Low-temperature Bio-plotting Process for Hard Tissue Regeneration: Fabrication, Characterisation and *In Vitro* Cellular Activities. *J Mater Chem B*, 2:5785. DOI: 10.1039/c4tb00931b.
15. Bhattacharjee T, Zehnder SM, Rowe KG, *et al*., 2015, Writing in the Granular Gel Medium. *Sci Adv*, 1:e1500655. DOI: 10.1126/sciadv.1500655.
16. Highley CB, Rodell CB, Burdick JA, 2015, Direct 3D Printing of Shear-thinning Hydrogels into Self-healing Hydrogels. *Adv Mater*, 27:5075–9. DOI: 10.1002/adma.201501234.
17. Hinton TJ, Jallerat Q, Palchesko RN, *et al*., 2015, Three-dimensional Printing of Complex Biological Structures by Freeform Reversible Embedding of Suspended Hydrogels. *Sci Adv*, 1:e1500758. DOI: 10.1002/adma.201501234.
18. Hinton TJ, Hudson A, Pusch K, *et al*., 2016, 3D Printing PDMS Elastomer in a Hydrophilic Support Bath via Freeform Reversible Embedding. *ACS Biomater Sci Eng*, 2:1781–6. DOI: 10.1021/acsbiomaterials.6b00170.
19. Rodriguez MJ, Dixon TA, Cohen E, *et al*., 2018, 3D Freeform Printing of Silk Fibroin. *Acta Biomater*, 71:379–87. DOI: 10.1016/j.actbio.2018.02.035.
20. Grosskopf AK, Truby RL, Kim H, *et al*., 2018, Viscoplastic Matrix Materials for Embedded 3D Printing. *ACS Appl Mater Interfaces*, 10:23353–61. DOI: 10.1021/acsami.7b19818.
21. Pan HM, Chen S, Jang TS, *et al*., 2019, Plant Seed-inspired Cell Protection, Dormancy, and Growth for Large-scale Biofabrication. *Biofabrication*, 11:025008. DOI: 10.1088/1758-5090/ab03ed.
22. Furuichi K, Oaki Y, Imai H, 2006, Preparation of Nanotextured and Nanofibrous Hydroxyapatite Through Dicalcium Phosphate with Gelatin. *Chem Mater*, 18:229–34. DOI: 10.1021/cm052213z.
23. Thanh NT, Maclean N, Mahiddine S, 2014, Mechanisms of Nucleation and Growth of Nanoparticles in Solution. *Chem Rev*, 114:7610–30. DOI: 10.1021/cr400544s.
24. Bastami A, Allahgholi M, Pourafshary P, 2014, Experimental and Modelling Study of the Solubility of CO2 in Various CaCl2 Solutions at Different Temperatures and Pressures. *Pet Sci*, 11:569–77. DOI: 10.1007/s12182-014-0373-1.
25. Hosoda N, Kato T, 2001, Thin-film Formation of Calcium Carbonate Crystals: Effects of Functional Groups of Matrix Polymers. *Chem Mater*, 13:688–93. DOI: 10.1021/cm000817r.
26. Gallagher PK, Johnson DW, 1973, The Effects of Sample Size and Heating Rate on the Kinetics of the Thermal Decomposition of CaCO3. *Thermochim Acta*, 6:67–83. DOI: 10.1016/0040-6031(73)80007-3.
27. Li ZY, Su YL, Xie BQ, *et al*., 2013, A Tough Hydrogel-hydroxyapatite Bone-like Composite Fabricated *In Situ* by the Electrophoresis Approach. *J Mater Chem B*, 1:1755–64. DOI: 10.1039/c3tb00246b.
28. Sarvestani AS, He XZ, Jabbari E, 2008, The role of filler-matrix interaction on viscoelastic response of biomimetic nanocomposite hydrogels. *J Nanomater*, 2008:9. DOI: 10.1155/2008/126803.
29. Song X, Zhu C, Fan D, *et al*., 2017, A Novel Human-like Collagen Hydrogel Scaffold with Porous Structure and Sponge-like Properties. *Polymers*, 9:638. DOI: 10.3390/polym9120638.
30. Sarvestani AS, Jabbari E, 2008, A Model for the Viscoelastic Behavior of Nanofilled Hydrogel Composites Under Oscillatory Shear Loading. *Polym Compos*, 29:326–36. DOI: 10.1002/pc.20416.
31. Desimone MF, Helary C, Quignard S, *et al*., 2011, *In Vitro* Studies and Preliminary *In Vivo* Evaluation of Silicified Concentrated Collagen Hydrogels. *ACS Appl Mater Interfaces*, 3:3831–8. DOI: 10.1021/am2009844.
32. van Hoogmoed CG, Busscher HJ, de Vos P, 2003, Fourier Transform Infrared Spectroscopy Studies of Alginate-PLL Capsules with Varying Compositions. *J Biomed Mater Res Part A*, 67A:172–8. DOI: 10.1002/jbm.a.10086.
33. Ibrahim S, Kothapalli CR, Kang QK, *et al*., 2011, Characterization of Glycidyl Methacrylate-crosslinked Hyaluronan Hydrogel Scaffolds Incorporating Elastogenic Hyaluronan Oligomers. *Acta Biomater*, 7:653–65. DOI: 10.1016/j.actbio.2010.08.006.
34. Berzina-Cimdina L, Borodajenko N, 2012, Research of Calcium Phosphates Using Fourier Transform Infrared Spectroscopy. InTech, Rijeka. DOI: 10.5772/36942.
35. Dotzauer DM, Dai J, Sun L, *et al*., 2006, Catalytic Membranes Prepared Using Layer-by-layer Adsorption of Polyelectrolyte/Metal Nanoparticle Films in Porous Supports. *Nano Lett*, 6:2268–72. DOI: 10.1021/nl061700q.
36. Ahmed SR, Kim J, Tran VT, *et al*., 2017, *In Situ* Self-assembly of Gold Nanoparticles on Hydrophilic and Hydrophobic Substrates for Influenza Virus-sensing Platform. *Sci Rep*, 7:44495. Available from: https://www.nature.com/articles/srep44495#supplementary-information. DOI: 10.1038/srep44495.
37. Jakus AE, Taylor SL, Geisendorfer NR, *et al*., 2015, Metallic

Architectures from 3D-printed Powder-based Liquid Inks. *Adv Funct Mater*, 25:6985–95. DOI: 10.1002/adfm.201503921.

38. Murphy WL, Mooney DJ, 2002, Bioinspired Growth of Crystalline Carbonate Apatite on Biodegradable Polymer Substrata. *J Am Chem Soc*, 124:1910−7. DOI: 10.1021/ja012433n.
39. Discher DE, Janmey P, Wang YL, 2005, Tissue Cells Feel and Respond to the Stiffness of Their Substrate. *Science*, 310:1139−43. DOI: 10.1126/science.1116995.
40. Tamimi F, Sheikh Z, Barralet J, 2012, Dicalcium Phosphate Cements: Brushite and Monetite. *Acta Biomater*, 8:474–87. DOI: 10.1016/j.actbio.2011.08.005.
41. Han WT, Jang T, Chen S, *et al*., 2020, Improved Cell Viability for Large-scale Biofabrication with Photo-crosslinkable Hydrogel Systems Through a Dual-photoinitiator Approach. *Biomater Sci*, 8:450–61. DOI: 10.1039/c9bm01347d.
42. Huang W, Yang S, Shao J, *et al*., 2007, Signaling and Transcriptional Regulation in Osteoblast Commitment and Differentiation. *Front Biosci J Virtual Lib*, 12:3068–92. Doi: 10.2741/2296.
43. Huebsch N, Arany PR, Mao AS, *et al*., 2010, Harnessing Traction-mediated Manipulation of the Cell/Matrix Interface to Control Stem-cell fate. *Nat Mater*, 9:518–26. DOI: 10.1038/nmat2732.
44. Bai X, Gao M, Syed S, *et al*., 2018, Bioactive Hydrogels for Bone Regeneration. *Bioact Mater*, 3:401–17.
45. Gaharwar AK, Mihaila SM, Swami A, *et al*., 2013, Bioactive Silicate Nanoplatelets for Osteogenic Differentiation of Human Mesenchymal Stem Cells. *Adv Mater*, 25:3329–36. DOI: 10.1002/adma.201300584.
46. Sahoo S, Teh TK, He P, *et al*., 2011, Interface Tissue Engineering: Next Phase in Musculoskeletal Tissue Repair. *Ann Acad Med Singapore*, 40:245–51.
47. Seidi A, Ramalingam M, Elloumi-Hannachi I, *et al*., 2011, Gradient Biomaterials for Soft-to-hard Interface Tissue Engineering. *Acta Biomater*, 7:1441–51. DOI: 10.1016/j.actbio.2011.01.011.
48. Khanarian NT, Jiang J, Wan LQ, *et al*., 2012, A Hydrogel-mineral Composite Scaffold for Osteochondral Interface Tissue Engineering. *Tissue Eng Part A*, 18:533–45. DOI: 10.1089/ten.tea.2011.0279.
49. Liverani L, Boccaccini AR, 2018, Multilayered Scaffolds for Interface Tissue Engineering Applications. Woodhead Publishing, Sawston, United Kingdom. pp. 107–22.
50. Patel S, Caldwell JM, Doty SB, *et al*., 2018, Integrating Soft and Hard Tissues Via Interface Tissue Engineering. *J Orthop Res*, 36:1069–77. DOI: 10.1002/jor.23810.
51. Bracaglia LG, Smith BT, Watson E, *et al*., 2017, 3D Printing for the Design and Fabrication of Polymer-based Gradient Scaffolds. *Acta Biomater*, 56:3-13. DOI: 10.1016/j.actbio.2017.03.030.

ORIGINAL ARTICLE

Effects of Topology Optimization in Multimaterial 3D Bioprinting of Soft Actuators

Ali Zolfagharian[1]*, Martin Denk[2], Abbas Z. Kouzani[1], Mahdi Bodaghi[3], Saeid Nahavandi[4], Akif Kaynak[4]

[1]School of Engineering, Deakin University, Geelong 3216, Australia

[2]Institute for Material and Building Research, Munich University of Applied Sciences, Munich, 80335, Germany

[3]Department of Engineering, School of Science and Technology, Nottingham Trent University, Nottingham, NG11 8NS, United Kingdom

[4]Institute for Intelligent Systems Research and Innovation (IISRI), Deakin University, Geelong, 3216, Australia

Abstract: Recently, there has been a proliferation of soft robots and actuators that exhibit improved capabilities and adaptability through three-dimensional (3D) bioprinting. Flexibility and shape recovery attributes of stimuli-responsive polymers as the main components in the production of these dynamic structures enable soft manipulations in fragile environments, with potential applications in biomedical and food sectors. Topology optimization (TO), when used in conjunction with 3D bioprinting with optimal design features, offers new capabilities for efficient performance in compliant mechanisms. In this paper, multimaterial TO analysis is used to improve and control the bending performance of a bioprinted soft actuator with electrolytic stimulation. The multimaterial actuator performance is evaluated by the amplitude and rate of bending motion and compared with the single material printed actuator. The results demonstrated the efficacy of multimaterial 3D bioprinting optimization for the rate of actuation and bending.

Keywords: Multimaterial, Three-dimensional bioprinting, Topology optimization, Soft actuator, Soft robot

***Corresponding Author:** Ali Zolfagharian, School of Engineering, Deakin University, Geelong, 3216, Australia; a.zolfagharian@deakin.edu.au

Received: February 17, 2020**;** ***Accepted:*** March 17, 2020**;** ***Published Online:*** April 10, 2020

Citation: Zolfagharian A, Denk M, Kouzani AZ, *et al*., 2020, Effects of Topology Optimization in Multimaterial 3D Bioprinting of Soft Actuators, *Int J Bioprint*, 6(2):260. DOI: org/10.18063/ijb.v6i2.260.

1 Introduction

Manufacturing in robotics has become easier with the introduction of three-dimensional (3D) printing, enabling processing of key components in a single step, thus circumventing separate manufacturing and assembly processes[1]. The emergence of soft robotics accompanied by the advancements in additive manufacturing enabled design and production of creative soft robots that are capable of handling fragile objects and accomplishing delicate work[2]. The recent proliferation of four-dimensional-printed soft robots stems from both developments in the additive manufacturing and research in responsive materials[3,4]. Printing in layers permits variation of mechanical properties across the cross section by appropriate variation of layering materials with different mechanical and thermal properties[5]. Furthermore, instead of solid infill, the 3D printing process allows printing of porous layers which may improve flexibility and bending amplitude of the resulting composites[6]. The adoption of machine learning-based design in 3D printing of composite structures involves practical trials until the desired output is achieved[7-10]. However, the non-linear and temperature sensitive behavior of

polymeric soft actuators make the design more challenging[9]. Finite element analysis (FEA) could be used as a digital tool in conjunction with topology optimization (TO) to simulate the behavior of soft actuators before proceeding with the fabrication process[11]. Computer-aided design and the performance attributes of the design are assessed by optimization engines to save the labor and time in finalizing the design in an additive manufacturing-oriented design approach[12].

There have been a number of studies on the dynamic response of hydrogels to external stimuli where hydrogels were 3D printed into shape memory plastics to produce structures that exhibit reversible volumetric strains of up to 10 times the original volumes, thus simulating muscle behavior[13-15]. Reversible bending motion of a hydrogel was demonstrated in an electrochemical cell where the electrochemically induced actuation was achieved by the osmotic pressure caused by the Donnan effect[16]. In another study, electroactive polymers were used to manifest reversible movement due to the diffusion of dopant anions through a porous membrane within the layered structure of the composite polymer[17].

This paper investigates the optimization of the multimaterial printing of electrically responsive 3D bioprinted soft actuator with respect to actuation performance. FEA and TO were used to investigate the effect of material configuration on bending amplitude of the soft actuator at constant volume fraction. This study demonstrates an approach to optimized design that can be applied to other similar soft robot and actuator systems.

2 Two-material TO of soft actuator

TO aims at optimizing design by arranging material placement. For example, materials can be removed from low stress areas and applied to the locations of high stress resulting in a porous structure with variable density. Common TO methods, namely, solid isotropic material with penalization (SIMP)[18], bidirectional evolutionary structural optimization (BESO)[19], and level set[20] can be used to design a structure with maximum stiffness density. The structural optimization method permits the normalized density of 1 and ρmin, where ρmin describes the minimum material value, to not to create singular matrices[21].

The actuation of bioprinted polyelectrolyte hydrogel used in this paper is caused by the Donnan effect where the applied voltage causes an ionic concentration gradient in the direction of the applied electric field that initiates an osmotic pressure gradient within the hydrogel, causing the reversible bending of the actuator. In recent study, the relationship between the actuator deflection, applied voltages, ion concentration, and reaction parameters to achieve the maximum deflection were determined. Moreover, it was demonstrated that the actuator deflection was pattern dependent and the lattice patterned specimen exhibited larger bending deflection compared to that of cast solid actuator[22]. Although the latticed sample enabled better bending performance, the pattern can be further optimized to maximize bending using equal quantity of the material.

In this study, we designed a soft actuator with an optimized lattice pattern using two different materials. In this regard, boundary conditions were defined based on a cantilever beam with a distributed force caused by osmotic pressure created in the electrolyte. The objective of this study is to optimize the actuator performance through material configurations in different layers while maintaining the volume fraction of the material.

The loading and boundary conditions are illustrated in **Figure 1**. A stress-based TO would require several constraints that increase the complexity of computation; moreover, the non-linearity of the stresses would cause computational overload due to convergence difficulties[23]. The TO modeling for the soft actuator was based on the SIMP approach and the design goal set to minimum strain energy or maximum stiffness with optimal structural configuration. To control the actuator stiffness and the optimization convergence, a volume constraint was set[24].

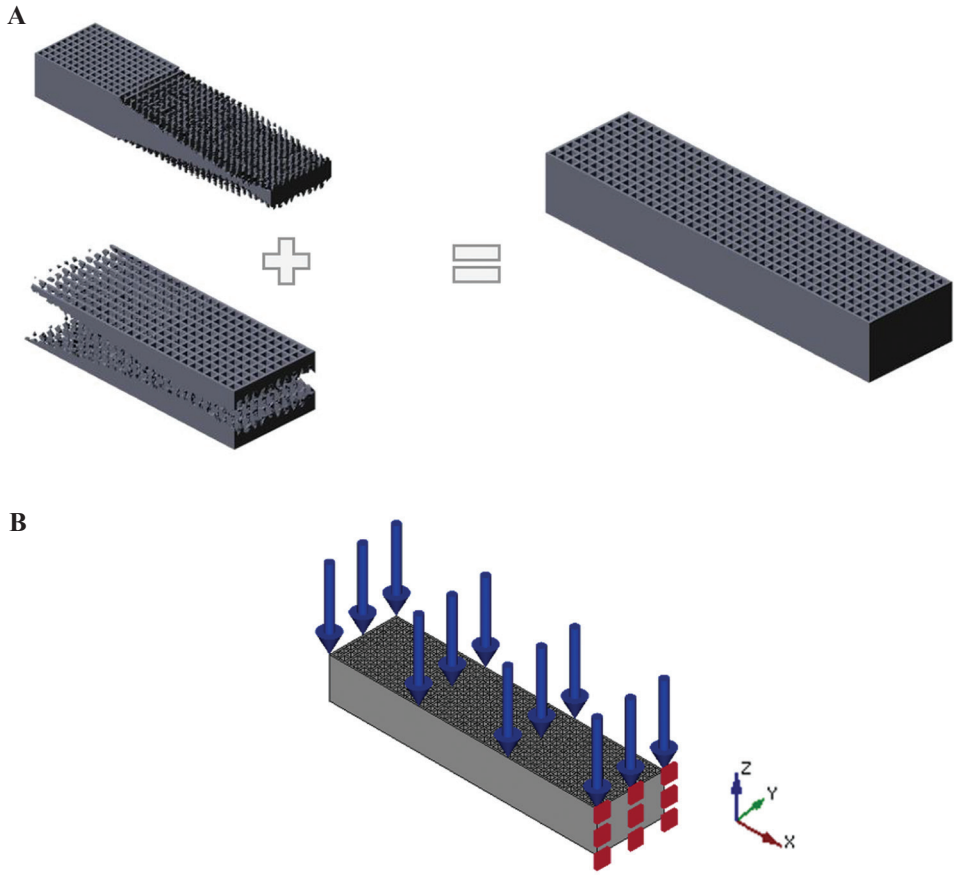

Figure 1. Computer-aided design models of the actuators (A) two-material three-dimensional printing, (B) mechanical forces and boundary constraints.

2.1 Sensitivity analysis

Direct objectives, such as stresses and strains, could be used to determine sensitivities. The strain compliance change with respect to the improved variant, $\Pi_{Strain} = \frac{1}{2}\boldsymbol{u}^T\boldsymbol{K}\boldsymbol{u}$, is opted as the most common approach[25,26]. A combination of both solid and distributed material models is used for the determination of the sensitivities[27]. The strain energy of the element can be used when the element size does not have a significant effect on the magnitude of the local strain energy. The strain energy density, $\bar{\Pi}_{obj}$, is calculated as an appropriate objective function for each element, e, to optimize uneven structured meshes as follows:

$$\bar{\Pi}_{obj,e} = \frac{\partial \Pi_{Strain}}{\partial \Omega} = \frac{1}{2}\frac{\partial \boldsymbol{u}^T\boldsymbol{K}\boldsymbol{u}}{\partial \Omega} \quad (1)$$

Where, $\boldsymbol{K}$ and $\boldsymbol{u}$ are the stiffness matrix and the node displacement vectors over the field design, Ω, which is transferred into N discrete elemental counterparts. Defining continuous design variables $0<\boldsymbol{\rho}_e<1$, the design domain, Ω. By applying a power law, interpolation and information of the material properties, $\boldsymbol{E}_1$ and $\boldsymbol{E}_2$, a single element Young's modulus, $\boldsymbol{E}_e$, could be described as follows[28]:

$$\boldsymbol{E}_e(\rho_e) = \boldsymbol{E}_2 + (\boldsymbol{E}_1 - \boldsymbol{E}_2)\rho_e^p, e = 1,2,\ldots,N \quad (2)$$

Furthermore, the elemental stiffness matrix, $\boldsymbol{K}_e$ for two materials then could be derived as follows:

$$\boldsymbol{K}_e = \boldsymbol{K}_{0,e}\left(\boldsymbol{E}_2 + (\boldsymbol{E}_1 - \boldsymbol{E}_2)\rho_e^p\right), e = 1,2,\ldots,N \quad (3)$$

Where, $\boldsymbol{K}_{0,e}$ is a single elemental stiffness matrix for a unit solid material. The strain energy density of each element with the volume V_e and the node displacement $\boldsymbol{u}_e$ could be obtained as follows:

$$\bar{\Pi}_{obj,e} = \frac{1}{2}\frac{\boldsymbol{u}_e^T\boldsymbol{K}_e\boldsymbol{u}_e}{V_e} \quad (4)$$

By differentiating the element-wise strain energy with respect to the normalized element

density ρ_e appropriate sensitivities for a particular element can calculated as follows[27,29,30]:

$$\frac{\partial \Pi_{obj,e}}{\partial \rho_e} = \frac{1}{2V_e}\left(\frac{\partial \boldsymbol{u}_e^T}{\partial \rho_e}\boldsymbol{K}_e\boldsymbol{u}_e + \boldsymbol{u}_e^T\partial\frac{\partial \boldsymbol{K}_e}{\partial \rho_e}\boldsymbol{u}_e + \boldsymbol{u}_e^T\boldsymbol{K}_e\frac{\partial \boldsymbol{u}_e}{\partial \rho_e}\right. \tag{5}$$

Applying the system equation $\boldsymbol{Ku} = \boldsymbol{f}$ to a single element considering the design variable yields the following partial differential form:

$$\boldsymbol{K}_e\frac{\partial \boldsymbol{u}_e}{\partial \rho_e} + \frac{\partial \boldsymbol{K}_e}{\partial \rho_e}\boldsymbol{u}_e = \frac{\partial \boldsymbol{f}_e}{\partial \rho_e} \tag{6}$$

Since the external load does not depend on the density values, Equation (6) yields:

$$\frac{\partial \boldsymbol{K}_e}{\partial \rho_e}\boldsymbol{u}_e + \boldsymbol{K}_e\frac{\partial \boldsymbol{u}_e}{\partial \rho_e} = 0 \tag{7}$$

Accordingly, Equation (7) can be rearranged to:

$$\boldsymbol{K}_e\frac{\partial \boldsymbol{u}_e}{\partial \rho_e} = -\frac{\partial \boldsymbol{K}_e}{\partial \rho_e}\boldsymbol{u}_e \tag{8}$$

Transposing Equation (8) leads to:

$$\left(\boldsymbol{K}_e\frac{\partial \boldsymbol{u}_e}{\partial \rho_e}\right)^T = \left(-\frac{\partial \boldsymbol{K}_e}{\partial \rho_e}\boldsymbol{u}_e\right)^T \tag{9}$$

Using the symmetric stiffness matrix, Equation (9) can be expressed as follows:

$$\frac{\partial \boldsymbol{u}_e^T}{\partial \rho_e}\boldsymbol{K}_e = -\boldsymbol{u}_e^T\frac{\partial \boldsymbol{K}_e}{\partial \rho_e} \tag{10}$$

Inserting Equations (10) and (9) into Equation (5), the strain energy density sensitivity becomes:

$$\frac{\partial \Pi_{obj,e}}{\partial \rho_e} = \frac{1}{2V_e}\left(-\boldsymbol{u}_e^T\frac{\partial \boldsymbol{K}_e}{\partial \rho_e}\boldsymbol{u}_e + \boldsymbol{u}_e^T\partial\frac{\partial \boldsymbol{K}_e}{\partial \rho_e}\boldsymbol{u}_e - \boldsymbol{u}_e^T\frac{\partial \boldsymbol{K}_e}{\partial \rho_e}\boldsymbol{u}\right. \tag{11}$$

which simplifies to:

$$\frac{\Pi_{Obj,e}}{\partial \rho_e} = -\frac{1}{2V_e}\boldsymbol{u}_e^T\frac{\partial \boldsymbol{K}_e}{\partial \rho_e}\boldsymbol{u}_e. \tag{12}$$

Differentiation of the material law, Equation (2) results in:

$$\frac{\partial \boldsymbol{K}_e}{\partial \rho_e} = \boldsymbol{K}_{0,e}\left(\boldsymbol{E}_2 - \boldsymbol{E}_1\right)\boldsymbol{p}\rho_e^{p-1} \tag{13}$$

Having obtained u_e by solving the system of equations with a distributed density and material properties[25,27], and inserting Equation (13) in Equation (12), the sensitivity could be determined:

$$\frac{\bar{\Pi}_{\boldsymbol{Obj,e}}}{\partial \boldsymbol{\rho_e}} = -\frac{1}{2\boldsymbol{V_e}}\left(E_2 - E_1\right)\boldsymbol{p}\rho_e^{p-1}\boldsymbol{u}_e^T\boldsymbol{K}_{0,e}\boldsymbol{u}_e, \tag{14}$$

2.2 Sensitivity filtering

The checkerboard structure issue caused by direct use of the selected sensitivities was sorted out using higher order elements, despite longer calculation time. Sensitivity filtering is utilized by applying an increased limit to the checkerboard structure and smoother contours, as shown in **Figure 2**[26]. Using this approach resulted in poorly defined contours instead of checkerboard patterns. Digital pixel structures are adapted to the finite element mesh to allow the image processing results to be directly applied to TO problem[31,32].

As shown in the flowchart of TO algorithm in **Figure 3,** the SIMP method was implemented to solve the optimization, in which design variables are defined based on the densities of the discretized elements[33-35]. The mechanical loadings and constraints of the optimization problem were modeled through loading and boundary conditions, as shown in **Figure 1**. The aim is to maximize the deflection of the actuator by optimization of the configuration of the printed layers. The optimization problem is solved iteratively by incorporating the sensitivity guidance. Subsequently, a volume constraint is set to minimize the structural stiffness of the actuator and ensure the convergence of the algorithm[36]. In addition, a standard method of moving asymptotes was employed for each material density to conform to the volume constraint imposed into the optimization.

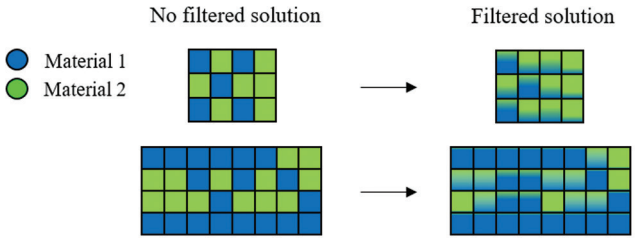

Figure 2. Schematics of two-material topology optimization filtering.

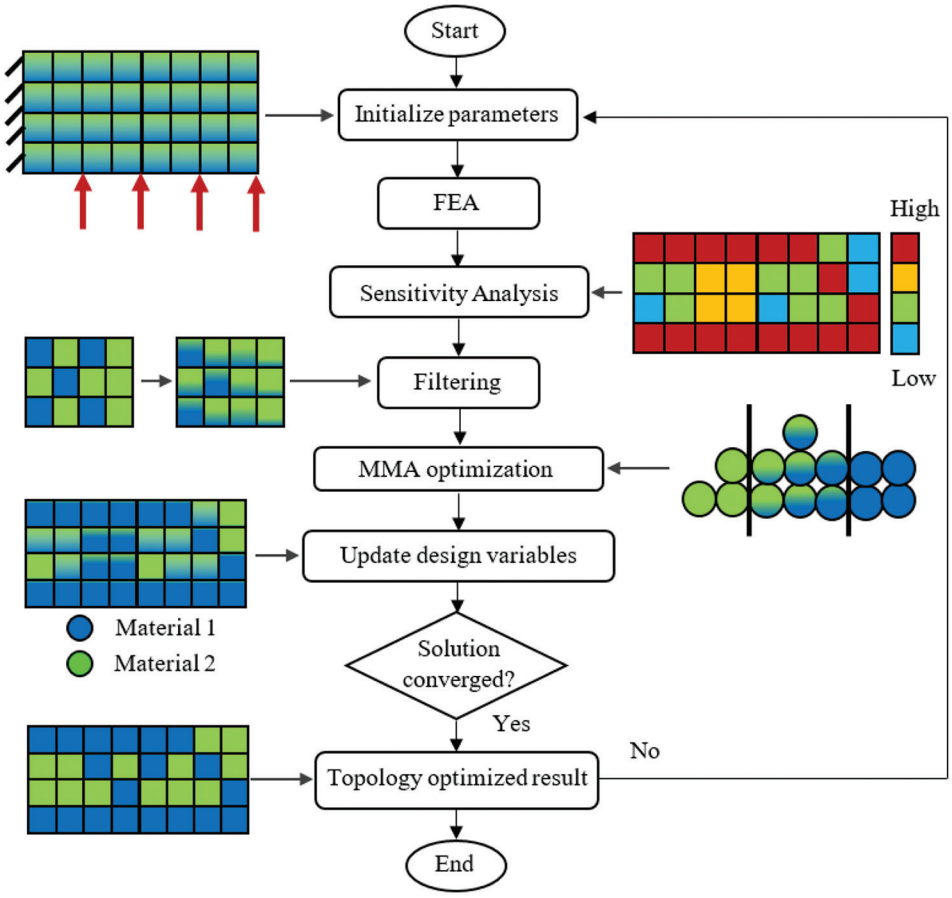

Figure 3. Two-material topology optimization algorithm utilized in this study.

The equivalent optimal solution for 3D printing of two-material configuration at actuator layers is illustrated in **Figure 4** where the volume fraction constraint is applied using two different materials for each layer. The results of optimization with respect to volume fraction and objective function over a number of iterations are presented in **Figure 5**. These results demonstrate the graduate decrease of the objective function with increasing number of iterations until reaching a minimum at iteration 19 when the volume fraction criterion is fulfilled.

3 Fabrication of the 3D bioprinted actuator

3D bioprinting fabrication of hydrogel-based soft actuators requires determination of accurate process parameters to achieve timely coagulation of the extruded strand from the printer nozzle. The previous studies have utilized various synthesis techniques, such as using cross-linking agents or using high-molecular-weight polymer inks, to preserve the structural integrity of the 3D-printed hydrogels on extrusion[37]. Wet spinning and solvent casting are other common methods of 3D-printed hydrogel extrudate solidification[38].

In this paper, however, the liquid hardening method was applied to chitosan hydrogel[22]. The TO algorithm is exported to an EnvisionTEC GmbH Bioplotter. A mixture of chitosan (Sigma-Aldrich, Australia) and acetic acid solution poured into the bioplotter syringe. The hardening of the extruded strand was carried out in 0.25 M sodium hydroxide solution. The statistical significance of the 3D printing procedure for developing chitosan actuators has already been developed and can be accessed in earlier works[22,39]. The two-material bioprinted actuator is shown in **Figure 6.** 3D-printed hydrogel pastes were made with different molecular weights and concentrations to function as two different materials with varying density

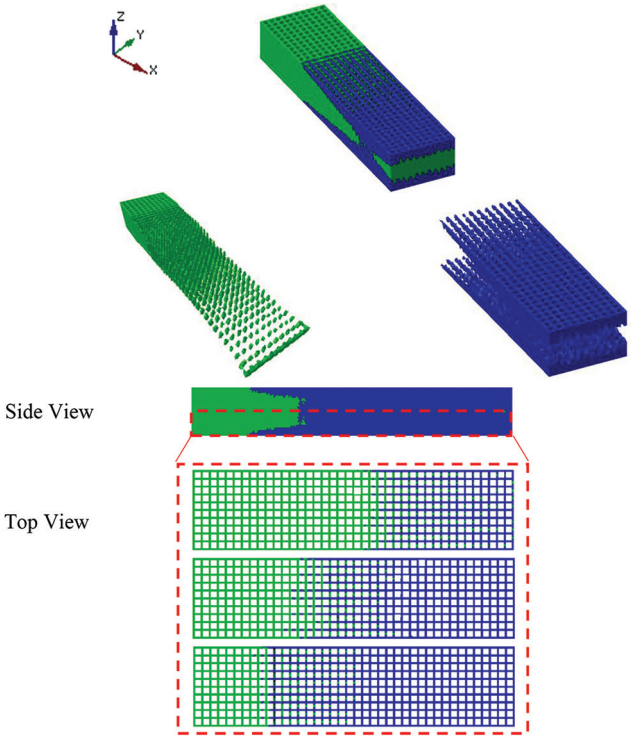

Figure 4. Two-material topology optimization layers' configuration of bioprinted actuator.

and modulus properties so that the different configurations of them could be optimized. The 3D printing hydrogel pastes for the TO actuator were made with variable density and Young's moduli with ratios of $\frac{E_2}{E_1} = 10.44$ and $\frac{\rho_2}{\rho_1} = 1.56$, respectively. All the samples are 3D printed in same size of 25 mm ×5 mm × 1.5 mm. The volume fractions of the materials 1 and 2 are printed as follows: 31%, 59%, and 91% of material 1 and 69%, 41%, and 9% of material 2 in three subsequent layers.

The average density of triplet 3D-printed actuator samples was measured using an electronic Qualitest Densimeter - SD-200L as 0.72 ± 0.06 g/cm^3, 1.12 ± 0.14 g/cm^3, and 0.81 ± 0.09 g/cm^3 for materials 1, 2, and multimaterial specimens, respectively. The average modulus of the three actuators made from material 1, 2, and multimaterial was measured as 6.8 ± 0.74 MPa, 71 ± 2.91 MPa, and 31.07 ± 5.44 MPa, respectively.

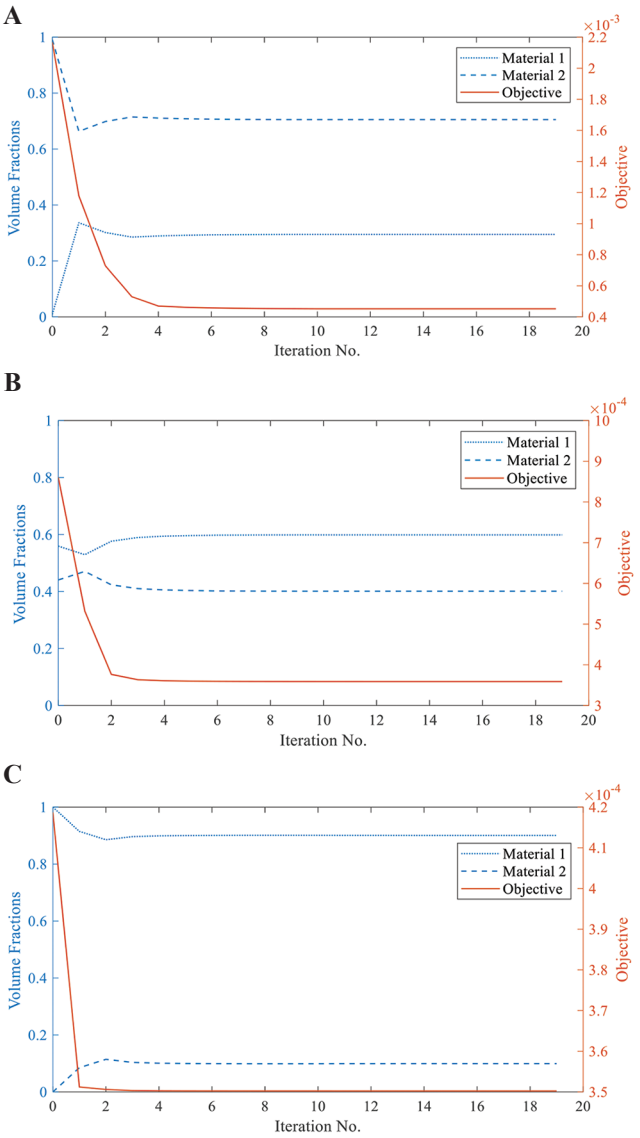

Figure 5. Objective and volume fraction results over iterations at different layers with the constant total volume fraction (A) layer 1; B) layer 2; and (C) layer 3.

4 Results and discussion

The efficiency of the two-material TO for the improvement of the performance of the bioprinted actuator was demonstrated through a series of experiments. A bending index incorporating the initial length of the actuator (L) as well as X and Y coordinates of the actuator tip is defined, as shown in **Figure 7A**. The X and Y points are recorded with a webcam (Logitech C920) mounted on a

custom-made scaffold, as shown in **Figure 7B**. The experiment and the computational tool were implemented in MATLAB using a low-cost USB interface Arduino Nano-based driver hardware and a motor driver breakout board for the input voltage modulation. The recorded images were processed through several steps for measuring the X and Y value[40]. The calibration of camera for bending measurement in this study was carried out using the checkerboard method while features of the webcam were obtained by utilizing the Camera Calibration Toolbox in MATLAB to minimize the reprojection error as mean pixel error of 2.07[41]. The measurement set up including a signal generator, two stainless steel electrodes were immersed in 0.2 M NaOH electrolyte solution. A paper clip was used to fix one end of the soft actuator in the electrolyte solution, letting the planar bending of the endpoint occur due to osmotic pressure caused by input signal applied on electrodes.

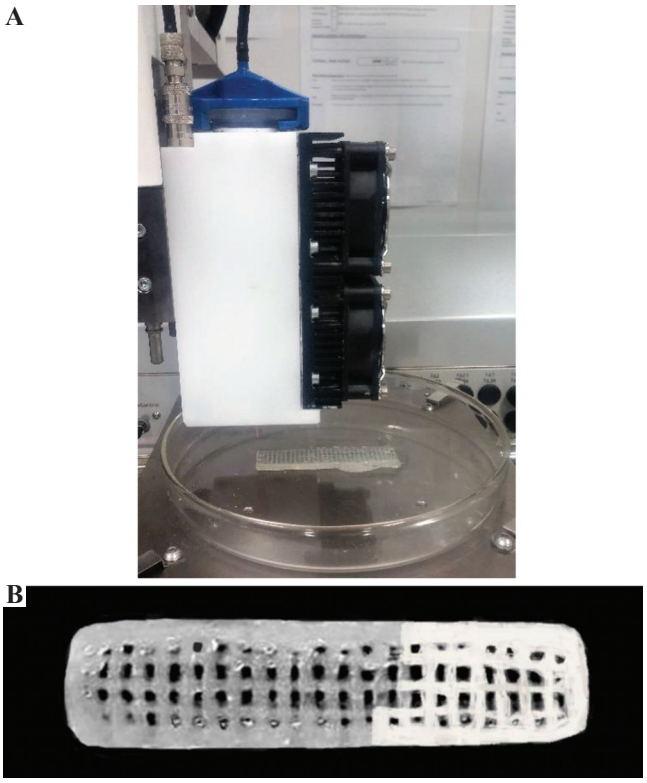

Figure 6. (A) Three-dimensional bioprinting; (B) two-material topology optimized bioprinted actuators.

The actuator's hysteresis behavior was investigated through cyclic "ON-OFF" input signals. A cyclic signal of ±8 V amplitude was applied to the electrodes and the average of three repeated experiments on the bioprinted actuators made entirely of material 1 and material 2 is shown in **Figure 8**. The results revealed the hysteresis behavior of the actuators over the time of the applied signal with differences mainly observed in the peak magnitudes. It is evident that with repeating cycles the polyelectrolyte actuator's functionality plunges. The actuator absorbs the moisture and causes swelling, giving rise to large dilatational strains in the plastic region. The semi-crystalline nature of the actuator has an influence on its degradation behavior over bending cycles. Different concentrations of chitosan content lead to different crystallinity which is thought to affect the hysteresis behavior of the actuator by changing its modulus[42]. The deviation of up to 30% from

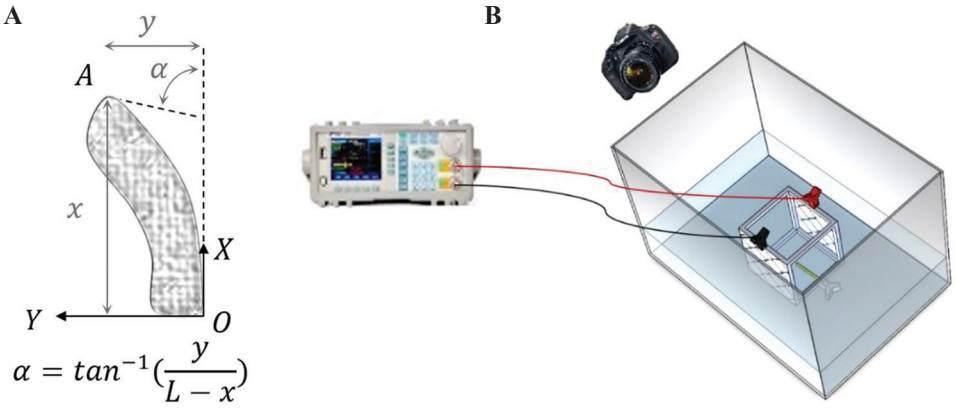

Figure 7. (A) Bending index of the actuator and (B) the measurement set up.

maximum endpoint deflection in the subsequent cycle is observed by means of peak envelop lines, as shown in **Figure 8**. Further experiments were conducted to compare the bending behavior of the two-material topology-optimized actuator with entirely one material actuator. The results proved the performance improvement of the two-material TO soft actuator compared to the entirely bioprinted one, as shown in **Figures 9 and 10**. Looking at the details of **Figure 10**, it can be seen that the two-material TO bioprinted actuator exhibited larger bending compared to the bioprinted material 2 lattice during the actuation process. Accordingly, when the input signal was turned off the bending relaxation of the topology-optimized actuator took placed at 0.022 rad/s which is greater than that shown by the material 2 bioprinted soft actuator at 0.013 rad/s with the same volume fraction but lighter structure. Due to this reason and vastly voltage driven model of the polyelectrolyte actuator, the deflections of both actuators at the completion of cycle are quite alike. However, TO bioprinted actuator always outpaced the non-optimized one at all the tests during the voltage "ON" interval.

The bending of the 3D-printed polyelectrolyte actuators could be determined based on the Donnan equilibrium theory[43], osmotic pressure difference $\Delta\pi$ between both sides of the polyelectrolyte actuator according to a formula developed by Shiga[16,44], in which the osmotic pressure difference $\Delta\pi$ was equal to the maximum tensile stress σ as follows: $\Delta\pi = \sigma = \frac{6DEY}{L^2}$ (15)

where, E is the elastic modulus, Y the bending deflection, D the thickness, and L length of the actuator prior to bending. Therefore, when the dimensions (D, L, E) are constant, the larger osmotic pressure difference $\Delta\pi$ results in greater bending deflection.

There are several electroactuation and electrochemical factors contributing to the

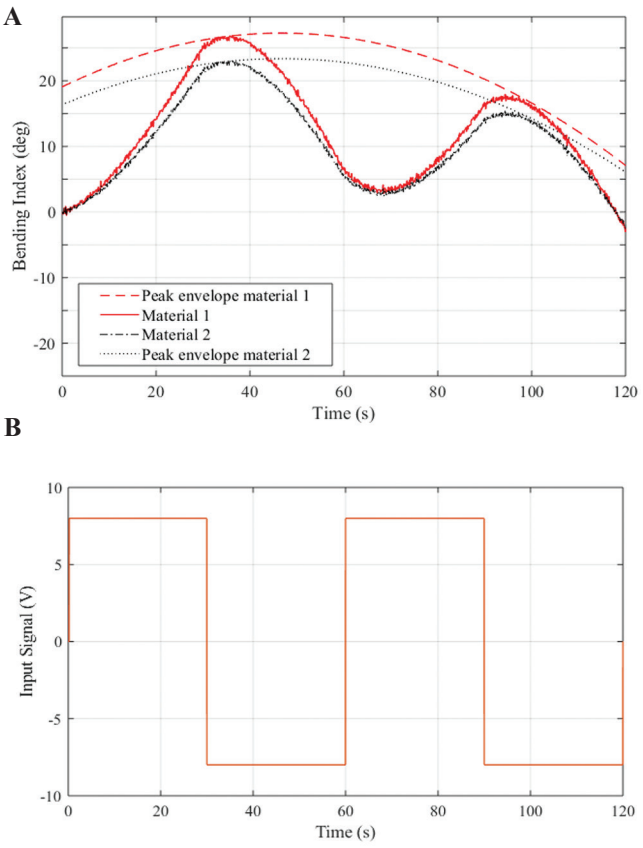

Figure 8. (A and B) Experimental results of three-dimensional-printed actuators entirely made of material 1 and material 2 under cyclic input signal of 8 V.

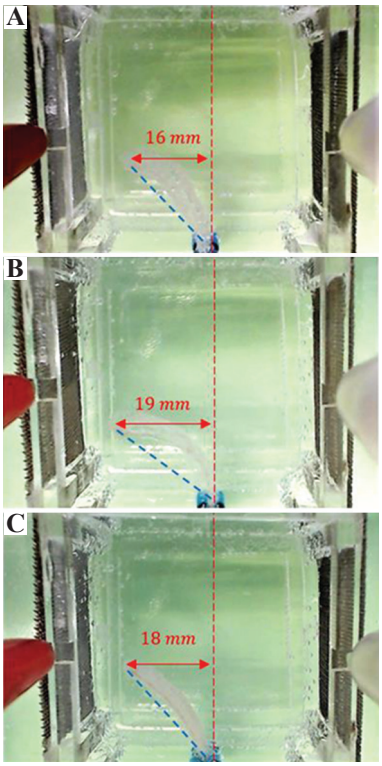

Figure 9. A schematic comparison of bioprinted actuators end point after 40 s; (A) material 2; (B) material 1; (C) two-material topology optimized.

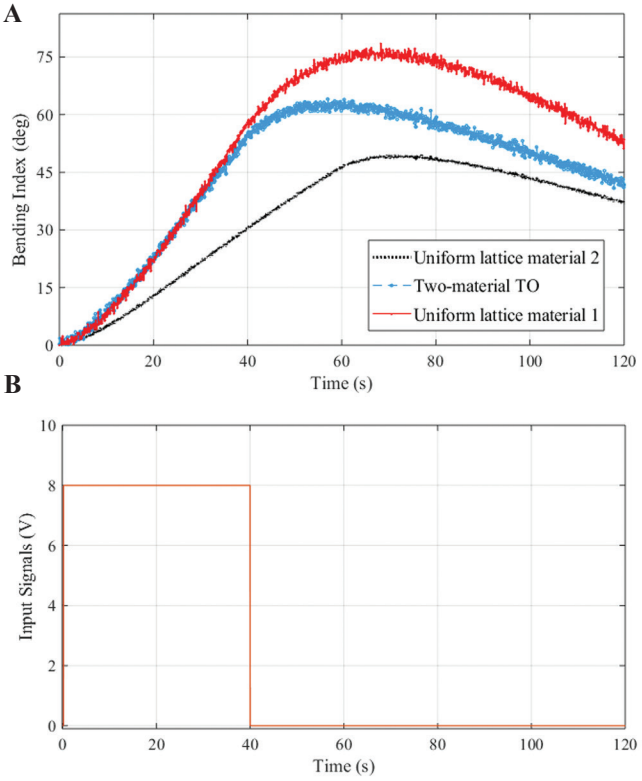

Figure 10. (A and B) Deflection of bioprinted actuators under 8 V input signal. The standard deviations of the average triplet sample results were calculated as 3.21°, 2.88°, and 2.49° for material 1, two-material topology optimization, and material 2 actuators.

performance polyelectrolyte actuators. For the polyelectrolyte actuator placed at the center of the electrolytic cell, the bending started as soon as the voltage stimulus applied to the electrodes. It was observed that the time required for the actuator tip to reach its peak varied as per the rigidity of the material and its response to the electrical voltage. In our study, electrochemical effects were not incorporated into the TO algorithm. However, it has already been reported that the electroactivity of the 3D-printed chitosan actuator had an optimum performance in the specific concentration of the NaOH solution. The electroactivity increased with the NaOH concentration to a certain extent, followed by the decline of the osmotic pressure at the interface of the hydrogel actuator due to a phenomenon called shield effect where the ion migration is hindered. Hence, the inflow of water to once side of the actuator decreased leading to a slower rate of swelling and as a consequence smaller bending index.

The electroactivity of the 3D-printed polyelectrolyte actuator increased as the DC voltage increased. Yet, at higher voltages of more than 10 V, the electrochemical reactions intensify leading to significant acceleration of the electrochemically generated ion waves and electrolysis bubbles in the cell. These circumstances require further computational fluid dynamics analysis to be incorporated into the TO algorithm, which is beyond the scope of our study.

The 3D-printed bioactuator developed here is used as an *ad hoc* to demonstrate the capability of TO for functionality enhancement. The contribution of the TO may be influenced by optimization of synthesis parameters to improve the overall electro-chemo-mechanical performance of the actuator. In other words, the bending amplitude of such actuators could be more substantial when TO is combined with optimized synthesis. The main cause of smaller bending amplitude in our sample is attributed to the characteristic of polyelectrolyte hydrogel actuators that are highly dependent on electrical stimulus and once the input signal is turned off, there is a back relaxation in bending. The lack of 3D printing fidelity for certain extrudate systems may reduce the improvement predicted by TO mainly due to the open loop process of 3D printing. In the current systems, there is no feedback control on the printing process parameters to compensate for uncertainties during 3D printing. The lack of precise control in factors such as ambient temperature, moisture, and instrument vibrations could lead to imperfect representation of the TO model. Further, research in optimizing the 3D printing of stimuli-responsive hydrogels in conjunction with TO could result in significant functionality enhancement of bioprinted actuators.

5 Conclusion

In this study, TO was introduced to bioprinted soft actuators to boost the mechanical performance of the system in bending. A multimaterial TO

actuator was designed and bioprinted to maximize the bending performance. It was shown through a series of experiments that the two-material TO improves the bending performance compared to uniformly bioprinted soft actuator due to optimized materials configuration within the stack of layers with constant volume. The results demonstrate the efficacy of multimaterial TO-based design to bring about the full potential of the performance of bioprinted soft actuators.

References

1. Cohen E, Trimmer BA, Vikas V, *et al*., 2015, Design Methodologies for Soft-Material Robots Through Additive Manufacturing, From Prototyping to Locomotion. in ASME 2015 International Design Engineering Technical Conferences and Computers and Information in Engineering Conference. American Society of Mechanical Engineers, New York. DOI: 10.1115/detc2015-47507.
2. Bodaghi M, Damanpack A, Liao W, 2017, Adaptive Metamaterials by Functionally Graded 4D Printing. *Mater Des*, 135:26–36. DOI: 10.1016/j.matdes.2017.08.069.
3. Choong YY, Maleksaeedi S, Eng H, *et al*., 2020, High Speed 4D Printing of Shape Memory Polymers with Nanosilica. *Appl Mater Today*, 18:100515. DOI: 10.1016/j.apmt.2019.100515.
4. Zolfagharian A, Khoo S, Kouzani A, *et al*., 2016, Evolution of 3D Printed Soft Actuators. *J Sens Actuators A Physical*, 250:258–72. DOI: 10.1016/j.sna.2016.09.028.
5. Bodaghi, M., Zolfagharian A, Serjouei A, *et al*., 2020, Reversible Energy Absorbing Meta-Sandwiches by 4D FDM Printing. *Int J Mech Sci*, 173:105451. DOI: 10.1016/j.ijmecsci.2020.105451.
6. Maute K, Tkachuk A, Wu J, *et al*., 2015, Level set Topology Optimization of Printed Active Composites. *J Mech Des*, 137:111402.
7. Yu C, Jiang J, 2020, A Perspective on Using Machine Learning in 3D Bioprinting. *Int J Bioprint*, 6:95. DOI: 10.18063/ijb.v6i1.253.
8. Hamel CM, Roach DJ, Long KN, *et al*., 2019, Machine-learning Based Design of Active Composite Structures for 4D Printing. *J Smart Mater Struct*, 28:65005. DOI: 10.1088/1361-665x/ab1439.
9. Bodaghi M, Noroozi R, Zolfagharian A, *et al*., 2019, 4D Printing Self-morphing Structures. *J Mater*, 12:1353. DOI: 10.3390/ma12081353.
10. Zolfagharian A, Kaynak A, Khoo SY, *et al*., 2018, Pattern-driven 4D Printing. *J Sens Actuators A Physical*, 274:231–43. DOI: 10.1016/j.sna.2018.03.034.
11. Zolfagharian A, Denk M, Bodaghi M, *et al*., 2019, Topology-Optimized 4D Printing of a Soft Actuator. *J Acta Mech Solida Sin*, 253:1–13. DOI: 10.1007/s10338-019-00137-z.
12. Lee J, Sing S, Yeong W, 2020, Bioprinting of Multimaterials with Computer-aided Design/Computer-aided Manufacturing. *Int J*, 6:47. DOI: 10.18063/ijb.v6i1.245
13. Zhang B, Chrisey DB, Cristescu R, *et al*., 2020, Solvent-based Extrusion 3D Printing for the Fabrication of Tissue Engineering Scaffolds. *Int J Bioprint*, 6:211. DOI: 10.18063/ijb.v6i1.211.
14. Kaynak A, Zolfagharian A, 2019, Stimuli-Responsive Polymer Systems Recent Manufacturing Techniques and Applications. Multidisciplinary Digital Publishing Institute, Switzerland. DOI: 10.3390/ma12152380.
15. Pilate F, Mincheva R, De Winter J, *et al*., 2014, Design of Multistimuli-responsive Shape-memory Polymer Materials by Reactive Extrusion. *Chem Mater*, 26:5860–7. DOI: 10.1021/cm5020543.
16. Shiga T, Kurauchi T, 1990, Deformation of Polyelectrolyte Gels under the Influence of Electric Field. *J Appl Polym Sci*, 39:2305–20. DOI: 10.1002/app.1990.070391110.
17. Li Y, Sun Y, Xiao Y, *et al*., 2016, Electric Field Actuation of tough Electroactive Hydrogels Cross-linked by Functional Triblock Copolymer Micelles. *ACS Appl Mater Interfaces*, 8:26326–31. DOI: 10.1021/acsami.6b08841.
18. Sigmund O, Maute KJ, 2013, Optimization, Topology Optimization Approaches. *Struct Multidiscip Optim*, 48:1031–55. DOI: 10.1007/s00158-013-0978-6.
19. Huang X, Xie YM, 2007, Design, Convergent and Mesh-independent Solutions for the bi-directional Evolutionary Structural Optimization Method. *Finite Elem Anal Des*, 43:1039–49. DOI: 10.1016/j.finel.2007.06.006.
20. van Dijk NP, Maute K, Langelaar M, *et al*., 2013, Level-set Methods for Structural Topology Optimization: A Review. 48:437–72. DOI: 10.1007/s00158-013-0912-y.
21. Bendsøe MP, Sigmund O, 1999, Material Interpolation Schemes in Topology Optimization. *J Arch Appl Mech*., 69:635–54.
22. Zolfagharian A, Denk, Bodaghi M, *et al*., 2018, Polyelectrolyte Soft Actuators: 3D Printed Chitosan and Cast Gelatin. *J 3D Print Addit Manuf*, 5:138–50. DOI: 10.1089/3dp.2017.0054.
23. Yang R, Chen C, 1996, Stress-based Topology Optimization. *J Struct Optim*, 12:98–105.
24. Hongying Z, 2018, Development of Topology Optimized 3D Printed Soft Grippers and Dielectric Soft Sensors, Theses and

Dissertations.

25. Schumacher A, 2013, Mathematische Grundlagen der Optimierung, in Optimierung mechanischer Strukturen. Springer, Berlin. pp. 45–55. DOI: 10.1007/978-3-642-34700-9_3.
26. Harzheim L, 2016, Der Natur in die karten geschaut optimierungsverfahren aus dem bereich der bionik. In: Karosseriebautage Hamburg. Springer, Berlin. pp. 3–16. DOI: 10.1007/978-3-658-14144-8_1.
27. Huang X, Xie M, 2010, Evolutionary Topology Optimization of Continuum Structures: Methods and Applications. John Wiley & Sons, New York.
28. Zhang H, Kumar AS, Chen F, *et al*., 2019, Topology Optimized Multimaterial Soft Fingers for Applications on Grippers, Rehabilitation, and Artificial Hands. *J IEEE/ASME Trans Mechatron*, 24:120–31. DOI: 10.1109/tmech.2018.2874067.
29. He D, Liu SJ, 2008, BESO Method for Topology Optimization of Structures with High Efficiency of Heat Dissipation. *Int J Simul Multidiscip Des Optim*, 2:43–8. DOI: 10.1051/smdo:2008005.
30. Kim MG, Kim JH, Cho SH, 2010, Topology Design Optimization of Heat Conduction Problems Using Adjoint Sensitivity Analysis Method. *Adv Mech Eng*, 23:683–91.
31. Gersborg-Hansen A, Bendsøe MP, Sigmund O, 2005, Topology Optimization Using the Finite Volume Method. *Struct Multidiscipl Optim*, 50:523–35. DOI: 10.1007/s00158-005-0584-3.
32. Kaup IA, 2018, Rekonstruktion Verrauschter Nichtregelmäßig Abgetasteter Bilddaten. Bachelor Thesis.
33. Svanberg K, 1987, The Method of Moving Asymptotes a New Method for Structural Optimization. 24:359–73.
34. Wiedemann J, 2007, Leichtbau: Elemente und Konstruktion. Springer-Verlag, Berlin.
35. Tavakoli R, Mohseni SM, 2014, Alternating Active-phase Algorithm for Multimaterial Topology Optimization Problems: A 115-line MATLAB Implementation. *Struct Multidiscip Optim*, 49:621–42. DOI: 10.1007/s00158-013-0999-1.
36. Zhang H, Wang Y, Cao J, *et al*., 2018, Topology Optimized Design, Fabrication and Evaluation of a Multimaterial Soft Gripper. In: 2018 IEEE International Conference on Soft Robotics (RoboSoft). DOI: 10.1109/robosoft.2018.8405363.
37. Lee JM, Yeong WY, 2016, Design and Printing Strategies in 3D Bioprinting of Cell-Hydrogels: A Review. *Adv Healthc Mater*, 5:2856–65. DOI: 10.1002/adhm.201600435.
38. Wu Q, Maire M, Lerouge S, *et al*., 2016, Solvent-cast 3D Printing of Chitosan Hydrogel Scaffolds for Guided Cell Growth. Front. Bioeng. Biotechnol. Conference Abstract: 10th World Biomaterials Congress. DOI: 10.3389/conf.FBIOE.2016.01.00336.
39. Zhang J, Allardyce BJ, Rajkhowa R, *et al*., 2018, 3D Printing of Silk Particle-reinforced Chitosan Hydrogel Structures and their Properties. *ACS Biomater Sci Eng*, 4:3036–46. DOI: 10.1021/acsbiomaterials.8b00804.
40. Zolfagharian A, Kouzani AZ, Khoo SY, *et al*., 2018, 3D Printed Soft Parallel Actuator. *J Smart Mater Struct*, 27:45019. DOI: 10.1088/1361-665x/aaab29.
41. Bouguet JY, 2010, Camera Calibration Toolbox for Matlab. International Conference on Indoor Positioning and Indoor Navigation.
42. Choong YY, Maleksaeedi S, Eng H, *et al*., 2017, 4D Printing of High Performance Shape Memory Polymer Using Stereolithography. *Mater Des*, 126:219–25. DOI: 10.1016/j.matdes.2017.04.049.
43. Donnan FG, 1924, The Theory of Membrane Equilibria. *Chem Rev*, 1:73–90.
44. Zolfagharian A, Kouzani AZ, Khoo SY, *et al*., 2017, Development and Analysis of a 3D Printed Hydrogel Soft Actuator. *J Sen Actuators A Physical*, 265:94–101. DOI: 10.1016/j.sna.2017.08.038.

ORIGINAL ARTICLE

Investigating the Effect of Carbon Nanomaterials Reinforcing Poly(ε-Caprolactone) Printed Scaffolds for Bone Repair Applications

Yanhao Hou, Weiguang Wang*, Paulo Bártolo

Department of Mechanical, Aerospace and Civil Engineering, School of Engineering, Faculty of Science and Engineering, The University of Manchester, Manchester, UK

Abstract: Scaffolds, three-dimensional (3D) substrates providing appropriate mechanical support and biological environments for new tissue formation, are the most common approaches in tissue engineering. To improve scaffold properties such as mechanical properties, surface characteristics, biocompatibility and biodegradability, different types of fillers have been used reinforcing biocompatible and biodegradable polymers. This paper investigates and compares the mechanical and biological behaviors of 3D printed poly(ε-caprolactone) scaffolds reinforced with graphene (G) and graphene oxide (GO) at different concentrations. Results show that contrary to G which improves mechanical properties and enhances cell attachment and proliferation, GO seems to show some cytotoxicity, particular at high contents.

Keywords: Biomanufacturing, Graphene, Graphene oxide, Poly(ε-caprolactone), Scaffolds, Tissue engineering

***Corresponding Author:** Weiguang Wang, Department of Mechanical, Aerospace and Civil Engineering, School of Engineering, Faculty of Science and Engineering, The University of Manchester, Manchester, UK; weiguang.wang@manchester.ac.uk

Received: March 10, 2020; ***Accepted:*** April 01, 2020; ***Published Online:*** April 21, 2020

Citation: Hou Y, Wang W, Bartolo P, 2020, Investigating the Effect of Carbon Nanomaterials Reinforcing Poly(ε-Caprolactone) Printed Scaffolds for Bone Repair Applications, *Int J Bioprint*, 6(2):266. DOI: 10.18063/ijb.v6i2.266

1 Introduction

Large scale bone defects caused by bone cancer surgeries, accidents, injuries, infections and chronic health conditions, represent relevant clinical problems. Due to the limited regenerative capabilities of bone, current clinical therapies, in most cases based on the use of biological grafts, are not effective. Scaffold-based bone tissue engineering is an alternative approach with potential to overcome major limitations of biological grafts such as pain and morbidity in donor sites, limited quantity and availability, deep infection and hematoma risk (autografting), rejection, diseases transmission, limited supply (allografting), and ethical problems (xenografting). Scaffolds are three-dimensional (3D) biocompatible and biodegradable porous physical substrates for cells to attach, proliferate, and differentiate[1-3]. They must have adequate mechanical properties, geometry and morphology, surface characteristics and must be easily sterilized[4]. Their capacity to stimulate cells is also another important requirement. Due to the piezoelectric and reverse piezoelectric nature of bone, electrical signals are critical physiological stimuli that strongly affect cell behavior controlling cell migration, adhesion, differentiation, DNA synthesis, and protein secretion[5]. A wide range of polymers (e.g., poly(glycolic acid), poly(lactic acid), poly(ε-caprolactone) [PCL], and poly(lactide-co-glycolide)), ceramic materials (e.g., hydroxyapatite [HA] and β-tricalcium phosphate [TCP]), and composites have been used to produce bone

scaffolds[6-8]. Multiple additive manufacturing technologies such as material extrusion, powder bed fusion, vat photopolymerization, and material or binder jetting techniques have been explored for the fabrication of bone tissue engineering scaffolds using a wide range of materials[9-11]. PCL, a semi-crystalline aliphatic polymer, has been successfully used by our group for bone tissue engineering scaffolds. We investigated the degradation kinetics of such scaffolds as a function of scaffold topology[12,13], the effect of processing conditions on the morphological development/ microstructure formation during the printing process[14,15] and surface modification strategies to improve cell attachment, proliferation, and differentiation[16,17]. To improve the bioactivity of PCL scaffolds, PCL/HA and PCL/TCP scaffolds containing different amounts of ceramic particles were also investigated and the results showed that scaffolds containing HA present better human adipose-derived stem cells (hADSCs) attachment and proliferation and TCP scaffolds present improved mechanical properties. Despite the promising results obtained with these scaffolds, they are not electrically conductive, which is a limiting characteristic of bone regeneration. To address this issue, our group also developed strategies to induce electroconductive properties on PCL-based scaffolds by mixing PCL with conductive polymers[18] or with low concentration of other conductive materials such as graphene (G) and carbon nanotubes (CNTs)[17,19,20].

The previous studies demonstrated that the addition of low concentration of G (up to 1 wt.%), two-dimensional single-atom-thick sheets of carbon atoms bound in hexagonal lattice structures[21], can enhance the hydrophilicity, topology, and the mechanical property of PCL scaffolds[17,22]. The *in vitro* biological studies show that cell attachment, proliferation, and differentiation of hADSCs can be stimulated by the addition of G fillers[20,22,23]. Huang *et al.*[24] investigated the use of additive manufacturing to produce scaffolds containing different loadings of multi-walled CNT (MWCNT) (0.25, 0.75, and 3 wt.%). Results showed that the addition of MWCNTs enhances protein adsorption, mechanical, and biological properties. Recently, Huang *et al.*[25] investigated 3D printed porous scaffolds containing aligned MWCNTs and nano-HA (nHA), mimicking the natural bone tissue from the nanoscale to macroscale level. MWCNTs with similar dimensions as collagen fibers were coupled with nHA and mixed within a PCL matrix. PCL/HA/MWCNTs scaffolds exhibited increased mechanical properties, cell proliferation, osteogenic differentiation, and scaffold mineralization. Wang *et al.*[20] assessed PCL, PCL/G, and PCL/CNTs from chemical, physical, and biological points of view. Results confirmed that the addition of both G and CNT allows the fabrication of scaffolds with improved properties. It also showed that scaffolds containing G present better mechanical properties and high cell-affinity improving cell attachment, proliferation, and differentiation.

Graphene oxide (GO), a single monomolecular layer of graphite with many functionalities including the presence of carbonyl, carboxyl, epoxide, and hydroxyl groups[26], is a candidate material for the fabrication of electro-active scaffolds. Scaffolds containing GO (concentrations up to 1.5 wt.% and 5 mg/mL) produced through a wide range of non-additive manufacturing techniques have been reported[27-29]. Results suggest that due to the presence of GO produced scaffolds presented no cytotoxicity against hADSCs, controlled degradation, and enhanced protein adsorption. This paper investigates the mechanical, wettability, and biological properties of PCL scaffolds containing different concentrations of G or GO produced through material extrusion additive manufacturing[30].

2 Materials and methods

2.1 Scaffolds fabrication

G nanosheets were synthesized from graphite by water-assisted liquid-phase exfoliation as reported before by Wang *et al*. and GO nanosheets (Sigma-Aldrich, UK) were purchased from Sigma-Aldrich. G and GO nanosheets were mixed with PCL pellets (CAPA 6500) (Perstorp, UK) through a melt blending process at different concentrations (1 wt.%, 2 wt.%, and 3 wt.%). PCL

pellets and reinforcements were heated at 150°C and mixed together in a crucible for 30 min. The material was stirred for 30 min to disperse the fillers homogenously. After cooling down for 3 h, the mixed materials were then cut into pellets and prepared for printing. Scaffolds were produced using the screw-assisted material extrusion additive manufacturing system 3D DiscoveryTM Evolution Bench-top (regenHU, Switzerland). The following design and processing parameters were considered: Fiber layout of 0°/90°, melt temperature of 90°C, screw rotation rate of 8 rpm, deposition velocity of 13 mm/s, slice thickness of 270 μm, and pressure of 6 bars. These parameters are considered to guarantee constant filament diameter of 330 μm after printing.

2.2 Morphological evaluation

Morphological characterization was performed through scanning electron microscopy (SEM). FEI Quanta 250 SEM (Thermo Fisher Scientific, USA) was used to capture images of both the top surface and cross-section of the scaffolds, using an accelerating voltage of 10 kV. Before image capturing, the scaffolds were cut into 3 mm blocks and coated with a thin layer of metal (10 nm gold) using the EMITECH K550X sputter coater (Quorum Technologies, UK). The obtained images were processed by ImageJ (NIH, USA).

2.3 Mechanical evaluation

To determine the mechanical properties of the scaffolds, according to American Society for Testing and Materials standards[31,32], uniaxial compression tests were conducted on the INSTRON X testing system (High Wycombe, UK) with a 100 N load cell. The scaffolds were cut into blocks of 3 mm of width, 3 mm of length, and 4mm of height. Compression tests were performed in dry state with the strain ranging from 0 to 0.3 mm/mm (30%) and a displacement rate of 0.5 mm/min. Force F and corresponding displacement Δh were measured by sensors while the samples were compressed, and then transformed into stress σ and strain ε values. The compressive modulus and compressive strength of the scaffolds were calculated using the software Origin (OriginLab, USA).

2.4 Surface wettability evaluation

Apparent water-in-air contact angle (WCA) tests were carried out with a KSV CAM 200 system (KSV Instruments, Finland) to evaluate the surface hydrophilicity of the scaffolds. 2 ml of distilled water was dropped on the surface of the scaffold using a micrometric liquid dispenser (Hamilton, USA) and the drop shape was recorded with a DMK 21F04 FireWire monochrome camera (Imaging Source, Germany). Attention Theta software (Biolin Scientific, Sweden) automatically calculates the contact angle.

2.5 Biological studies

In vitro, biological studies were conducted using hADSCs (Invitrogen, USA). hADSCs were defrosted and cultured in MesenPRO RS™ basal medium (Thermo Fisher Scientific, USA) in T75 cell culture flasks (Sigma-Aldrich, UK) at standard conditions (37°C, 5% CO_2 concentration, and 95% humidity) in a New Brunswick® Galaxy 170 R incubator (Eppendorf, USA). Cells were harvested at approximate 80% confluence using 0.05% trypsin-EDTA (Invitrogen, USA) and Centra® MP4 Refrigerated Centrifuge (Thermo Fisher Scientific, USA) (1200 rpm, 150 s) before cell seeding. Cells ranging from passage 2 to 6 were considered for biological evaluation.

Before cell seeding, scaffolds were sterilized in 99.8% ethanol (Thermo Fisher Scientific, USA) for 4 h, transferred to a 24-well plate, and rinsed with Dulbecco's Phosphate-Buffered Saline (PBS) (Thermo Fisher Scientific, USA). 50000 cells (counted by Cellometer Auto 1000 Bright Field Cell Counter [Nexcelom Bioscience, USA]) in 0.8 mL medium were seeded on each scaffold sample and empty well (control group).

The viability and proliferation of cells were evaluated at 1, 3 and 7 days after cell seeding using the Alamar Blue assay, which can quantitatively monitor the metabolic activity of cells and potential cytotoxicity of scaffolds[33]. At each particular time point, 1 mL of medium

containing 0.001% Alamar Blue (Sigma-Aldrich, UK) was added to each well and incubated at standard conditions for 4 h. Then, 150 μL liquid from each well was transferred into a 96-well plate and the fluorescence intensity was measured by a Multi-Detection Microplate Reader Synergy HT (BioTec, USA) (excitation wavelength of 530 nm and the emission wavelength of 590 nm).

For the preparation of confocal imaging, the pre-fixed (with 10% neutral buffered formalin) cell-seeded scaffolds were rinsed in PBS and added with 1 ml 0.1% Triton X-100 (Sigma-Aldrich, UK) to permeabilize cell membrane. Afterward, 1 ml of 5% w/w fetal bovine serum (Sigma-Aldrich, UK) in PBS was added to each sample and incubated at room temperature for 1 h to block non-specific binding. The samples were then rinsed and added Alexa Fluor 488 phalloidin (Thermo Fisher Scientific, USA) and 4' 6-diamidino-2-phenylindole (Thermo Fisher Scientific, USA) under the manufacturer's recommended concentration, and incubate in the dark. The images were captured by a Leica SP8 LIGHTNING confocal microscope (Leica, Germany).

2.6 Data analysis

All experiments have at least three repeats ($n \geq 3$) and data represent mean ± standard deviation. One-way analyses of variance with Tukey test were applied using Origin software. The significance levels were set at * $P < 0.05$, ** $P < 0.01$, and *** $P < 0.001$ compared with control (PCL), # $P < 0.05$, ## $P < 0.01$, and ### $P < 0.001$ compared with different concentrations of the same material, & $P < 0.05$, && $P < 0.01$, and &&& $P < 0.001$ compared with the same concentration of different materials.

3 Results and discussion

3.1 Morphological evaluation

SEM images of the fiber surface are presented in **Figure 1**. Actual scaffold images and both top surface and cross-section SEM images of the scaffolds are presented in **Figure 2**. As observed, the addition of G or GO seems to create a smooth surface on the printed filaments. **Table 1** shows that the printed scaffolds present an average filament diameter of 333.33 ± 8.32 μm (the designed value was 330 μm), regular square pores with an average pore size of 336.65 ± 16.92 μm in the vertical direction (top surface, the designed value was 350 μm), and 218.69 ± 22.03 μm in the horizontal direction (cross-section, the designed value was 210 μm). These differences between the measured values and designed values are due to rheological effects (viscosity, shear-thinning, and viscoelastic properties) associated to the different material compositions.

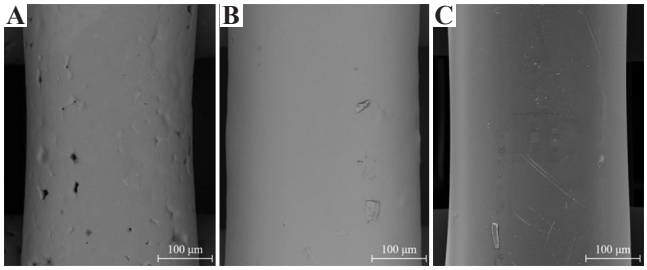

Figure 1. Scanning electron microscopy images of the fiber surface on (A) poly(ε-caprolactone), (B) 3 wt.% graphene, and (C) 3 wt.% graphene oxide scaffolds.

3.2 Mechanical evaluation

Figure 3 represents the strain-stress curve and **Figure 4** represents both compressive modulus and compressive strength values of PCL, PCL/G, and PCL/GO scaffolds. As observed, the addition of G significantly increases the compressive modulus from 78.32 ± 5.22 MPa (PCL) to 136.74 ± 4.55 MPa (3 wt.% G). The same trend can be found in terms of compressive strength, which increases from 2.69 ± 0.27 MPa (PCL) to 3.13 ± 0.13 MPa (3 wt.% G). All PCL/G scaffolds were statistically different from the PCL scaffolds.

In the cases of PCL/GO scaffolds, the addition of GO slightly increased the compressive modulus from 78.32 ± 5.22 MPa (PCL) to 91.35 ± 4.51 MPa (1 wt.% GO), which then decreased to 84.08 ± 3.93 MPa (3 wt.% GO). In terms of compressive strength, the incorporation of GO fillers decreased the compressive strength from 2.69 ± 0.27 MPa (PCL) to 2.06 ± 0.11 MPa (3 wt.% GO). All

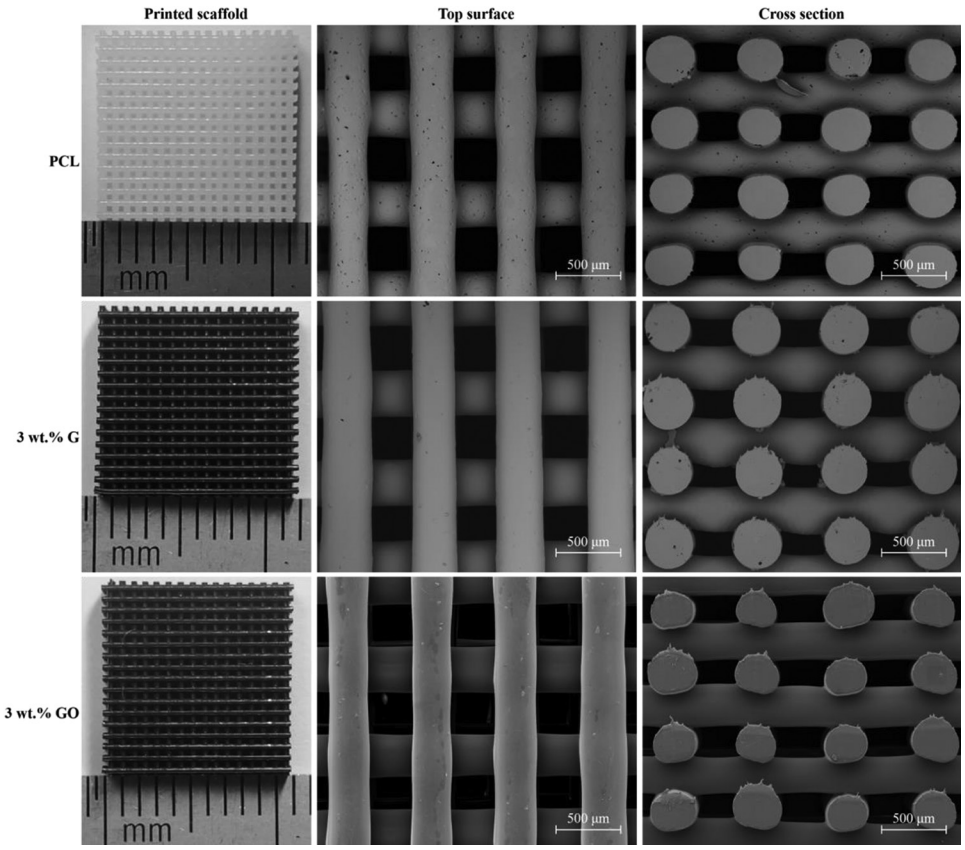

Figure 2. Actual images, top surface, and cross-section scanning electron microscopy images of different printed scaffolds.

Table 1. Fiber diameter and pore size values of the scaffolds considering different material compositions (n=9).

Scaffolds	Fiber diameter (µm)	Pore size (vertical) (µm)	Pore size (horizontal) (µm)
Designed	330	350	210
PCL	323.23±19.68	341.38±16.03	211.82±19.51
1 wt.% G	338.00±6.78	319.13±5.57	203.60±15.89
2 wt.% G	337.45±12.58	316.63±12.82	183.10±7.53
3 wt.% G	342.33±16.69	329.38±23.00	221.40±16.98
1 wt.% GO	332.56±14.61	340.54±16.48	246.57±12.56
2 wt.% GO	320.67±18.87	366.25±30.28	242.70±8.53
3 wt.% GO	339.05±27.34	343.23±39.56	221.63±17.17

PCL/GO results are significantly different from PCL/G, but not significantly different from PCL scaffolds.

In the case of G fillers, the increase in the mechanical properties can be attributed to the intrinsic properties of the fillers, dispersion and distribution of the fillers, and adhesion between fillers and matrix (PCL). However, in the case of GO fillers, the addition of fillers into the matrix over a certain critical value (reported as 0.1 wt.%) the GO nanosheets become too close to each other[34]. Due to Van der Waals forces, GO fillers tend to stack together making it more difficult to disperse and limiting load transfer[34].

Results also show that the fabricated scaffolds have mechanical properties in the same order of magnitude as human trabecular bone. Depending on gender and age, human trabecular bone presents

compressive modulus ranging from 50 to 1500 MPa with the mean value of 194 MPa, and the compressive strength ranging from 1 to 30 MPa with the mean value of 3.55 MPa[35-38].

3.3 Surface wettability evaluation

Table 2 shows the WCA results at 0, 5, and 10 s after the water droplet was dropped on the samples surfaces. PCL scaffolds present the highest contact angle value of 89.28 ± 1.36° at 0 s which slightly decreases to 87.91 ± 1.71° after 10 s, typical of hydrophobic surfaces. In the case of scaffolds containing G, the values are lower than PCL scaffolds, ranging between 87.25 ± 0.82° (1 wt.% G) to 84.12 ± 1.44° (3 wt.% G) at 0 s and 86.10 ± 0.74° (1 wt.% G) to 82.40 ± 0.92° (3 wt.% G) after 10 s. In the case of scaffolds containing GO, the values are also lower than PCL scaffolds, ranging between 82.79 ± 0.35° (1 wt.% GO) and 82.03 ± 1.47° (3 wt.% GO) at 0 s. After 10 s, the values vary between 81.73 ± 0.06° (1 wt.% GO) and 81.52 ± 1.52° (2 wt.% G). Changes on the wettability, particularly in the case of GO, can be attributed to the hydrophilic O, OH, and COOH groups of the GO nanosheets. These results also show that the addition of G and GO has a minor effect on the contact angle.

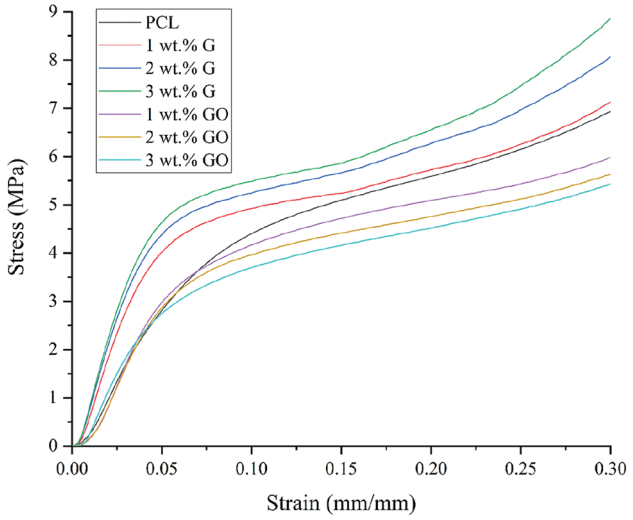

Figure 3. Strain-stress curve of different scaffolds.

3.4 Biological studies

Confocal microscopy images (**Figure 5**), showing cell nuclei stained blue and cell actin stained green, suggest that all scaffolds can support cell attachment and proliferation along the fibers. **Figure 6** shows the metabolic activity of cells at different time points after cell seeding. In this figure, the fluorescence intensity is proportional to the number of metabolically active cells.

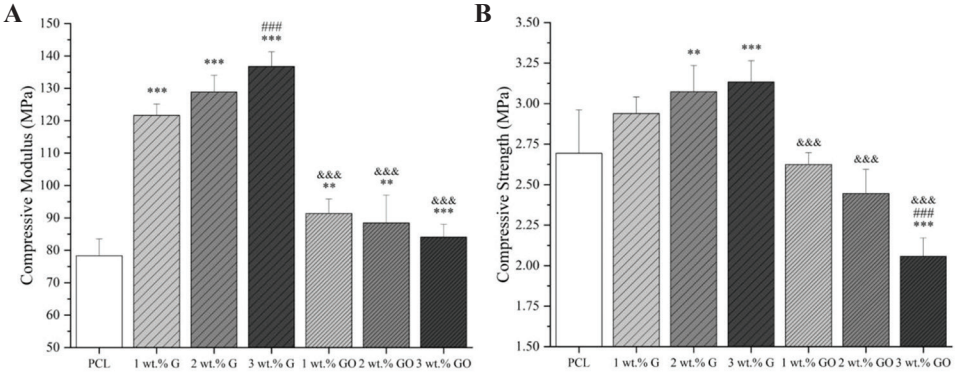

Figure 4. Mechanical properties of scaffolds with different material composition (A) compressive modulus; (B) compressive strength (n = 5).

Table 2. WCA results of scaffolds with different carbon material contents after 0, 5, and 10 s (n=5).

Time	PCL	1 wt.% G	2 wt.% G	3 wt.% G	1 wt.% GO	2 wt.% GO	3 wt.% GO
0 s	89.28±1.36°	87.25±0.82°	84.13±0.50°	84.12±1.44°	82.79±0.35°	82.22±0.89°	82.03±1.47°
5 s	88.48±1.82°	86.41±0.81°	83.73±0.66°	83.64±1.43°	82.07±0.35°	81.62±1.48°	81.67±1.28°
10 s	87.91±1.71°	86.10±0.74°	83.30±1.06°	82.40±0.92°	81.73±0.06°	81.52±1.52°	81.57±1.26°

WCA: Water-in-air contact angle

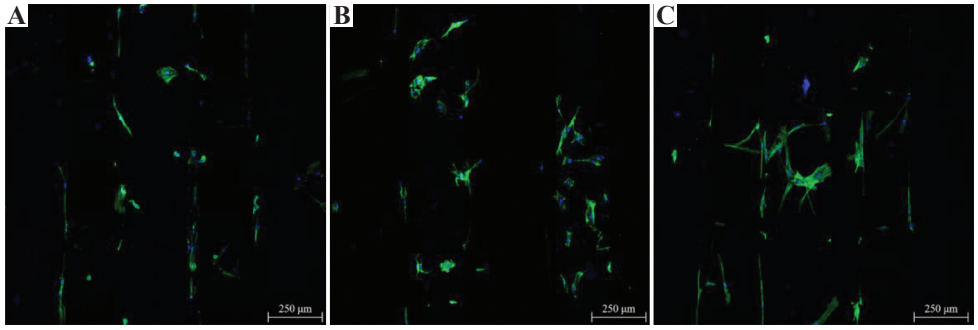

Figure 5. Confocal microscopy images of cell-seeded scaffolds (A) poly(ε-caprolactone), (B) 3 wt.% graphene, and (C): 3 wt.% graphene oxide, 7 days after cell seeding.

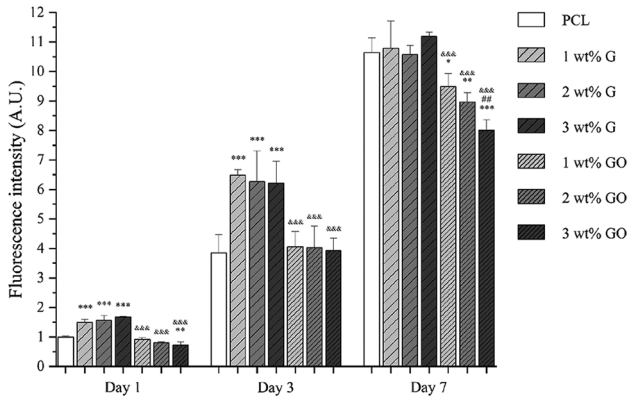

Figure 6. Cell viability/proliferation results 1, 3, and 7 days after cell seeding on different scaffolds (n = 5) (the fluorescence intensity of cell-seeded PCL scaffolds at day 1 was set as 1).

As observed, at day 1 and day 3 after cell seeding, PCL/G scaffolds show significantly higher fluorescence intensity than PCL scaffolds and PCL/GO scaffolds, but there is no statistical difference between the scaffolds with different filler contents. After 7 days of cell seeding, there is no statistical difference between PCL scaffolds and PCL/G scaffolds. However, in the case of PCL/GO scaffolds, the fluorescence intensity is significantly lower than PCL scaffolds and PCL/G scaffolds. Results seem to indicate that the fluorescence intensity decreases with the addition of GO content.

4 Conclusions

This paper investigates additively manufactured PCL, PCL/G, and PCL/GO scaffolds for bone repair applications. Printed scaffolds presented similar pore size and filament diameter as designed. Results show that PCL/G scaffolds present high compressive modulus and strength. The addition of GO reduces the WCA but after 7 days of cell seeding PCL/GO exhibit reduced cell metabolic activity than PCL and PCL/G scaffolds suggesting potential cytotoxicity effects particularly for high levels of GO. Results also show that both G and GO fillers can improve the surface wettability of the scaffolds, showing hydrophilicity. Moreover, from the biological evaluation, it was possible to observe that the G fillers promote cell attachment, viability, and proliferation while GO fillers reveal an opposite trend.

Acknowledgments

Author Weiguang Wang acknowledge the funding Rosetrees and Stoneygate Trust Young Enterprise Fellowship (Ref: A2750/M874) provided by Rosetrees Trust (charity number 298582) and Stoneygate Trust (charity number 1119976). This project has been also supported by the University of Manchester and the Engineering and Physical Sciences Research Council (EPSRC) of the UK, the Global Challenges Research Fund (GCRF), grant number EP/R01513/1.

Conflicts of interest

The authors declare that they have no conflicts of interest.

References

1. Langer R, Vacanti JP, 1993, Tissue Engineering. *Science*, 260:920–6.

2. Bártolo PJ, Almeida HA, Rezende RA, *et al*., 2008, Advanced Processes to Fabricate Scaffolds for Tissue Engineering. In: Virtual Prototyping and Bio Manufacturing in Medical Applications. Springer, Berlin, pp. 149–70. DOI: 10.1007/978-0-387-68831-2_8.
3. Feng P, Jia J, Peng S, *et al*., 2020, Graphene Oxide-driven Interfacial Coupling in Laser 3D Printed PEEK/PVA Scaffolds for Bone Regeneration. *Virtual Phys Prototyp*, 2020:1–16. DOI: 10.1080/17452759.2020.1719457.
4. Lee JM, Ng WL, Yeong WY. 2019, Resolution and Shape in Bioprinting: Strategizing Towards Complex Tissue and Organ Printing. *Appl Phys Rev*, 6:011307. DOI: 10.1063/1.5053909.
5. Shuai C, Yang W, Peng S, *et al*., 2018, Physical Stimulations and Their Osteogenesis-Inducing Mechanisms. 2018:1–4. DOI: 10.18063/ijb.v4i2.138.
6. Lai Y, Li Y, Cao H, *et al*., 2019, Osteogenic Magnesium Incorporated into PLGA/TCP Porous Scaffold by 3D Printing for Repairing Challenging Bone Defect. *Biomaterials*, 197:207–19. DOI: 10.1016/j.biomaterials.2019.01.013.
7. Paris JL, Lafuente-Gómez N, Cabañas MV, *et al*., 2019, Fabrication of a Nanoparticle-containing 3D Porous Bone Scaffold with Proangiogenic and Antibacterial Properties. *Acta Biomater*, 86:441–9. DOI: 10.1016/j.actbio.2019.01.013.
8. Liu D, Nie W, Li D, *et al*., 2019, 3D Printed PCL/SrHA Scaffold for Enhanced Bone Regeneration. *Chem Eng J*, 362:269–79. DOI: 10.1016/j.cej.2019.01.015.
9. Harun WS, Kamariah MS, Muhamad N, *et al*., 2018, A Review of Powder Additive Manufacturing Processes for Metallic Biomaterials. *Powder Technol*, 327:128–51. DOI: 10.1016/j.powtec.2017.12.058.
10. Wu H, Fahy WP, Kim S, *et al*., 2020, Recent Developments in Polymers/polymer Nanocomposites for Additive Manufacturing. *Prog Mater Sci*, 111:100638. DOI: 10.1016/j.pmatsci.2020.100638.
11. An J, Teoh JE, Suntornnond R, *et al*., 2015, Design and 3D Printing of Scaffolds and Tissues. *Eng Proc*, 1:261–8. DOI: 10.15302/j-eng-2015061.
12. Domingos M, Chiellini F, Cometa S, *et al*., 2020, Evaluation of *in vitro* Degradation of PCL Scaffolds Fabricated via BioExtrusion. Part 1: Influence of the Degradation Environment. *Virtual Phys Prototyp*, 5:65–73. DOI: 10.1080/17452751003769440.
13. Domingos M, Chiellini F, Cometa S, *et al*., 2011, Evaluation of *in vitro* Degradation of PCL Scaffolds Fabricated via BioExtrusion Part 2: Influence of Pore Size and Geometry. *Virtual Phys Prototyp*, *6*, 157-165. DOI: 10.1080/17452751003769440.
14. Liu F, Vyas C, Poologasundarampillai G, *et al*., 2018, Structural Evolution of PCL during Melt Extrusion 3D Printing. *Macromol Mater Eng*, 303:1700494. DOI: 10.1002/mame.201700494.
15. Liu F, Vyas C, Poologasundarampillai G, *et al*., 2018, Process-Driven Microstructure Control in Melt-Extrusion-Based 3D Printing for Tailorable Mechanical Properties in a Polycaprolactone Filament. *Macromol Mater Eng*, 303:1800173. DOI: 10.1002/mame.201800173.
16. Liu F, Wang W, Mirihanage W, *et al*. 2018, A Plasma-assisted Bioextrusion System for Tissue Engineering. *Cirp Ann Manufact Technol*, 67:229–32. DOI: 10.1016/j.cirp.2018.04.077.
17. Wang WG, Caetano G, Ambler WS, *et al*., 2016, Enhancing the Hydrophilicity and Cell Attachment of 3D Printed PCL/Graphene Scaffolds for Bone Tissue Engineering. *Materials*, 9(12):992. DOI: 10.3390/ma9120992.
18. Wibowo A, Vyas C, Cooper G, *et al*., 2020, 3D Printing of Polycaprolactone Polyaniline Electroactive Scaffolds for Bone Tissue Engineering. *Materials*, 13:512. DOI: 10.3390/ma13030512.
19. Wang W, Junior JR, Nalesso PR, *et al*., 2019, Engineered 3D Printed poly(ε-caprolactone)/Graphene Scaffolds for Bone Tissue Engineering. *Mater Sci Eng C*, 100:759–70. DOI: 10.1016/j.msec.2019.03.047.
20. Wang WG, Huang BY, Byun JJ, *et al*., 2019, Assessment of PCL/Carbon Material Scaffolds for Bone Regeneration. *J Mech Behav Biomed Mater*, 93:52–60. DOI: 10.1016/j.jmbbm.2019.01.020.
21. Cooper DR, D'Anjou B, Ghattamaneni N, *et al*., 2012, Experimental Review of Graphene. *ISRN Condensed Matter Phys*, 2012:56. DOI: 10.5402/2012/501686.
22. Wang W, Caetano GF, Chiang WH, *et al*., 2016, Morphological, Mechanical and Biological Assessment of PCL/Pristine Graphene Scaffolds for Bone Regeneration. *Int J Bioprint*, 2:95–104. DOI: 10.18063/ijb.2016.02.009.
23. Caetano GF, Wang W, Chiang WH, *et al*., 2018, 3D-Printed Poly(ε-caprolactone)/Graphene Scaffolds Activated with P1-Latex Protein for Bone Regeneration. *3d Print Addit Manuf*, 5:127–37. DOI: 10.1089/3dp.2018.0012.correx.
24. Huang B, Vyas C, Roberts I, *et al*., 2019, Fabrication and Characterisation of 3D Printed MWCNT Composite Porous Scaffolds for Bone Regeneration. *Mater Sci Eng C*, 98:266–78. DOI: 10.1016/j.msec.2018.12.100.
25. Huang B, Vyas C, Byun JJ, *et al*., 2020, Aligned Multi-walled Carbon Nanotubes with Nanohydroxyapatite in a 3D Printed Polycaprolactone Scaffold Stimulates Osteogenic

Differentiation. *Mater Sci Eng C*, 108:110374. DOI: 10.1016/j.msec.2019.110374.

26. Dreyer DR, Park S, Bielawski CW, *et al*., 2010, The Chemistry of Graphene Oxide. *Chem Soc Rev*, 39:228–40.
27. Sivashankari PR, Prabaharan M, 2020, Three-dimensional Porous Scaffolds based on Agarose/chitosan/graphene Oxide Composite for Tissue Engineering. *Int J Biol Macromol*, 146:222–31. DOI: 10.1016/j.ijbiomac.2019.12.219.
28. Saravanan S, Vimalraj S, Anuradha D, 2018, Chitosan Based Thermoresponsive Hydrogel Containing Graphene Oxide for Bone Tissue Repair. *Biomed Pharmacother*, 107:908–17. DOI: 10.1016/j.biopha.2018.08.072.
29. Zhang J, Zhu S, Song K, *et al*., 2020, 3D Reduced Graphene Oxide Hybrid Nano-copper Scaffolds with a High Antibacterial Performance. *Mater Lett*, 267:127527. DOI: 10.1016/j.matlet.2020.127527.
30. Min Lj, Leong SS, Miaomiao Z, Yee WY, 2018, 3D Bioprinting Processes: A Perspective on Classification and Terminology. *Int J Bioprint*, 4:151.
31. ASTM International, 2016, Standard Test Method for Compressive Properties of Rigid Cellular Plastics. ASTM International, West Conshohocken, PA.
32. ASTM International, 2015, Standard Test Method for Compressive Properties of Rigid Plastics. ASTM International, West Conshohocken, PA.
33. Ahmed SA, Gogal RM Jr., Walsh JE, 1994, A New Rapid and Simple Non-radioactive Assay to Monitor and Determine the Proliferation of Lymphocytes: An Alternative to [3H] thymidine Incorporation Assay. *J Immunol Methods*, 170:211–24. DOI: 10.1016/0022-1759(94)90396-4.
34. Ramazani S, Karimi M. 2015, Aligned Poly(ε-caprolactone)/ Graphene Oxide and Reduced Graphene Oxide Nanocomposite Nanofibers: Morphological, Mechanical and Structural Properties. *Mater Sci Eng C*, 56:325–34. DOI: 10.1016/j.msec.2015.06.045.
35. Thomson RC, Yaszemski MJ, Powers JM, *et al*., 1996, Fabrication of Biodegradable Polymer Scaffolds to Engineer Trabecular Bone. *J Biomater Sci Polym Ed*, 7:23–38. DOI: 10.1163/156856295x00805.
36. Williams JM, Adewunmi A, Schek RM, *et al*., 2005, Bone Tissue Engineering Using Polycaprolactone Scaffolds Fabricated via Selective Laser Sintering. *Biomaterials*, 26:4817–27. DOI: 10.1016/j.biomaterials.2004.11.057.
37. Porter BD, Oldham JB, He LS, *et al*., 2000, Mechanical Properties of a Biodegradable Bone Regeneration Scaffold. *J Biomech Eng*, 122:286–8. DOI: 10.1115/1.429659.
38. Lotz JC, Gerhart TN, Hayes WC, 1990, Mechanical Properties of Trabecular Bone from the Proximal Femur: A Quantitative CT Study. *J Comput Assist Tomogr*, 14:107–14. DOI: 10.1097/00004728-199001000-00020.

ORIGINAL ARTICLE

Customized Fabrication Approach for Hypertrophic Scar Treatment: 3D Printed Fabric Silicone Composite

Lung Chow[1], Kit-Lun Yick[1]*, Mei-Ying Kwan[1], Chun-Fai Yuen[2], Sun-Pui Ng[3], Annie Yu[4], Joanne Yip[1]

[1]Institute of Textiles and Clothing, The Hong Kong Polytechnic University, Hong Kong

[2]University Research Facility in 3D Printing, The Hong Kong Polytechnic University, Hong Kong

[3]Division of Science, Engineering and Health Studies, College of Professional and Continuing Education, The Hong Kong Polytechnic University, Hong Kong

[4]Department of Advanced Fibro Science, Kyoto Institute of Technology, Japan

Abstract: Hypertrophic scars (HS) are considered to be the greatest unmet challenge in wound and burn rehabilitation. The most common treatment for HS is pressure therapy, but pressure garments may not be able to exert adequate pressure onto HS due to the complexity of the human body. However, the development of three-dimensional (3D) scanning and direct digital manufacturing technologies has facilitated the customized placement of additively manufactured silicone gel onto fabric as a component of the pressure therapy garment. This study provides an introduction on a novel and customized fabrication approach to treat HS and discusses the mechanical properties of 3D printed fabric reinforced with a silicone composite. For further demonstration of the suggested HS therapy with customized silicone insert, silicone inserts for the finger webs and HS were additively manufactured onto the fabric. Through the pressure evaluation by Pliance X system, it proved that silicone insert increases the pressure exerted to the HS. Moreover, the mechanical properties of the additively manufactured fabric silicone composites were characterized. The findings suggest that as compared with single viscosity print materials, the adhesive force of the additively manufactured silicone and fabric showed a remarkable improvement of 600% when print materials with different viscosities were applied onto elevated fabric.

Keywords: Three-dimensional printing, Soft material, Textile fabric, Pressure therapy, Hypertrophic scars

***Corresponding Author:** Kit-Lun Yick, Institute of Textiles and Clothing, The Hong Kong Polytechnic University, Hong Kong; tcyick@polyu.edu.hk

Received: February 21, 2020; ***Accepted:*** April 01, 2020; ***Published Online:*** April 24, 2020

Citation: Chow L, Yick KL, Kwan MY, *et al*., 2020, Customized Fabrication Approach for Hypertrophic Scar Treatment: 3D Printed Fabric Silicone Composite, *Int J Bioprint*, 6(2):262. DOI: 10.18063/ijb.v6i2.262.

1 Introduction

Additive manufacturing, which is known as three-dimensional (3D) printing or rapid prototyping, has been widely adopted in the medical field for fabricating implants, orthoses, and prostheses over the past decade. Recently, the development of 3D printing of flexible and stretchable materials using direct ink writing (DIW) in which the printer extrudes materials out of nozzles have created novel applications in clinical research areas. For example, Zhou *et al*.[1] had produced 3D printed silicone prosthetic noses using DIW and Ahmad Fozi *et al*.[2] had proposed customized silicone facial padding for the hypertrophic scar (HS) management of burn patients using additive manufacturing. The prescribed silicone facial padding takes into consideration patient specific anatomic features which can then exert adequate pressure distribution onto the face, thus improving

scar control for optimum treatment efficacy. Apart from that, Unkovskiy *et al*.[3] also developed a silicone facial prosthesis for rehabilitation treatment based on the direct digital manufacturing (DDM) technique which uses additive manufacturing technologies. DDM is characterized by flexible and lean production process which do not require injection and mold making process[4,5]. It is evident that personalized products can be more readily produced with the use of additive manufacturing to cater to each individual patient based on his/her conditions and needs.

HS is considered to be the greatest unmet challenge in wound and burn rehabilitation. HS is an abnormality in which the epidermis is greatly thickened and collagen is irregularly deposited[6]. As a result, the injured area is thickened, raised, and erythematous in appearance which tremendously affect the quality of life[7]. Apart from cosmetic impairment, functional sequelae can also occur[8]. HS tissue has less elasticity than normal skin tissue, and subsequently, the range of motion of the joints can be limited[9]. The skin is the primary interface between humans and the environment, and therefore is more prone to injury. The most frequent sites for burns in human body part are hand, and when the skin of the hand receives a burn injury and an HS is formed, the range of motion of the fingers decreases[10]. Although the mechanism of treatment process for scars is not well understood, some of the most common rehabilitation treatments for HS in the past decade are the use of pressure therapy and silicone gel sheets[11,12]. Silicone (polysiloxane) is the representative material used for treating HS and has a flexible structure of a backbone chain with alternating oxygen and silicon atoms[13]. Back in early 1980s, Perkins and Davey[14] first suggested the potential of using silicone sheets for treating burn scars. A few years later, silicone in scar treatment was adopted and tested by different researchers[15,16]. The mechanisms of silicone therapy in scars treatment have been suggested by different researchers and the possible suggested effects of silicone include increased skin temperature, hydration of scars, and polarization of scar tissue[17-21]. In practice, pressure therapy is typically used to treat burn victims by providing a continuous pressure of about 25 mmHg to inhibit the growth of HS and encourage its maturation through pressure garments, face masks, casts, splints, or conformers[22-26]. However, the human body has a complex geometry, which means that the pressure exerted onto certain anatomical parts with a concave surface cannot properly inhibits the growth of HS[27]. Therefore, a variety of different materials such as thermal plastic, silicone sheets, or hydrogels are inserted between the skin and the pressure garment to exert adequate pressure onto different body parts and in the case of HS, induce extra pressure onto the scar for effective treatment[17,28]. However, these additional inserted materials like silicone sheets are usually larger in size than the HS[17]. The unnecessary pressure and coverage will cause excessive sweating, pruritus or even contact dermatitis of the healthy skin next to the HS[17,29]. Another limitation of pressure therapy is material deterioration with gradual loss of pressure with use. During the application of pressure therapy, repeated joint movements stretch the pressure therapy garment which reduces the elasticity of the fabric[30]. As a result, the pressure therapy garment has to be replaced or adjusted after a period of time to ensure adequate pressure performance and effectively treat HS to facilitate recovery. To improve the treatment process, different types of therapies can be collectively applied at the same time[31]. Li-Tsang *et al*.[32] concluded that the integration of pressure and silicone gel sheeting therapy has a positive and better effect in reducing scar thickness than the conventional use of pressure garments.

In this study, we propose an innovative and customized fabrication approach with the use of 3D scanning and DDM of silicone technology. Medical-grade silicone is extruded through a nozzle directly onto the fabric based on 3D scanned data to provide an accurately sized insertion material which would optimize the pressure delivery. Hence, adequate pressure is induced onto the HS by the printed silicone gel with the benefit of silicone treatment while the individual variations of the anatomical features are also taken into consideration. This combined therapy which integrates pressure and

silicone sheet therapy provides a more effective result in reducing the scar thickness. Since the amount of pressure induced by a pressure garment also depends on the mechanical properties of the fabric, the influence of 3D printed silicone gel on the mechanical behavior and tension decay after repeated extensions of the warp-knitted fabric used for pressure therapy garments was also determined to provide new insights into the wider application of 3D printing, such as clinical applications, flexible electronics and wearable products, and development of soft robotics and actuators.

2 Materials and methods

2.1 3D modeling and fabrication

The geometry of the hands of a patient with HS was obtained using a structured light handheld 3D scanner (Artec Eva, Luxembourg). After scanning was completed, the scanned images were registered using Artec Studio 13. The registered point cloud data were then imported into processing software (Materialise Magics) and converted into 3D mesh models for the fabrication process. The models for printing were based on the amount of redness and protrusion of the HS and point cloud data. After obtaining the desired models, the model meshes and coordinates were adjusted with reference to the required orientation and dimensions of silicone gel, as well as the method of garment prototyping before the fabrication process took place.

Warp knitted fabric made of a blend of nylon (83%) and spandex (17%) with a total weight of 165 g/m^2 and 0.226 mm in thickness, which is the typical type of fabric used for pressure therapy garment, was applied as the reinforcement of the composite. In consideration of the adhesion of the fabric and printed silicone gel, two print mixtures with two different viscosities were prepared. A biocompatible silicone elastomer (SILBIONE® RTV 4410 1:1 A and B) was mixed with 0.2 and 2 wt% of a silicone thickener (THI-VEX™), respectively, and degassed for 3D printing onto the fabric. The 3D printing was carried out using a 3D-printer (3D-Bioplotter® Manufacturer Series) and the settings and printing toolpaths are shown in **Table 1** and **Figure 1,** respectively.

To characterize the mechanical properties of the printed composite, the samples were additively manufactured at 20 × 100 × 2.24 mm for cyclic tensile testing, the size stated in ASTM D5169 Standard Test Method for Shear Strength (Dynamic Method) of Hook and Loop Touch Fasteners and ASTM D638-14 Standard Test Method for Tensile Properties of Plastics (Type V specimens) to test the adhesive force and tensile properties, respectively. The adhesive behavior of three different samples was evaluated. The 3D printing parameters of the samples are listed in **Table 2**. Note that, pigment was added into the print mixture for visualization and surface morphology investigation purposes, and no pigment was added to the samples for the mechanical characterization. Furthermore, the surface morphology of the ASTM D5169 samples was observed using an optical microscope.

Table 1. Parameters of different print mixtures of 3D-Printing process.

Print mixture	SILBIONE® RTV 4410 1:1 A and B+0/0.2/.2.0 wt% THI-VEXTM
Nozzle diameter (mm)	0.4
Printing speed (mm/s)	20
Build Platform temperature (°C)	70
Head temperature (°C)	0
Path width (mm)	~0.6
Inner structure pattern(°)	0,90

3D: Three-dimensional

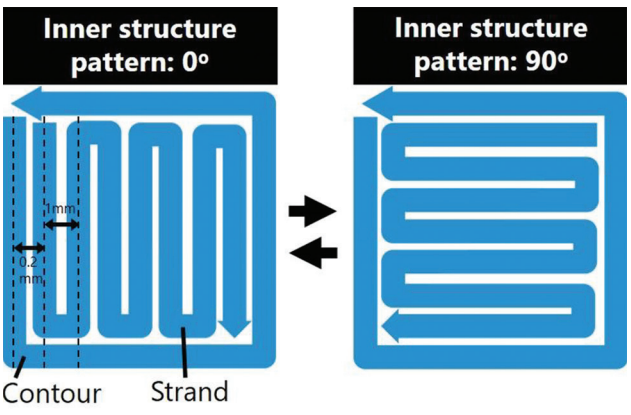

Figure 1. 3D printing toolpath.

Table 2. 3D printing parameters of the test samples.

Testing	ASTM D5169			Cyclic tensile testing	ASTM D638-14 Type V	
Sample code	0.2 wt%_ Thickener_0.4 mm	0.2 wt%_ Thickener	2 wt%_Thickener	Fabric silicone composite	Silicone	Fabric silicone composite
Print mixture for the first layer	SILBIONE® RTV 4410 1:1 A and B+0.2 wt% THI-VEX™		SILBIONE® RTV 4410 1:1 A and B+2 wt% THI-VEX™	SILBIONE® RTV 4410 1:1 A and B+0.2 wt% THI-VEX™	SILBIONE® RTV 4410 1:1 A and B+2 wt% THI-VEX™	SILBIONE® RTV 4410 1:1 A and B+0.2 wt% THI-VEX™
Print mixture for the others layer	SILBIONE®+2 wt% THI-VEX™					
Distance between the build platform and fabric (mm)	0.4	0 (Direct contact)	0 (Direct contact)	0.4	0 (Direct contact)	0.4
No. of layer	10	10	10	8	3	3
No. of sample	5	5	5	1	1	1

3D: Three-dimensional

2.2 Mechanical characterization

The tensile properties of the fabricated composite and silicone gel were determined using the Instron 5566 universal mechanical test frame in accordance with ASTM D638-14 (Type V specimen) at a speed of 100 mm/min. The viscosity of silicone print mixtures with different concentration of thickener was tested by a rotational viscosity meter at 0°C. The adhesion between the printed silicone and fabric was tested in accordance with ASTM D5169 at a speed of 305 mm/min. The dynamic stress-strain behavior of the composite with repeated extension and recovery cycles was measured to determine the loss of fabric tension which would result in pressure degradation. A total of 3000 tensile cycles were carried out with the Instron 5566 for the fabric and fabric silicone composite samples, and the tensile values were recorded. The parameters were a strain of 50%, gauge length of 40 mm, and speed of 500 mm/min.

2.3 Pressure garment production and pressure characterization

The patterns of pressure garment were developed based on the scanned hand geometry data and three reduction factors (namely, 0, 10%, and 20% reduction in the width of the patterns), respectively. A total of six pressure garments were custom-made and their corresponding amount of pressure dosage applied onto the HS with or absence of silicone insert was measured and analyzed. The fabric applied was same as the one for silicone composite printing.

The exerted pressure to HS was evaluated by NOVEL Pliance X system. The sensor was inserted between the pressure garment and the skin while the hand was kept in a static relax position on a table for 20 s for static pressure recording.

3 Results and discussion

3.1 Scanned geometry and structure of fabricated composites

First, the models for 3D printing (**Figure 2A** and **B**) were created based on the 3D- scanned geometry of the hand to allow optimum fit of the insertion

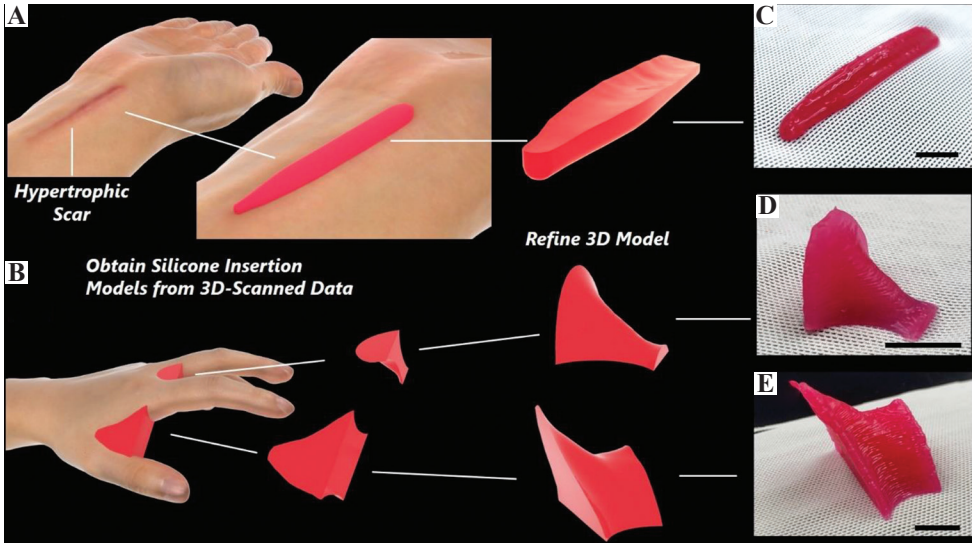

Figure 2. Schematic of workflow and production process of additively manufactured silicone inserts: Three-dimensional (3D) scanned geometry of (A) hypertrophic scars (HS) with refined insertion models and (B) hand with refined web insertion models. Photo of 3D printed: (C) Insertion for the HS; (D) and (E) web insertion for webspace between second and third digits; Scale bar: 10 mm.

materials. After that, the 3D models were refined, and the model orientation was adjusted for printing. Finally, the 3D models were imported into the 3D-printer (3D-Bioplotter® Manufacturer Series) for the additive manufacturing process. **Figure 2C-E** is the photo of the silicone inserts which can function as orthoses to prevent web space contractures during therapy[17,33]. When comparing the traditional manual insert material production and the 3D printing process, the 3D printing production process minimizes human errors in orthosis design and achieves a reliable and repeatable geometry of inserts. Once the silicone insert was 3D printed on fabric, it could be sewn as a part of the pressure garment to increase pressure onto the specific body region and prevent the distal migration of scars. For silicone gel sheet therapy, the planar shape of silicone gel sheet is usually larger than the size of HS regardless of the 3D body shapes and curvatures, thus leading to displacements, ill-fitting, and discomfort during the treatment, **Figure 3A** and **B**. When comparing with silicone gel sheet therapy, the accurate geometric shape of the printed silicone inserts prevents negative impacts such as excessive sweating, pruritus, and contact dermatitis of the healthy skin next to the HS, **Figure 3C**. Moreover, the silicone inserts can administer the right amount of pressure at the interface between the scar and garment for effective scar reduction by combining and reinforcing the pressure, hydration, and static electricity stimulation together[17].

3.2 Mechanical performance of fabricated composites

3.2.1 Adhesion force

To achieve an additive manufactured product with high resolution, a print silicone mixture with high viscosity needs to be used. However, high viscosity silicone mixtures do not easily diffuse through fabric; hence, resulted in poor shear strength of the 3D printed silicone and fabric. To prevent the pressure garment fabric and 3D printed silicone inserts from separating during wearing, a multi-material printing approach was adopted to improve the force of the adhesion. The schematic of this approach is shown in **Figure 4**. During the printing process, a lower viscosity (around 7400 Mpa·s) silicone mixture was used in the first printed layer, while a higher viscosity (around 1,080,000 Mpa·s) silicone mixture was used in the other printed layers. The viscosity curve of the silicone print mixtures with different thickener contents at 0°C, which is the temperature of the print head, as a

Figure 3. Differences between the suggested hypertrophic scars (HS) treatment with customized silicone insert and traditional silicone gel sheet therapy: (A) Photograph of the HS; (B) Demonstration of tropical silicone gel sheet therapy; (C) Demonstration of suggested HS treatment with customized silicone insert.

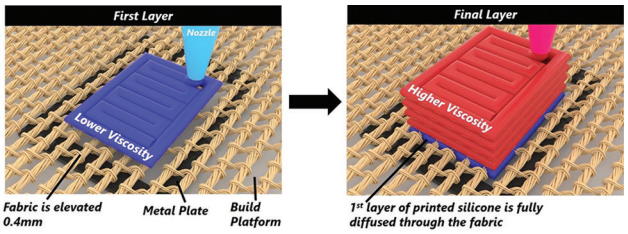

Figure 4. Schematic of multi-material approach on elevated fabric.

reference shown in **Figure 5A** for various materials printing on fabric. Theoretically, lower viscosity of print mixture is easier to diffuse through the fabric. However, too low viscosity print mixture may cause the undesirable diffusion and migration of the silicone mixture, adversely affecting the control of the printing process and the ultimate size and shape of the printed composite. **Figure 5B** and **C** shows the problem of extremely low viscosity print mixture during printing. The first layer of printed silicone mixture in **Figure 5B** without thickener which spread along the print platform before curing and causing improper size of printed material. Therefore, 0.2 wt% thickener was added to increase the viscosity of mixture from around 2300 to 7400 Mpa·s for the first layer of printing (**Figure 5C**). To further improve the adhesion between the fabric and silicone, a metal plate was placed between the fabric and the build platform that the fabric specimen was elevated to accommodate the deposition of silicone mixture. At the same time, the temperature of the build platform was set to 70ºC to facilitate the curing of the 3D printed silicone to create a stable base for the above layers.

The adhesion force of the samples was determined using ASTM D5169, which is used to examine the adhesion of 3D printed materials and textiles[34]. The schematic diagram of ASTM D5169 is shown in **Figure 5D**. Images of the 3D printing process of ASTM D5169 samples for mechanical characterization and the printed sample are shown in **Figure 5E** and **F**.

The maximum shearing force of the 0.2 wt%_ Thickener _0.4 mm elevated sample is around 60 N which is a 600% improvement in comparison to the result of 2 wt%_Thickener sample; **Figure 5G** and **H**. When comparing the 0.2 wt%_Thickener _0.4 mm and 0.2 wt%_Thickener samples, the elevation of fabric increases around 50% of maximum shearing force. To investigate the surface morphology of the samples, blue and red pigments were added to the print mixtures of the first and other layers, respectively. It is shown in **Figure 5Ii** and **Iii** that more of the silicone mixture has diffused through the fabric in 0.2 wt%_Thickener_0.4 mm sample when compared to 0.2 wt%_Thickener sample which demonstrates the effect of the elevating the layer of fabric. For the 0.2 wt%_Thickener_0.4 mm elevated sample, due to the elevation of fabric, extra capacity is provided for the diffusion of the silicone mixture. As a result, a sandwich structure composite was fabricated, which consists of two silicone outer skins and a fabric core structure. The sandwich structure of sample increases the contact surface area between the silicone and fabric and, at the same time, creates mechanical barriers that interlock the porous fabric. Consequently, the adhesive force of this sample is significantly higher since tearing of silicone is required to separate the silicone from the fabric. In contrast, the silicone mixture with high viscosity 2 wt%_Thickener sample did not diffuse through the fabric or absorbed by the yarn,

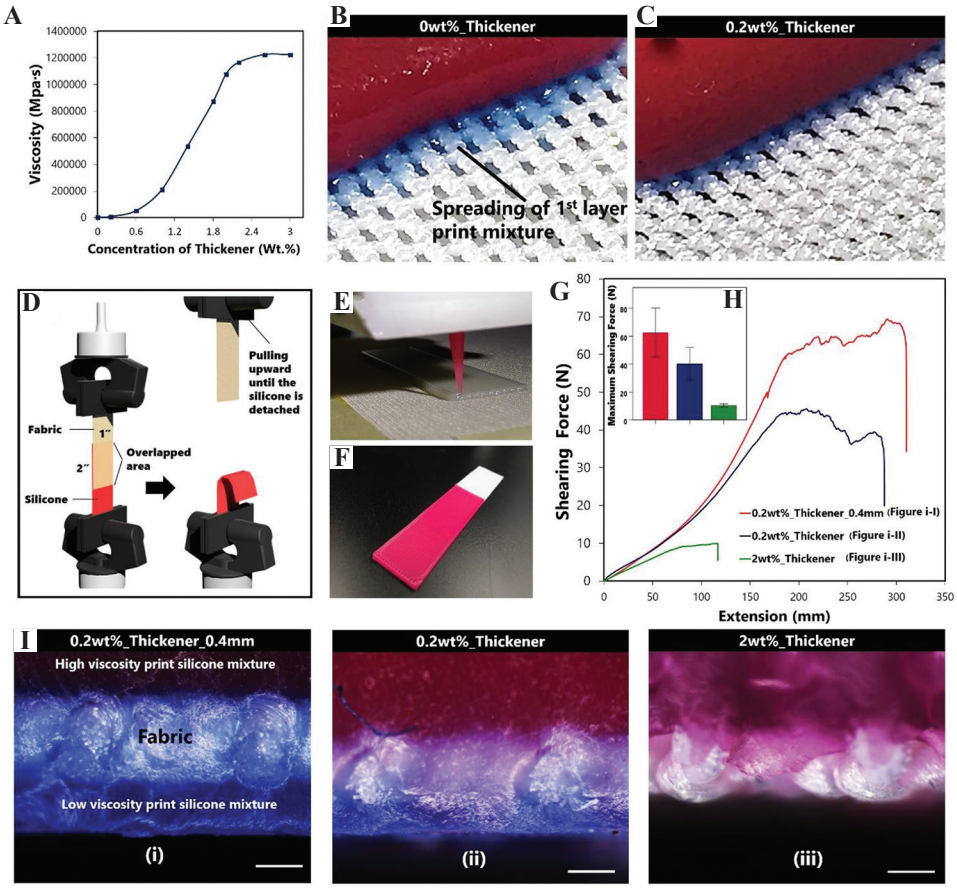

Figure 5. Investigation of adhesion of three-dimensional (3D) printed silicone on fabric: (A) Viscosity curve of the silicone print mixtures with different thickener contents; (B) and (C) demonstration of the problem of extremely low viscosity of print mixture for first layer printing, (D) schematic of ASTM D5169; (E) image of 3D printing process of ASTM D5169; (F) image of a ASTM D5169 sample; (G) plotted shearing forces versus extension; (H) maximum shearing force comparison; (I) cross-sectional observation of (i) 0.2 wt%_Thickener_0.4 mm sample, (ii) 0.2 wt%_Thickener sample, and (iii) 2 wt%_ Thickener sample; Scale bar: 200 μm.

as shown in **Figure 5Iiii**. Therefore, its shear strength is mainly contributed by the adhesion and friction of the silicone and fabric and result in much lower shearing strength than the other samples.

The proposed printing approach here shows a dramatic improvement of adhesion (600% in shear strength) between the fabric and silicone which demonstrates its potential for customizing any type of application, such as wearable electronics, soft robotics, engineered foot insoles, and orthotic bracewear.

Although the use of the proposed multi-material approach on elevated fabric improves the adhesion of the printed material and fabric, the size of the print model should be considered. As the fabric has high flexibility, the distance between the build platform and fabric can be reduced due to gravity, especially in the middle of the elevated area if a large print model is required. As a result, the adhesion between the fabric and silicone can be reduced. Furthermore, the shape of the model for printing can be affected due to the caving-in of the fabric.

3.2.2 Tensile properties

The durability of a material is a key element of pressure therapy because undependable materials

may create significant challenges when determining the pattern size of garments. Conventional materials for pressure therapy garments such as nylon/spandex blended warp knitted fabrics will deform and lose their elasticity, which reduce pressure delivery and the treatment effectiveness[30,35]. Silicone, however, has excellent resilience that the material is able to withstand repeated functional loading without dimensional changes[35]. The stress of the composite consists of the fabric and silicone is lower than the fabric itself due to the lower strength of the used silicone when comparing with the materials of fabric. **Figure 6A** is the comparison of tensile properties of the fabric and fabric silicone composite before and after 3000 cycles of tensile testing. In terms of the deformation and change in the Young's modulus, the fabric silicone composite showed less reduced tensile strength after 3000 cycles of testing. More

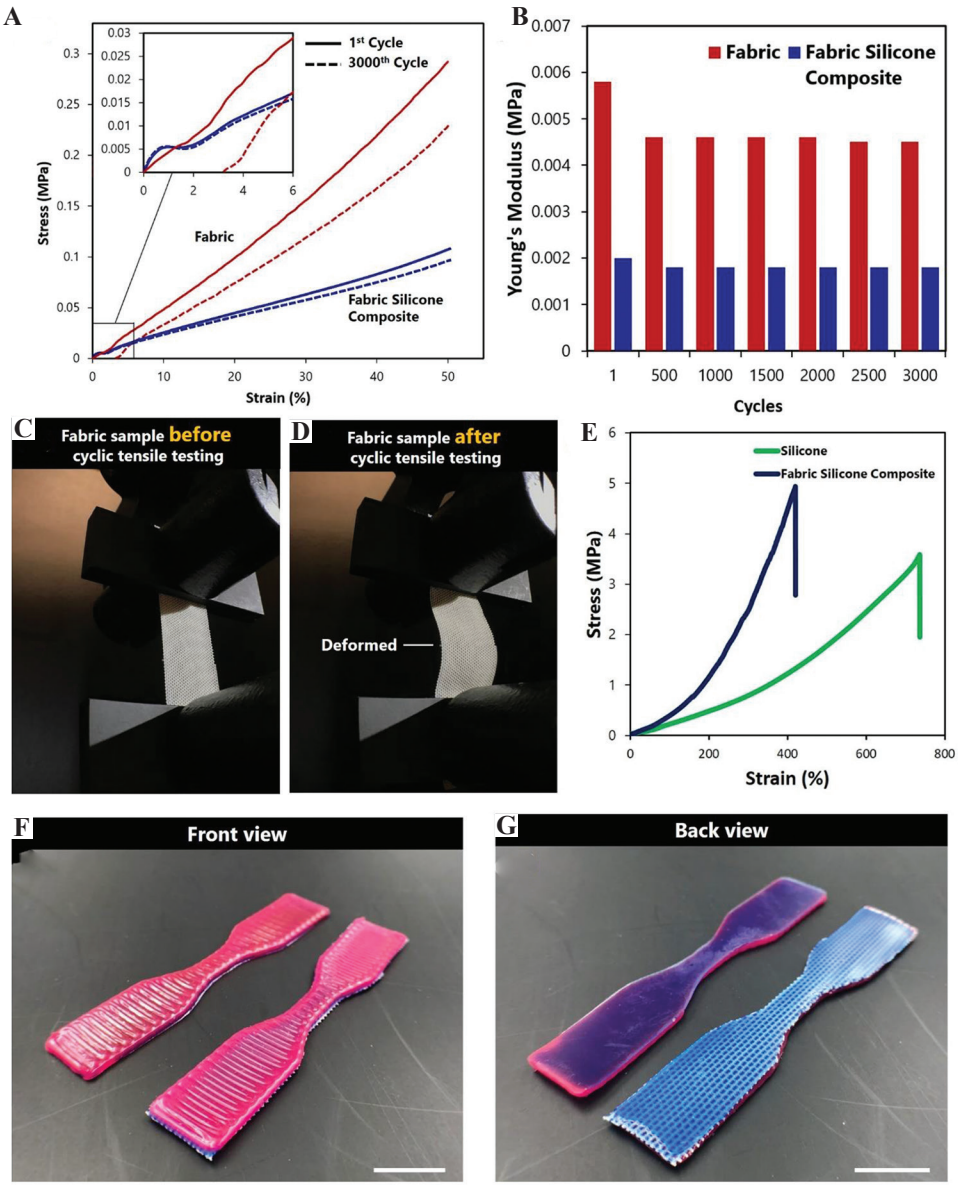

Figure 6. Investigation of deterioration of material and tensile properties: (A) Stress-strain curves of fabric and fabric silicone composite samples before and after cyclic tensile testing; (B) Young's modulus of fabric and fabric silicone composite samples; (C) and (D) fabric sample before and after cyclic tensile testing; (E) stress-strain curves of fabric and fabric silicone composite samples; (F) and (G) front and back view of ASTM D638 samples; scale bar: 10 mm.

detailed changes in the Young's modulus for every 500 cycles are shown in **Figure 6B**. The percentage of decline in the Young's modulus of the fabric silicone composite sample was 55% less than that of the fabric sample after 3000 cycles of testing. There was approximately 3% deformation that can be found in the fabric sample after 3000 cycles of testing while no deformation can be found for the fabric silicone composite. The images in **Figure 6C** and **D** show the deformation of the fabric after 3000 cycles of testing. The reason of the fabric deformation after tensile cycles could be explained by the friction between the fiber and yarn in the complex interlooping fabric structure. When the tensile force is applied onto the fabric, the fabric is extended and the loop is deformed in the vertical direction. Once the force is released, the yarn and fiber fail to recover to their original shapes due to the high friction induced by the large contact surface area between the fibers and yarns. The experimental result evidently proved that the fabricated fabric silicone composite has a better durability in shape recovery and mechanical properties after extension and recovery since the silicone matrix stabilizes the structure of the fabric which results in higher elasticity. As a result, the pressure garment is able to exert adequate pressure onto the skin of patients during wear to provide better pressure therapy treatment. Apart from material fatigue, we have also shown the tensile properties of the fabric silicone composite and silicone samples using ASTM D638; **Figure 6E**. The fabricated samples are shown in **Figure 6F** and **G**. The fabric reinforcement approach improved the strength of the 3D printed silicone. Our example shows the means of modifying the mechanical behavior of 3D printed soft material using a fabric reinforcement method in a flexible way. Another advantage of the fabric reinforcement

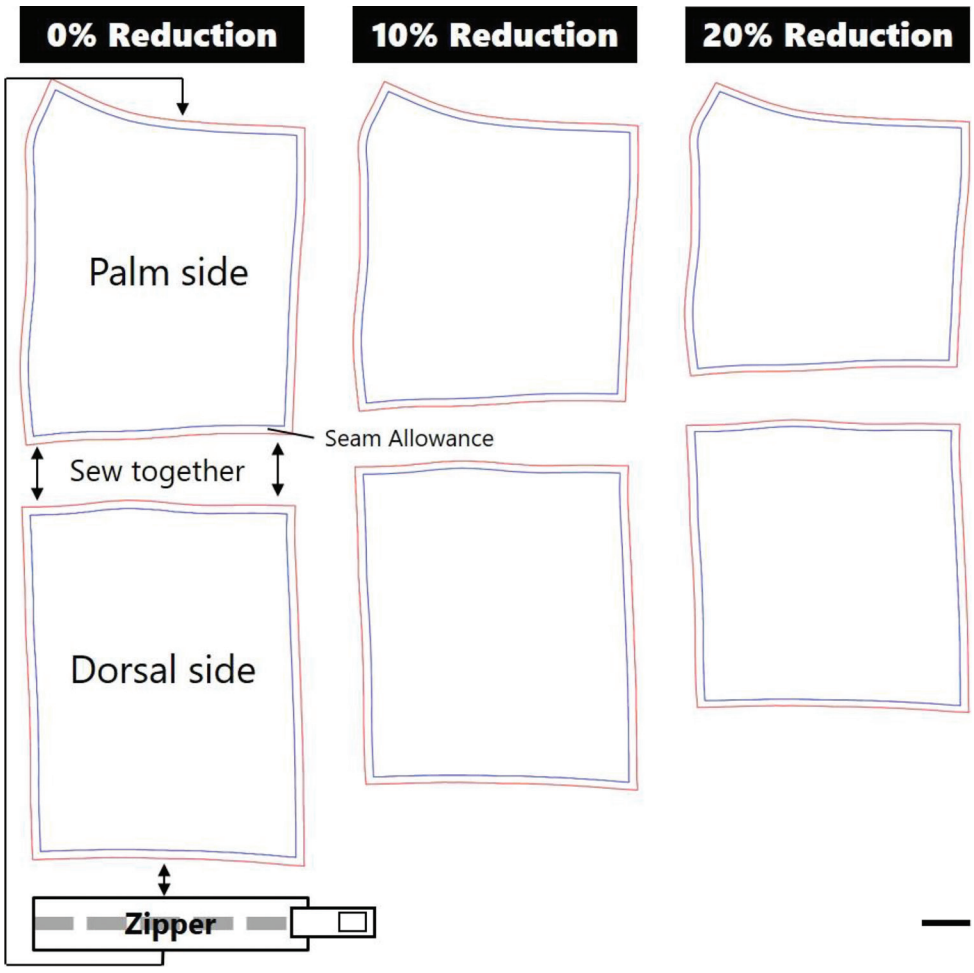

Figure 7. Patterns of the pressure garment and the assembly method; scale bar: 10 mm.

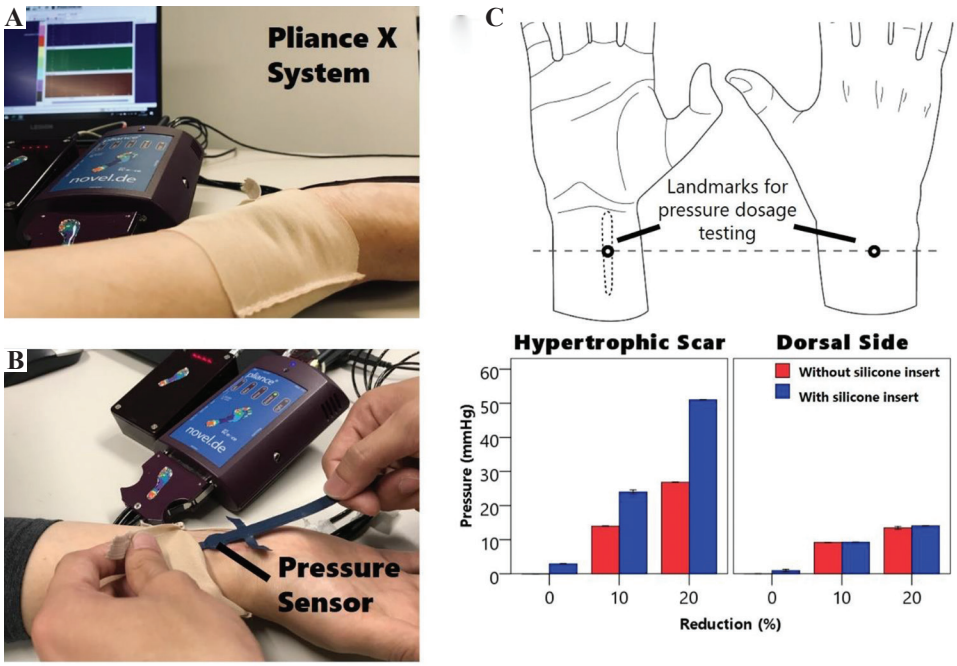

Figure 8. Pressure dosage evaluation by Pliance X System: (A) The overview and setup of Pliance X System; (B) insertion of the pressure sensor between the hypertrophic scars and pressure garment; (C) the differences of pressure dosage between traditional pressure therapy and the suggested customized silicone insert pressure therapy.

approach is that sewing of soft material can be realized due to the core fabric structure. The reinforced soft material can be stitched with various materials such as smart and shape memory materials, or optical fibers which are convenient for developing smart textiles, and wearable and electronic devices.

3.3 Effect of silicone insert on pressure delivery

Figure 7 shows the patterns of the pressure garment in different reduction factors and the assembly method. In our study, the NOVEL Pliance X system was adopted for measuring the interface pressure generated by the pressure garment which had been evaluated and validated for accuracy by different researchers[36,37]. The system was characterized by the slim size of sensor which is <10 mm in diameter and 1 mm in thickness. **Figure 8A** shows the overview of Pliance X system and **Figure 8B** demonstrates the process of inserting the sensor between the pressure garment and the HS. Due to the tiny size of the sensor, it can be inserted under the pressure garment easily. The landmarks for pressure dosage testing and the result can be referred to **Figure 8C**. The result clearly proved the silicone insert can specifically increase the interfacial pressure between the insert and the HS in all garment size (reduction) conditions, while its influence of pressure on other body regions (dorsal side) was somewhat subtle. The result indicates that 10% size reduced garment with silicone insert could exert around 25 mmHg pressure to the HS to encourage their maturation and inhibit their growth. Although the 20% size reduced garment could also exert around 25 mmHg pressure to the HS, the patients had major difficulties to put on the garment and fasten the zipper which may adversely affect the practical use of pressure garment with high risk of injuries to the skin. It may induce excessive pressures onto the healthy skin, leading to limitations of movements and discomfort to the patient. In this study, the integrated 3D printed silicone insert and pressure therapy can exert the specific and adequate amount of pressure onto different body parts to effectively treat HS, thus benefiting burn patients toward a quicker recovery.

4 Conclusion

In this study, we have introduced an innovative and customized fabrication approach for HS treatment by utilizing 3D scanning and DDM of silicone technology. The 3D printed fabric silicone composite is customized based on the geometry of the HS and hand obtained from a 3D scanning process, and as a component of a pressure therapy garment. To demonstrate the application of DDM of silicone technology to pressure therapy gloves, inserts for the finger webs and HS have been additively manufactured.

The results of the mechanical characterization show that our new additively manufactured fabric silicone composite is less likely to deform with better durability as opposed to the conventional warp knitted fabric used for pressure therapy garments that experiences a gradual loss of fabric tension and pressure after repeated wear. Through the pressure characterization, the result also indicates our suggested that HS therapy can effectively and specifically exert adequate pressure to the scar location, while preserving the wearing comfort of non-scar body parts.

It is anticipated that the approach proposed in this study would not be limited to pressure garment therapy but opens up another means of customization where products can be designed for specific purposes with individual variations such as anatomically engineered foot insoles and orthotic bracewear. The experimental results also demonstrate the possibility of modifying the mechanical behavior of 3D printed soft material using the fabric reinforcement approach which creates new insights for clinical applications, flexible electronics, and wearable products, as well as in the development of soft robotics and actuators.

Acknowledgments

We acknowledge financial support from the Research Grant Council for funding this research project through project account PolyU 152097/18E and technical support from the University Research Facility in 3D Printing (U3DP).

Disclosure statement

No potential conflicts of interest were reported by the authors.

References

1. Zhou L, Gao Q, Fu J, *et al.*, 2019, Multi-Material 3D Printing of Highly Stretchable Silicone Elastomer. *ACS Appl Mater Interfaces*, 11(26):23573–83. DOI: 10.1021/acsami.9b04873.
2. Fozi MA, Salleh MN, Ismail KA, 2019, Development of 3D-printed Customized Facial Padding for Burn Patients. *Rapid Prototyp J*, 25(1):55–61. DOI: 10.1108/rpj-09-2017-0179.
3. Unkovskiy A, Spintzyk S, Brom J, *et al.*, 2018, Direct 3D Printing of Silicone Facial Prostheses: A Preliminary Experience in Digital Workflow. *J Prosthet Dent*, 120(2):303–8. DOI: 10.1016/j.prosdent.2017.11.007.
4. Gibson I, 2015, In: Rosen DW, Stucker B, editors. Additive Manufacturing Technologies: 3D Printing, Rapid Prototyping, and Direct Digital Manufacturing. 2nd ed. Springer, New York. DOI: 10.1007/978-1-4939-2113-3_16.
5. Bibb R, 2015, In: Dand E, Paterson A, editors. Medical Modelling: The Application of Advanced Design and Rapid Prototyping Techniques in Medicine. 2nd ed. Woodhead Publishing, Cambridge.
6. Li-Tsang CW, Feng B, Huang L, *et al.*, 2015, A Histological Study on the Effect of Pressure Therapy on the Activities of Myofibroblasts and Keratinocytes in Hypertrophic Scar Tissues After Burn. *Burns*, 41(5):1008–16. DOI: 10.1016/j.burns.2014.11.017.
7. Yu A, Yick KL, 2018, Compression and stretch fit garments. In: Engineering of High-Performance Textiles. Woodhead Publishing, Sawston, United Kingdom. pp. 279-303. DOI: 10.1016/b978-0-08-101273-4.00011-1.
8. Cho YS, Jeon JH, Hong A, *et al.*, 2014, The Effect of Burn Rehabilitation Massage Therapy on Hypertrophic Scar after Burn: A Randomized Controlled Trial. *Burns*, 40(8):1513–20. DOI: 10.1016/j.burns.2014.02.005.
9. Dewey WS, Richard RL, Parry IS, 2011, Positioning, Splinting, and Contracture Management. *Phys Med Rehabil Clin*, 22(2):229–47.
10. Kwan P, Hori K, Ding J, *et al.*, 2009, Scar and Contracture: Biological Principles. *Hand Clin*, 25(4):511–28. DOI: 10.1016/j.hcl.2009.06.007.
11. Carney BC, Liu Z, Alkhalil A, *et al.*, 2017, Elastin is Differentially Regulated by Pressure Therapy in a Porcine

Model of Hypertrophic Scar. *J Burn Care Res*, 38(1):28–35. DOI: 10.1097/bcr.0000000000000413.

12. Wei Y, Wang Y, Zhang M, *et al.*, 2018, The Application of 3D-printed Transparent Facemask for Facial Scar Management and its Biomechanical Rationale. *Burns*, 44(2):453–61. DOI: 10.1016/j.burns.2017.08.006.
13. Liravi Fand Toyserkani E, 2018, Additive manufacturing of silicone structures: A review and prospective. *Addit Manufact*, 24:232–42. DOI: 10.1016/j.addma.2018.10.002.
14. Perkins K, Davey R, Wallis K, 1983, Silicone Gel: A New Treatment for Burn Scars and Contractures. *Burns*, 9(3):201–4. DOI: 10.1016/0305-4179(83)90039-6.
15. Mercer NGS, 1989, Silicone Gel in the Treatment of Keloid Scars. *Plast Surg Nurs*, 9(4):162.
16. Quinn K, Evans J, Courtney J, *et al.*, 1985, Non-pressure Treatment of Hypertrophic Scars. *Burns*, 12(2):102–8. DOI: 10.1016/0305-4179(85)90035-x.
17. Van den Kerckhove E, Stappaerts K, Boeckx W, *et al.*, 2001, Silicones in the Rehabilitation of Burns: A Review and Overview. *Burns*, 27(3):205–14. DOI: 10.1016/s0305-4179(00)00102-9.
18. Gilman TH, 2003, Silicone Sheet for Treatment and Prevention of Hypertrophic Scar: A New Proposal for the Mechanism of Efficacy. *Wound Repair Regen*, 11(3):235–6. DOI: 10.1046/j.1524-475x.2003.11313.x.
19. Ko WJ, Na YC, Suh BS, *et al.*, 2013, The Effects of Topical Agent (Kelo-cote or contractubex) Massage on the Thickness of Post-burn Scar Tissue Formed in Rats. *Arch Plast Surg*, 40(6):697–704. DOI: 10.5999/aps.2013.40.6.697.
20. Di Rocco G, Gentile A, Antonini A, *et al.*, 2011, Enhanced Healing of Diabetic Wounds by Topical Administration of Adipose Tissue-Derived Stromal Cells Overexpressing Stromal-Derived Factor-1: Biodistribution and Engraftment Analysis by Bioluminescent Imaging. *Stem Cells Int*, 2011:304562. DOI: 10.4061/2011/304562.
21. Berman B, Perez OA, Konda S, *et al.*, 2007, A Review of the Biologic Effects, Clinical Efficacy, and Safety of Silicone Elastomer Sheeting for Hypertrophic and Keloid Scar Treatment and Management. Malden, USA. pp. 1291–303. DOI: 10.1111/j.1524-4725.2007.33280.x.
22. Bosworth C, 2002, Burn Trauma: Management and Nursing Care. 2nd ed. Whurr, London.
23. Macintyre L, Gilmartin S, Rae M, 2007, The Impact of Design Variables and Aftercare Regime on the Long-term Performance of Pressure Garments. *J Burn Care Res*, 28(5):725–33. DOI: 10.1097/bcr.0b013e318148c999.
24. Leung P, Ng M, 1980, Pressure Treatment for Hypertrophic Scars Resulting from Burns. *Burns*, 6(4):244–50. DOI: 10.1016/s0305-4179(80)80007-6.
25. Rivers E, Strate R, Solem L, 1979, The Transparent Face Mask. *Am J Occup Ther*, 33(2):108–13.
26. Staley MJ, Richard RL, 1997, Use of Pressure to Treat Hypertrophic Burn Scars. *Adv Wound Care*, 10(3):44-6.
27. Yu A, Yick KL, Ng SP, *et al.*, 2016, Orthopaedic Textile Inserts for Pressure Treatment of Hypertrophic Scars. *Textile Res J*, 86(14):1549–62. DOI: 10.1177/0040517515573409.
28. Pendleton H, Schultz-Krohn W, 2018, Pedretti's Occupational Therapy: Practice Skills for Physical Dysfunction. 8th ed. Elsevier Health Sciences, Amsterdam, Netherlands.
29. Uslu AA, Sürücü AA, Korkmaz AM, *et al.*, 2019, Acquired Localized Hypertrichosis Following Pressure Garment and/or Silicone Therapy in Burn Patients. *Ann Plast Surg*, 82(2):158–61. DOI: 10.1097/sap.0000000000001686.
30. Yu A, Yick KL, Ng SP, *et al.*, 2013, Prediction of Fabric Tension and Pressure Decay for the Development of Pressure Therapy Gloves. *Textile Res J*, 83(3):269–87. DOI: 10.1177/0040517512456757.
31. Juckett G, Hartman-Adams H, 2009, Management of Keloids and Hypertrophic Scars. *Am Fam Phys*, 80(3):253–60.
32. Li-Tsang CW, Zheng YP, Lau JC, 2010, A Randomized Clinical Trial to Study the Effect of Silicone Gel Dressing and Pressure Therapy on Posttraumatic Hypertrophic Scars. *J Burn Care Res*, 31(3):448–57. DOI: 10.1097/bcr.0b013e3181db52a7.
33. Kamal RM, Khalaf MM, Elshazely A, *et al.*, 2016, Dynamic Splint Versus Static Splint and Active Range of Motion in Treatment of Post Burn Hand Contracture. *Int J PharmTech Res*, 9(6):75–83.
34. Narula A, Pastore CM, Schmelzeisen D, *et al.*, 2018, Effect of Knit and Print Parameters on Peel Strength of Hybrid 3-D Printed Textiles. *J Textiles Fibrous Mater*, 1:1–5. DOI: 10.1177/2515221117749251.
35. Hearle JW, 2008, In: Morton WE, editor. Physical Properties of Textile Fibres. 4th ed. Elsevier Science, Burlington.
36. Lai CH, Li-Tsang CW, 2009, Validation of the Pliance X System in Measuring Interface Pressure Generated by Pressure Garment. *Burns*, 35(6):845–51. DOI: 10.1016/j.burns.2008.09.013.
37. Wiseman J, Simons M, Kimble R, *et al.*, 2018, Reliability and Clinical Utility of the Pliance X for Measuring Pressure at the Interface of Pressure Garments and Burn Scars in Children. *Burns*, 44(7):1820–8. DOI: 10.1016/j.burns.2018.05.002.

ORIGINAL ARTICLE

3D-printed Biomimetic Bioactive Glass Scaffolds for Bone Regeneration in Rat Calvarial Defects

Krishna C. R. Kolan[1]*, Yue-Wern Huang[2], Julie A. Semon[2], Ming C. Leu[1]

[1]Department of Mechanical and Aerospace Engineering, Missouri University of Science and Technology, Rolla, Missouri, USA

[2]Department of Biological Sciences, Missouri University of Science and Technology, Rolla, Missouri, USA

Abstract: The pore geometry of scaffold intended for the use in the bone repair or replacement is one of the most important parameters in bone tissue engineering. It affects not only the mechanical properties of the scaffold but also the amount of bone regeneration after implantation. Scaffolds with five different architectures (cubic, spherical, x, gyroid, and diamond) at different porosities were fabricated with bioactive borate glass using the selective laser sintering (SLS) process. The compressive strength of scaffolds with porosities ranging from 60% to 30% varied from 1.7 to 15.5 MPa. The scaffold's compressive strength decreased significantly (up to 90%) after 1-week immersion in simulated body fluids. Degradation of scaffolds is dependent on porosity, in which the scaffold with the largest surface area has the largest reduction in strength. Scaffolds with traditional cubic architecture and biomimetic diamond architecture were implanted in 4.6 mm diameter full-thickness rat calvarial defects for 6 weeks to evaluate the bone regeneration with or without bone morphogenetic protein 2 (BMP-2). Histological analysis indicated no significant difference in bone formation in the defects treated with the two different architectures. However, the defects treated with the diamond architecture scaffolds had more fibrous tissue formation and thus have the potential for faster bone formation. Overall, the results indicated that borate glass scaffolds fabricated using the SLS process have the potential for bone repair and the addition of BMP-2 significantly improves bone regeneration.

Keywords: Selective laser sintering, Bioactive borate glass, *In vivo* bone formation, Porosity, Pore geometry, Scaffold architecture

***Corresponding Author:** Krishna C. R. Kolan, Department of Mechanical and Aerospace Engineering, Missouri University of Science and Technology, Rolla, Missouri, USA; kolank@mst.edu.

Received: April 2, 2020; ***Accepted:*** April 16, 2020; ***Published Online:*** April 29, 2020

Citation: Kolan KCR, Huang YW, Semon JA, *et al*., 2020, 3D-printed Biomimetic Bioactive Glass Scaffolds for Bone Regeneration in Rat Calvarial Defects. *Int J Bioprint*, 6(2):274. DOI: 10.18063/ijb.v6i2.274

1 Introduction

Since the discovery of Bioglass® by Dr. Hench in 1969, researchers have identified a wide range of glass and glass-ceramic compositions for bone repair as well as soft tissue applications[1-3]. The advantage of utilizing silicate-based bioactive glasses for bone repair is their conversion to hydroxyapatite (HA), the main mineral constituent of bone, that can readily integrate with surrounding tissue[2]. The research on bioactive glasses has evolved from traditional SiO_2 networks to highly resorbable glass compositions based on B_2O_3 networks as researchers have focused on developing borate and borophosphate glasses for biological applications due to the ability to support angiogenesis and offer faster degradation[4]. Several studies have investigated gradual replacement of SiO_2 in silicate glass with B_2O_3 and reported the effects of glass dissolution, tissue infiltration, and cell culture compatibility of the borosilicate glasses[5,6]. Borate glass is chemically less durable in comparison to silicate

glass and consequently, it degrades at a faster rate which allows quick release of calcium, boron, and other ionic dissolution products and provides rapid HA formation[7]. Hence, in this study, biomimetic borate glass scaffolds for bone regeneration in rat calvarial defects were fabricated and characterized in terms of material composition, porosity, architecture, and mechanical properties.

Among different additive manufacturing (AM) techniques, the powder bed fusion and vat photopolymerization techniques enable the fabrication of complex lattice structures mimicking natural bone architectures, which is much more difficult to achieve with material extrusion techniques[8-10]. Thus, laser powder bed fusion processes like selective laser sintering (SLS) can be used to create scaffolds with different architectures to study the effects of pore shape on the mechanical properties of scaffolds and their associated bone regenerative capacity. Several methods were proposed to create scaffold CAD models that possess a gradient of porosity, conformity, and architectures that closely mimic human trabecular bone[11-16]. Several challenges exist in the powder bed fusion-based 3D printing of ceramic/glass scaffolds with complex pores of size ranging from 100 to 600 μm because of the ceramic/glass material properties and sintering requirements[17]. In the recent past, there has been interested in the fabrication of ceramic and glass structures using the selective laser melting process with the help of high-temperature preheating of substrate[18-20]. Nevertheless, an indirect method that involves additional post-processing after green part fabrication allows for controlled structural densification avoiding glass crystallization[21,22]. Unlike metallic scaffolds, bioactive glass scaffolds degrade upon implantation *in vivo* or after soaking in simulated body fluids (SBF), thereby affecting their structural integrity. Factors that influence this outcome include, but are not limited to, bioactive glass composition, scaffold porosity, and pore geometry (which affects surface area for reaction). Therefore, investigating the effect of porosity and pore geometry on the degradation of scaffolds made with bioresorbable materials, such as bioactive glasses, could help design implants to repair diverse regions of the skeletal system with different structural and biological requirements.

The effect of scaffold architecture on mechanical properties, cell proliferation, and bone regeneration has been investigated using polymer and metallic scaffolds[23-26]. There are inconclusive reports on the influence of pore size on bone regeneration. While some reports suggested pore sizes in the range of 100 – 300 μm are beneficial for bone growth, other studies demonstrated increase bone tissue growth with pores >300 μm and up to 800 μm[27,28]. Some of these studies were performed using bioceramic scaffolds and others were performed on biopolymer and metallic (titanium-based) scaffolds that do not degrade like bioactive glass. Bone repair using scaffolds made from resorbable materials such as bioactive glasses is likely to have distinct characteristics as the scaffold properties change post-implantation in the dynamic *in vivo* environment. For example, silicate-based glasses degrade slowly even *in vivo* because of the chemical stability of the SiO_2 network. A recent *in vivo* evaluation of silicate-based glass scaffolds showed that about half of the scaffold (unconverted glass) still remained in the defect region after 6 months[29]. However, borate glass fibers used to treat a calvarial defect were reported to degrade more quickly, with most of the glass converted to HA and resulting in better bone regeneration in comparison to silicate glasses[30].

The scaffold architecture could also play an important role in *in vitro* cell proliferation, differentiation, and bone regeneration, with some studies suggesting pore curvature driven tissue growth[24,31-33]. Although these *in vitro* observations were, in general, in agreement with theoretical predictions, the influence of curvature on tissue regeneration has not been demonstrated *in vivo*. Pore geometry, pore size, and porosity are interrelated. Importantly, the resorbable nature of borate glass could further complicate the mechanism of the bone regeneration process *in vivo,* relative to more predictable bone formation in metallic, or biopolymer scaffolds.

In the present study, we hypothesized that a borate glass scaffold with biomimetic architecture would have sufficient strength and stiffness for

non-loading bone repair and increase the bone regeneration in a critical-sized bone defect. To test this hypothesis, we compared the structural and mechanical properties of the borate glass scaffolds with five different architectures, namely, cubic, spherical, x, gyroid, and diamond. Degradation of scaffolds in SBF was assessed. Subsequently, cubic and diamond architecture scaffolds were chosen to evaluate the bone regeneration in a rat calvarial defect model. Cubic architecture represented a traditional lattice design whereas diamond architecture represented a biomimetic architecture that mimics natural bone, which has previously been shown to promote cell proliferation *in vitro*[34]. The treatment groups included borate glass scaffolds with or without bone morphogenetic protein-2 (BMP-2), an established osteogenesis inducing protein in this study.

2 Materials and methods

2.1 Scaffold fabrication

Bioactive borate glass (13-93B3 glass; nominal composition in wt % – 56.6% B_2O_3, 5.5% Na_2O, 11.1% K_2O, 4.6% MgO, 18.5% CaO, 3.7% P_2O_5) with an average particle size of ~12 μm was used in this research. Borate glass particles were mixed with a polymeric binder and then dry ball-milled to obtain the feedstock powder for the SLS machine (DTM Sinterstation 2000). The binder content, feedstock preparation, and scaffold fabrication parameters established previously for silicate glass (laser power – 5 W, scan speed – 508 mm/s, scan spacing – 0.23 mm, layer thickness – 76.2 μm, 15 wt % binder) were adopted in this study[35]. The fabricated parts were heat treated in a furnace (Vulcan Benchtop, York, PA) to remove the polymeric binder and sintered at 570°C for 1 h.

2.2 Scaffold assessment

Scaffolds measuring 5 × 5 × 5 mm^3 were used for compression tests and scaffolds measuring 10 × 10 × 10 mm^3 were used to measure porosity using Archimedes method. The scaffold's pore size was measured using an optical microscope. A cross-head speed of 0.5 mm/min was used during the compression tests with a mechanical load frame (Instron 4469, Norwood, MA). Five samples in each set were used and the average values were reported with standard deviation. X-ray diffraction (XRD) analysis (Philips X-Pert, Westborough, MA) was performed on the as-received borate glass powder, sintered scaffolds, as well as the dried scaffolds after soaking in the SBF to confirm the crystalline-like formations on the scaffold surface, the amorphous nature of borate glass, and its conversion. Scanning electron microscopy (SEM) (S-570, Hitachi Co., Tokyo, Japan) was used to analyze the surface morphology of the scaffold.

2.3 Degradation tests

An established protocol was used to prepare the SBF solution[36]. Samples were ultrasonically cleaned 3 times using ethanol and then dried in an oven overnight before kept in the SBF solution (100 ml of solution was used for 1 g of the scaffold). The scaffolds were soaked in an incubator maintained at 37°C. To evaluate the scaffold degradation, compression tests were conducted on soaked scaffolds in their wet condition. At least three samples in each set were used and the average values with standard deviations were reported.

2.4 Scaffold preparation before implantation

For *in vivo* tests, cubic and diamond scaffolds were grinded to the required dimensions (~1.5 mm thick disks having 4.6 mm in diameter), ultrasonically washed thrice (5 min each) with ethanol, dried in air and then heat sterilized overnight at 250°C. Six animals were used for each treatment group and scaffolds with ~50% porosity were used for this study. Experiments were carried out with or without the use of BMP-2. Animals were randomized to different types of scaffold, based on the presence or absence of BMP-2. Scaffolds were soaked in SBF for 6 h and then dried at room temperature overnight before loading BMP-2 to roughen the surface for improved protein adhesion. BMP-2 was dissolved in citric acid (10 μg in 100 μl) and 10 μl of the solution was loaded on each scaffold

(equivalent of 1 µg per scaffold). Scaffolds were kept in the refrigerator overnight for protein adhesion before implantation. The adhesion and release of BMP-2 from borate glass scaffolds were assumed to be similar to the release of bovine serum albumin (BSA) from borate glass scaffolds fabricated using the SLS process. Therefore, the protocol of loading BMP-2 was developed based on the release of BSA from borate glass scaffolds that occurred over a period of 4 days. **Table 1** shows the experimental plan of scaffold placement in Sprague Dawley rats.

Table 1. Borate glass scaffold placement in rat calvarial defects.

Without BMP-2			With BMP-2		
Animal #	**Left side**	**Right side**	**Animal #**	**Left side**	**Right side**
1	D	D	7	D	D
2	D	D	8	D	D
3	D	C	9	D	C
4	C	D	10	C	D
5	C	C	11	C	C
6	C	C	12	C	C

C: Cubic; D: Diamond.

2.5 Surgical procedure

Animal care and use were approved by the Missouri S&T Institutional Animal Care and Use Committee. Twelve 12-week-old male Sprague Dawley rats (~350 g in body weight) were anesthetized with a 0.6 ml ketamine/xylazine (200 mg ketamine and 20 mg xylazine per 4 ml) abdominal injection. A full-thickness defect measuring 4.6 mm in diameter was created in the central area of each parietal bone using a hand drill and trephine bur (ACE Surgical Supply Co. Inc., Brockton, MA) under constant irrigation with saline solution without disturbing the dura mater. AutoClip® wound closing system (Braintree Scientific, Inc., Braintree, MA) was used for site closure and animals were given 0.2 ml of penicillin subcutaneously and ketoprofen (3 mg/kg body weight) intramuscularly post-surgery. After 6 weeks, animals were euthanized by means of CO_2 inhalation and samples from defect sites with surrounding bone were harvested for subsequent examination.

2.6 Histological processing

The harvested samples were fixed in 10% buffered formaldehyde for ~3 days, soaked in DI water overnight, and bisected in half. Samples were decalcified in Cal-Ex II simultaneous Fixative/ Decalcifier (Fisher Scientific, Pittsburgh, PA) solution by changing the solution every 2 days during the 1st week and then once every 4 days for about ~4 weeks. The samples were dehydrated with a series of ethanol solutions by a microwave dehydration technique (EBSciences H2850 Microwave Processor). Briefly, the sample temperature was set to ~37°C and the samples were heated for about 2.5 min in the microwave followed by 12.5 min of idle time. The samples were then soaked in xylene solution followed by paraffin mounting at 45°C using a paraffin mounting system (Leica EG 1150H, Buffalo Grove, IL). Specimens were cut at 5 µm thin sections and mounted on glass slides. Slides were stained with hematoxylin and eosin (H&E) and Masson's trichrome to determine the amount of new bone tissue and fibrous tissue. Optical images of stained sections were taken with an Olympus BX 50 microscope.

2.7 Histomorphometric analysis

Histomorphometric analysis was carried out using the stitched optical images (with Microsoft Image Composite Editor software) of the stained sections and ImageJ software[37]. The percentage of new bone formed in defects was evaluated from the optical images. The total defect area was defined as the region between the two boundaries formed during the drilling process. The remaining scaffold and the tissue within were identified. The newly formed bone was outlined and measured within the defect area and expressed as a percentage of the total defect area. The measurements were blinded and performed by persons with no knowledge of the treatment groups.

2.8 Statistical analysis

The data were reported as the mean ± standard deviation. Analysis of differences in means was

performed using a one-way analysis of variance with Tukey's *post hoc* test. The statistical significance was set at $P < 0.05$.

3 Results and discussion

3.1 Fabrication and structural assessment

CAD models of scaffolds with five different architectures and their unit cells are shown in **Figure 1A**. The porosity of cubic and X architectures is a function of the size of the unit cell and the diameter of the struts. In the case of spherical architecture, the porosity is a function of the diameter of the sphere subtracted from a unit cube. These three architectures represent the most commonly used scaffold designs for bone tissue engineering fabricated by AM techniques. The diamond and gyroid architectures were designed to create surfaces with constant mean curvature and to mimic natural trabecular bone architecture[38]. These surfaces were generated using open-source software called K3DSurf (http://k3dsurf.sourceforge.net/) and were converted to CAD files for fabrication (**Figure 1A**). The representative optical microscope images of scaffolds with varying porosities are shown in **Figure 1B**. **Figure 1C** shows representative scaffolds of each architecture and **Figure 1D** shows the diamond architecture scaffolds with different porosities.

Scaffolds were designed to have 50%, 60%, 70%, and 80% volumetric porosity but the measured apparent porosities (**Table 2**) were lower than the designed values. The overall deviation between designed and apparent porosities was ~19% for spherical, diamond, gyroid scaffolds, ~17% for cubic scaffolds, and ~25% for X scaffolds. The difference between the designed and apparent porosity was the most for X scaffolds and the least for cubic scaffolds. This was due to the powder particles getting stuck inside the pores during the excess powder removal from the "green body" (SLS fabricated part before post-processing). These powder particles were sintered during heat treatment, thereby reducing the overall porosity. It is recommended that this effect and the resulting difference in porosity be accounted in the designs before scaffold fabrication using the SLS process. The adhered powder particles in the green body also affected the overall scaffold pore sizes, shown in **Table 2**. Overall, scaffold pore sizes varied

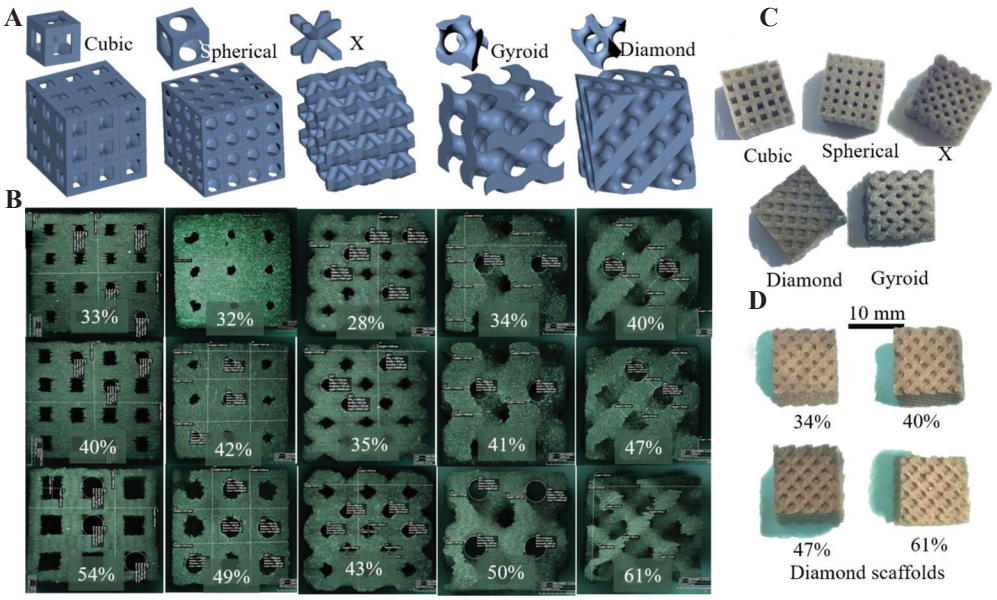

Figure 1. (A) Unit cells and scaffold architectures: Cubic, spherical, X, gyroid, and diamond, (B) representative optical images of 5 × 5 × 5 mm^3 borate glass scaffolds with corresponding architectures at three different porosities used for compression tests, (C) representative scaffold of each architecture measuring 10 × 10 × 10 mm^3 used to measure porosity, and (D) 10 × 10 × 10 mm^3 diamond architecture scaffolds at four different porosities (34% – 61%).

Table 2. Scaffold porosity and pore size.

Architecture	Designed versus apparent (%)				Measured average pore size (μm)			
	50	60	70	80	50	60	70	80
Cubic	33±2	40±2	54±1	66±3	0.5±0.02	0.7±0.02	1.0±0.04	1.3±0.02
Spherical	32±1	42±3	49±3	61±1	0.5±0.04	0.6±0.05	1.0±0.04	1.0±0.04
X	28±2	35±3	43±2	55±0	0.5±0.03	0.6±0.02	0.7±0.03	1.2±0.10
Diamond	34±2	40±1	47±1	61±1	0.8±0.01	0.9±0.01	1.0±0.04	1.2±0.05
Gyroid	34±1	41±1	49±1	60±1	0.8±0.01	0.9±0.01	1.0±0.03	1.1±0.04

between 0.5 and 1.3 mm. X architecture scaffolds had the smallest pores which are consistent with the X scaffolds having the largest difference between the designed and apparent porosities. The difficulty in removing adhered powder from the X scaffold pores of green bodies contributed to its lowest porosity and most reduced pore size. The average pore size of scaffolds designed with 80% porosity ranged from 0.9 mm to 1.3 mm, and the scaffolds designed with 50% porosity ranged from 0.5 mm to 0.8 mm. In theory, unit cell pore size varies along the Z-height, with it being the smallest at the end and the largest at the center of the unit cell. Therefore, true scaffold pore size has a range of values instead of being a constant value.

Several parameters limit the accuracy of fabricating scaffolds, including scaffold architecture, the resolution of the machine, layer thickness, binder content, and particle size. The laser spot diameter of the SLS machine was 0.45 mm and therefore, it was not feasible to fabricate scaffolds with struts smaller than this limit (<0.45 mm). The laser spot could have heated and melted particles adjacent to the scanning area, effectively reducing the designed pore size. Smaller particles are easier to remove from the green body scaffold pores, causing less deviation from the actual design. However, smaller particles require higher binder content because of the increased surface area that could increase the shrinkage and deviations between designed and fabricated parts. The amount of binder and the particle size was optimized for scaffold fabrication in our previous work[35]. One key aspect in designing the architecture was considering scaffold manufacturability. For instance, in spherical scaffolds, porosity is a function of the diameter of the sphere that is subtracted from the solid unit cube to obtain the unit cell of spherical architecture. **Figure 2A** shows unit cells of spherical and cubic scaffolds and their pore shapes and pore sizes. Decreasing sphere diameter to lower porosity would hinder the removal of powder particles from the scaffold. Hence, unit cell pores were designed to enable fabrication and removal of powder particles. The pore volume variation for cubic and spherical unit cells is shown in **Figure 2B**.

3.2 Effect of porosity and pore geometry on mechanical strength

Compressive strengths of borate glass scaffolds with different porosities are shown in **Figure 3A**. Among the five architectures investigated in this study, cubic scaffolds had the highest compressive strength (15.5 ± 1.9 MPa) and X scaffolds had the lowest strength (4.9 ± 1.2 MPa) at low porosity (~35%). The biomimetic architectures (gyroid and diamond scaffolds) had compressive strengths of 9.5 ± 2.5 MPa and 6.8 ± 1.6 MPa, respectively. The scaffold compressive strengths at low porosity were near the high end of the range of compressive strength for human trabecular bone (~2 – ~12 MPa), whereas the strengths at high porosity levels (>55%) were near the low end of the spectrum[39]. Cubic architecture scaffolds have pillars in the axial direction that carry a majority of the load in compression tests before structural failure, while the other architectures lacked a similar feature. X architecture scaffolds provided the least resistance in compression because of the 45° oriented struts. The compressive strength for all scaffold types was ~4 MPa or less at high porosities, which falls at the lower range of the trabecular bone compressive strength[39].

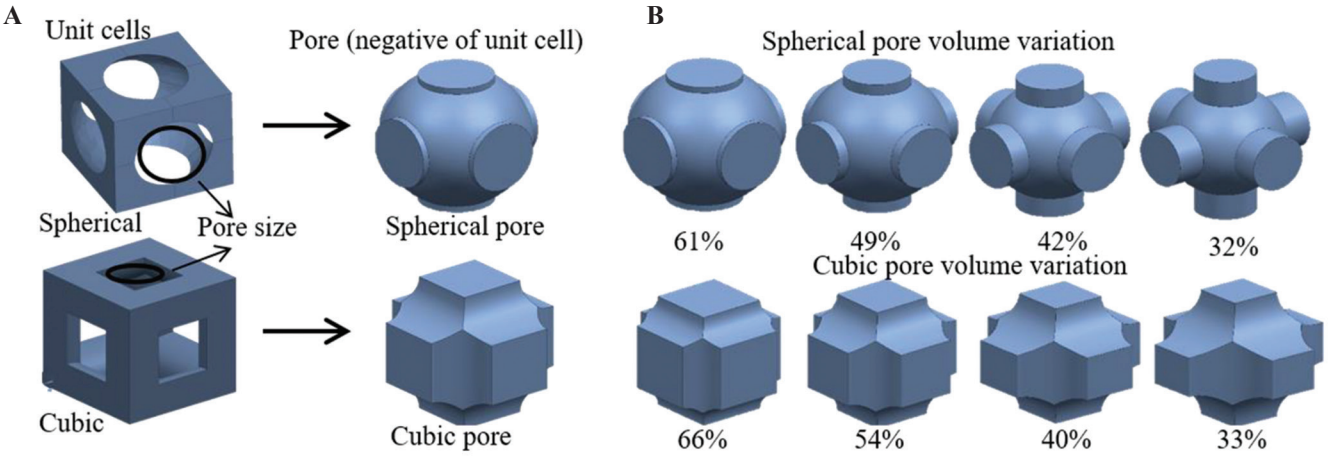

Figure 2. (A) Unit cells and pore shapes of cubic and spherical architecture scaffolds, (B) pore volume variation of spherical and cubic scaffolds with porosity. Cylindrical extensions to the spherical pores were designed to maintain sufficient pore size for powder removal from the scaffold.

Overall, the differences in scaffold compressive strength at higher porosities (>55%) were not as significant as they were at lower porosities (<35%). Architecture of scaffold contributes to cell proliferation, tissue growth, and scaffold structural integrity. Therefore, it is crucial to optimize the porosity and architecture of a scaffold, depending on the application. Another important aspect of the scaffold structural integrity is the elastic modulus during compression which measures the scaffold stiffness. Scaffolds with higher stiffness are not desired in load-bearing applications as they are known to cause stress shielding effect. However, as borate glass scaffolds fabricated using the SLS process do not possess enough structural strength for load-bearing applications and are suitable for non-load bearing applications and, the scaffold stiffness may not play a major role in bone regeneration. Nevertheless, compressive modulus values of all scaffold types are summarized in **Table 3**. Although the values are significantly less than the human trabecular bone elastic modulus (~10 GPa), the values are similar to or slightly lower than that of a rat calvaria (1.5 – 4 GPa)[39-41].

Regression models have been proposed to estimate the strength of a porous ceramic part based on the void shape[42-45]. Duckworth first proposed the exponential dependence of relative strength using the equation below[44]:

Table 3. Compressive modulus of scaffolds at designed porosities (in GPa).

Scaffold	50	60	70	80
Cubic	1.9±0.3	1.2±0.3	0.7±0.1	0.6±0.2
Spherical	1.8±0.2	1.1±0.4	0.8±0.1	-
X	1.0±0.2	0.8±0.2	0.3±0.0	-
Diamond	1.0±0.2	1.0±0.1	0.6±0.1	0.3±0.0
Gyroid	1.4±0.3	1.1±0.2	0.8±0.2	0.4±0.1

$$\sigma = \sigma_o e^{-BP} \quad (1)$$

where,

σ - Strength of porous part; σ_o - Strength of dense part;

B - Empirical constant (pore shape factor); p - Porosity fraction;

Mechanical properties of porous ceramic parts are dependent on porosity and pore shape. The results reported in the studies above showed that the B value in the equation above varied between 5 and 9 for different ceramic materials and pore shapes[43-46]. This model was adopted for structures with basic pore shapes of oblate, elliptical, and spherical[47]. Although the equation was developed for nonrandom porous mullite ceramic parts, it was reported that the compressive strength of ceramic lattice structures fit the model with independent modification of either the pore shape or the pore size[46]. In our current study, scaffolds had an open lattice structure and pores were highly

interconnected, unlike the closed pores used in the studies above. Hence, the compressive strength variation with porosity did not fit well with equation (1) and therefore, a slightly modified version of equation (1) was used to fit the data by introducing an additional empirical constant, A, as given below:

$$\sigma = A\sigma_o e^{-BP} \quad (2)$$

where,

σ - Strength of lattice; σ_o - Strength of dense part; *A, B* - Empirical constant; p - Porosity fraction;

Figure 3B shows the compressive strength versus porosity data for all scaffolds with different architectures fitted with the proposed model (equation 2). The compressive strength (σ_o), compressive modulus and density of the fully dense parts (ϕ 5 mm cylinders; 6 mm in length) were measured as 32.2 ± 6.4 MPa, 4.6 ± 0.8 GPa, and 2.16 g/cc, respectively. The equations fitted are given below:

Cubic scaffold: $\sigma = 3.9\sigma_o e^{-6.3p}$

X scaffold: $\sigma = 1.4\sigma_o e^{-6.6p}$

Spherical scaffold: $\sigma = 0.7\sigma_o e^{-2.7p}$

Gyroid scaffold: $\sigma = 2.9\sigma_o e^{-6.5p}$

Diamond scaffold: $\sigma = 1.3\sigma_0 e^{-5.3p}$

With the exception of the spherical scaffold, A value was >1 for all scaffolds and B value varied between 5.3 and 6.6 and were in agreement with other studies (B value varied between 5 and 9)[46,47]. For spherical scaffolds, A was <1 and B was <5. To verify the applicability of this trend to scaffolds made with other materials, silicate glass scaffolds were fabricated with the same five architectures and at similar porosity levels. Compressive strength data for silicate glass scaffolds were fitted to the model ($R^2 > 0.98$) to obtain the following set of equations for different architectures:

Cubic scaffold: $\sigma = 4.0\sigma_o e^{-6.7p}$

Gyroid scaffold: $\sigma = 1.1\sigma_o e^{-6.0p}$

Spherical scaffold: $\sigma = 0.6\sigma_0 e^{-3.1p}$

Diamond scaffold: $\sigma = 2.2\sigma_o e^{-8.6p}$

X scaffold: $\sigma = 1.3\sigma_o e^{-7.5p}$

The silicate glass strength, modulus, and density of the fully dense parts were 84.34 ± 5.95 MPa, 5.47 ± 1.05 GPa, and 2.3 g/cc, respectively. As can be seen from the fitted equations for silicate glass scaffolds, A was <1 and B was <5 for spherical scaffold, while A was >1 and B varied between 5 and 9 for the remaining scaffolds. This behavior of spherical scaffolds was consistent for borate glass and silicate glass scaffolds. In the formulation of equation (2), it was assumed that the empirical constants, A and B, in the model could be functions of not only the pore shape but also the pore shape variation with porosity. For cubic, X, gyroid, and diamond unit cells, the

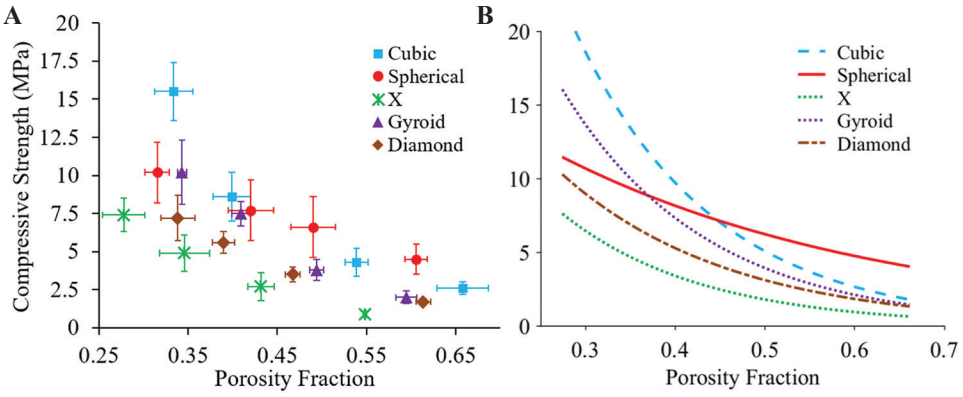

Figure 3. Compression test results: (A) Compressive strength of borate glass scaffolds with five architectures at different porosity levels. Vertical and horizontal error bars represent the standard deviations of measured compressive strength and porosities, respectively, (B) curve fitting of strength versus porosity fraction with R^2 value for all curves is >0.98.

overall pore shape remained relatively constant with increasing porosity. However, for spherical unit cell, pore shape at higher porosity (60%) is different from pore shape at lower porosity (30%). The variation of pore shapes of cubic and spherical architectures is shown in **Figure 2B**. To enable fabrication of spherical scaffolds at lower porosities, the unit cell design was modified to include cylindrical extensions to maintain the pore size resulting in pore shape variation for the spherical unit cell (**Figure 2B**). This variation in pore shape could be the reason for the different ranges of A and B values for spherical scaffolds in comparison to the remaining four architectures. To validate the above model, the data point at 32% porosity for spherical scaffolds was excluded and the remaining data for silicate glass scaffolds were fitted with the model. Following this, the A value was 1.4 and the B value was 5.0, which indicated model agreement. This suggests that empirical constants, A and B, could represent the pore shape variation in addition to the pore shape and porosity.

3.3 Scaffold degradation in SBF

The scaffolds were mechanically tested in their wet state after immersion in SBF for 1 week. The compressive strength measured for most scaffolds was about 3 MPa or less, which is near the low end of the range of compressive strength (~2 – ~12 MPa) of human trabecular bone[29]. The only exception to this was spherical scaffolds at 32% porosity, which had a compressive strength of ~4 MPa. A significant reduction in compressive modulus values for all scaffolds was also observed after 1 week, soaking in SBF. Cubic scaffolds had the highest compressive modulus ranging from 1.2 to 0.2 GPa, and X scaffolds had the lowest modulus ranging from 190 to 52 MPa, after soaking in SBF for 1 week. **Figure 4A** shows scaffold compressive strengths of all scaffold types and **Figure 4C** shows typical borate glass scaffold transformation after soaking. **Figure 4B** shows the percentage reduction in the compressive strength of scaffold types at lower (<35%) and higher (>55%) porosities. For high porosity, there was over a 90% decrease in scaffold strength, irrespective of the scaffold architecture. At low porosities, there was at least a 50% strength reduction for all scaffold regardless of their architecture. Among all scaffold types, diamond scaffolds showed a strength reduction that was consistently >80%, irrespective of the scaffold porosity. The percentage strength reduction varied from 80% to 92% for diamond scaffolds and from 76% to 94% for X scaffolds. These two scaffold architectures showed the largest strength reduction at all porosities.

SEM images were analyzed for any crystal-like formations on the bioactive glass surfaces that typically appear after immersion in SBF. **Figure 5** shows SEM images of a representative X architecture scaffold taken out of SBF after 1 week. The outer surface morphology of borate and silicate glass scaffolds at lower magnification is shown in **Figures 5A and C**, respectively. The

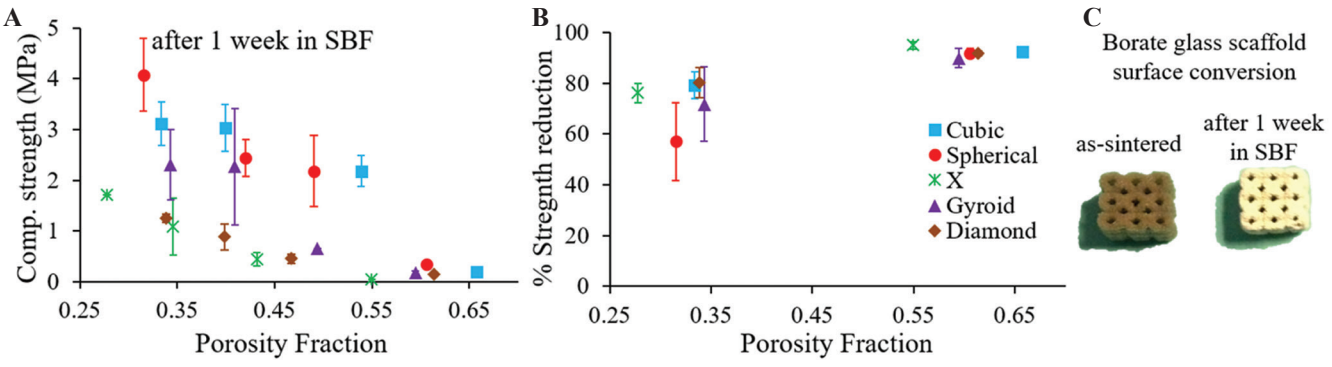

Figure 4. (A) Compressive strength of soaked scaffolds after 1 week in simulated body fluids (SBF), (B) comparison of percentage strength reduction for scaffolds with different architectures at lower and higher porosities, (C) optical image showing the physical transformation of the scaffold surface after soaking in SBF for 1 week.

corresponding higher magnification images are shown in **Figures 5B and D**. These images show the rounded spheroid-like formations on the borate glass scaffold surface, unlike needle-like crystal formations on silicate glass scaffold surface, similar to observations made by other researchers with these glasses[5,35]. The needle-like formations on silicate glass surface were confirmed as crystalline HA using XRD, whereas spheroid-like formations on borate glass surface were not confirmed to any known crystalline formations. This behavior of borate glass is not uncommon as it was reported earlier that it could take more than 60 days to form a crystalline calcium phosphate layer in SBF and it also depends on the strut size[48,49]. This was also observed in some previous work which found the presence of Ca^{2+} and PO_3^{4-} on the reacted surface of the borate glass, indicating an amorphous calcium phosphate or carbonate-substituted apatite formation[50,51].

The degradation of scaffolds made with resorbable materials depends on the material composition and porosity. Scaffold degradation is related to its surface area and the type of soaking solution (SBF in this study). Scaffolds with higher porosity degraded the most (~90% strength reduction in 1 week) irrespective of architecture. This was due to the higher surface area per unit volume and large pores, all measuring about ~1 mm (**Table 1**), that increased the efficiency of the ionic exchange with SBF and made the degradation process more rapid. To comprehend the trends in scaffolds with lower porosities, the unit cell surface area of each architecture (based on the CAD model) was plotted against the percentage strength reduction, as shown in **Figure 6**. Overall, the plot indicated a higher strength reduction with increasing surface area to volume ratio (SA/V). The SA/V data points for gyroid and diamond scaffolds form a distinguishable group from cubic, spherical, and X scaffolds. However, for a given SA/V ratio (for example, SA/V ratio of 2), diamond scaffolds show higher strength reduction in comparison to cubic and spherical scaffolds despite having a similar porosity. This indicates that the lattice structure and pore geometry do play an important role in controlling scaffold degradation, especially in the case of scaffolds made with bioresorbable materials such as bioactive glasses. Moreover, it should be noted that the actual SA/V values would be higher than the CAD values because of the surface roughness that is inherent to parts fabricated using the SLS process.

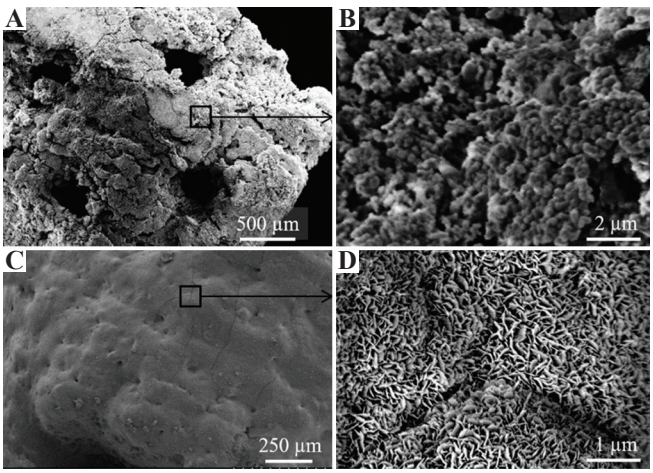

Figure 5. Scanning electron microscopy images of borate glass and silicate glass scaffolds at low and high magnifications after immersion in simulated body fluids for 1 week: (A and B) Borate glass outer surface morphology and rounded, irregular spheroid-like formations, (C and D) silicate glass scaffold surface and well defined needle-like crystalline structures at higher magnification.

3.4 New bone formation

Scaffolds were firmly integrated with the surrounding bone and pores were filled with

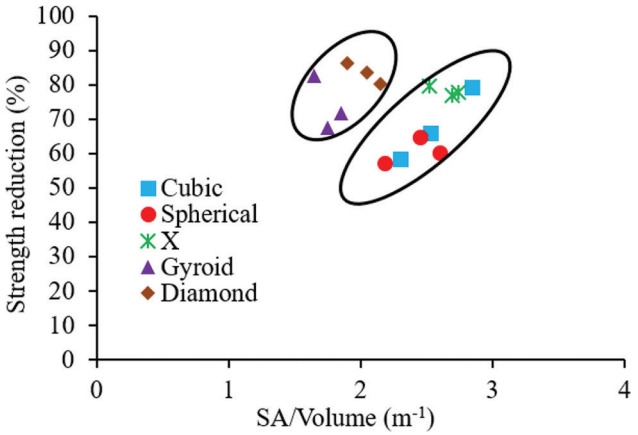

Figure 6. Percentage reduction in compressive strength of a scaffold versus the ratio of total surface area to volume of different architectures.

fibrous tissue with osteoblasts lining the pore-glass interface. **Figure 7** shows H&E stained and Masson's trichrome stained sections of full-thickness rat calvarial defect regions implanted with cubic and diamond scaffolds for 6 weeks with or without the presence of BMP-2. Although scaffolds designed at 70% porosity were planned for implantation, the apparent porosities of scaffolds used were ~54% (cubic) and ~47% (diamond) with an average pore size of 1 mm for both scaffold types. The defects treated with cubic and diamond scaffolds without BMP-2 (**Figures 7A-D**) showed no significant in new bone formation. However, small isolated pockets of new bone tissue formed inside some defects and approximately 6% of the total defect area was new bone tissue, including at the outer edges and the bottom of the defect. No statistical differences existed between scaffold types. The average overall new bone tissue formed in defects treated with cubic and diamond scaffolds as a percentage of the total defect area was 5.8 ± 1.0% and 6.2 ± 1.7%, respectively (**Figures 7A-D and 8**). In contrast, a significant amount of new bone tissue formation was observed in defects treated with cubic and diamond scaffolds loaded with BMP-2 (**Figures 7E-H and 8**). New bone tissue formed in defects implanted with cubic and diamond scaffolds occupied 39.9 ± 15.1% and 37.1 ± 13.8% of the total defect area, respectively. After normalization based on the scaffold porosities, the percentage of new bone tissue formed in cubic and diamond scaffolds was ~74% and ~79%, respectively. Despite the higher normalized bone formation in diamond scaffolds, the result was not statistically significant ($P = 0.8$).

Magnified images of the H&E stained sections of defects treated with borate glass scaffolds (cubic and diamond) without BMP-2 are shown in **Figure 9**.

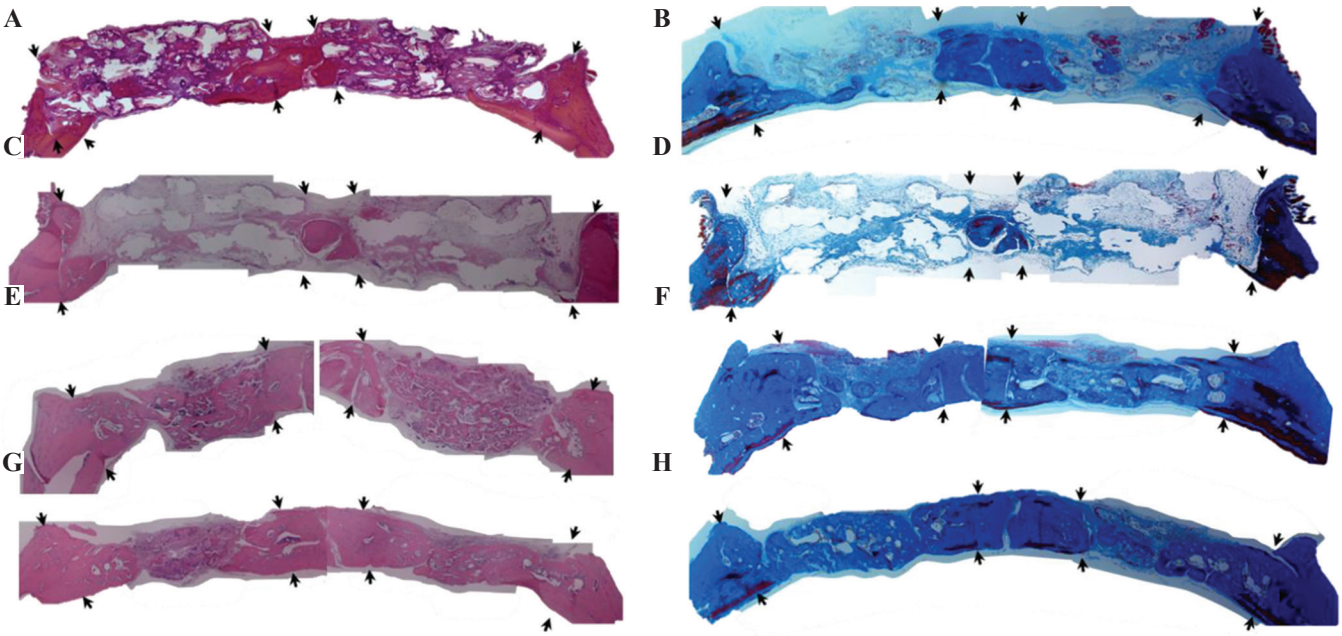

Figure 7. Hematoxylin and eosin stained sections (left) and Masson's trichrome stained sections (right) of calvarial defect regions with four different treatment groups: (A) Cubic scaffolds without bone morphogenetic protein 2 (BMP-2), (B) Cubic (left) and Diamond (right) scaffolds without BMP-2, (C and D) diamond scaffolds without BMP-2, (E and F) cubic scaffolds with BMP-2, and (G and H) diamond scaffolds with BMP-2. The arrows in the pictures point to the borders of the defect region. Dense color (pink in H&E and blue in trichrome) in sections indicates mineralized bone tissue, white/background color indicates remaining scaffold in the defect region. Red/maroon color in trichrome stained sections indicates new bone. There was no significant new bone tissue formation in defects treated with scaffolds without BMP-2. Defects treated with "scaffolds and BMP-2" show significant new bone formation. The difference in tissue formation between cubic and diamond scaffolds even with BMP-2 was not significant.

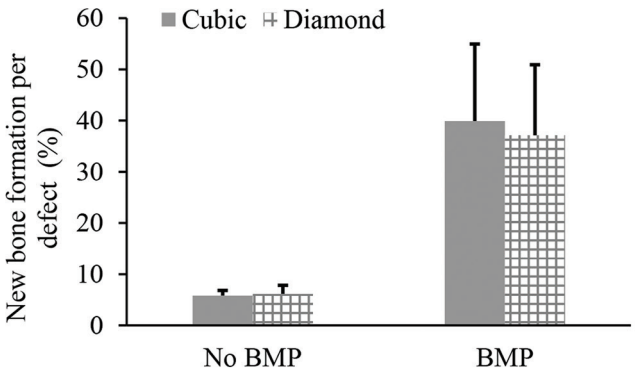

Figure 8. Percentage of new bone tissue formation in cubic and diamond scaffolds quantified based on the total defect area. The bone growth between scaffold designs with or without bone morphogenetic protein 2 (BMP-2) was not statistically different. The bone formation in defects treated with BMP-2 was statistically significant ($P = 0$).

Figures 9A and B show the tissue formation inside the diamond and cubic pores. In both cases, new bone tissue formation can be observed at the edges of the defect and in pores that are present on the underside of the defect (just above dura matter), as shown in the inset images. In addition, more mature dense fibrous tissue was formed in diamond pores in comparison to cubic pores (**Figures 9C and D**). There was a high density of osteoblasts lining the diamond scaffold surface, seen as dark purple stained cells, and indicated by arrows in **Figure 9A**. However, this was not apparent in cubic scaffolds (**Figure 9B**). Magnified images of the osteoblasts lining the scaffold surface, newly formed bone tissue, and fibroblasts in the connective tissue are shown in **Figures 9C and D**. Qualitative assessment of H&E stained sections and trichrome stained sections indicated a higher fibrous connective tissue in the diamond pores in comparison to the cubic pores. **Figures 9E and F** show new mineralized bone in pores and dense connective tissue yet to become bone. The presence of dense connective tissue and marrow-like pockets in those regions indicates the presence of endothelial cells which enable blood vessel formation and new bone tissue formation. Longer treatment duration (>6 weeks) could have resulted in significantly higher bone formation in

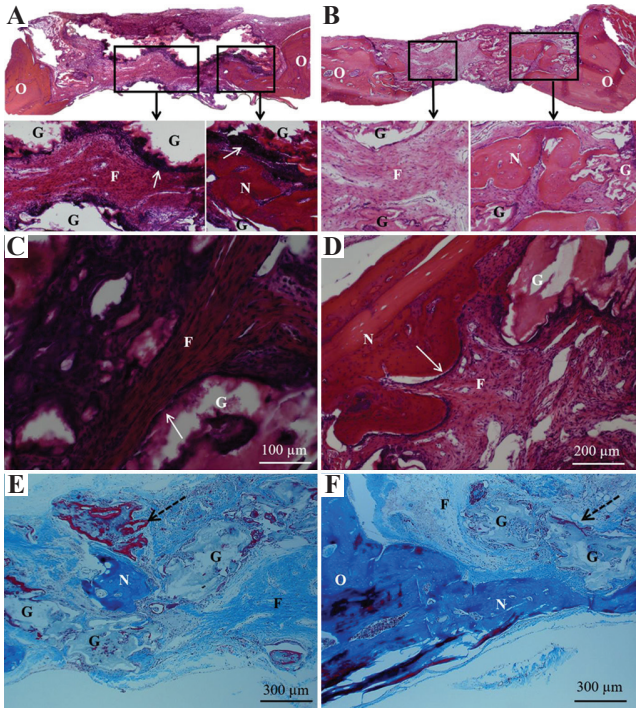

Figure 9. Histological sections of defect regions treated without bone morphogenetic protein 2 after 6 weeks. (A) Hematoxylin and eosin (H&E) stained sections of diamond scaffold, (B) H&E stained sections of cubic scaffold with the inset figures showing fibrous tissue in the pores and arrows indicating osteoblast cells lining the edges of the diamond glass scaffold strut, (C and D) magnified images of different regions of diamond scaffold showing fibrous connective tissue, newly formed bone tissue, and remaining glass, (E) Masson's trichrome stain showing pocket of mineralized bone tissue in the pore and the new bone tissue (red) surrounding the glass filament indicated by dotted arrow, (F) Trichrome stain showing mineralized bone tissue formed adjacent to host bone tissue and from the bottom side of the defect (above dura matter). N – new mineralized bone, O – original host bone, G – remaining glass, F – fibrous connective tissue.

diamond scaffolds in comparison to cubic scaffolds based on the maturity of the fibrous tissue.

Our results showed significant new bone formation in scaffolds treated with BMP-2. Uncontrolled release or high doses of BMP-2 can result in negative consequences, including tumor formation and undesired bone growth in

soft tissue[52,53]. As expected, addition of BMP-2 significantly increased new bone formation to almost 40%, based on the total defect area, and almost filled the entirety of the pores. Our results are consistent with a recent study that showed the addition of BMP-2 at the same concentration (1 μg per defect) to defects treated with HA microspheres for the same time frame also created approximately 40% new bone in a 4.6 mm diameter rat calvarial defect[54]. The above study investigated the role of relaxin, a pregnancy hormone, to control and enhance BMP-2 release to reduce the need for high concentrations of BMP-2. It was reported that the addition of 0.05 μg of relaxin to 0.5 μg of BMP-2 induced higher bone formation compared to 1 μg of BMP-2 alone per defect. In the future, a combination of relaxin and BMP-2 together with biomimetic architecture (such as diamond) could further enhance bone regeneration and repair.

As new bone formation was about 6% for both scaffold types without BMP-2, the results obtained in this study are largely in agreement with *in vivo* assessments using borate-based bioactive glasses by other researchers. **Table 4** concisely summarizes *in vivo* results using doped and undoped borate glasses. The implantation time for most studies was 8 or 12 weeks, though one study had a 6-week time point to evaluate the bone growth in defect regions using material extrusion 3D-printed scaffolds and reported approximately 6% new bone formation[55]. The material extrusion 3D-printed scaffolds had pores in the range 150 – 300 μm unlike the 1 mm pores of the cubic and diamond scaffolds used in this study. Other studies mentioned in **Table 4** utilized scaffolds made with polymer foam replication technique, freeze-drying technique, and pressed short fiber technique that have significantly smaller pore sizes, thinner strut diameters, and higher porosities. The amount of bone formation in terms of defect region was reported in the range of 9 – 28% after 12 weeks of implantation. A relatively higher amount of bone formation (up to 30%) was reported when scaffolds were made with copper and zinc doped borate glass. Higher bone growth for all the above scaffolds could be due to smaller pore size range and higher porosities compared to the scaffolds used in this study, which were limited by the laser spot size of the SLS process. The role of pore size is not completely understood as there exist reports with mixed results when using scaffolds with a range of pore sizes for bone regeneration[28]. While some studies have reported that average pore sizes in the range of 100 – 300 μm are effective for bone tissue growth, others have suggested large pores in the range of 600 –1000 μm are better for tissue growth[56,57]. Another study suggested a nonlinear effect of pore size on bone tissue regeneration for

Table 4. In vivo assessment of borate-based bioactive glasses for bone regeneration.

Study	Scaffold type	Defect and treatment duration	Porosity (%) and pore size (μm)	New bone formation
Gu *et al*.[55,58]	3D-printed grid-like and pressed short fibers	Φ4.6 mm rat cranial – 6 and 12 weeks	47 and 150 – 300 (grid-like) 58 and 50 – 550 (pressed fibers)	Grid-like 6% (6 weeks) 9% (12 weeks) pressed fibers 20% (12 weeks)
Bi *et al*.[30]	Pressed short fibers	Φ4.6 mm rat cranial – 12 weeks	58 and 50 – 500	15%
Bi *et al*.[59]	3D-printed grid-like and freeze drying	6 mm femur 12 weeks	50 and 140 – 250 (grid-like) 47 and 50 – 150 (freeze drying)	26% (grid-like) and 28% (freeze drying)
Wang *et al*.[60,61]	Polymer foam replication	Φ5.0 mm rat cranial – 8 weeks	80 – 89 and 200 – 400	16% (undoped) 29% (Zn doped) 30% (Cu coped)
This study	SLS	Φ4.6 mm rat cranial – 6 weeks	47 – 54 and 1000	6% (no BMP-2) 40% (BMP-2)

polymer scaffolds with 100 – 300 μm pores having an accelerated effect during the first 4 weeks which quickly fell off after 8 weeks of implantation[27]. If that was the case, grid-like borate glass scaffolds with 150 – 300 μm pores should have higher bone formation within 6 weeks in comparison to SLS scaffolds with 1 mm pore size used in this study. Since this was not observed, nonlinear effects of pore sizes on bone regeneration might not be the case for bioresorbable material scaffolds. The qualitative comparison of H&E stains reported in other *in vivo* studies (**Table 4**) showed that bone formation was mainly through the infiltration of fibrous tissue and initiated from the dura mater side of the scaffold. This is in strong agreement with our study. In addition, the quantification of bone growth as 6% in our study compared to 15% in other studies could be subject to a large deviation.

In our previous study, diamond and gyroid architecture scaffolds made with silicate glass showed significant cell proliferation *in vitro* in comparison to cubic scaffolds[34]. Nevertheless, a significant difference in *in vivo* bone growth for diamond scaffolds versus cubic scaffolds was not observed in the current study. However, qualitative analysis indicated a more mature fibrous tissue in defects treated with diamond scaffolds. While the fibrous tissue in the diamond scaffold appears to have osteocytes, indicating that it has almost transformed into new bone, while the fibrous tissue from the central region of the cubic scaffold appears to be soft tissue. This indicates that it would take longer to form new bone within the cubic scaffold in comparison to the diamond scaffold. Faster maturation of fibrous tissue in the diamond scaffold could be attributed to the curvature that drives the fibrous tissue, and thereby osteoblasts and osteocytes, to orient and adapt to the pore geometry. A scaffold's mechanical properties are known to influence cell proliferation, differentiation, and bone regeneration[62]. However, the mechanical properties could not be a major factor in a calvarial defect model because it is not for load-bearing application, and studies showed no apparent correlation between scaffold compressive modulus, strength, and bone formation (**Table 4**). It is likely that scaffold material (e.g. silicate glass, borate glass, or HA), pore size, porosity, and architecture play a more important role than strength and modulus in a calvarial defect model. Moreover, there was no significant difference in compressive strength and modulus of cubic (4.3 MPa and 0.7 GPa) and diamond (3.5 MPa and 0.6 GPa) scaffolds used for *in vivo* assessment in this study. Therefore, the difference in bone and fibrous tissue formation is more likely due to architecture.

This study demonstrated the fabrication of biomimetic borate glass scaffolds using the SLS process. The faster degradation of borate glass scaffolds was likely because of the increased surface area associated with the SLS part surface roughness. After immersion in SBF for 1 week, SLS borate glass scaffolds showed a 60% – 90% reduction in strength, depending on the architecture. This data provide an opportunity to design an implant to repair defect sites based on the strength requirements of the skeletal region. This shows the potential of the laser powder bed fusion process for bone repair by utilizing a combination of architecture, porosity, and choice of bioactive glass for scaffold fabrication. For example, diamond architecture could be the choice for an implant fabricated with a bioactive glass having a slower degradation rate (such as silicate glass) as diamond scaffolds degrade faster and have the potential to provide more bone regeneration *in vivo*. In a similar fashion, if high structural integrity is needed for tissue repair in a load-bearing bone, a lower porosity design using a cubic or spherical architecture could be the best option to slow down degradation. The laser powder bed fusion process can be used to manufacture bioactive glass scaffolds for bone repair with controlled degradation by selecting the appropriate geometric design and material combinations.

4 Conclusions

Borate-based bioactive glass scaffolds with different porosities and pore sizes were fabricated using the SLS process, with scaffold porosities varying from 30% to 60% and pore sizes varying from 0.5 to 1.2 mm. Scaffold strength and

degradation *in vitro* are dependent on porosity and architecture. Among the five different architectures considered in this study (cubic, spherical, x, gyroid, and diamond), cubic scaffolds provided the highest compressive strength (16 MPa) at lower porosities (<35%) and spherical scaffolds had the highest strength (4 MPa) at higher porosities (>60%). Gyroid and diamond scaffolds recorded greater strength reduction after 1-week immersion in SBF, likely because of their biomimetic architectures mimicking natural bone. This study has shown that powder bed fusion processes can be used to fabricate scaffolds with controlled rates of strength degradation and bone regeneration by selecting appropriate architecture and bioactive glass composition. These scaffolds can be used to repair specific regions of trabecular bone, based on functional requirements. Cubic and diamond scaffolds with ~50% porosity and ~1 mm pore size were used to treat a full-thickness 4.6 mm diameter rat calvarial defect with or without BMP-2. There was no significant difference in mineralized bone formation for defects treated with cubic and diamond architectures after 6 weeks of implantation. However, a higher percentage of fibrous connective tissue and high osteoblast activity was observed in the defects treated with diamond scaffolds. The addition of BMP-2 significantly increased the bone regeneration from 6% (without BMP-2) to 40% of the defect area.

Acknowledgments

The glasses used in this work were provided by Mo-Sci Corporation, Rolla, MO. Authors thank Natalie Holl for help on technical editing and acknowledge the assistance of Jacob Mendez and Bradley Bromet for image analysis.

References

1. Jones JR, 2013, Review of Bioactive Glass: From Hench to Hybrids. *Acta Biomater*, 9:4457–86.
2. Hench LL, 2006, The Story of Bioglass®. *J Mater Sci Mater Med*, 17:967–78.
3. Greenspan D, 2019, Bioglass at 50-A Look at Larry Hench's Legacy and Bioactive Materials. *Biomed Glas*, 5:178–84. DOI: 10.1515/bglass-2019-0014.
4. Rahaman MN, Day DE, Bal BS, *et al*., 2011, Bioactive Glass in Tissue Engineering. *Acta Biomater*, 7:2355–73.
5. Fu Q, Rahaman MN, Fu H, *et al*., 2010, Silicate, Borosilicate, and Borate Bioactive Glass Scaffolds with Controllable Degradation Rate for Bone Tissue Engineering Applications. I. Preparation and *In Vitro* Degradation. *J Biomed Mater Res Part A*, 95A:164–71. DOI: 10.1002/jbm.a.32824.
6. Jung S, Day D, 2009, Conversion Kinetics of Silicate, Borosilicate, and Borate Bioactive Glasses to Hydroxyapatite. *Phys Chem Glas*, 50:85–8.
7. Balasubramanian P, Kolzow J, Chen RR, *et al*., 2018, Boron-containing Bioactive Glasses in Bone and Soft Tissue Engineering. *J Eur Ceram Soc*, 38:855–69.
8. Yuan S, Shen F, Chua CK, *et al*., 2019, Polymeric Composites for Powder-based Additive Manufacturing: Materials and Applications. *Prog Polym Sci*, 91:141–68.
9. Ng WL, Lee JM, Zhou M, *et al*., 2020, Vat Polymerization-based Bioprinting Process, Materials, Applications and Regulatory Challenges IOP Science. *Biofabrication*, 12:022001. DOI: 10.1088/1758-5090/ab6034.
10. Goh GD, Yap YL, Tan HK, *et al*., 2020, Process Structure Properties in Polymer Additive Manufacturing via Material Extrusion: A Review. *Crit Rev Solid State Mater Sci*, 45:113–33. DOI: 10.1080/10408436.2018.1549977.
11. Cai S, Xi J, 2008, A Control Approach for Pore Size Distribution in the Bone Scaffold Based on the Hexahedral Mesh Refinement. *CAD Comput Aided Des*, 40:1040–50. DOI: 10.1016/j.cad.2008.09.004.
12. Melchels FP, Bertoldi K, Gabbrielli R, *et al*., 2010, Mathematically Defined Tissue Engineering Scaffold Architectures Prepared by Stereolithography. *Biomaterials*, 31:6909–16. DOI: 10.1016/j.biomaterials.2010.05.068.
13. Challis VJ, Roberts AP, Grotowski JF, *et al*., 2010, Prototypes for Bone Implant Scaffolds Designed via Topology Optimization and Manufactured by Solid Freeform Fabrication. *Adv Eng Mater*, 12:1106–10. DOI: 10.1002/adem.201000154.
14. Feng J, Fu J, Li Z, *et al*., 2018, A Review of the Design Methods of Complex Topology Structures for 3D Printing. *Vis Comput Ind Biomed Art*, 1:5.
15. Wang G, Shen L, Zhao J, *et al*., 2018, Design and Compressive Behavior of Controllable Irregular Porous Scaffolds: Based on Voronoi-Tessellation and for Additive Manufacturing. *ACS Biomater Sci Eng*, 4:719–27. DOI: 10.1021/acsbiomaterials.7b00916.
16. Ng WL, Chua CK, Shen YF, *et al*., 2019, Print Me An Organ! Why We Are Not There Yet. *Prog Polym Sci*, 97:101145.

DOI: 10.1016/j.progpolymsci.2019.101145.

17. Sing SL, Yeong WY, Wiria FE, *et al*., 2017, Direct Selective Laser Sintering and Melting of Ceramics: A Review. *Rapid Prototyp J*, 23:611–23. DOI: 10.1108/rpj-11-2015-0178.
18. Datsiou KC, Saleh E, Spirrett F, *et al*., 2019, Additive Manufacturing of Glass with Laser Powder Bed Fusion. *J Am Ceram Soc*, 102:4410–4. DOI: 10.1111/jace.16440.
19. Yves-Christian H, *et al*., 2010, Net Shaped High Performance Oxide Ceramic Parts by Selective Laser Melting. In: Physics Procedia. Vol. 5. Elsevier B.V., Berlin, pp. 587–94. DOI: 10.1016/j.phpro.2010.08.086.
20. Verga F, Mario B, Laura C, *et al*., 2020, Laser-based Powder Bed Fusion of Alumina Toughened Zirconia. *Addit Manuf*, 31:100959. DOI: 10.1016/j.addma.2019.100959.
21. Kolan KC, Leu MC, Hilmas GE, *et al*., 2011, Fabrication of 13-93 Bioactive Glass Scaffolds for Bone Tissue Engineering Using Indirect Selective Laser Sintering. *Biofabrication*, 3:025004. DOI: 10.1088/1758-5082/3/2/025004.
22. Goodridge RD, Dalgarno KW, Wood DJ, *et al*., 2006, Indirect Selective Laser Sintering of an Apatite-mullite Glass-Ceramic for Potential Use in Bone Replacement Applications. *Proc Inst Mech Eng Part H J Eng Med*, 220:57–68. DOI: 10.1243/095441105x69051.
23. Van Bael S, Chai YC, Truscello S, *et al*., 2012, The Effect of Pore Geometry on the *In Vitro* Biological Behavior of Human Periosteum-Derived Cells Seeded on Selective Laser-melted Ti6Al4V Bone Scaffolds. *Acta Biomater*, 8:2824–34. DOI: 10.1016/j.actbio.2012.04.001.
24. Zadpoor AA, 2015, Bone Tissue Regeneration: The Role of Scaffold Geometry. *Biomater Sci*, 3:231–45. DOI: 10.1039/c4bm00291a.
25. Ouyang P, Dong H, He X, *et al*., 2019, Hydromechanical Mechanism behind the Effect of Pore Size of Porous Titanium Scaffolds on Osteoblast Response and Bone Ingrowth. *Mater Des*, 183:108151. doi.org/10.1016/j.matdes.2019.108151.
26. Gariboldi MI, Best SM, 2015, Effect of Ceramic Scaffold Architectural Parameters on Biological Response. *Front Bioeng Biotechnol*, 3:151. DOI: 10.3389/fbioe.2015.00151.
27. Roosa SM, Kemppainen JM, Moffitt EN, *et al*., 2010, The Pore Size of Polycaprolactone Scaffolds has Limited Influence on Bone Regeneration in an *In Vivo* Model. *J Biomed Mater Res Part A*, 92:359–68. DOI: 10.1002/jbm.a.32381.
28. Perez RA, Mestres G, 2016, Role of Pore Size and Morphology in Musculo-skeletal Tissue Regeneration. *Mater Sci Eng C*, 61:922–39. DOI: 10.1016/j.msec.2015.12.087.
29. Lin Y, Liu X, Xiao W, *et al*., 2015, Long-term Bone Regeneration, Mineralization and Angiogenesis in Rat Calvarial Defects Implanted with Strong Porous Bioactive Glass (13-93) Scaffolds. *J Non Cryst Solids*, 432:4–13. DOI: 10.1016/j.jnoncrysol.2015.04.008.
30. Bi L, Jung S, Day D, *et al*., 2012, Evaluation of Bone Regeneration, Angiogenesis, and Hydroxyapatite Conversion in Critical-sized Rat Calvarial Defects Implanted with Bioactive Glass Scaffolds. *J Biomed Mater Res Part A*, 100A:3267–75. DOI: 10.1002/jbm.a.34272.
31. Bidan CM, Kommareddy KP, Rumpler M, *et al*., 2013, Geometry as a Factor for Tissue Growth: Towards Shape Optimization of Tissue Engineering Scaffolds. *Adv Healthc Mater*, 2:186–94. DOI: 10.1002/adhm.201200159.
32. Bidan CM, Kommareddy KP, Rumpler M, *et al*., 2012, How Linear Tension Converts to Curvature: Geometric Control of Bone Tissue Growth. *PLoS One*, 7:e36336. DOI: 10.1371/journal.pone.0036336.
33. Rumpler M, Woesz A, Dunlop JW, *et al*., 2008, The Effect of Geometry on Three-dimensional Tissue Growth. *J R Soc Interface*, 5:1173–80.
34. Kolan KC, Thomas A, Leu MC, *et al*., 2015, *In Vitro* Assessment of Laser Sintered Bioactive Glass Scaffolds with Different Pore Geometries. *Rapid Prototyp J*, 21:152–8. DOI: 10.1108/rpj-12-2014-0175.
35. Kolan KC, Leu MC, Hilmas GE, *et al*., 2012, Effect of Material, Process Parameters, and Simulated Body Fluids on Mechanical Properties of 13-93 Bioactive Glass Porous Constructs Made by Selective Laser Sintering. *J Mech Behav Biomed Mater*, 13:14–24. DOI: 10.1016/j.jmbbm.2012.04.001.
36. Kokubo T, Takadama H, 2006, How Useful is SBF in Predicting *In Vivo* Bone Bioactivity? *Biomaterials*, 27:2907–15. DOI: 10.1016/j.biomaterials.2006.01.017.
37. Schindelin J, Arganda-Carreras I, Frise E, *et al*., 2012, Fiji: An Open-source Platform for Biological-image Analysis. *Nat Methods*, 9:676–82. DOI: 10.1038/nmeth.2019.
38. Melchels FP, Barradas AM, van Blitterswijk CA, *et al*., 2010, Effects of the Architecture of Tissue Engineering Scaffolds on Cell Seeding and Culturing. *Acta Biomater*, 6:4208–17. DOI: 10.1016/j.actbio.2010.06.012.
39. Carter DR, Hayes WC, 1976, Bone Compressive Strength: The Influence of Density and Strain Rate. *Science*, 194:1174–6. DOI: 10.1126/science.996549.
40. Wu D, Isaksson P, Ferguson SJ, *et al*., 2018, Young's Modulus of Trabecular Bone at the Tissue Level: A Review. *Acta Biomater*, 78:1–12. DOI: 10.1016/j.actbio.2018.08.001.
41. Freitas GP, Lopes HB, Souza AT, *et al*., 2019, Cell Therapy: Effect of Locally Injected Mesenchymal Stromal Cells

Derived from Bone Marrow or Adipose Tissue on Bone Regeneration of Rat Calvarial Defects. *Sci Rep*, 9:13476. DOI: 10.1038/s41598-019-50067-6.

42. Gibson LJ, Ashby MF, 1982, The Mechanics of Three-Dimensional Cellular Materials. *Proc R Soc A Math Phys Sci*, 382:43–59.
43. Ryshkewitch E, 1953, Compression Strength of Porous Sintered Alumina and Zirconia. *J Am Ceram Soc*, 36:65–8.
44. Duckworth W, 1953, Discussion of Ryshkewitch Paper. *J Am Ceram Soc*, 36:68.
45. Rice RW, 1996, Evaluation and Extension of Physical Property-porosity Models Based on Minimum Solid Area. *J Mater Sci*, 31:102–18.
46. Hattiangadi A, Bandyopadhyay A, 2000, Strength Degradation of Nonrandom Porous Ceramic Structures under Uniaxial Compressive Loading. *J Am Ceram Soc*, 83:2730–6. DOI: 10.1111/j.1151-2916.2000.tb01624.x.
47. Rice RW, 1993, Comparison of Stress Concentration Versus Minimum Solid Area Based Mechanical Property-porosity Relations. *J Mater Sci*, 28:2187–90. DOI: 10.1007/bf00367582.
48. Deliormanl AM, 2012, *In Vitro* Assessment of Degradation and Bioactivity of Robocast Bioactive Glass Scaffolds in Simulated Body Fluid. *Ceram Int*, 38:6435–44. DOI: 10.1016/j.ceramint.2012.05.019.
49. Deliormanli AM, Rahaman MN, 2012, Direct-write Assembly of Silicate and Borate Bioactive Glass Scaffolds for Bone Repair. *J Eur Ceram Soc*, 32:3637–46. DOI: 10.1016/j.jeurceramsoc.2012.05.005.
50. Kolan KC, Semon J, Bromet B, *et al*., 2019, Bioprinting with Human Stem Cells-laden Alginate-gelatin Bioink and Bioactive Glass for Tissue Engineering. *Int J Bioprint*, 5:3. DOI: 10.18063/ijb.v5i2.2.204.
51. Murphy C, Kolan K, Li W, *et al*., 2017, 3D Bioprinting of Stem Cells and Polymer/Bioactive Glass Composite Scaffolds for Tissue Engineering. *Int J Bioprinting*, 3:54–64. DOI: 10.18063/ijb.2017.01.005.
52. Hustedt JW, Blizzard DJ, 2018, The Controversy Surrounding Bone Morphogenetic Proteins in the Spine: A Review of Current Research. In: Getting to Good: Research Integrity in the Biomedical Sciences. Vol. 87. Springer International Publishing, Basel, Switzerland, pp. 9–22.
53. Carragee EJ, Chu G, Rohatgi R, *et al*., 2013, Cancer Risk After Use of Recombinant Bone Morphogenetic Protein-2 for Spinal Arthrodesis. *J Bone Joint Surg Am*, 95:1537–45. DOI: 10.1016/j.spinee.2013.11.026.
54. Injamuri S, Rahaman MN, Shen Y, *et al*., 2020, Relaxin Enhances Bone Regeneration with BMP-2-Loaded Hydroxyapatite Microspheres. *J Biomed Mater Res Part A*, 108:1231–42. DOI: 10.1002/jbm.a.36897.
55. Gu Y, Bal B, Rahaman N, *et al*., 2015, *In Vivo* Evaluation of Scaffolds with a Grid-Like Microstructure Composed of a Mixture of Silicate (13-93) and Borate (13-93B3) Bioactive Glasses. John Wiley and Sons, Inc., New York, pp. 53–64. DOI: 10.1002/9781119040392.ch6.
56. Karageorgiou V, Kaplan D, 2005, Porosity of 3D Biomaterial Scaffolds and Osteogenesis. *Biomaterials*, 26:5474–91. DOI: 10.1016/j.biomaterials.2005.02.002.
57. Sopyan I, Gunawan, 2013, Development of Porous Calcium Phosphate Bioceramics for Bone Implant Applications: A Review. *Recent Patents Mater Sci*, 6:238–52. DOI: 10.2174/18744648113069990012.
58. Gu Y, Huang W, Rahaman MN, *et al*., 2013, Bone Regeneration in Rat Calvarial Defects Implanted with Fibrous Scaffolds Composed of a Mixture of Silicate and Borate Bioactive Glasses. *Acta Biomater*, 9:9126–36. DOI: 10.1016/j.actbio.2013.06.039.
59. Bi L, Zobell B, Liu X, *et al*., 2014, Healing of Critical-size Segmental Defects in Rat Femora Using Strong Porous Bioactive Glass Scaffolds. *Mater Sci Eng C*, 42:816–24. DOI: 10.1016/j.msec.2014.06.022.
60. Wang H, Zhao S, Xiao W, *et al*., 2015, Three-dimensional Zinc Incorporated Borosilicate Bioactive Glass Scaffolds for Rodent Critical-sized Calvarial Defects Repair and Regeneration. *Colloids Surfaces B Biointerfaces*, 130:149–56. DOI: 10.1016/j.colsurfb.2015.03.053.
61. Wang H, Zhao S, Zhou, J, *et al*., 2014, Evaluation of Borate Bioactive Glass Scaffolds as a Controlled Delivery System for Copper Ions in Stimulating Osteogenesis and Angiogenesis in Bone Healing. *J Mater Chem B*, 2:8547–57. DOI: 10.1039/c4tb01355g.
62. Hart NH, Nimphius S, Rantalainen T, *et al*., 2017, Mechanical Basis of Bone Strength: Influence of Bone Material, Bone Structure and Muscle Action. *J Musculoskelet Neuronal Interact*, 17:114–39.

ORIGINAL ARTICLE

Combined Porogen Leaching and Emulsion Templating to produce Bone Tissue Engineering Scaffolds

Robert Owen[1,2,3], Colin Sherborne[2], Richard Evans[4], Gwendolen C. Reilly[1,2], Frederik Claeyssens[1,2]*

[1]Department of Materials Science and Engineering, INSIGNEO Institute for in silico Medicine, University of Sheffield, UK

[2]Department of Materials Science and Engineering, The Kroto Research Institute, University of Sheffield, UK

[3]Regenerative Medicine and Cellular Therapies, School of Pharmacy, University of Nottingham Biodiscovery Institute, University Park, UK

[4]Bioengineering, Interdisciplinary Programmes Engineering, University of Sheffield, UK

Abstract: Bone has a hierarchy of porosity that is often overlooked when creating tissue engineering scaffolds where pore sizes are typically confined to a single order of magnitude. High internal phase emulsion (HIPE) templating produces polymerized HIPEs (polyHIPEs): highly interconnected porous polymers which have two length scales of porosity covering the 1–100 µm range. However, additional larger scales of porosity cannot be introduced in the standard emulsion formulation. Researchers have previously overcome this by additively manufacturing emulsions; fabricating highly microporous struts into complex macroporous geometries. This is time consuming and expensive; therefore, here we assessed the feasibility of combining porogen leaching with emulsion templating to introduce additional macroporosity. Alginate beads between 275 and 780 µm were incorporated into the emulsion at 0, 50, and 100 wt%. Once polymerized, alginate was dissolved leaving highly porous polyHIPE scaffolds with added macroporosity. The compressive modulus of the scaffolds decreased as alginate porogen content increased. Cellular performance was assessed using MLO-A5 post-osteoblasts. Seeding efficiency was significantly higher and mineralized matrix deposition was more uniformly deposited throughout porogen leached scaffolds compared to plain polyHIPEs. Deep cell infiltration only occurred in porogen leached scaffolds as detected by histology and lightsheet microscopy. This study reveals a quick, low cost and simple method of producing multiscale porosity scaffolds for tissue engineering.

Keywords: Polymerized high internal phase emulsions, Emulsion templating, Alginate, Multiscale porosity, Bone tissue engineering

***Corresponding Author:** Frederik Claeyssens, Department of Materials Science and Engineering, The Kroto Research Institute, University of Sheffield, UK; f.claeyssens@sheffield.ac.uk

Received: March 06, 2020; ***Accepted:*** April 01, 2020; ***Published Online:*** April 30, 2020

Citation: Owen R, Sherborne C, Evans R, *et al*., 2020, Combined Porogen Leaching and Emulsion Templating of Bone Tissue Engineering Scaffolds, *Int J Bioprint*, 6(2):265. DOI: org/10.18063/ijb.v6i2.265

1 Introduction

Native bone has a hierarchical structure with a range of pore sizes that span multiple length scales[1]. Inclusion of this multiscale porosity when producing bone tissue engineering scaffolds is often overlooked with pore sizes typically confined to a single order of magnitude. However, it has been demonstrated that a multiscale porosity enhances *in vitro* and *in vivo* performance of scaffolds[2-4]. The reason for this is that different size pores promote different functions. Smaller, well interconnected cell-scale porosities promote cell proliferation, migration, and nutrient diffusion, while pore sizes of at least 50 µm but ideally >300 µm have been reported as beneficial for osseous tissue deposition[5-7].

Polymerized high internal phase emulsions (polyHIPEs) are highly porous materials well suited for three-dimensional (3D) cell culture and tissue engineering, and classically have porosity at

two length-scales: a larger bulk porosity typically in the region of 30 – 50 μm which is interconnected by smaller (1 – 5 μm) pores[8-18]. As the name suggests, polyHIPE scaffolds are initially formulated as an emulsion. These are typically created by mixing a hydrophobic monomer, crosslinker, initiator, and a suitable surfactant to form the continuous phase of the emulsion, then slowly adding an aqueous internal phase. This creates a water-in-oil (W/O) emulsion where the constant mixing breaks the water into isolated droplets dispersed throughout the continuous monomer phase. To form a high internal phase emulsion (HIPE), the internal phase volume ratio must exceed 74% of the total emulsion as this ensures that droplets form interconnects when polymerized. The continuous phase can be polymerized using either ultraviolet (UV) light or thermal curing; afterward the internal phase drains away leaving behind a highly porous polyHIPE[19].

The parameters used during the emulsification process directly affect the structure of the final polyHIPE material. Physical actions such as the speed of mixing[20,21], the rate at which water is added[22] and the emulsion temperature[23] all affect internal phase dispersion, geometry, and the final porosity as the droplets act as a template for the continuous phase to polymerize around. Furthermore, the type and quantity of the emulsion constituents also affect the final architecture, including the internal phase volume[24], monomer type[25,26], solvent addition[17], concentration of the surfactant (or particles in Pickering emulsions)[21,27], initiator solubility[28], and the concentration of electrolytes in the aqueous phase[26]. All these affect porosity and/or pore interconnectivity of the polyHIPE. The commercial success of Alvetex®, a polystyrene polyHIPE, shows the suitability of this class of materials for 3D cell culture[29]. However, these membranes are only 200 μm thick as cellular penetration into the bulk material is limited, primarily because of factors such as diminishing mass transport and nutrient availability. Furthermore, with polyHIPE scaffolds created from hydrophobic monomers, surface treatments such as plasma etching/coating are necessary to overcome the inherent hydrophobicity of the material. This reduces maximum scaffold thickness as these treatment methods have limited depth penetration into the material[30].

These limitations can be overcome by introducing another tier of porosity into the polyHIPE network in the form of larger (>200 μm) pores[8]. This creates a multiscale porosity scaffold ideal for bone tissue engineering with pore sizes over three length-scales: pore interconnects, standard polyHIPE pores, and additional macropores. Approaches to creating larger pores inherent in the polyHIPE have focused on creating large water droplets in the initial emulsion. This can be done using high temperatures or solvents to destabilize the emulsion in a controlled way to cause droplets of water to coalesce into larger ones[23]. However, as these changes affect the entire HIPE and larger droplets are formed *in lieu* of smaller ones, this means that a further scale of porosity is not added. Another limitation to this approach is the effect on pore interconnectivity. Pore interconnects form during polymerization between adjacent water droplets if the film of continuous phase surrounding the droplets is sufficiently thin. Below this threshold, the contraction of the material as it polymerizes causes small interconnecting pores to form[31]; hence, monomers that have high shrinkage during polymerization create more interconnectivity in the polyHIPE scaffold[25]. Larger water droplets have a thicker continuous phase film surrounding them which will be more resistant to these contraction forces, resulting in fewer interconnects.

An alternative approach to introduce an additional, larger scale of porosity to the polyHIPEs is by 3D printing the HIPE in additive manufacture. By building structures from polyHIPE struts that do not exceed the inherent depth limitations of traditionally manufactured polyHIPEs, porous scaffolds capable of filling larger defects can be produced[8]. This approach results in multiscale, hierarchical, and interconnected porous scaffolds that have superior nutrient and waste transport while benefiting tissue regeneration. They have smaller (1 – 50 μm) microscale pores that benefit cellular performance and larger pores (>300 μm) that facilitate ingrowth and permit large quantities of extracellular matrix

deposition and vascularization[32]. PolyHIPE-based additive manufacturing techniques by which this is achievable include emulsion extrusion[33,34] and microstereolithography-based approaches[8,9,13,35,36]. The latter has the ability to rapidly polymerize the emulsions and, as we demonstrated recently, inclusion of light-absorbers can afford tight control over the final architecture[8-10,13].

However, 3D printing emulsions using additive manufacturing technologies require expensive equipment and the trade-off for such architectural fidelity is manufacture speed[9]. In applications where high levels of control over architecture are essential, such as investigations into the effects of geometry or the production of patient-specific scaffolds[37], clearly the slower speed of production is worthwhile. Nevertheless, for more generic 3D cell culture applications using stereolithography can have high initial setup costs and be time intensive[38,39]. Therefore, identifying a simpler approach to introducing a multiscale porosity is warranted. One potential avenue is particulate leaching.

Solvent casting/particulate leaching is a conventional approach to creating scaffold porosity. This process involves dissolving a polymer in a solvent such as dimethylformamide or chloroform then casting around a porogen such as crystals of sugar or salt[40-42]. These types of porogen are readily available, cheap, and insoluble in hydrophobic solvents. However, this technique can cause limited pore interconnectivity as there is not sufficient contact between the porogens to have a continuous porosity, resulting in "skin" forming around the pores during solvent evaporation. This results in samples often having to be thin to ensure even porogen dispersal and removal[43,44]. This limitation is alleviated when casting a HIPE around a porogen as the water droplets are deformable ensuring close contact with the porogen. Providing that the porogen material facilitates an open surface porosity, interconnectivity between the emulsion and the voids left by the porogen can be achieved[19]. As sugar and salt are water-soluble, they are unsuitable porogens for polyHIPEs as they would dissolve in the aqueous internal phase. Therefore, it is essential to identify a porogen that is insoluble in both emulsion phases whilst giving an open surface porosity. We hypothesize that one such material is alginate, a naturally derived polysaccharide commonly used in tissue engineering due to its biocompatibility, biodegradability, and abundant availability[45]. By incorporating alginate beads into the HIPE, then polymerizing and subsequently dissolving the alginate, an additional, larger scale of porosity can be quickly, easily and cheaply introduced to the polyHIPE-based scaffolds.

To test this hypothesis, we blended HIPEs with alginate beads at either 50 or 100 wt% of the initial emulsion volume to create polyHIPE scaffolds with a multiscale porosity ranging from 1 to 1000 μm. These were compared to standard polyHIPE materials with a hierarchy of porosity ranging from 1 to 100 μm. To evaluate their performance, MLO-A5 murine post-osteoblasts were cultured for 14 days, with cell proliferation and bone-like matrix deposition by histology and lightsheet microscopy assessed.

2 Materials and methods

Unless otherwise stated, all materials were sourced from Sigma-Aldrich, UK.

2.1 Alginate bead synthesis

Sodium alginate was dissolved in deionized water (diH_2O) at 3 wt% while being mixed (350 rpm) on a magnetic stirrer hot-plate maintained at 30°C. To create the beads, this solution was loaded into a 3 mL fluid dispensing barrel (Nordson EFD), sealed using a dispensing piston (InterTronic), and injected through a 30 gauge tip (internal diameter 0.15 mm, Nordson EFD) from a height of 100 mm into a cross-linking solution of calcium chloride (20 wt% in diH_2O) using a mechanical syringe pump (Ultra 2800 Positive Displacement Dispenser, Nordson EFD) at 0.2195 mL/s. Beads below 710 μm were selectively collected through sieving and stored in diH_2O until needed. To assess size distribution, 50 images were taken of bead populations (Motic Images Plus software) and diameters measured using Fiji[46,47].

2.2 PolyHIPE synthesis

For the continuous phase of the emulsion, the monomer 2-ethylhexyl acrylate (26 g) was mixed with the crosslinker trimethylolpropane triacrylate (7 g). The surfactant Hypermer B246-SO-(MV) was added at 10 wt% (3.3 g) relative to the total weight of the acrylates (33 g) and mixed until dissolved. To create the emulsion, 2 g of this stock solution was taken and a photoinitiator (diphenyl (2,4,6-trimethylbenzoyl) phosphine oxide/2-hydroxy-2-methylpropiophenone) was added at 5 wt% (0.1 g). This solution was continuously mixed at 350 rpm using a paddle stirrer (Pro40 scientific stirrer, SciQuip). While mixing, diH_2O (diH_2O, 18 mL) was added dropwise to form a 90 vol% W/O HIPE. Where alginate beads were incorporated, beads were patted dry and weighed, then either 50 or 100 wt% relative to the total amount of emulsion was added to the HIPE (e.g. 100 wt% means 4 g of beads were added to 4 g of HIPE). The blend was then stirred for a further 2 min at 350 rpm to homogenize the beads. Herein, these three compositions will be referred to as "plain," "50 wt%," and "100 wt%" polyHIPEs. This refers to the content of the alginate bead porogen in the HIPE.

To polymerize the emulsion, it was poured into a square, PTFE mold with a glass base and top (45 × 45 × 6.2 mm), filled with approximately 12.5 mL of HIPE and placed under 100 W UV light (Omnicure S1500 with adjustable spot collimating adaptor, Excelitas Technologies), for 180 s on both sides. With these dimensions and exposure times the polyHIPEs were fully cured with no cavity left in the center of the monolith. The polyHIPEs were removed from the mold and washed in acetone to remove any uncured monomer. To remove the alginate, polyHIPEs were soaked in 0.2 M sodium citrate in diH_2O for 2 h with sonication. The samples were then dried overnight under vacuum. A schematic of the fabrication process is given in **Figure 1**. To produce cubes for cell culture the outer surfaces, including the top surface and polymer skin on the glass cured sides, were removed using a scalpel. The remaining bulk polyHIPE was then cut into 5 × 5 × 5 mm cubes.

To produce cylinders for mechanical testing, the HIPE was polymerized in a 3 mL syringe (internal diameter 8.2 mm). The cylinders were washed using the same methods described above and then cut into 10 mm lengths. The surface skin surrounding the outside of these cylinders was retained to keep a constant volume of material.

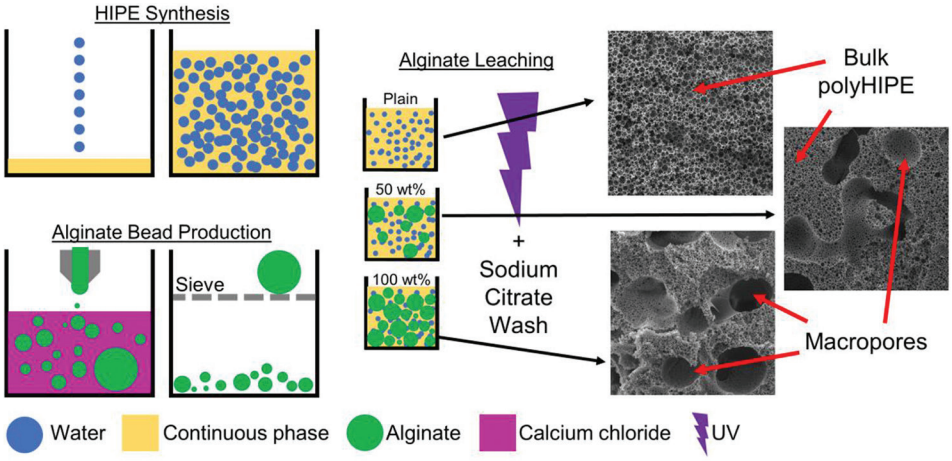

Figure 1. Schematic detailing the alginate-leached polymerized high internal phase emulsions synthesis. A 90% internal phase volume HIPE is synthesized by adding water to the continuous phase. Alginate beads are produced by injecting an alginate solution to calcium chloride and sieving. Alginate beads are then mixed into HIPEs at either 0, 50 or 100 wt% of the HIPE. Emulsions are then UV polymerized, washed in acetone and the alginate dissolved using sodium citrate. Macropores within the bulk of the polyHIPE left by alginate beads are clearly visible in the 50 and 100 wt% scaffolds.

2.3 Scanning electron microscopy (SEM)

Samples were sputter coated with gold (SC500, Emscope) to improve conductivity before imaging (XL-20 SEM, Philips).

2.4 Mechanical testing

Compressive testing was performed on a BOSE ElectroForce 3200 with a 450 N load cell at a rate of 0.01 mm/s to a maximum displacement of 4 mm. The samples were placed centrally on parallel compression plates and a preload of 1 N applied before test initiation. The compressive modulus was calculated from the force-displacement curves.

2.5 Plasma modification

To increase hydrophilicity for cell culture, polyHIPE samples were air plasma treated (Zepto W6 Plasma System, Diener Electronic). The samples were placed uniformly on a flat aluminum foil wrapped stage and placed centrally in the plasma chamber. A range of parameters were tested as charring readily occurred in the particulate leached polyHIPEs. The final parameters used were 15 W at an initial pressure of 0.4 mbar for 1 min.

2.6 Cell culture

MLO-A5 murine post-osteoblasts (kindly donated by Dr. Lynda Bonewald, University of Missouri) were used for all experiments. Cells were passaged in gelatin-coated flasks in basal media (BM) consisting of alpha-minimum essential medium (alpha-MEM) (Lonza, UK) with 10% fetal bovine serum (FBS, Labtech, UK), 2 mM L-glutamine, 100 U/mL penicillin, and 100 µg/mL streptomycin.

To sterilize, scaffolds were placed in 70% ethanol and put under vacuum to remove all air. After 90 min, ethanol was exchanged for phosphate-buffered saline (PBS) and orbitally shaken at 150 rpm for 15 min. The washing stage was repeated a further 2 times, then PBS was exchanged for BM for 1 h. Media were removed from the scaffolds for seeding.

To seed, scaffolds were placed in a 96 well plate. 350,000 MLO-A5 in 100 µL BM were added to the well, just covering the top scaffold surface. The seeding suspension was gently pulsed by manual pipetting every 45 min to improve seeding distribution. After 2 h, scaffolds were transferred to a 48 well plate so that only adhered cells remained. Cell viability (PrestoBlue) was quantified to determine baseline cell numbers, then scaffolds were maintained in supplemented media (SM) consisting of BM with 5 mM beta-glycerolphosphate and 50 µg/mL ascorbic acid 2-phosphate. Media were changed every 2 – 3 days.

2.7 Cell viability

Viability was quantified on days 0, 7, and 14 by PrestoBlue which measures metabolic activity. PrestoBlue reagent was diluted 1:10 in Hank's Balanced Salt Solution. 1 mL was added to each well and incubated for 1 h. 200 µL of the reduced solution was then transferred in triplicate to a black 96 well plate and the fluorescence measured on a plate reader (Tecan infinite 200-pro, λ_{ex} 540 nm, λ_{em} 590 nm). Scaffolds were rinsed in PBS before adding fresh SM.

2.8 Mineralized matrix deposition

Calcium and collagen deposition were quantified on days 7 and 14 by alizarin red S (ARS) and direct red 80 (DR80), respectively, as previously reported Owen *et al*.[48] Briefly, the samples were rinsed twice in PBS then fixed by immersion in 3.7% formaldehyde for 30 min. Scaffolds were rinsed twice in diH_2O, and then submerged in 1 w/v% ARS in diH_2O for 30 min to stain for calcium. Stained samples were washed repeatedly in diH_2O until wash water remained clear, then air dried and photographed. To quantify, scaffolds were submerged in 1 mL 5% perchloric acid and orbitally shaken for 15 min at 100 rpm. 150 µL was then transferred in triplicate to a 96 well plate and read at an absorbance of 405 nm (Tecan infinite 200-pro). The concentration of ARS was determined from a standard curve. Scaffolds were then washed 3 times in diH_2O before immersing in 1 w/v% DR80 in saturated picric acid for 1 h to stain for collagen. Stained samples were washed repeatedly in diH_2O until wash water

remained clear, then air dried and photographed. To quantify, scaffolds were submerged in 1 mL of 0.2 M sodium hydroxide: methanol and orbitally shaken for 15 min at 100 rpm. 150 μL was then transferred in triplicate to a 96 well plate and read at an absorbance of 540 nm (Tecan infinite 200-pro). The concentration of DR80 was determined from a standard curve.

2.9 Histology

Scaffold infiltration was assessed on days 7 and 14 by histology. Scaffolds were fixed as above before being submerged in optimal cutting temperature medium (Leica) and placed under vacuum for 1 h then snap-frozen in liquid nitrogen. Sections were obtained using a cryostat (Leica CM1860 UV) at −24°C at 10 m thickness, mounted onto a glass slide and stained with hematoxylin and eosin. After staining, the samples were preserved under a cover glass and imaged under a Motic microscope using a digital camera.

2.10 Lightsheet microscopy

As a further measure of cell ingress, live/dead staining was performed on day 14 and assessed by lightsheet microscopy. Scaffolds were rinsed in PBS then stained in 2 μM calcein AM (live cells) in PBS for 30 min at room temperature. Scaffolds were then rinsed in PBS, submerged in 20 μg/mL propidium iodide (dead cells) in alpha-MEM for 5 min at room temperature, then rinsed twice in PBS. Scaffolds were then cut using a scalpel (one vertical and one horizontal) so that internal surfaces could be imaged to assess ingrowth.

To image through lightsheet microscopy (Z.1 lightsheet microscope, Zeiss), scaffold sections were mounted in 0.8 vol% agarose in diH_2O in glass capillaries (size 4, Zeiss). Two 10 × NA 0.2 illumination optics (Zeiss) were used to illuminate the samples in combination with a W plan-apochromat 20 ×/1.0 objective (Zeiss). The samples were excited using a 405 nm (20 mW) and a 488 nm (50 mW) laser. Z-stacks were taken and a maximum projection image created using the Bio-Formats plug-in for Fiji[49].

2.11 Statistical analysis

All statistical analysis was performed in GraphPad Prism (version 7.00). Data presented as mean ± standard deviation. Compressive moduli were compared by one-way analysis of variance (ANOVA) with Tukey's post-test. Cell culture results were compared by two-way ANOVA with Tukey's post-test. Mineral and collagen quantification are normalized to the "plain polyHIPE" at each time point. The differences were considered significant when $P < 0.05$ (*) and are indicated on the figures and in the legend. All cell culture experiments were repeated twice in triplicate.

3 Results

3.1 Alginate porogen leaching within polyHIPEs creates multiscale porosity

Alginate beads were created by injecting the alginate solution through a 30 G needle into 0.2 M calcium chloride solution at 0.2195 mL/s before passing through a 710 μm sieve. The size distribution of sieved alginate beads fitted a Gaussian distribution with diameters ranging from 275 μm to 780 μm, with a modal range bead size of 500-550 μm and a mean diameter was 532 μm (**Figure 2A**). A small number of beads exceeded the 710 μm sieve mesh size due to bead deformation during sieving. There was no further sieving or intentional separation of the alginate beads into different sizes.

A polyHIPE with multiscale porosity was created when alginate beads were mixed into the HIPE before polymerization. SEM images of plain (0 wt%, **Figure 2B and C**), 50 wt% (**Figure 2D and E**), and 100 wt% (**Figure 2F and G**) polyHIPEs reveal the macroporosity present in the material when alginate beads were incorporated. Pore sizes ranged from ~1 to 10 μm for the polyHIPE pore interconnects, ~10 to 50 μm for the polyHIPE emulsion pores, and up to ~780 μm for the alginate bead porogen pores. At 100 wt%, macropores formed by alginate-leaching frequently interconnected, leaving large channels throughout the scaffold. The polymer struts at the interface of the bulk polyHIPE porosity and the pores formed

by the alginate beads are smooth and form an open porosity with a similar morphology to the polyHIPE surface that cures against air on the top of the emulsion.

3.2 Porogen leaching of polyHIPEs decreases the compressive modulus

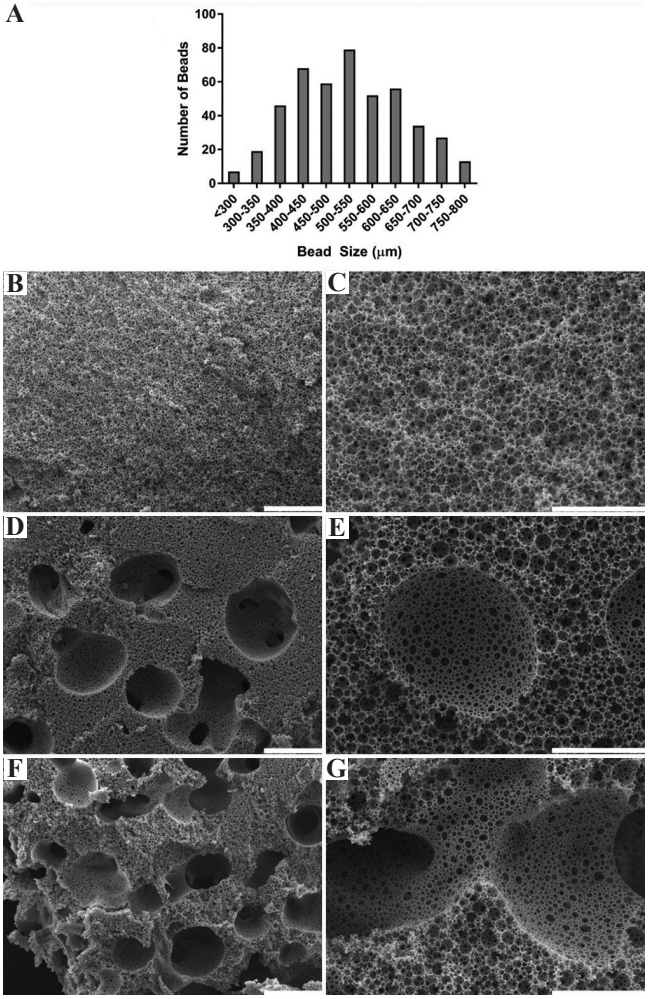

Figure 2. (A) Alginate bead size distribution after sieving. Low (B, D, F, scale bars 500 μm) and high (C, E, G, scale bars 200 μm) magnification scanning electron microscopy images of (B and C) plain polymerized high internal phase emulsions (polyHIPEs), (D and E) 50 wt% alginate bead polyHIPEs, and (F and G) 100 wt% alginate bead polyHIPEs. Large macropores left by alginate beads clearly visible in the 50 and 100 wt% polyHIPEs (D-G), with interconnection between macro pores occurring at the highest wt% (G).

The compressive modulus of the polyHIPE decreased as alginate bead content increased (**Figure 3**). A linear relationship was observed between wt% of alginate beads and compressive moduli ($R^2 = 0.998$).

3.3 Porogen leached polyHIPE had superior mineralized matrix distribution

Seeding efficiency was significantly higher on the 100 wt% alginate porogen leached polyHIPE scaffolds in comparison to plain scaffolds, with approximately 30% higher metabolic activity observed on day 0 ($P < 0.05$, **Figure 4A**). By day 14, metabolic activity was still significantly higher (100 wt% vs. plain, $P < 0.05$). Calcium deposition by ARS staining was greatest on the plain scaffold in comparison to both porogen leached scaffolds on day 7 ($P < 0.05$), but there was no significant difference by day 14 (**Figure 4B**). Collagen deposition by DR80 staining on the 50 wt% polyHIPEs was significantly lower on day 7 in comparison to 100 wt% polyHIPEs ($P < 0.05$), with no significant differences between any group

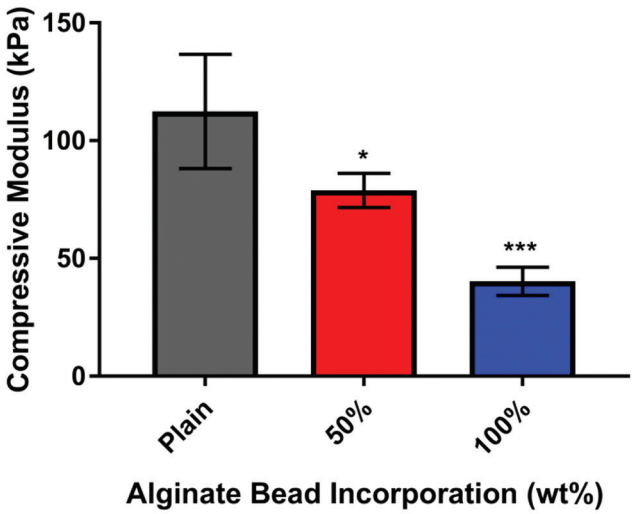

Figure 3. Compressive modulus of polymerized high internal phase emulsions (polyHIPEs) at different alginate bead incorporation. Porogen leaching with alginate significantly reduced the compressive moduli at 50 wt% ($P < 0.05$) and 100 wt% ($P < 0.001$) in comparison to plain polyHIPEs ($n = 4$).

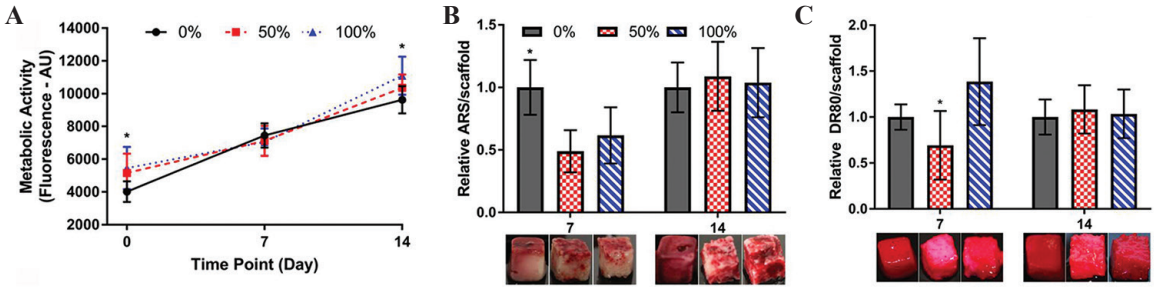

Figure 4. Cell growth and mineralized matrix deposition on polymerized high internal phase emulsions (polyHIPE) scaffolds. (A) Metabolic activity over 14 days, 100 wt% significantly higher than plain on day 0 and 14 ($P < 0.05$). (B) Calcium deposition on days 7 and 14. Typical mineral staining for each condition shown immediately below each bar. Plain significantly higher than 50 wt% and 100 wt% on day 7 ($P < 0.05$), no significant differences by day 14. (C) Collagen deposition on days 7 and 14. Typical collagen staining for each condition showed immediately below each bar. 50 wt% had significantly less collagen than 100 wt% on day 7 ($P < 0.05$), no significant differences by day 14. Matrix staining is confined to the outer surfaces on plain polyHIPEs at both time points, whereas in alginate-leached polyHIPEs, penetration into the bulk of the material is visible.

by day 14. For plain scaffolds, both ARS and DR80 staining remained confined to the exterior scaffold surfaces at both time points. However, on alginate-leached scaffolds, positive staining was observed deeper within the bulk of the material.

3.4 Cell ingrowth is superior in porogen leached polyHIPE scaffolds

In porogen leached scaffolds, cell infiltration is visible much further into the scaffold, with the greatest ingrowth observed in the 100 wt% scaffolds (**Figure 5**). In plain scaffold cells are constrained to the exterior surface and first 2 – 3 rows of polyHIPE pores, achieving a maximum infiltration distance of approximately 50 µm. In contrast, in the 50 wt% scaffolds cellular penetration had reached a depth of approximately 200 µm by day 7 and up to 450 µm by day 14. For the 100 wt% scaffolds, infiltration depths over 600 µm from the outer surface were observed at both time points.

3.5 Cells remain viable within the center of the porogen leached polyHIPE scaffolds

Live/dead staining assessed by lightsheet microscopy was performed on day 14. After staining, the samples were cut horizontally and vertically and placed into the lightsheet microscope to image the internal surfaces of the samples and assess cell ingrowth. The external seeding surface is on the right side of each image.

On the plain scaffold, cells were confined to the scaffold surface, with no cell ingrowth past the first layers of pores (**Figure 6A**). In the 50 wt% porogen leached scaffold, viable cells were visible over the internal network of the scaffold, although a higher concentration of dead cells was present further into the structure (**Figure 6B**). For the 100 wt% scaffold identifying the edge of the scaffold was more difficult, as there was no clear linear region due to the high macroporosity. The cells were visible deep into the scaffold internal network and were predominately viable (green) cells (**Figure 6C**). Due to the autofluorescence of the polyHIPE material, there is a weak green signal throughout the imaging.

4 Discussion

In this study, we combined alginate bead porogen leaching with emulsion templating to introduce an additional, larger length-scale of porosity to polyHIPEs, creating a multiscale porosity over three length-scales. To the best of our knowledge, this is the first-time such multiscale porous polyHIPEs have been fabricated using a single-step alginate porogen leaching approach.

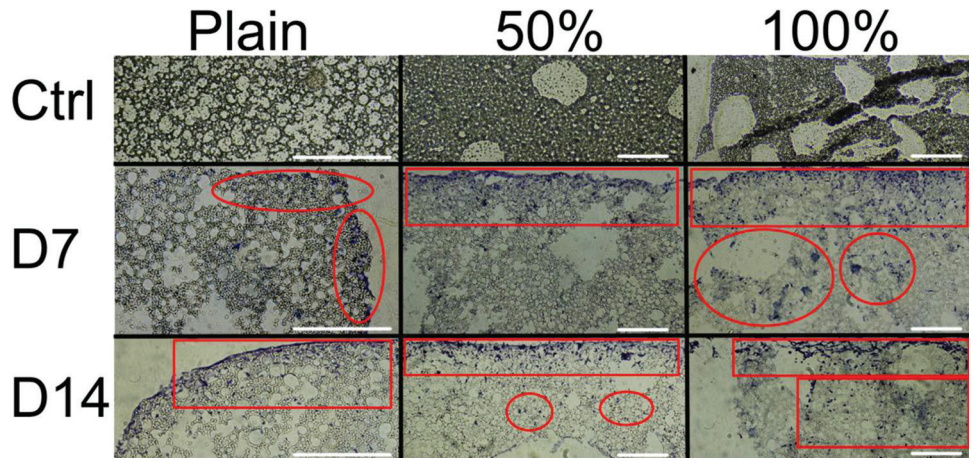

Figure 5. Representative histological sections of plain, 50 wt% and 100 wt% polymerized high internal phase emulsions scaffolds. (Top row) control, cell free sections (Middle and bottom rows) day 7 and 14 ingrowth, respectively. Ingrowth is highlighted in red circled regions. Cells are confined to the top surface in plain scaffolds, whereas infiltration through the material is present in alginate leached scaffolds. The greatest infiltration occurs in the 100 wt% scaffolds. Scale bars 200 μm.

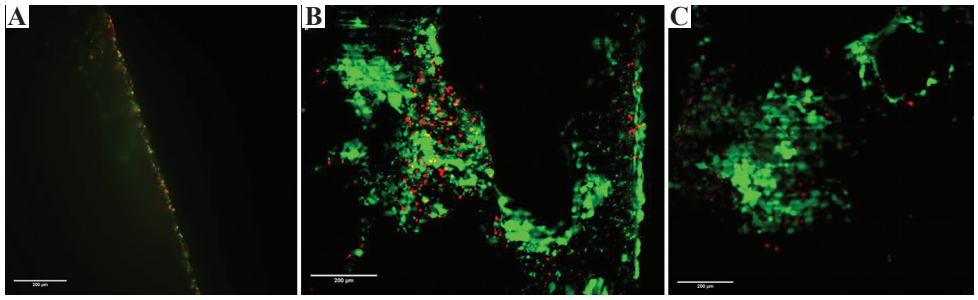

Figure 6. Representative lightsheet microscopy of live (green)/dead (red) staining on polymerized high internal phase emulsions (polyHIPE) scaffolds. Right side of the images is the external surface, further left is deeper into the material. The polyHIPE material auto-fluoresces in the green wavelength. (A) Plain scaffolds – cells were confined to the scaffold surface (B and C) 50 and 100 wt%, respectively – cell ingrowth occurs deep into the material with a lower observed number of dead cells in the 100 wt% composition Scale bars 200 μm.

The effect of porosity on the culture of MLO-A5 post-osteoblast cells was studied, highlighting the potential of this scaffold manufacturing method for bone tissue engineering related applications. We propose alginate porogen leaching as a cheap and simple method to produce additional larger pores within the polyHIPE scaffolds.

We envisage that these porous materials will be useful as 3D substrates for bioprinting. They will allow complex tissues to be engineered that include multiple cell types by combining these new materials with the spatially controlled deposition of cells through bioprinting. In addition, there is an emergent research field exploring formulations of HIPEs that are compatible with bioprinting[34] and this combination will, in our viewpoint, lead to a powerful new hybrid technology to build 3D organs.

To the best of our knowledge, only one previous study has investigated combining particulate leaching with emulsion templating of materials. This approach first sintered poly(methyl methacrylate) (PMMA) beads for 24 h to fuse them together to create a sacrificial mold, then HIPE was poured over these sintered beads and polymerized. Subsequently, the PMMA was dissolved by

ethyl acetate leaving a polyHIPE with ~100 μm macropores from the PMMA beads[50]. While this approach successfully generated multiscale porosity polyHIPEs, it is complex and time consuming. This is due to the extended sintering time and the use of Soxhlet washing to remove the PMMA and residual solvent; both essential steps to form the macropores and minimize cytotoxicity. Furthermore, the 100 μm macropores introduced here are still a limiting factor as vascularization requires larger macropores[6]. In addition, as cellular penetration also depends on pore size and monolith thickness[51,52], ingrowth can be further improved by introducing larger macropores as shown here. Importantly, our findings showing that an increased macroporosity increases cell infiltration agree with those of Paljevac *et al.,* which demonstrates its value in tissue engineering and 3D cell culture[50].

Alternative work within our group has focused on using stereolithography to introduce this larger length-scale hierarchical porosity into polyHIPEs[8-11,13], and various alternative additive manufacturing techniques have also been used by other groups[33,35]. While these approaches produce structures with well-defined architectures; they are not without their limitations. Laser-based systems are expensive to set up and control over the final structure requires time-consuming process optimization. Furthermore, the emulsions scatter light; therefore, for high resolution 3D printing the addition of light-absorbers is needed to control the polymerized region[9]. Therefore, in applications where a multiscale porosity is beneficial, but the final scaffold architecture does not have to be precisely defined, for example, initial 3D cell culture investigations, a more straightforward approach, such as porogen leaching may be desirable.

In emulsion templating, the internal phase acts as a template for the continuous phase to polymerize around. This is like porogen leaching in that the monomer is polymerized around something immiscible with it. The size of the water droplets directly affects the pore size, as does the size of the sugar/salt crystals in porogen leaching. The benefit of using a liquid porogen rather than crystals is that it can be deformed to accommodate a high packing efficiency yielding a much higher porosity. At high water volume ratios (>74%), droplets are forced to deform and become polygonal but remain separated by a thin layer of the monomer/surfactant solution. This thin monomer film is a precursor for interconnectivity as the monomer contracts during polymerization to create interconnecting holes between adjacent pores[31]. However, creating numerous large pores (>200 μm) solely by tailoring the emulsion conditions to have large water droplets will often result in limited pore interconnectivity. This is because the large water droplets are surrounded by a thick monomer film that resists the contraction forces that create interconnectivity during polymerization. On the other hand, smaller droplets of water have a higher surface area, so the monomer layer surrounding it will be thinner and more prone to the contraction forces that create the interconnectivity[25]. As shown here, the addition of a non-emulsion-based method is ideal for creating large pores independent of the emulsion conditions.

Alginate beads with a size distribution between 275 and 780 μm were made by injecting an alginate solution into a calcium chloride solution. The size distribution of the alginate beads represents the range that could be produced when using the fastest injection speed on the mechanical syringe pump and forcing the alginate solution through a 30 G needle. Some of the alginate beads had a slight non-spherical shape, which is most likely because of a combination of high injection speed, the viscosity of the injected alginate solution not having enough time in flight to form a sphere, and the fast gelation of these beads as they hit the calcium chloride solution. It required the maximum injection speed of the pump (0.2195 mL/s through a 3 mL syringe) and small needle size to extrude the viscous alginate solution fast enough to produce the smallest droplets. However, this occasionally caused some alginate solution to leak past the syringe's internal plastic seal during the injection process. In turn, this would reduce the internal syringe pressure and therefore the speed at which the alginate solution was being injected

into the calcium chloride solution, thus forming larger beads.

In initial experiments (data not shown), we produced very large millimeter-sized beads when a slower speed or larger gauge needle was used. Furthermore, very large beads were often created when setting up and removing the syringe as the alginate solution could occasionally drop into the calcium chloride solution; hence, all alginate beads above 780 μm were sieved out after bead manufacture was complete. The alginate beads were not sieved further, as we wanted to preserve the size distribution to create a range of macropores within the polyHIPE; a polydisperse bead distribution should have a better packing efficiency than a monodisperse one yielding an interconnected macropore network throughout the scaffold. However, alternative direct fabrication methods to have tighter control over alginate bead size and shape may be desirable. These could include electrospraying[53] and microfluidics[54] to produce a more monodisperse size distribution.

The ratios of alginate beads (0, 50, and 100 wt%) relative to the initial HIPE weight were chosen as this broad range affords us a baseline understanding of the feasibility of combining alginate bead porogen leaching with emulsion templating and their effect on the polyHIPE scaffold morphology. Here, alginate beads were incorporated into the HIPE at up to 100 wt% of the emulsion with no visual signs of emulsion destabilization. The polymer struts of the polyHIPE surface that has cured against the alginate beads have a smooth surface composed of numerous pores of different sizes. Rather than the classical polyHIPE morphology observed in the bulk of the plain polyHIPE, the pore shape at this interface appears different as the water droplets in the initial emulsion have been pressed and deformed against the smooth alginate surface before polymerization. Regardless of the shape of the alginate bead the polyHIPE retained an open pore surface and overall mirrored the curved shape of the alginate it cured against. The polymerized boundary layer between the alginate surface and polyHIPE had open connected pores. We assume this is because the alginate beads are 97% water and therefore will have a thin layer of water surrounding them. This means that the emulsion interface around these large alginate beads should be the same as if it were a water droplet – it will be surrounded by a thin film of surfactant stabilized monomer that on polymerization would contract to create an open surface porosity. As the alginate beads have been made in a separate process to the emulsion, both the porosity in the polyHIPE from the water droplets and the macropores from the alginate beads can be controlled independently to each other, unlike when heating or solvent destabilization is used[23].

As expected, when porosity increased compressive modulus decreased (**Figure 3**). Interestingly, as porosity increased the standard plasma treatment applied to polyHIPEs to increase hydrophilicity in our group resulted in sample charring (data not shown)[17]. We hypothesize that this is due to the high energy ions in the plasma impacting and accumulating within the polyHIPE macropores introduced by alginate bead leaching, resulting in localized heating and charring. This is supported by greater charring occurring in the 100 wt% than the 50 wt% alginate porogen leached polyHIPE scaffolds, and the apparent localization of the charring to the macropores. In the plain polyHIPEs which do not possess these macropores, these ions are carried over the surface of the polyHIPE meaning that no charring occurs. To alleviate this, the combination of lower power, reduced starting pressure to increase air flow rate, and shorter treatment times were tested, finding that a 70% reduction in power eliminated the charring entirely whilst still reducing the hydrophobicity of the scaffold.

Seeding efficiency was significantly greater in the 100 wt% scaffolds than the plain polyHIPEs as the larger pores allowed cells and media to penetrate the porous network more easily (**Figure 4A**). Although there was no significant difference at day 7, metabolic activity was significantly higher in 100 wt% samples than plain polyHIPEs by day 14. PrestoBlue measures the reduction of resazurin to fluorescent resorufin. This must be completely eluted from the samples for the fluorescence to correlate to the cell number. This is more difficult

in highly porous samples where cells reside deep within the scaffold encased in extracellular matrix than in plain polyHIPE scaffolds where cells are all the outer edges. Therefore, it is likely that cell number could be increasingly underestimated as scaffold porosity increases.

At day 7, mineralized matrix deposition was lower in porogen leached polyHIPEs than plain ones (**Figure 4B and C**). As osteoblasts do not begin to deposit mineralized matrix until confluent[54], the increased potential for ingrowth into porogen leached samples likely meant that MLO-A5 were still in a proliferative state, at this time point, hence the lower calcium deposition. These differences were no longer present by day 14, which indicate a faster rate of matrix deposition in the porogen leached scaffolds in the 2nd week than the plain. Furthermore, a similar quantity of mineralized matrix was deposited in the alginate-leached scaffolds to the plain scaffolds by day 14 despite having a significantly reduced culture area due to the presence of alginate beads during polymerization (up to 50% less total material in the case of the 100 wt% scaffolds). Considering all scaffolds had the same exterior dimensions (5 × 5 × 5 mm), this indicates a better distributed neo-tissue formation throughout the alginate leached scaffolds. Photographs of scaffolds before destaining show how mineral distribution was more uniform in the porogen leached scaffolds at both time points, whereas it was confined to the exterior surfaces in plain scaffolds. These observations on matrix distribution from low magnification photographs agree with the histology and lightsheet microscopy (**Figures 5 and 6)**. In both techniques, cells and matrix in plain polyHIPEs are only apparent on the outer perimeter of the scaffold. In contrast, infiltration readily occurred on porogen leached scaffolds, with the greatest ingrowth occurring on the most porous scaffolds and viable cells being present in the scaffold millimeter(s) from the outer surface. This deeper infiltration likely occurs for two reasons. First, the connected macroporosity left by the alginate beads provides a facile route for cells to enter the bulk of the scaffold during seeding. Second, improved diffusion throughout the scaffold due to the additional macroporosity encourages deeper cell penetration into the polyHIPE network as cells have greater nutrient availability and waste transport in comparison to plain scaffolds at these deeper locations.

In summary, we have shown that alginate-bead porogen-leaching of polyHIPEs can be performed in a single-step process. This quickly and easily produces multiscale porosity scaffolds with pore sizes spanning three orders of magnitude (1 – 1000 μm). This approach enhances initial cell seeding efficiency, promotes ingrowth and uniform matrix deposition, and allows cells to remain viable deep within the scaffold. Overall, these findings have implications in tissue engineering of both bone and other tissues due to the ability to recreate the hierarchical porosities observed in a wide range of natural biological tissues.

Authors' contributions

Conceptualization (RO, GR, FC), data curation (RO), formal analysis (RO, CS, RE), funding acquisition (RO, GR, FC), investigation (RO, CS, RE), methodology (RO, CS, RE), project administration (RO, CS, RE, GR, FC), resources (GR, FC), supervision (RO, CS, GR, FC), validation (RO, CS, RE, GR, FC), visualization (RO), writing – original draft (RO), and writing – review and editing (RO, GR, FC).

Conflicts of interest

The are no conflicts of interest to declare

Acknowledgments

We acknowledge funding from the Engineering and Physical Sciences Research Council (Grant no. EP/L505055/1 and EP/N509735/1) and Biotechnology and Biological Sciences Research Council (Grant no. BB/F016840/1). We also acknowledge the EPSRC Henry Royce Institute funding (Grant No. EP/P02470X/1) for the light sheet microscope.

References

1. Wu S, Liu X, Yeung KW, *et al.*, 2014, Biomimetic Porous Scaffolds for Bone Tissue Engineering. *Materials Sci Eng R*

Rep, 80:1–36.

2. Gupta D, Singh AK, Dravid A, *et al.*, 2019, Multiscale Porosity in Compressible Cryogenically 3D Printed Gels for Bone Tissue Engineering. *ACS Appl Mater Interfaces*, 11:20437–52. DOI: 10.1021/acsami.9b05460
3. Rustom LE, Boudou T, Nemke BW, *et al.*, 2017, Multiscale Porosity Directs Bone Regeneration in Biphasic Calcium Phosphate Scaffolds. *ACS Biomater Sci Eng*, 3:2768–78. DOI: 10.1021/acsbiomaterials.6b00632
4. Woodard JR, Hilldore AJ, Lan SK, *et al.*, 2007, The Mechanical Properties and Osteoconductivity of Hydroxyapatite Bone Scaffolds with Multi-scale Porosity. *Biomaterials*, 28:45–54. DOI: 10.1016/j.biomaterials.2006.08.021
5. Roosa SM, Kemppainen JM, Moffitt EN, *et al.*, 2010, The Pore Size of Polycaprolactone Scaffolds has Limited Influence on Bone Regeneration in an *in vivo* Model. *J Biomed Mater Res A*, 92:359–68. DOI: 10.1002/jbm.a.32381
6. Vand K, Kaplan D, 2005, Porosity of 3D Biomaterial Scaffolds and Osteogenesis. *Biomaterials*, 26:5474–91. DOI: 10.1016/j.biomaterials.2005.02.002
7. Land LQ, Choong C, 2013, Three-dimensional Scaffolds for Tissue Engineering Applications: Role of Porosity and Pore Size. *Tissue Eng Part B Rev*, 19:485-502. DOI: 10.1089/ten.teb.2012.0437
8. Owen R, Sherborne C, Paterson T, *et al.*, 2016, Emulsion Templated Scaffolds with Tunable Mechanical Properties for Bone Tissue Engineering. *J Mech Behav Biomed Mater*, 54:159–72. DOI: 10.1016/j.jmbbm.2015.09.019
9. Sherborne C, Owen R, Reilly GC, *et al.*, 2018, Light-based Additive Manufacturing of PolyHIPEs: Controlling the Surface Porosity for 3D Cell Culture Applications. *Mater Des*, 156:494–503. DOI: 10.1016/j.matdes.2018.06.061
10. Malayeri A, Sherborne C, Paterson T, *et al.*, 2016, Osteosarcoma growth on trabecular bone mimicking structures manufactured via laser direct write. *Int J Bioprint*, 2:67–72. DOI: 10.18063/ijb.2016.02.005
11. Owen R, Sherborne C, Reilly GC, *et al.*, 2015, Data for the Analysis of PolyHIPE Scaffolds with Tunable Mechanical Properties for Bone Tissue Engineering. *Data Brief*, 5:616–20. DOI: 10.1016/j.dib.2015.09.051
12. Paterson TE, Gigliobianco G, Sherborne C, *et al.*, 2018, Porous Microspheres Support Mesenchymal Progenitor Cell Ingrowth and Stimulate Angiogenesis. *APL Bioeng*, 2:026103. DOI: 10.1063/1.5008556
13. Wang AJ, Paterson T, Owen R, *et al.*, 2016, Photocurable High Internal Phase Emulsions (HIPEs) Containing Hydroxyapatite for Additive Manufacture of Tissue Engineering Scaffolds with Multi-scale Porosity. *Mater Sci Eng C*, 67:51–8. DOI: 10.1016/j.msec.2016.04.087
14. Whitely M, Rodriguez-Rivera G, Waldron C, *et al.*, 2019, Porous PolyHIPE Microspheres for Protein Delivery from an Injectable Bone Graft. *Acta Biomat*, 93:169–79. DOI: 10.1016/j.actbio.2019.01.044
15. Lee A, Langford CR, Rodriguez-Lorenzo LM, *et al.*, 2017, Bioceramic Nanocomposite Thiol-acrylate polyHIPE Scaffolds for Enhanced Osteoblastic Cell Culture in 3D. *Biomat Sci*, 5:2035–47. DOI: 10.1039/c7bm00292k
16. Dikici BA, Reilly GC, Claeyssens F, 2020, Boosting the Osteogenic and Angiogenic Performance of Multiscale Porous Polycaprolactone Scaffolds by *in vitro* Generated Extracellular Matrix Decoration. *ACS Appl Mater Interfaces*, 12:12510–24. DOI: 10.1021/acsami.9b23100
17. Dikici BA, Sherborne C, Reilly GC, *et al.*, 2019, Emulsion Templated Scaffolds Manufactured from Photocurable Polycaprolactone. *Polymer*, 175:243–54. DOI: 10.1016/j.polymer.2019.05.023
18. Dikici BA, Dikici S, Reilly GC, *et al.*, 2019, A Novel Bilayer Polycaprolactone Membrane for Guided Bone Regeneration: Combining Electrospinning and Emulsion Templating. *Materials* (*Basel*), 12:12162643. DOI: 10.3390/ma12162643
19. Cameron NR, 2005, High Internal Phase Emulsion Templating as a Route to Well-defined Porous Polymers. *Polymer*, 46:1439–49. DOI: 10.1016/j.polymer.2004.11.097
20. Krajnc PH, 2014, PolyHIPEs from Methyl Methacrylate: Hierarchically Structured Microcellular Polymers with Exceptional Mechanical Properties. *Polymer*, 55:4420–4. DOI: 10.1016/j.polymer.2014.07.007
21. Iand G, Silverstein MS, 2010, Polymerized pickering HIPEs: Effects of synthesis parameters on porous structure. *J Polym Sci Part A Polym Chem*, 48:1516–25. DOI: 10.1002/pola.23911
22. Bokhari M, Carnachan RJ, Przyborski SA, *et al.*, 2007, Emulsion-templated Porous Polymers as Scaffolds for Three Dimensional Cell Culture: Effect of Synthesis Parameters on Scaffold Formation and Homogeneity. *J Mater Chem*, 17:4088–94. DOI: 10.1039/b707499a
23. Carnachan RJ, Bokhari M, Przyborski SA, *et al.*, 2006, Tailoring the Morphology of Emulsion-templated Porous Polymers. *Soft Matter*, 2:608–16. DOI: 10.1039/b603211g
24. Richez A, Deleuze H, Vedrenne P, *et al.*, 2005, Preparation of Ultra-low-density Microcellular Materials. *J Appl Polym Sci*, 96:2053–63. DOI: 10.1002/app.21668
25. Xu H, Zheng X, Huang Y, *et al.*, 2016, Interconnected Porous Polymers with Tunable Pore Throat Size Prepared via

Pickering High Internal Phase Emulsions. *Langmuir*, 32:38–45. DOI: 10.1021/acs.langmuir.5b03037

26. Williams JM, Gray AJ, Wilkerson MH, 1990, Emulsion Stability and Rigid Foams from Styrene or Divinylbenzene Water-in-oil Emulsions. *Langmuir*, 6:437–44. DOI: 10.1021/la00092a026
27. Williams JM, Wrobleski DA, 1988, Spatial Distribution of the Phases in Water-in-oil Emulsions. Open and Closed Microcellular Foams from Cross-linked Polystyrene. *Langmuir*, 4:656–62. DOI: 10.1021/la00081a027
28. Robinson JL, Moglia RS, Stuebben MC, *et al.*, 2013, Achieving Interconnected Pore Architecture in Injectable PolyHIPEs for Bone Tissue Engineering. *Tissue Eng Part A*, 20:1103–12. DOI: 10.1089/ten.tea.2013.0319
29. Knight E, Murray B, Carnachan R, *et al.*, 2011, Alvetex®: Polystyrene Scaffold Technology for Routine Three Dimensional Cell Culture. In: Haycock JW, editor. 3D Cell Culture: Methods and Protocols. Humana Press, Totowa, NJ. pp. 323–40. DOI: 10.1007/978-1-60761-984-0_20
30. Viswanathan P, Johnson DW, Hurley C, *et al.*, 2014, 3D Surface Functionalization of Emulsion-Templated Polymeric Foams. *Macromolecules*, 47:7091–8. DOI: 10.1021/ma500968q
31. Cameron NR, Sherrington DC, Albiston L, *et al.*, 1996, Study of the Formation of the Open-cellular Morphology of Poly(styrene/divinylbenzene) polyHIPE Materials by cryo-SEM. *Colloid Polym Sci*, 274:592–5. DOI: 10.1007/bf00655236
32. Stevens M Mand George J H, 2005, Exploring and Engineering the Cell Surface Interface. *Science*, 310:1135–8.
33. Sears NA, Dhavalikar PS, Cosgriff-Hernandez EM, 2016, Emulsion Inks for 3D Printing of High Porosity Materials. *Macromol Rapid Commun*, 37:1369–74. DOI: 10.1002/marc.201600236
34. Sears N, Dhavalikar P, Whitely M, *et al.*, 2017, Fabrication of Biomimetic Bone Grafts with Multi-material 3D Printing. *Biofabrication*, 9:025020. DOI: 10.1088/1758-5090/aa7077
35. Susec M, Ligon SC, Stampfl J, *et al.*, 2013, Hierarchically Porous Materials from Layer-by-layer Photopolymerization of High Internal Phase Emulsions. *Macromol Rapid Commun*, 34:938–43. DOI: 10.1002/marc.201300016
36. Johnson DW, Sherborne C, Didsbury MP, *et al.*, 2013, Macrostructuring of Emulsion-templated Porous Polymers by 3D Laser Patterning. *Adv Mater*, 25:3178–81. DOI: 10.1002/adma.201300552
37. Lee JM, Ng WL, Yeong WY, 2019, Resolution and Shape in Bioprinting: Strategizing Towards Complex Tissue and Organ Printing. *Appl Phys Rev*, 6:011307. DOI: 10.1063/1.5053909
38. Ng WL, Lee JM, Zhou M, *et al.*, 2020, Vat Polymerization-based Bioprinting Process, Materials, Applications and Regulatory Challenges. *Biofabrication*, 12:022001. DOI: 10.1088/1758-5090/ab6034
39. Zhang J, Hu Q, Wang S, *et al.*, 2020, Digital Light Processing Based Three-dimensional Printing for Medical Applications. *Int J Bioprint*, 6:1–10.
40. Thadavirul N, Pavasant P, Supaphol P, 2014, Development of Polycaprolactone Porous Scaffolds by Combining Solvent Casting, Particulate Leaching, and Polymer Leaching Techniques for Bone Tissue Engineering. *J Biomed Mater Res Part A*, 102:3379–92. DOI: 10.1002/jbm.a.35010
41. Kim TG, Chung HJ, Park TG, 2008, Macroporous and Nanofibrous Hyaluronic Acid/collagen Hybrid Scaffold Fabricated by Concurrent Electrospinning and Deposition/leaching of Salt Particles. *Acta Biomater*, 4:1611–9. DOI: 10.1016/j.actbio.2008.06.008
42. Sin D, Miao X, Liu G, *et al.*, 2010, Polyurethane (PU) Scaffolds Prepared by Solvent Casting/particulate Leaching (SCPL) Combined with Centrifugation. *Mater Sci Eng C*, 30:78–85. DOI: 10.1016/j.msec.2009.09.002
43. Bencherif SA, Braschler TM, Renaud P, 2013, Advances in the Design of Macroporous Polymer Scaffolds for Potential Applications in Dentistry. *J Periodontal Implant Sci*, 43:251–61. DOI: 10.5051/jpis.2013.43.6.251
44. Hutmacher DW, 2001, Scaffold Design and Fabrication Technologies for Engineering Tissues State of the Art and Future Perspectives. *J Biomater Sci Polym Ed*, 12:107–24.
45. Venkatesan J, Bhatnagar I, Manivasagan P, *et al.*, 2015, Alginate Composites for Bone Tissue Engineering: A Review. *Int J Biol Macromol*, 72:269–81.
46. Schindelin J, Arganda-Carreras I, Frise E, *et al.*, 2012, Fiji: An Open-source Platform for Biological-image Analysis. *Nat Methods*, 9:676–82. DOI: 10.1038/nmeth.2019
47. Schneider CA, Rasband WS, Eliceiri KW, 2012, NIH Image to Image J: 25 Years of Image Analysis. *Nat Methods*, 9:671–5. DOI: 10.1038/nmeth.2089
48. Owen R, Bahmaee H, Claeyssens F, *et al.*, 2020, Comparison of the Anabolic Effects of Reported Osteogenic Compounds on Human Mesenchymal Progenitor-derived Osteoblasts. *Bioengineering* (*Basel*), 7:7010012. DOI: 10.3390/bioengineering7010012
49. Linkert M, Rueden CT, Allan C, *et al.*, 2010, Metadata Matters: Access to Image Data in the Real World. *J Cell Biol*, 189:777–82.
50. Paljevac M, Gradišnik L, Lipovšek S, *et al.*, 2018, Multiple-Level Porous Polymer Monoliths with Interconnected Cellular

Topology Prepared by Combining Hard Sphere and Emulsion Templating for Use in Bone Tissue Engineering. *Macromol Biosci*, 18:1700306. DOI: 10.1002/mabi.201700306

51. Hayward AS, Eissa AM, Maltman DJ, *et al.*, 2013, Galactose-functionalized PolyHIPE Scaffolds for Use in Routine Three Dimensional Culture of Mammalian Hepatocytes. *Biomacromolecules*, 14:4271–7. DOI: 10.1021/bm401145x
52. Akay G, Birch MA, Bokhari MA, 2004, Microcellular polyhipe Polymer Supports Osteoblast Growth and Bone Formation *in vitro*. *Biomaterials*, 25:3991–4000. DOI: 10.1016/j.biomaterials.2003.10.086
53. Workman VL, Dunnett SB, Kille P, *et al.*, 2008, On-Chip Alginate Microencapsulation of Functional Cells. *Macromol Rapid Commun*, 29:165–70. DOI: 10.1002/marc.200700641
54. Beck GR Jr., Zerler B, Moran E, 2001, Gene Array Analysis of Osteoblast Differentiation. Cell Growth Differ, 12:61–83.

ORIGINAL ARTICLE

Development of a 3D-printed Medication Label for the Blind and Visually Impaired

Yijun Wong[1], Yihua Xu[2,3], Lifeng Kang[2]*, Kevin Yi-Lwern Yap[4]*

[1]Department of Pharmacy, National University of Singapore, 18 Science Drive 4, Singapore 117543, Singapore

[2]School of Pharmacy, Faculty of Medicine and Health, University of Sydney, Pharmacy and Bank Building A15, Science Road, NSW 2006, Sydney, Australia

[3]College of Pharmaceutical Sciences, Zhejiang University, Hangzhou, 310058, China

[4]Department of Public Health, School of Psychology and Public Health, La Trobe University, Melbourne, Australia

Abstract: This study explored the potential of three-dimensional printing (3DP) technology in producing a three-dimensional (3D) medication label for blind and visually impaired (BVI) patients to ease their drug administration. Different variations of label wordings, dosing instructions, and medication identifiers were designed with reference to guidelines by the American Foundation for the Blind. Shapes and symbols were used as dosing instructions and medication identifiers to the patient's medical conditions. Prototype designs were created with common graphics computer-assisted drafting software and 3D-printed using acrylonitrile butadiene styrene as the polymer filament. Feedback was then obtained from five people with normal vision and four BVI persons. The initial prototype comprised four components, namely, medication name and strength, patient's name, dosing instruction, and medication identifier. A revised label comprising the latter two components was developed after feedback by BVI persons. Words were in all uppercase and regular font type, with a 5-mm center-to-center letter spacing. Elevation heights of the letters alternated between 1 mm and 1.5 mm. A half sphere represented the medication dose unit, while vertical lines and a horizontal center line with alternating elevation of arrowheads represented the frequency of administration and the medication's consumption in relation to food, respectively. Symbols based on target organs were used as medication identifiers. With rapid advancements in 3DP technologies, there is tremendous potential for producing 3D labels in patients' medication management.

Keywords: Blind, Medication label, Pharmacy, Prescription label, Three-dimensional printing, Visually impaired

***Corresponding Authors:** Lifeng Kang, Email: lifeng.kang@sydney.edu.au and Kevin Yi-Lwern Yap, Email: K.Yap@latrobe.edu.au

Received: April 10, 2020**;** ***Accepted:*** April 21, 2020; ***Published Online:*** April 30, 2020

Citation: Wong Y, Xu Y, Kang L, *et al*., 2020, Development of a 3D-printed medication label for the blind and visually impaired, Int J Bioprint, 6(2):276. http://dx.doi.org/10.18063/ijb.v6i2.276

1 Introduction

According to the World Health Organization, there are ~2.2 billion people globally estimated to be blind and visually impaired (BVI), among which majority are 50 years and above[1]. In the United States, ~23.7 million American adults (61% women, 39% men) experience vision loss[2]. The average age of these BVI persons is 62 years[3], which is in sync with the global trend. The risk of vision loss increases exponentially with age due to chronic eye diseases and aging processes[4]. This is of concern as the proportion of the elderly is expected to increase from 617 million (8.5% of the world's population) to nearly 1.6 billion (17%) by the year 2050[5].

While medication compliance is challenging for many patients, this is even more so for BVI patients, who face additional challenges. The World Health Organization defines low vision as acuity <6/18 and blindness as acuity <3/60[6]. When sight is limited or absent, these patients

may not be able to read the text or identify and comprehend important information on conventional printed medication labels[7]. This visual limitation puts them in the same or higher risk than the general population for drug-related problems associated with improper use of medications[8], such as concomitant medication use and consuming wrong dosages[9]. The difficulties experienced by BVI patients are also compounded by other issues, such as similar container shapes and sizes, or being prescribed with multiple medications[6]. Studies have reported that blind Americans have an average of 3.3 health conditions[1]. This is particularly of concern for elderly BVI patients because they tend to have more co-morbidities and more medications because of age.

The most common approach that BVI patients use to read medication labels is having someone else (e.g., caregiver) read to them[10], which creates dependency and undermines self-determination and well-being. This is especially so for individuals who are used to being self-sufficient before suffering from their medical condition. They may feel more diminished and vulnerable as they play a less active role in managing their health[11]. Furthermore, communication challenges arise as information is transcribed from the pharmacist or physician to the patient through a third party[7]. In addition, patient confidentiality is compromised for those who do not wish to have their health information disclosed to others. Their rights to object to disclosure are diminished as they have no other meaningful alternative of reading the medication labels, other than relying on someone else[11].

Other approaches that visually-impaired patients use to manage their medications include the use of handheld magnifiers and reading glasses to enlarge their medication labels, and relying on memory to remember instructions provided during a face-to-face counseling session with their health-care provider, of which the former method is inapplicable for the blind[12]. These methods present risks for these patients, especially those who are prescribed with multiple medications, each with differing instructions.

Several auxiliary communication aids are available, including Braille embossers and Audible Prescription Labeling Systems (APLS). Braille embossers can print medication information and enable information accessibility at will[11]. However, only a small percentage of BVI patients can read Braille[13]. Furthermore, pharmacists are not formally trained to read the Braille printout, thus are unable to ensure information accuracy. Braille printouts are also often bulky and large, thereby challenging the ease of affixation on medications[11]. On the other hand, APLS aids rely on human voice recordings, where an electronic form of prescription information is stored in a microchip that is embedded in the medication label. BVI patients can then use a hand-held reader to decode the label information[11]. However, this is not scalable as reading and comprehension abilities vary among BVI patients[11]. To this end, it is necessary to develop an auxiliary aid that addresses the needs of BVI patients and the limitations of existing aids.

Recently, additive manufacturing, commonly known as three-dimensional printing (3DP) technology has been used widely in various fields, such as manufacturing for product prototyping[14], customization of hearing aids and dental crowns[15], and manufacture of volumetric tactile symbols for tactile maps to teach geography to BVI persons. By harnessing the potential of 3DP technologies, tactile aids may be developed to provide BVI patients with important information regarding their medications through their sense of touch.

Multiple 3DP technologies have been used for biological and medical applications, for example, stereolithography apparatus (SLA) and inkjet printing[16,17]. SLA uses liquid photopolymer resins and laser to create 3D structures. Hou *et al*. utilized SLA to generate a simplified artificial skin model useful for rapidly screening nanoparticles for their transdermal penetration capacity[18]. Inkjet bioprinters deliver a controlled amount of bioink to the desired printing surface, forcing the content to flow continuously or drop out from the nozzle[19]. Xu *et al*. created complex cellular structures by inkjet printing of primary embryonic hippocampal and cortical neurons[20].

On the other hand, fusion deposition modeling (FDM), also known as fused filament fabrication (FFF), using a temperature-controlled extrusion nozzle to deposit a viscous molten thermoplastic polymer into a 3D structure, is among the most widely used 3DP technologies due to its availability and affordability. Rimington *et al*. used skeletal muscle cells in multiple scaffolds printed by FDM with biopolymers to study cellular behaviors[21]. FDM has also been used to manufacture medical instruments[22].

Various FDM printable materials have been reported, for example, ceramics[23,24], metal[25], polylactic acid[26], and acrylonitrile butadiene styrene (ABS)[21,26]. ABS is a strong and durable material. Previously, we used ABS to print molds to make dental anesthetic patches[27] and oral capsules for controlled drug release[28]. Domingo-Espin *et al*. identified several parameters in the FDM printing process that affected the lifespan of ABS materials[29].

In this study, we used an FDM printer to produce 3D ABS medication labels for BVI patients. Our hypothesis is that 3D labels are useful as an aid for BVI patients to manage their medications. In addition, this project aims to identify the features that make a 3D medication label more patient-centric and user-friendly for BVI patients.

2 Materials and methods

2.1 3D label design and printing

Different variations of format parameters, inclusive of the label wordings, dosing instructions, and medication identifiers, were designed, 3D-printed, and visually inspected by the authors at the first instance. The label wordings were designed with reference to format styles recommended by American Foundation for the Blind (AFB) guidelines[10]. Variations in letter case, type style, center-to-center letter spacing, and elevation of letters were printed. For example, medication names were printed in regular and bold fonts, as well as using an all uppercase style compared to an upper- and lower-case combination. The center-to-center spacing of each letter in the word design was varied between 1 mm and 5 mm, using 1-mm intervals, while height variations of the words above 0.38 mm were also printed following previous studies[30]. As the words could not be printed intact if the elevations were <0.5 mm, subsequent word designs were printed in height increments of 0.5 mm, 1.0 mm, and 1.5 mm instead. Word designs with elevations of 0.5 mm, 1.0 mm, and 1.5 mm were printed with a center-to-center letter spacing of 4 mm and 5 mm, since there was residual material in the printed prototype when the letter spacing was <3 mm. For the medication names to be felt more distinctively by touch, letters with alternating height elevations were printed and compared against uniform elevations. For letters with alternating height elevations, different variations in height were also printed.

Shapes and symbols were used to design the dosing instructions of medications. Three parameters were considered. These included the dose units, frequency of administration per day, and how the medication would be taken with regards to food. For dose units, different shapes representing different dosage forms (e.g., half sphere and oval representing a tablet and capsule, respectively) and a universal half-sphere shape to represent all dosage forms were printed. For the frequency of administration, vertical and horizontal lines were printed. For medication timing with reference to food, left and right arrows would indicate that the medication has to be taken before and after food, respectively, while a double-pointing arrow would indicate that the medication could be taken without regard to food. Hence, a 3DP medication label with three half spheres, three vertical lines, and a right arrow would indicate an instruction to take three tablets 3 times a day after food (**Figure 1**).

In addition, symbols were also designed to serve as medication identifiers to the medical condition of the patient. The medication identifiers were classified based on common chronic diseases in Singapore[31] and the target organs of the medications (**Table 1**). All medication identifiers were printed in different sizes and elevation heights.

The printing of the labels followed a standard FDM process, in which the thermoplastic polymer ABS was deposited layer by layer to form the labels[32]. The 3D model of symbols was designed

using AutoCAD 2015 (Autodesk Inc., CA, USA), while words were first typed out in Arial font at size 32 using Inkscape™ vector graphic editor (version 0.91, Sodipodi, USA), then exported as Drawing eXchange Format files (**Figure 2**). AutoCAD was used to create the 3D model of the words at a scale of 0.2 and 0.25 of the original font sizes. AutoCAD design files were exported as stereolithography format to be compatible with the XYZware printer software (version 1.4.1, Kinpo Group, CA, USA). The 3D printing process was carried out using the XYZ da Vinci 1.0 printer (XYZprinting Inc., Lake Forest, CA, USA). The 3D printer operated using FFF technology[29], in which a polymer strand (1.75 mm) was heated

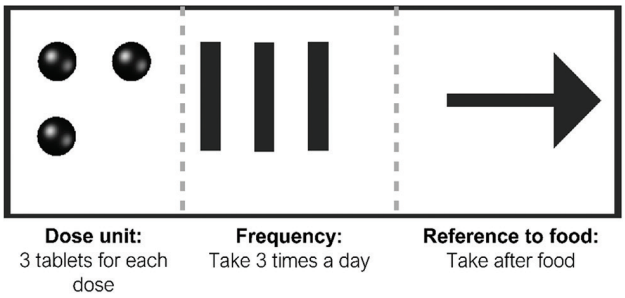

Figure 1. Illustration of directions for use design with the respective symbols' representations.

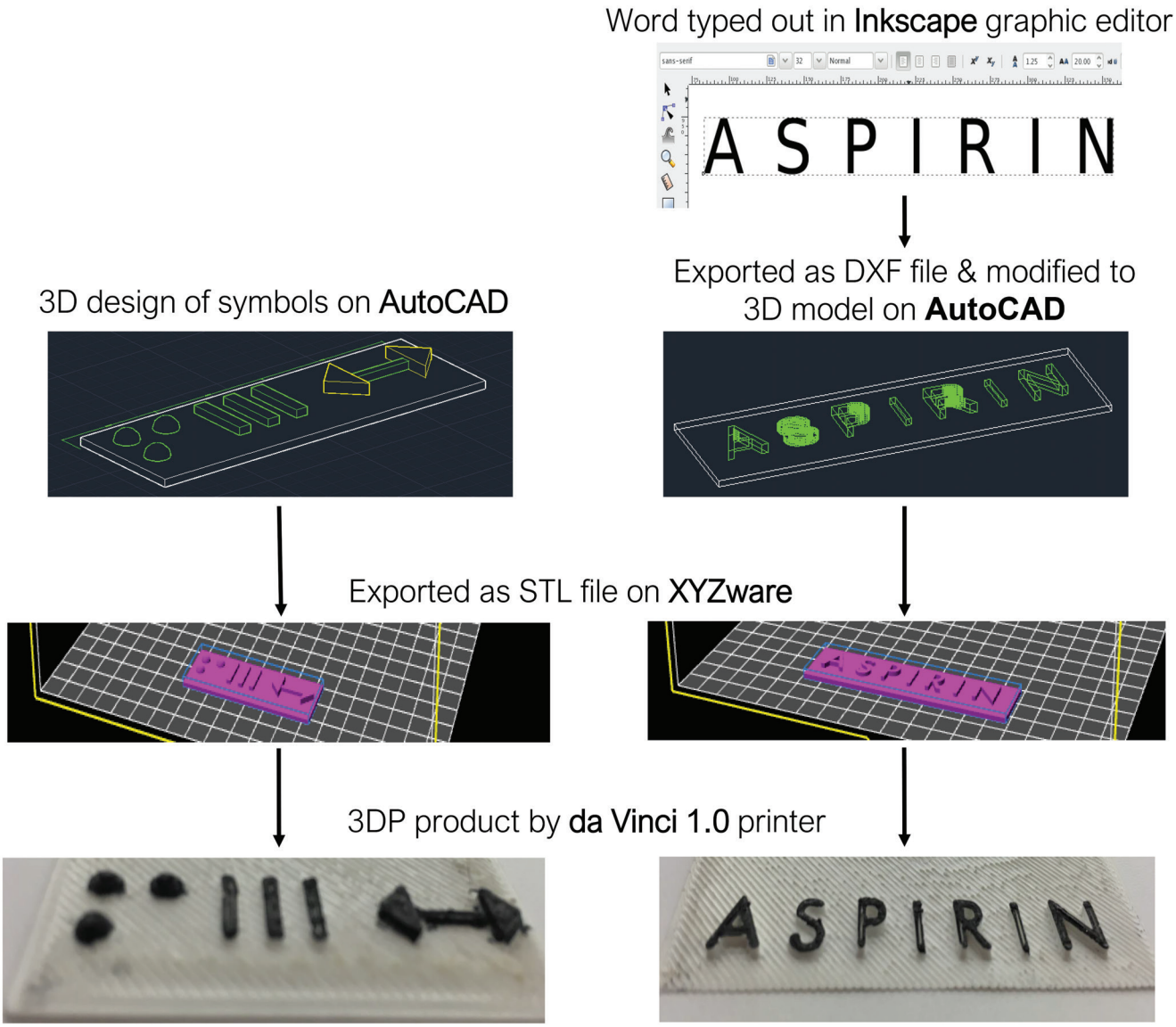

Figure 2. Process of creating the 3D-printed medication label.

Table 1. Formatting variations for the three-dimensional medication label prototypes. The preferred variations are italicized and underlined.

Format parameters	Variations	Pictorial examples of format parameters
Letter case	*All uppercase*; Upper & lower	
Type style	*Regular*; Bold	
Letter spacing	1,2,3,4,*5 mm*	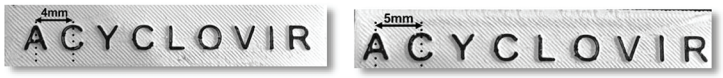
Elevation of letters	Height – 0.38 to 1.5 mm. *1.0 & 1.5 mm* Elevation – Uniform; *Alternating*	Uniform elevation  Alternating elevation  Height variation of alternating elevation: 0.5 & 1.0 mm; *1.0 & 1.5 mm*; 0.6 & 1.2 mm; 0.8 & 1.5 mm
Dose unit	*Universal shape*; Different shapes for different dosage forms	Universal shape (half sphere)  Different shapes for different dosage forms  Tablet (half sphere) Capsule (oval) Syrup (square)
Frequency of administration	*Vertical lines*; Horizontal lines	Vertical lines  Horizontal lines 
Medication to be taken with regards to food	Centre line – Vertical; *Horizontal*	Vertical centre line  Horizontal centre line  Elevation– Uniform; *Alternating*

(*Contd...*)

Table 1. (*Continued*)

Format parameters	Variations	Pictorial examples of format parameters
Type of identifier	Based on disease; *Based on target organ*	Based on disease  Diabetes  Hypertension  Lipid disorders 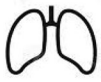 Asthma; Chronic obstructive pulmonary disease (COPD)  Anxiety; Bipolar disorder; Dementia; Depression; Parkinson's disease; Schizophrenia; Stroke  Cancer Based on target organ  Brain  Eye  Lung  Heart  Gastric  Liver  Kidney  Female reproductive  Male reproductive  Blood 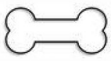 Bone  Muscle
Identifier size	1.0cm x 1.0cm; *1.5cm x 1.5cm*; 2.0cm x 2.0cm	
Elevation	0.38 to 1.5 mm, *1.0mm*	

to semi-solid state and extruded through a small nozzle tip (0.4 mm) on a build platform (20 cm × 20 cm)[33], to form a layer that represented a cross-section of the object. Subsequent layers formed on top of each other in the direction of the z-axis[34]. The polymer filament used was ABS. The layer height of the extruded polymer filament was set to 0.1 (finest) and 3D density was set to high (50%).

2.2 Pilot testing by BVI patients

The variations of the format parameters were shown to five individuals with normal vision to obtain their preferences for the 3DP medication

label. Their preferences for the parameters were combined to develop the initial 3DP label prototype, which was then shown to four target users to obtain their feedback and suggestions for improvement. These users were selected because of their close interactions with BVI patients or personal experiences as BVI persons. They comprised a geriatric pharmacist, an executive from the Dialogue in the Dark (DiD) Singapore[35], and two visually-impaired persons who worked at DiD Singapore as guides.

3 Results

The initial label prototype consisted of four components (medication name and strength, patient's name, dosing instruction, and medication identifier) split into four rows (**Figure 3**). The latter two components were further divided into four columns represented by symbols. From the responses of the five individuals with normal vision, they preferred word designs of a 0.25 scale, in an all uppercase style and regular font type, with a 5-mm center-to-center letter spacing (**Table 1**). It was proposed that the 3DP label be of 10 cm × 6.5 cm × 0.15 cm (length × breadth × height), which meant that each row of the prototype could only comprise up to eight letters. The individuals also preferred that the letters in the word design be of elevation heights that alternated between 1 mm and 1.5 mm.

With regards to the dosing instruction, a universal shape of a half sphere was preferred by the individuals to represent the medication dose unit regardless of dosage form, and vertical lines were preferred over horizontal lines to convey the frequency of administration. A horizontal center line with an alternating elevation of arrowheads and center line was preferred to convey information regarding the medication's consumption time in relation to food, and medication identifiers based on the target organs were preferred over identifiers based on diseases. The optimal size of the medication identifier was 1.5 cm × 1.5 cm and its preferred elevation height was 1 mm. The individuals also preferred a convex elevation for the label prototype.

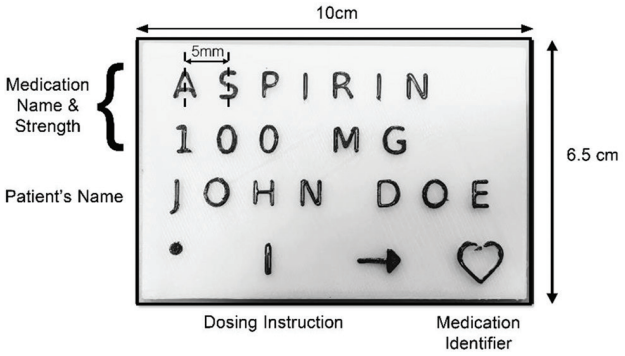

Figure 3. An example of the initial 3D-printed medication label prototype.

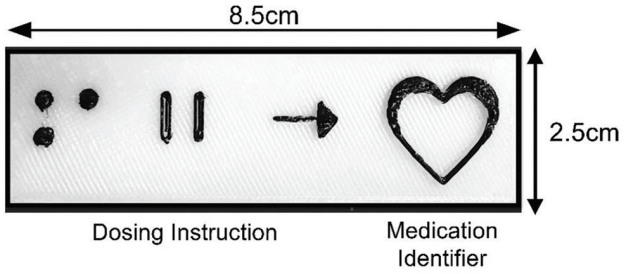

Figure 4. Revised design example of the 3D-printed medication label.

When the initial 3DP medication label prototype was shown to the target users, their feedback was that the words were too small and could not be felt clearly. They suggested that font size and center-to-center letter spacing should be increased but were mindful that the resultant label might be too large to be affixed to the medication packaging if this was done. In terms of word design, short forms of medication names were suggested as some 3DP letters could be confused with each other. Furthermore, using alphabets for the words might not be useful to the elderly BVI population who were English illiterate.

The target users were supportive of the symbols in the 3DP label prototype as they currently used similar approaches to manage their medication regimens. Both the dosing instructions and medication identifiers were well received by the target group as this information was their top priority compared to medication names. However, they suggested that the symbols for the medication identifiers should be enlarged and more elevated to make it more distinctive for the blind and elderly

BVI patients who had a poorer sense of touch. They also noted that if symbols were used in the 3DP medication label, the BVI patients would also need to learn and memorize the meaning of each symbol at the point of dispensing and counseling by the pharmacist.

Based on the feedback provided by the target users, a revised 3DP medication label design was developed. In the new design, medication names were removed since these would still be reflected on the conventional medication label provided at the point of dispensing. However, medication identifiers would be enlarged and more elevated while the dosing instructions would still retain their original format as the initial label prototype (**Figure 4**).

4 Discussion

In this study, a medication label prototype for BVI patients was designed and created through 3DP. From our knowledge, this is the first study that explores the potential of 3DP technology for medication labeling for BVI patients. Feedback from target users showed that 3DP labels would potentially be useful for BVI patients to manage their medications at home. The label could exist alongside the main conventional dispensed label for medications, which contains all legally required information about the patient's prescription, such as the patient's name, medication name and strength, and dosing instructions[36]. However, unlike the conventional label, the 3DP label would only consist of the dosing instructions and medication identifiers. This combination would allow for space optimization on the 3DP label, as well as enable it to be appropriately affixed to the medication packaging. If needed, additional 3DP labels containing other information about the medications (e.g., medication name and strength) could also be provided to patients.

The potential of 3DP technology was explored for medication labeling in this project as it is a rapidly advancing field and may potentially circumvent certain issues with auxiliary aids for communicating medical information to BVI patients. 3D printers cost as low as US$1000 and this is expected to decrease lower as it continues its evolution to be a desk-top commodity[37]. While Braille embossers have been used to print medication information[11], only a small percentage of BVI patients and health-care professionals can read Braille. Furthermore, the setting up of a multilingual APLS system can be useful to a multilingual society, but can be costly[38]. On the other hand, the ease of transmitting and editing designs in CAD files among users[37], such as hospitals and clinics, reduces cost and labor and can allow for standardization of 3DP labels across prescription and non-prescription medications. Moreover, a 3DP label can complement face-to-face counseling, as it allows users to access the medication information independently and at will. When complemented with appropriate training, the 3DP label can be understood by the vast majority of BVI patients and health-care professionals, and it can be affixed securely to medication packaging. In addition, the independence regained by BVI patients in terms of their own medication management can enhance their confidence in managing activities of daily living, strengthening person-centricity, and dignity.

Elevation of alphabets was used for the word design on the 3DP medication label as Braille would not be widely understood by majority of BVI patients. To keep the formatting of words familiar to BVI persons, the word design on the 3DP label was adapted from the format style guidelines by the AFB[10], such as using a sans serif font of more than 18-point size, non-italicized and not condensed, and using black letters on a contrasting white background. Interestingly, the preferred letter case format for the 3DP label was an all uppercase style, which differed from the AFB recommendation guidelines of a combination of upper- and lower-case letters. Our respondents suggested that an all uppercase style was preferred because the lowercase style of the letters "a," "o," and "e" could be confused with each other when relying purely on a sense of touch. However, our results were similar to another study by McDonald *et al*.[39], which also observed that their participants found it easier to interpret capitalized words through touch. There were concerns regarding the

use of English words due to the low literacy levels among elderly BVI patients and those who lost their vision early in their lives. Furthermore, as tactile acuity is lower than the sense of vision[12], the words on the 3DP label could have been too complicated to be perceived by the sense of touch compared to simple tactile shapes.

The use of shapes and symbols for the dosing instructions and medication identifiers were received positively by the target users, probably because it would be more intuitive for those who were less literate[10], and thus could address the challenge of literacy levels in our patients. However, a universal half-sphere shape was preferred over different shapes representing different dosage forms, as it could be confusing to users and required them to remember the meanings of many symbols. It was also suggested that the symbols be enlarged and more elevated so as to improve its user-friendliness for the blind. Our results were similar to another study by Ramsamy-Iranah *et al*.[40], which suggested that a larger height contrast for 3D symbols was more easily differentiated from other components by the blind. These findings reflect the need for a solution that is able to provide comprehensive medication information to BVI patients, yet simple in delivery. Such a solution would require trade-offs, underpinned by harmony between information comprehensiveness and individual intuition. The trade-offs for 3DP medication labels to be implemented in clinical practice would be the size of the labels and the high initial costs of producing it, which would require a decision on its cost-benefit by target end-users and the health-care system.

There were several limitations in this project. As this was a proof-of-concept project, the 3D printer used was not a high-end product. As such, the print resolution by the FFF was limited by nozzle diameter and resulted in higher layer thickness; hence, only elevations of some increments could be printed, and this also led to a poorer resolution of the printed objects. In addition, the deformation of the 3DP products occurred, which led to some components not being produced in alignment with the design. This contributed at times to inadequate separation among letters and between letters and the background. However, the best variations of the 3DP labels were shown to the target users and it was also communicated that the labels were only a prototype and would be more aesthetically pleasing with improvements in technology with time. In addition, feedback could only be obtained from a small sample size. Future work could further identify the perceptions and preferred formatting parameters of the 3DP label in a larger patient cohort, and the role of 3DP labels in complementarity with the main dispensing labels and other auxiliary approaches for BVI patients to manage their medications could also be studied.

5 Conclusion

The label consists of dosing instructions and medication identifiers that are represented by shapes and symbols. In addition, several features that make the 3DP label more patient-centric and user-friendly for BVI patients have been identified. With future advancements in 3DP technologies, there is great potential to produce 3DP labels in patients' medication management, so as to transform the last-mile delivery of health-care services by enabling patient independence and ownership against the backdrop of an aging population.

Acknowledgement

The authors thank the support provided by the Dialogue in the Dark (DiD) Singapore and School of Pharmacy, University of Sydney.

References

1. World Health Organization, 2019, Blindness and Vision Impairment. Available from: https://www.who.int/news-room/fact-sheets/detail/blindness-and-visual-impairment. [Last accessed on 2020 Apr 28].
2. American Foundation for the Blind, 2020, Facts and Figures on Adults with Vision Loss. American Foundation for the Blind, Arlington County. Available from: http://www.afb.org/info/blindness-statistics/adults/facts-and-figures/235. [Last accessed on 2020 Apr 19].
3. Zuckerman DM, 2020, Blind Adults in America: Their Lives and Challenges. Available from: http://center4research.org/wp-content/uploads/2010/05/blind02041.pdf. [Last accessed

on 2020 Apr 19].

4. Orrico KB, 2013, Caring for Visually Impaired Patients. *J Am Pharm Assoc*, 53:e142–50.
5. Cire B, 2016, World's Older Population Grows Dramatically. Available from: https://www.nih.gov/news-events/news-releases/worlds-older-population-grows-dramatically. [Last accessed on 2020 Apr 19].
6. World Health Organization, 2020, Change the Definition of Blindness. World Health Organization, Geneva. Available from: https://www.who.int/blindness/Change the Definition of Blindness.pdf. [Last accessed on 2020 Apr 19].
7. Sansgiry SS, Pawaskar MD, Bhounsule P, 2012, Over-the-counter Medication Purchase and Use by Blind Consumers. *J Health Care Poor Underserved*, 23:1048–57. DOI: 10.1353/hpu.2012.0095.
8. Wong TY, Chong EW, Wong WL, *et al.*, 2008, Prevalence and Causes of Low Vision and Blindness in an Urban Malay Population: The Singapore Malay Eye Study. *Arch Ophthalmol*, 126:1091–9. DOI: 10.1001/archopht.126.8.1091.
9. Zheng Y, Lavanya R, Wu R, *et al.*, 2011, Prevalence and Causes of Visual Impairment and Blindness in an Urban Indian Population: The Singapore Indian Eye Study. *Ophthalmology*, 118:1798–804. DOI: 10.1016/j.ophtha.2011.02.014.
10. American Foundation for the Blind, 2020, Guidelines for Prescription Labeling and Consumer Medication Information for People with Vision Loss. American Foundation for the Blind, Arlington County. Available from: https://www.afb.org/blindness-and-low-vision/your-rights/rx-label-enable-campaign/guidelines-prescription-labeling. [Last accessed on 2020 Apr 19].
11. Little J, 2006, Effective and Confidential Communication of Prescription Information: Accommodating the Blind and Visually-impaired. In: Mann WC, Helal AA, editors. Promoting Independence for Older Persons with Disabilities: Selected Papers from the 2006 International Conference on Aging. Disability and Independence. IOS Press,US.
12. McMahon JM, Curtis A, 2009, Methods of Reading Information on Labels of Prescription Medications by Persons Who Are Visually Impaired. *J Vis Impair Blind*, 103(5):303–8. DOI: 10.1177/0145482x0910300508.
13. Massof RW, 2009, The Role of Braille in the Literacy of Blind and Visually Impaired Children. *Arch Ophthalmol*, 127(11):1530–1. DOI: 10.1001/archophthalmol.2009.295.
14. Kaur S, 2012, How is Internet of the 3D Printed Products Going to Affect Our Lives? Pushing Frontiers with the First Lady of Emerging Technologies. *IETE Tech Rev*, 29(5):360–4. DOI: 10.4103/0256-4602.103164.
15. Rengier F, Mehndiratta A, von Tengg-Kobligk H, *et al.*, 2010, 3D Printing Based on Imaging Data: Review of Medical Applications. *Int J Comput Assist Radiol Surg*, 5(4):335–41. DOI: 10.1007/s11548-010-0476-x.
16. Gu BK. Kwon K, Park S.J., *et al*., 2018, 3D Bioprinting Technologies for Tissue Engineering Applications, Advances in Experimental Medicine and Biology. In: Chun HP, Kwon I, Khang G, editors. Cutting-Edge Enabling Technologies for Regenerative Medicine. Vol. 1078. Springer, Berlin. DOI: 10.1007/978-981-13-0950-2.
17. Mehrban N, Teoh GZ, Birchall MA, 2016, 3D Bioprinting for Tissue Engineering: Stem Cells in Hydrogels. *Int J Bioprint*, 2(1):20. DOI: 10.18063/ijb.2016.01.006.
18. Hou X, Liu S, Wang M, *et al.*, 2016, Layer-by-Layer 3D Constructs of Fibroblasts in Hydrogel for Examining Transdermal Penetration Capability of Nanoparticles. *SLAS Technol*, 22(4):447–53. DOI: 10.1177/2211068216655753.
19. Hong N, Yang GH, Lee J, *et al.*, 2018, 3D Bioprinting and its *In Vivo* Applications. *J Biomed Mater Res B Appl Biomater*, 106(1):444–59.
20. Xu T, Gregory CA, Molnar P, *et al.*, 2006, Viability and Electrophysiology of Neural Cell Structures Generated by the Inkjet Printing Method. *Biomaterials*, 27(19):3580–8. DOI: 10.1016/j.biomaterials.2006.01.048.
21. Rimington RP, Capel AJ, Christie SD, *et al.*, 2017, Biocompatible 3D Printed Polymers Via Fused Deposition Modelling Direct C2C12 Cellular Phenotype *In Vitro*. *Lab Chip*, 17(17):2982–93. DOI: 10.1039/c7lc00577f.
22. Culmone C, Gand S, Breedveld P, 2019, Additive Manufacturing of Medical Instruments: A State-of-the-Art Review. *Addit Manuf*, 27:461–73. DOI: 10.1016/j.addma.2019.03.015.
23. Swee LS, Wai YY, Florencia EW, *et al.*, 2017, Direct Selective Laser Sintering and Melting of Ceramics: A Review. *Rapid Prototyp J*, 23(3):611–23.
24. Galante R, Figueiredo-Pina C, Serro AP, 2019, Additive Manufacturing of Ceramics for Dental Applications: A Review. *Dent Mater*, 35(6):825–46. DOI: 10.1016/j.dental.2019.02.026.
25. Yu WH, Sing SL, Chua CK, *et al.*, 2019, Particle-Reinforced Metal Matrix Nanocomposites Fabricated by Selective Laser Melting: A State of the Art Review. *Prog Mater Sci*, 104:330–79. DOI: 10.1016/j.pmatsci.2019.04.006.
26. Goh GD, Yap YL, Tan HK, *et al.*, 2020, Process-Structure-Properties in Polymer Additive Manufacturing via Material Extrusion: A Review. *Crit Rev Solid State Mate Sci*, 45(2):113–33. DOI: 10.1080/10408436.2018.1549977.

27. Ou YH, Ou YH, Gu J*, et al.*, 2019, Personalised Anaesthetic Patches for Dental Applications. *Int J Bioprint*, 5:15. DOI: 10.18063/ijb.v5i2.203.
28. Lim SH, Chia SM, Kang L, *et al.*, 2016, Three-Dimensional Printing of Carbamazepine Sustained-Release Scaffold. *J Pharm Sci*, 105(7):2155–63. DOI: 10.1016/j.xphs.2016.04.031.
29. Domingo-Espin M, Travieso-Rodriguez JA, Jerez-Mesa R, *et al.*, 2018, Fatigue Performance of ABS Specimens Obtained by Fused Filament Fabrication. *Materials*, 11(12):2521. DOI: 10.3390/ma11122521.
30. Berla EP, 1982, Haptic Perception of Tangible Graphic Displays. In: Wand S, Foulke E, editors. Tactual Perception: A Sourcebook. Cambridge University Press, Cambridge. pp. 364–86.
31. Ministry of Health Singapore, 2020, Chronic Disease Management Programme (CDMP). Ministry of Health Singapore, Singapore. Available from: https://www.moh.gov.sg/policies-and-legislation/chronic-disease-management-programme-(cdmp). [Last accessed on 2020 Apr 19].
32. ASTM, 2015, ISO/ASTM52900-15 Standard Terminology for Additive Manufacturing-General Principles-Terminology. Available from: https://www.astm.org/standards/isoastm52900.htm. [Last accessed on 2020 Apr 19].
33. XYZPrinting, 2020, da Vinci 1.0. Available from: https://www.xyzprinting.com/en-us/product/da-vinci-1-0. [Last accessed on 2020 Apr 19].
34. Giannatsis Jand Dedoussis V, 2009, Additive Fabrication Technologies Applied to Medicine and Health Care: A Review. *Int J Adv Manuf Technol*, 40(1-2):116–27. DOI: 10.1007/s00170-007-1308-1.
35. Ngee Ann Polytechnic, 2020, Dialogue in the Dark. Available from: http://www.dialogueinthedark.com.sg. [Last accessed on 2020 Apr 19].
36. The United States Pharmacopeial Convention, 2012, Prescription Container Labeling. Pharmacopeia and National Formulary, United States. Available from: https://www.usp.org/sites/default/files/usp/webform/c17.pdf. [Last accessed on 2020 Apr 19]. DOI: 10.4135/9781412963855.n1200.
37. Campbell T, Williams C, Ivanova O, *et al*., Could 3D Printing Change the World? Technologies, Potential, and Implications of Additive Manufacturing. Available from: http://www.globaltrends.thedialogue.org/wp-content/uploads/2014/11/could-3d-printing-change-the-world-technologies-potential-and-implications-of-additive-manufacturing.pdf. [Last accessed on 2020 Apr 19]. DOI: 10.1089/3dp.2014.1501.
38. Englehardt JB, Allnatt R, Mariano A, *et al.*, 2001, An Evaluation of the Functionality and Acceptability of the Voice Prescription Label. DOI: 10.1177/0145482X0109501108.
39. McDonald S, Dutterer J, Abdolrahmani A, *et al.*, 2014, Tactile Aids for Visually Impaired Graphical Design Education. In: The 16th International ACM SIGACCESS Conference on Computers and Accessibility. ACM, Rochester, New York, USA. pp. 275–6. DOI: 10.1145/2661334.2661392.
40. Ramsamy-Iranah S, Maguire M, Gardner J, *et al.*, 2016, A Comparison of Three Materials Used for Tactile Symbols to Communicate Colour to Children and Young People with Visual Impairments. *Br J Vis Impair*, 34(1):54–71. DOI: 10.1177/0264619615610161.

INTERNATIONAL JOURNAL OF BIOPRINTING

ISSN (print): 2424-7723

ABOUT THE JOURNAL

International Journal of Bioprinting is a biannual, double-blind peer-reviewed, open access journal. This journal focuses on the use of 3D printing technology with materials that incorporate viable living cells or biological elements to produce tissue or biotechnological products. Further discourses and technological advancements in bioprinting are the goals behind acceptance of high-quality basic and applied research: from concept creation to fabrication of the bioprinting process, associated clinical applications as well as social implications.

Whioce Publishing, official publisher for the journal welcomes researchers to submit their papers relevant to bioprinting for consideration via **http://ijb.whioce.com/** For general enquiries and order for prints and reprints, please write in to **IJB@whioce.com** for a fast response.

SUBMIT YOUR PAPERS HERE

WHIOCE
PUBLISHING PTE. LTD.

ABOUT THE PUBLISHER

Whioce Publishing in Singapore is a registered publisher of excellent quality academic journals for an international readership. We deliver exceptional editorial support for the advancement and dissemination of scientific research by linking readers and researchers with networks and industries. We have ambitions to get our journals indexed in prominent databases such as EI, SCI, SSCI and AHCI, thereby aiming to be a first-class knowledge platform for researchers worldwide.

Whioce Publishing also engages in publishing e-books, organizing academic conferences and educational trainings, and providing translational services.

International Journal of Bioprinting is an
independent open access journal published
by Whioce Publishing Pte.Ltd.

WHIOCE PUBLISHING PTE. LTD.
PROVIDING
FIRST-CLASS SCIENTIFIC INFORMATION
FOR TOP SCHOLARS

Whioce Publishing Pte.Ltd.
7030 Ang Mo Kio Avenue 5
#04-15 Northstar@AMK
Singapore 569880
Tel: +65 65702707/65702718
Fax: +65 65702803

See **www.whioce.com/contact** for a full list of offices and contact information.

Whioce Publishing Pte.Ltd. is a company registered in Singapore (No. 201427293E), whose registered office is at 7030 Ang Mo Kio Avenue 5 #04-15 Northstar@AMK Singapore 569880